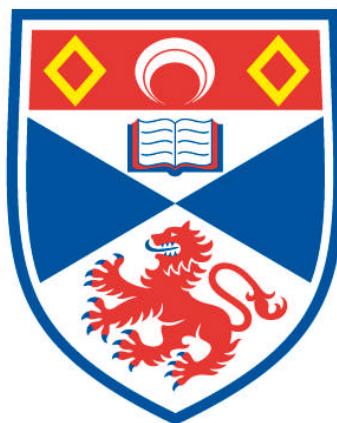


**THE PROMOTING ROLE OF AU IN THE PD-CATALYSED
SYNTHESIS OF VINYL ACETATE MONOMER**

Thomas Graham Owens

**A Thesis Submitted for the Degree of PhD
at the
University of St Andrews**



2007

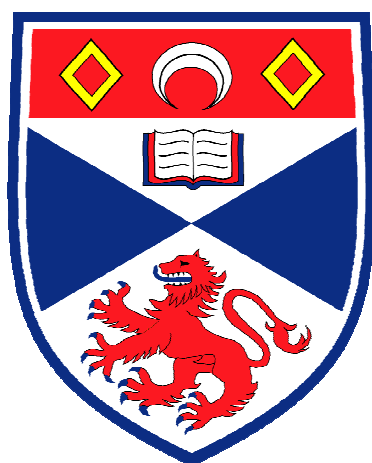
**Full metadata for this item is available in
Research@StAndrews:FullText
at:**

<http://research-repository.st-andrews.ac.uk/>

Please use this identifier to cite or link to this item:

<http://hdl.handle.net/10023/352>

This item is protected by original copyright



University
of
St Andrews

The promoting role of Au in the Pd-catalysed synthesis of Vinyl Acetate Monomer

Thesis submitted in accordance with the requirements
Of the University of St. Andrews for the degree
Of Doctor of Philosophy

Thomas Graham Owens

October 2006

Declaration

I, Thomas Owens, hereby certify that this thesis, which is approximately 47,000 words in length, has been written by me, that it is the record of work carried out by me and has not been submitted in any previous application for a higher degree.

Date:

Signature of Candidate:

I was admitted as a research student in October 2002 and as a candidate for the degree of PhD in October 2002. The higher study for which this is a record was carried out in the University of St. Andrews between 2002 and 2006.

Date:

Signature of Candidate:

I hereby certify that the candidate has fulfilled the conditions of the Resolution and Regulations appropriate for the degree of PhD in the University of St. Andrews and that the candidate is qualified to submit this thesis in application for that degree

Date:

Signature of Supervisor:

In submitting this thesis to the University of St Andrews I wish access to it to be subject to the following conditions: for a period of 2 years from the date of submission, the thesis shall be withheld from use. I understand, however, that the title and abstract of the thesis will be published during this period of restricted access; and that after the expiry of this period the thesis will be made available for use in accordance with the regulations of the University Library for the time being in force, subject to any copyright in the work not being affected thereby, and a copy of the work may be made and supplied to any bona fide library or research worker, that my thesis will be electronically accessible for personal or research use, and that the library has the right to migrate my thesis into new electronic forms as required to ensure continued access to the thesis. I have obtained any third-party copyright permissions that may be required in order to allow such access and migration.

Date:

Signature of Candidate:

Acknowledgements

Thanks must first go to my lab group in St. Andrews, particularly my supervisor, Dr. Chris Baddeley, for all his tireless work. Without his energy and enthusiasm this project would not be half of what it is and I thank him immensely for that. Thanks must also go to Tim Jones, Aoife Trant and Steve Francis for their help with the chemistry side of the project and making the lab such an enjoyable place to work.

An enormous thank you must go to my family, particularly my parents, who have supported me, both emotionally and financially, not just during my PhD but for my entire life. Without their support and love I would not have had the opportunities that I have and words simply cannot express my gratitude to them. Huge thanks to Lil, Gareth and G'Ma (and, of course, Spike) for simply being there when I needed them. A special mention must go to Rebecca who knows how special she is to me. Thank you for your patience during the last few months whilst I have been trying to finish and also for just being you and making me smile so much.

Thanks to everybody else who has been a part of my life during the four years I have been working on this project (and before) for all the good times. Particularly to Stu with whom I shared many a game of golf and plenty of inane and pointless, though thoroughly enjoyable, banter and to Louise who was there throughout all those long nights and stressful weeks and was always on hand when needed.

Finally, thanks must go to BP and EPSRC who have provided financial assistance and to CCLRC Daresbury for MEIS facility time. Thanks also to Bruce Williams at BP in Hull and Paul Bailey and Tim Noakes at Daresbury for their assistance with data acquisition and for many useful discussions throughout my PhD.

THE PROMOTING ROLE OF AU IN THE PD-
CATALYSED SYNTHESIS OF VINYL ACETATE
MONOMER

ABSTRACT

The growth of Au on Pd{111} has been studied by Medium Energy Ion Scattering (MEIS) and Scanning Tunnelling Microscopy (STM). A subsurface alloy has been identified with a structure different to that of either Pd or Au. The adsorption of acetic acid on Au/Pd bimetallic surfaces causes significant segregation of Pd to the top two layers of the surface. Acetic acid adsorption at 300 K occurs via two competing pathways on Au/Pd{111}. One pathway, involving the formation of adsorbed acetate, is observed at all compositions. A second pathway also occurs on Pd-rich surfaces whereby $\text{CO}_{(a)}$ and $\text{O}_{(a)}$ is formed at 300 K. The presence of Au quenches the rate of decomposition of adsorbed acetate. Acetate decomposition results in the formation of clusters which we assign to surface carbon and the presence of this surface carbon may quench the pathway to the formation of $\text{CO}_{(a)}$ from acetic acid. Deposition of K on the Au/Pd{111} bimetallic surface at room temperature also results in the segregation of Pd{111} to the surface. However the net effect of adsorbing acetic acid on K/Au/Pd{111} is that there is no real segregation of Pd – in contrast to the Au/Pd{111} system in the absence of K. A potassium carbonate species is formed on clean Pd{111} (and Au/Pd{111} surfaces when there is a significantly low (<10%) amount of Au in the surface layer). In cases of high Au coverage the carbonate is not formed upon addition of K. Dosing acetic acid onto the K/Au/Pd{111} surface results in the formation of a potassium acetate species and the loss of some carbonate. The process proceeds more rapidly on the more Pd-rich surfaces. Heating of the AcOH/K/Au/Pd{111} surface from room temperature results in the loss or decomposition of an acetate species at low temperature (*ca.* 500 K) followed by the decomposition of carbonate at higher temperature (*ca.* 700 K).

Abbreviations

AcOH	Acetic acid
AcOK	Potassium acetate
AES	Auger Electron Spectroscopy
AFM	Atomic Force Microscopy
CCLRC	Council for the Central Laboratory of the Research Councils
DFT	Density Functional Theory
DRIFTS	Diffuse Reflectance Infra-red Fourier Transform Spectroscopy
EDA	Ethylidene diacetate
EXAFS	Extended X-ray Absorption Fine Structure
fcc	face-centred cubic
FTIR	Fourier Transform Infra-Red
hcp	hexagonal close packed
(HR)EELS	(High Resolution) Electron Energy Loss Spectroscopy
L	Langmuir = 1×10^{-6} Torr.s
LEED	Low Energy Electron Diffraction
LEIS	Low Energy Ion Scattering
MEIS	Medium Energy Ion Scattering
ML	Mono-Layer
RAIRS	Reflection-Adsorption Infra-Red Spectroscopy
RBS	Rutherford Backscattering Spectroscopy
RDS	Rate Determining Step
STM	Scanning Tunnelling Microscopy
TPD	Temperature Programmed Desorption
UHV	Ultra-High Vacuum
UPD	Under-Potential Deposition
VA/VAM	Vinyl acetate / vinyl acetate monomer
XPS	X-ray Photoelectron Spectroscopy

Table of Contents

CHAPTER 1: Introduction and Literature Survey	1
1.1 Surfaces	1
1.2 VAM and its importance	5
1.3 VAM synthesis through the ages	6
1.4 Acetate on monometallic surfaces	22
1.5 Bimetallic Catalysis	40
1.6 K as a promoter on Pd and Au surfaces	57
1.7 Thesis synopsis	65
1.8 References	68
CHAPTER 2: Experimental Techniques	69
2.1 Temperature Programmed Desorption (TPD)	69
2.2 Low Energy Electron Diffraction (LEED)	72
2.3 Auger Electron Spectroscopy (AES)	81
2.4 Scanning Tunnelling Microscopy (STM)	85
2.5 Medium Energy Ion Scattering (MEIS)	92
2.6 Reflection-Absorption Infra-Red Spectroscopy (RAIRS)	116
2.7 Experimental set-up and sample preparation	121
2.8 References	123
CHAPTER 3: Au/Pd{111}	124
3.1 Introduction	124
3.2 Experimental section	125
3.3 Results	130
3.4 Discussion	153
3.5 Conclusion and future work	161
3.6 References	162

CHAPTER 4: AcOH/C/Au/Pd{111}	163
4.1 Introduction	163
4.2 Experimental section	165
4.3 Results	168
4.4 Discussion	184
4.5 Conclusion and future work	194
4.6 References	195
CHAPTER 5: AcOH/K/Au/Pd{111}	196
5.1 Introduction	196
5.2 Experimental section	197
5.3 Results	200
5.4 Discussion	219
5.5 Conclusion and future work	227
5.6 References	229
CHAPTER 6: Summary, Future Work and Publications	230
6.1 Summary	230
6.2 Future Work and Publications	233

CHAPTER 1: Introduction and Background

1.1 Surfaces

Reactions and processes occurring at the surfaces of metals and other materials encompass a number of fields, of which some of the most researched and important are heterogeneous catalysis, materials science and semi-conductor technology. The surface of the materials in each of these cases plays a pivotal role in directing the process down a particular path due to the fact that the surface is, obviously, the first part of the material to come into contact with any external species or reaction process. It has been well documented throughout the years that the surface of a material has different properties, both physical and chemical, from the bulk of the same material due primarily to the presence of a third dimension in the bulk, which is missing from the surface. This third bulk dimension, in essence, “locks” the bulk into a particular conformation whereas the top-most surface atoms can relax from their ideal bulk positions, giving rise to distinct electronic surface states which can be utilised. The creation of these states leads to a high amount of free energy on the surface, leading to a vastly increased reactivity at the surface.

Lowering the Gibbs free energy is the driving force for any chemical reaction but any process at a surface is highly complex dynamically as the top-most atoms are not rigidly held or static throughout the reaction but free to move (albeit restrictedly). This leads on to the fact that all surfaces (particularly metal ones) are dynamic in nature and their structures are known to be conditional upon their current environment. The nature of metal surfaces can therefore be vastly altered, which can result in the lowering of the surface free energy through relaxation and reconstruction. Certain previously inaccessible crystal planes can also be exposed which may have more reactivity towards certain substrates, thus increasing the activity of the surface.

Heterogeneous catalysis is a very important commercial and industrial process, responsible for a significant fraction of the output of the chemical industry. It proceeds by promoting a reaction by the addition of a substance (usually a metal in fine form) which itself is returned intact at the end of the reaction. The mechanism for this generally involves the provision of a surface by the metal on which the reaction can take place, often at vastly increased rates. This has led to two distinct but compatible types of research. The first type consists of the development of existing catalytic processes to maximise yield, efficiency and, ultimately, profit. This may involve optimising of reaction conditions and catalytically active materials for a known process, similar to the process development part of the drug and pharmaceutical industry. Other research focuses on the fundamental understanding of the surface and surface-adsorbate interactions, which will ultimately lead to the improvement of current processes and the ability to devise new processes from first principle understanding. This is done, primarily, by using idealised systems in which metal single crystals replace metallic particles and real surfaces. Single crystals are able to mimic, with differing degrees of success, “real” systems and are studied under ultra high vacuum (UHV) systems, which are chemically “clean”. This kind of study enables a fundamental understanding of atomic scale properties to be garnered. These understandings include knowledge of how and why processes take place on an atomic scale (mechanisms and kinetics for example), adsorbate-surface interactions and position of catalytically active sites. We may also gain insight into other factors that may be affected by substrates, such as changes in kinetics, catalyst activity and mechanism of a reaction.

The major drawbacks of this method, such as need for very high sensitivity of techniques and the fact that the sample area investigated is very small, are being

overcome more and more successfully with the development of new surface science techniques. Techniques nowadays are capable of investigating the properties of a surface down to the atomic and molecular levels and characterisation of surfaces is commonplace as a result of these techniques, some of which are sensitive enough to probe only the top-most layer, providing vital information about the surface quickly and reliably. Although, no one technique is capable of determining all the information required, combinations of techniques can be used together to build up a picture of the surface structure and composition as well as information about the reactions and properties associated with a given surface. This multi-disciplinary approach is becoming more refined on a regular basis and the number of techniques available is increasing every day.

A table of some of the more common techniques, including their physical basis and the information obtained from them can be found in Table 1.1.1 overleaf.

Zaera has recently published a paper entitled “*The surface chemistry of catalysis: new challenges ahead*”¹ in which he detailed the key directions in surface science for the advancement of the field of catalysis over the next few decades. The development of some of these techniques is critical to the fundamental understanding of surface catalysis.

Acronym	Technique	Physical Basis	Information Obtained
TPD	Temperature Programmed Desorption	Thermally induced desorption or decomposition of adsorbed species	Adsorption energies and composition of adsorbed species
LEED	Low Energy Electron Diffraction	Elastic backscattering of low energy electrons forming a diffraction pattern	Structure of surface and adsorbed overlayers
AES	Auger Electron Spectroscopy	Emission of electrons from surface atoms by electron, X-Ray or ion bombardment	Elemental analysis
STM	Scanning Tunnelling Microscopy	High resolution surface probing using the transfer of electrons between two close conducting surfaces	Surface and adsorbed overlayer structure down to atomic resolution
MEIS	Medium Energy Ion Scattering	Elastic and Inelastic scattering of medium energy ion beam (H^+ or He^+) by surface and bulk atoms	Structural and compositional analysis of surface and close sub-surface layers
RAIRS	Reflection Adsorption Infra-Red Spectroscopy	Vibrational excitation of surface atoms and adsorbed species using IR radiation	Structure and bonding of adsorbed species
XPS	X-Ray Photoelectron Spectroscopy	Emission of electrons from surface atoms by high frequency radiation	Surface and bulk electronic structure, surface composition and bonding environment
HREELS	High Resolution Electron Energy Loss Spectroscopy	Vibrational excitation of surface atoms and adsorbed species by inelastic reflection of low energy electrons	Structure and bonding of adsorbed species
EXAFS	Extended X-Ray Absorption Fine Structure	Interference effects during X-Ray emission	Atomic arrangement of surface and adsorbed species

Table 1.1.1 – Common UHV surface science techniques used for the characterisation of surfaces and the study of surface reactions. Techniques in bold indicate those used and/or detailed in this report.

Adapted from reference²

1.2 Vinyl Acetate Monomer (VAM) and its importance

VAM is a very important part of the polymer industry. It is used in the manufacture of many polymers and copolymers and is a relatively easy chemical to produce. According to a recent study carried out by Tecnon OrbiChem³, nearly 4 million tons of VAM were produced in 1999. This figure is expected to increase by ~3% per annum for the next decade. Just under 50% of this VAM was then used itself in the production of polyvinyl acetate and a further 35% is used in the production of polyvinyl alcohol. These figures are all expected to increase by 3-4% per annum and so it is vital to have a quick, easy, reproducible and, above all else, commercially viable and cost-effective way of producing high quality VAM in large quantities. Most of the major chemical companies produce VAM in some amount, for some it is their major product while for others it is only a minor component of their business. However, competition is significantly affected by the availability of fundamental technology required for cutting edge synthesis of VAM, which is controlled tightly by license regulations and patent laws. Developing new technology based on current synthetic routes is important but it is becoming increasingly necessary for companies to develop their own synthetic ideas in order to get ahead in the market, or indeed stay in touch.

VAM synthesis is undertaken on a massive scale by, amongst others, *bp*. However, understanding of the catalyst system used is limited and for this reason, fundamental surface science investigations are required, both on single crystal systems and “real” catalytic particles.

1.3 VAM synthesis through the ages

Moiseev *et al.* first reported the conversion of ethene and acetic acid (AcOH) to VAM in early 1960⁴. The process involved the use of chlorides of Pd and Cu and was used commercially by many companies, particularly ICI⁵. The main reaction investigated by ICI involved the absorption of ethylene into acetic acid solutions of palladous chloride. LiCl was also present as a promoter. In these reactions the Pd was believed to exist primarily as LiPdCl_3 and the kinetic studies carried out seemed to suggest that there was an active intermediate of the form $\text{LiPdCl}(\text{CH}_3\text{COO})(\text{C}_2\text{H}_4)$ or $\text{PdCl}(\text{CH}_3\text{COO})(\text{C}_2\text{H}_4)(\text{CH}_3\text{COOH})$ – or a combination of the two. At the time there was not enough information to determine between the two. A mechanism was produced to account for the formation of vinyl acetate and ethylidene diacetate (EDA),



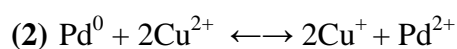
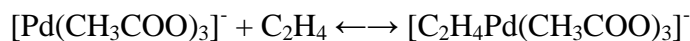
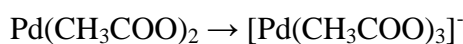
The reader is invited to investigate the initial ICI paper for a detailed description of the mechanism⁴. The effect of concentration of LiCl on the products formed was investigated. It was shown that vinyl acetate production was most favourable when the concentration of LiCl was low. It was believed that in the absence of chloride ligand there was no evidence of the ethylene isomerisation step and the formation of VAM (highly favourably) proceeded by hydride loss. It wasn't until the late 1960s that Bayer⁶ and Hoechst⁷ independently developed gas-phase heterogeneous processes involving Pd-based catalysts which were cleaner and produced fewer by-products. There were slight differences in the Bayer and Hoechst catalysts. Hoechst's had three components, $\text{Pd}(\text{CH}_3\text{COO})_2/\text{Cd}(\text{CH}_3\text{COO})_2$ and CH_3COOK and these were impregnated uniformly throughout the support (5mm spheres of silica). The $\text{Pd}^{(\text{II})}$ was

then reduced to Pd⁽⁰⁾ in a second stage. The Bayer catalyst on the other hand consisted of PdCl₂ and AuCl being impregnated and reduced to give a thin outer shell of metal atoms around the spherical pellet of silica. CH₃COOK was then impregnated uniformly throughout the catalyst, the Bayer catalyst was a forerunner to the later DuPont version which was patented in 1977⁸.

In the early 1970s the first real work into the mechanism of vinyl acetate formation from ethene oxidation was done. Samanos *et al.*⁹ reported research results on the mechanism and kinetics based on the knowledge at the time. The experimental method of producing VAM at the time was; ethene, oxygen and acetic acid with CH₃COONa in the presence of PdCl₂ as the catalyst and a redox system (Cu⁺/Cu²⁺ pair). The reaction was believed to occur in a manner similar to that of the homogeneous system and took place in two stages,



The co-ordinated ethene was believed to insert into one of the Pd-OOCCH₃ bonds of a palladium/alkali metal/acetate complex and then decompose to give palladium metal and VA,



An oxidant such as Cu²⁺ was used to reoxidise the Pd⁽⁰⁾ back to Pd^(II). This re-oxidation can occur in air but is generally too slow.

There was also patent literature produced regarding the gas phase synthesis with a Pd-base catalyst on a support in the presence of an alkali metal acetate promoter. The work Samanos *et al.* carried out focused on this gas phase synthesis. The investigations carried out were concentrated on determining the kinetics (which will not be covered – the reader is directed to the original paper) and also the effect of the amounts of CH₃COONa and Pd. The main conclusion centred on the reaction mechanism and supported the proposed mechanisms shown above. The elementary steps of the formations of Pd(CH₃COO)₂ were unknown but, due to the strong acetic adsorption it was assumed that the support remains saturated (physisorbed with respect to AcOH) and hence the following was put forward:



As a result of this work and competing work carried out by Kunigi and Fuzimoto¹⁰ it was decided by Nakamura and Yasui to carry out some more definitive work into the role of Pd(CH₃COO)₂ in the reaction.¹¹

General consensus at the time was divided, with Kunigi and Fuzimoto finding that Pd(CH₃COO)₂ was not present in the usual reaction conditions¹⁰ whereas Samanos alternately proposed that Pd(CH₃COO)₂ was in fact the catalytically active intermediate.⁹ Nakamura and Yasui aimed to clear the matter up as well as investigating the stability of the catalyst.

They showed that acetaldehyde was only formed in appreciable amounts under high partial pressures of acetic acid and high temperatures and that under all other conditions VAM was selectively formed (along with small amounts of CO₂).

Acetaldehyde is known to come from three combinations:

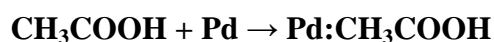
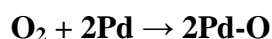
- ethene and water
- VAM and water
- VAM and AcOH

when Pd salt is the catalyst.

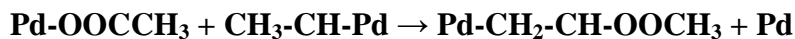
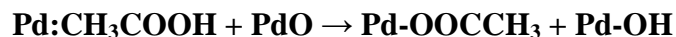
Yasui and Nakamura found that no acetaldehyde was detected when the reactions were catalysed by Pd metal. This backed up data which Kunigi et al. had also found. The theory was put forward that the acetaldehyde formed came from one of the reactions above catalysed by Pd(CH₃COO)₂, which was formed on the metal surface. The reader is directed to the initial paper for the reaction data on catalyst stability.¹¹ The conclusions drawn from the paper pointed towards a favourable VAM production at high T and low acetic acid partial pressure in which Pd(CH₃COO)₂ was not formed on the surface and consequently the acetaldehyde reaction was unfavourable.

Also the addition of CH₃COOK as a promoter was mentioned - it was believed that, although CH₃COOK has no effect on the formation of Pd(CH₃COO)₂, it was responsible for facilitating the decomposition of Pd(CH₃COO)₂ when formed.

Therefore, most of the Pd remained in metallic form throughout the reaction and the feed components would absorb onto the palladium surface:



The co-ordinated acetate should then react via a vinyl-palladium species to give VAM as below:¹¹



As previously mentioned, the original homogenous process was effective but highly corrosive. The newer heterogeneous vapour-phase processes were seen as being highly attractive due to the fact that it could be carried out in ordinary stainless steel equipment on plants.

A study was carried out in 1972 by Shetty *et al.*¹² to investigate the, then new, process as much of the information was still only available in patent literature. They investigated a variety of conditions, mostly catalyst based such as effect of flow rate, and also investigated the chemistry behind the catalysis, with the main conclusions being focused around the process development (*i.e.* gas composition).

The main contribution to the basic process came with the identification that CH₃COOK was a better promoter than both CH₃COONa and CH₃COOLi.¹² There was still no conclusive theory as to what the role of the CH₃COOK was (very little at all was known about this in fact).

A kinetic study of the vapour-phase reaction was carried out in 1978¹³ and managed to draw some interesting conclusions about the mechanism of reaction;

- (1) Adsorbed ethene and acetic acid are activated as a result of H-abstraction by the catalyst.
- (2) Oxygen adsorbs and then reacts in the molecular form
- (3) Dissociated ethene reacts with acetyl group and oxygen reacts with hydrogen – rate determining step (**RDS**)
- (4) CO₂ is then formed by degradation of acetic acid.

A different type of catalysis called Supported Liquid Phase Catalysis (SLPC) was tried by Zaidi¹⁴ in the 1980s in an attempt to overcome the deficiencies of both the homo and heterogeneous routes. In these catalysts, the support can immobilise the catalytic species on the surface, which helps to prevent the association of any unsaturated catalytic centres. This enhances the catalytic activity. The activity of Pd metal in the synthesis of VAM was well known by this time¹⁵.

It was also known, however, that solutions of some Pd^(II) salts deposited on charcoal were non-selective in VAM formation and formed a large amount of acetaldehyde as a by-product.⁸ It was reported the Pd^(II) reduction to Pd⁽⁰⁾ had lead to deposition of Pd metal occurring on occasions. Roney¹⁶ had predicted that there was an “optimum loading” of the catalyst solution with respect to the overall activity of these catalysts.

It was this effect that Zaidi decided to investigate and by the end of his research he was able to state that ethene could be selectively oxidised to VAM on SLPCs containing Pd and Li acetates on C.¹⁴ The loading conditions and temperature were both optimised and the reader requiring these values is directed to the original paper.¹⁶ His research also seemed to support the conclusions of Samanos *et al.*⁹ mentioned above regarding the mechanism of reaction although Zaidi was looking at liquid and

not gas phase, which was slightly different. Zaidi also believed that Pd^(II) was the catalytically active species, which disagreed with the work of Nakamura and Yasui¹¹ as well as Kunigi.¹⁰ Reilly and Lerou¹⁷ continued the work on SLPCs late into the 1990s and concluded that they were indeed very promising in the formation of vinyl acetate monomer when compared to both the analogous homogeneous and heterogeneous routes. However, they also concluded that further mechanistic and kinetic understanding was required before any solid evidence could be put forward suggesting SPLC as a sensible method for VAM formation. Reilly and Lerou theorise in depth about the SPLC mechanism and the interested reader is directed to the original paper for information.¹⁷

Moving into the early 90s, it became apparent that, although for nearly 30 years it had been known that the oxyacetylation of ethene to VAM could be catalysed by supported Pd and Pd alloys¹⁸, very little was known about the mechanism or kinetics of the basic reaction scheme. The main area of uncertainty centred on the role of acetic acid in the process. The kinetic order of acetic acid was hotly debated, with the reported value varying from 0⁹, through 0.5¹⁹ to 1²⁰. The role of the acetic acid in affecting the surface was similarly disputed.

The components involved in the scheme, acetic acid, ethene and VAM (as well as the alkali acetate salt which was known by this time to increase activity and selectivity, although an explanation as to why has still not been satisfactorily produced) contained several IR-active chromophores. Due to its very nature as a reflectance technique, Augustine and Blitz decided to use DRIFTS (instead of transmission FTIR) combined with MS to probe the workings of this system. The DRIFTS-MS system was believed to have greater surface selectivity.²¹

The rate of VAM formation as a function of partial pressure of acetic acid was calculated and seemed to agree with previous results⁹ which found that the reaction appeared to be governed by saturation kinetics in which the data could be described by a 1st-order Langmuir-Hinshelwood approximation. Further analysis of the data showed that this was not the case and acetic acid in fact was playing two different roles which both seemed to affect the rate of reaction.²¹

The first was purely catalytic and seemed to involve altering the surface energetics of the active site, resulting in a lowering of the activation barrier. The second was that acetic acid was a reactant and therefore had a non-zero contribution to the rate equation.

Of the two, the former should have a larger influence as it alters the exponent of the rate equation. Augustine *et al.* also suggested from their work that the η^1 -acetate species was the active form of acetic acid on the surface of the active catalyst.

The other major conclusion of the DRIFTS-MS work was that the active surface phase for this system consisted of Pd(CH₃COO)₂ like islands sitting on top of Pd metal or oxide crystallites. This conclusion was drawn by the use of TPD reactions in conjunction with the DRIFTS-MS and the reader is directed to the original paper for a more thorough, in-depth analysis.²¹

In the early 1990s, Crathorne *et al.*²² used isotopic kinetics to characterise the surface species of the Pd/Cd/silica and Pd/Au/silica catalyst mentioned above (Hoechst and Bayer respectively). The full batch of experiments allowed a detailed assessment of which surface species were present on the VAM catalyst during reaction.

The results are shown in the table below that is reproduced from the paper of Crathorne *et al.*²²

Surface species	Pd/Cd/silica/K (uniform impregnation)	Pd/Au/silica/K (shell impregnation)
	Concentration (μmolg^{-1})	Concentration (μmolg^{-1})
C ₂ H ₄	<1	<1
O ₂	<1.3	<2.6
VA	1.3	0.9
H ₂ O	154	230
AcOH	1800	1911

Table 1.3.1 – Inventory of Surface Species on working VAM catalysts. *Reproduced from reference*²²

As can be seen, the predominant species on the working catalyst is acetic acid. Values for the catalyst provided by the paper say that, for the Pd/Cd/silica/K catalyst, only 198 and 615 μmolg^{-1} Pd and K respectively is contained within the catalyst. Therefore most of the acid must be associated with the support. TPD experiments carried out also supported the conclusion that the major factor in acetic acid retention was the silica support, with the K and Pd only contributing secondary roles. Distribution of the acid is harder to quantify. The acid coverage is believed to be equivalent to about 3 ML but whether this is evenly distributed around the surface is unclear. It could be associated with the potassium acetate promoter, the metal centres or even with parts of the silica support.

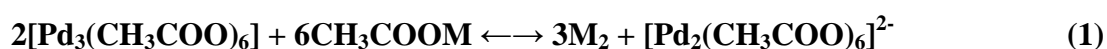
There was a main mechanistic implication that came out of the work done by Crathorne *et al.*²² They were able to expand on the work done initially by Nakamura and Yasui,¹¹ Zaidi¹⁴ and Samanos,⁹ which is mentioned previously, and try to make some headway with regard to a mechanism or reaction scheme. Crathorne *et al.* suggested that under normal working conditions, both catalysts possessed a high concentration of adsorbed acetic acid (~3 monolayers). This is obviously not enough to form a full co-ordination sphere and so therefore cannot be thought of as a true

liquid. This film must however play a significant role in the reaction since many catalyst features maximise retention (CH₃COOK and the support pore structure). Some acid on palladium adsorption is found by TPD but adsorption on both the CH₃COOK and the silica support might also be important. By looking at numbers of active sites and ethene/O₂ adsorption, Crathorne *et al.*²² were also able to predict that the reaction scheme was in fact a liquid-phase process proceeding via heterogeneous catalysis – supporting Zaidi’s initial observations.¹⁴

By this stage it was generally accepted that the method of formation of VAM was by a heterogeneous process closely related to the Bayer⁶ and Hoechst⁷ processes. The most common catalyst was a Pd-Au alloy with CH₃COOK added in large excess. There were still questions to be answered about the active phase of the catalyst however.

Kragten and van Santen decided that, since Pd solvates as palladium acetate in glacial acetic acid under any oxidising conditions²³, a homogeneous route was still possible, albeit probably as a side reaction to the heterogeneous process²⁴.

In the late 1990s they studied spectroscopically the homogeneous formation of VAM in the presence of palladium acetate. Solvated palladium acetate is believed to exist in at least three different forms, which are related to each other by means of equilibria. These equilibria can be controlled by the addition of alkali metal acetates²⁵ and are shown below,



where M represents an alkali metal

The Pd trimers are found to be completely converted to dimers when the solution contains either 0.5M lithium acetate or 0.2M sodium acetate. Decomposition of Pd acetate trimers is suspected to involve an S_N2 attack by acetate ions, acetic acid molecules or an acetate bridge. The concentration of the dimers depends on the Pd and acetate concentrations, as a result of the nature of the equilibria.²³ It is important to note that there are two general types of acetate groups, the bridging and the terminal (see Figure 1.3.1)

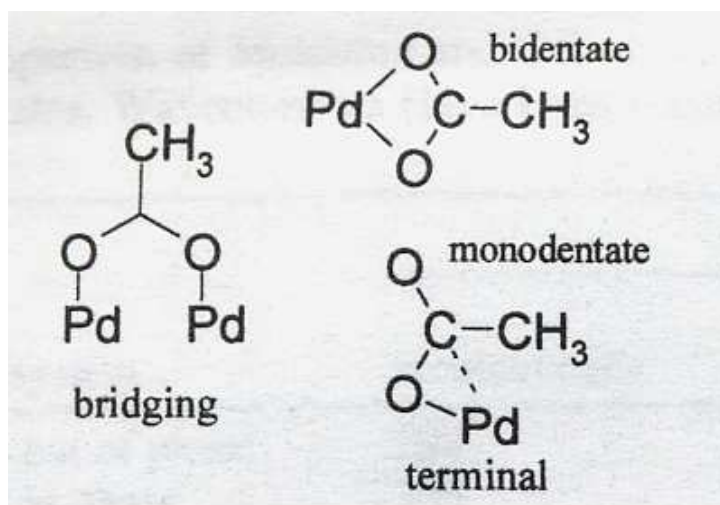


Fig 1.3.1 – Co-ordination modes of acetate. Taken from reference²³

Bridging or terminal acetates are present in the trimer and monomer respectively, whilst in the dimer a combination of both exists (see Figure 1.3.2).

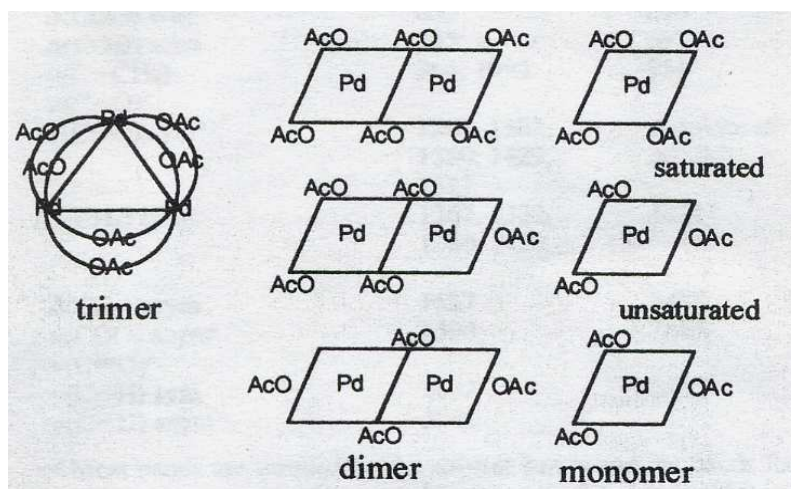


Fig 1.3.2 – Various Pd acetate species at increased unsaturation. Taken from reference²³

These different Pd species have been found to have different catalytic activities with respect to the acetoxylation of ethene to VAM. The activity is also found to increase in proportion to the Pd acetate and alkali metal acetate concentration, peaking at concentrations for the latter, which correspond to all the trimer being converted to dimer. Above this level, activity is inversely proportional to the alkali metal concentration leading to the conclusion that adding alkali metal acetate initially forms the catalytically active species. At higher concentrations however, the acetate ions begin to function as inhibitors.

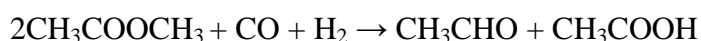
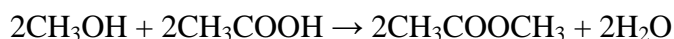
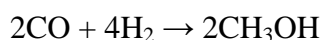
Kragten and van Santen²³ explained this as follows. When the alkali metal acetate concentration is low, the relatively inactive trimers are converted to the more active dimers. As concentration increases however, there are some less active species formed. These could either be monomers or dimers of Pd that are fully co-ordinated to acetate ligands. This is unfavourable as the ethene molecules are expected to co-ordinate to terminal positions on the dimer, which is followed by reaction to vinyl acetate. Without the presence of these vacant sites, a reaction cannot take place.²⁶ The maximum activity is therefore expected when the concentration of unsaturated Pd dimers is at its highest. The main conclusion of the study was that the Pd acetate species present in the acetic acid solvent are strongly dependent on the concentration of alkali metal added. UV/Vis and Raman spectroscopy has been used to study more thoroughly this dependency, as well as theoretical DFT calculations, which supported the physical results. The study also showed that dimeric, unsaturated Pd acetate species are the active species in the homogenous formation of vinyl acetate.²³

Goodman and his co-workers²⁷ have recently looked at kinetics of ethylene combustion in the synthesis of vinyl acetate over a Pd/SiO₂ catalyst. They determined

that CO₂ formation as a function of the partial pressures of C₂H₄ and O₂ exhibits a negative reaction order with respect to C₂H₄ and a positive order with respect to O₂. The ethylene combustion kinetics in the presence and absence of acetic acid were essentially the same, suggesting that ethylene combustion is primarily responsible for CO₂ formation in the synthesis of vinyl acetate from ethylene and acetic acid over unpromoted Pd. Further work by the same group has led to the conclusion that VAM synthesis is determined to be a structure-sensitive reaction that is best carried out over small rather than large Pd particles.²⁸ Goodman and his group also looked into the Pd/Au bimetallic system in an effort to reduce the formation of Pd carbide (PdC_x) during the synthesis of vinyl acetate.²⁹ He compared two Pd/SiO₂ catalysts with different particle sizes and a Pd/Au/SiO₂ mixed-metal catalyst. It was found that the smaller Pd particles showed greater resistance to the formation of PdC_x and also found the alloying of Au with Pd was very effective in preventing PdC_x formation during the synthesis of vinyl acetate.²⁹

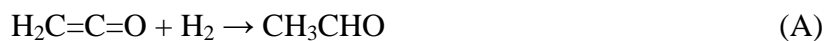
Within the last few years, Tysoe and his group investigated the Pd-catalysed formation of vinyl acetate and were able to report on the effect of oxygen on the surface³⁰. They showed that ethene (in the gas phase) reacted with a model-catalyst surface of η^2 -acetate moieties adsorbed on a Pd{111} surface pre-covered with a (2x2) oxygen overlayer, forming VAM. This implied that the acetate species is the precursor to formation of VAM. It was also possible to elucidate the reaction mechanism for the Pd-catalysed synthesis of vinyl acetate and they provided clear evidence that the reaction of ethene proceeded through the pathway initially proposed by Samanos,⁹ in other words by insertion of ethene into an adsorbed acetate species followed by β -hydride elimination forming vinyl acetate.³¹

Raw material costs encountered in the current ethene oxidative acetoxylation route has lead to some research into the synthesis of VAM from syngas. Colberg *et al.* undertook a comprehensive study of the possible techniques in the late 1990s.³² The previous attempts using syngas followed a reaction scheme along the lines of the one below,



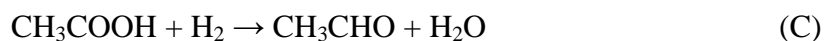
However, these efforts failed to generate a commercially viable process, due primarily to the large amounts of recycled acetic acid inherent with the process. This requires large commercial facilities and consequently is not cost effective when compared to the ethene acetoxylation route. Two potential schemes were put together to be investigated:

Scheme 1



Scheme 1 involves the conversion of acetic acid to ketene, followed by hydrogenation of the ketene to acetaldehyde under mild conditions. The acetaldehyde is then reacted with more ketene to form VAM directly.

Scheme 2



In Scheme 2, dimethyl ether is carbonylated to form acetic anhydride, which is then reacted with acetaldehyde to produce VAM. To avoid having to recycle acetic acid through a carbonylation unit, the acetic acid is hydrogenated to provide the acetaldehyde required in the second step. The final step is actually endothermic so this will be one of the challenges that need to be overcome in order to find a cost-effective alternative process.

Colberg *et al.*'s syngas paper focused on investigating four of the steps above in more detail.³² Their primary aim was to realise one of the preferred schemes described and find a way of producing VAM without the need for recycling acetic acid. The four new technologies being investigated were:

- (A) Hydrogenation of ketene to acetaldehyde
- (B) Production of VAM from ketene and acetaldehyde
- (C) Conversion of acetic acid back into acetaldehyde
- (D) Production of VAM from reactive distillation of acetic anhydride and acetaldehyde

The reader interested in the workings of the chemistry employed in the development of these processes is directed to the original paper for further details.³² Colberg *et al.* were able to conclude that they had made satisfactory progress with each of the four processes. Further work is continuing into these systems and;

*“When combined with established processes for the conversion of synthesis gas to acetic acid or acetic anhydride, these new technologies represent potential viable routes to the generation of VAM from synthesis gas.”*³²

Despite this new and innovative research into a syngas based route, as well as the renewed (if sporadic) interest in a homogeneous route, heterogeneous catalysis is still responsible for a vast amount of the VAM produced throughout the world.

The most common modern synthesis of VAM involves the basic ingredients of ethene, acetic acid and oxygen as well as a **bimetallic** Pd-Au catalyst, with an alkali metal acetate (usually K). It is known that the formation of Pd/Au alloys increases the selectivity of vinyl acetate formation with respect to pure Pd{111}³³, possibly due to an enhanced stabilisation of the surface acetate species.³⁴ The Pd/Au bimetallic system will be discussed later in the chapter as will the effect of K on metal surfaces.

There are currently two main areas of research in the field of vinyl acetate; commercially, companies are investing in upgrading their existing catalyst systems and concentrating primarily on issues of chemical engineering and materials science. However, a fundamental understanding of the surface science that takes place during the heterogeneous catalysis is also important. Consequently, more and more work is being done into the theory of surface-adsorbate interactions in a bid to understand the chemistry. The behaviour of acetate on a metal surface makes a sensible starting point for the in depth study of the fundamentals of the surface chemistry.

1.4 Acetate on monometallic metal surfaces

In the current standard VAM catalyst, acetic acid/acetate is considered to adsorb on a Pd/Au surface. The exact nature of this surface is dynamic and dependent on the composition of the surface and the conditions of production.

The behaviour of acetate and acetic acid has been studied on a variety of different surfaces, the majority of which have been monometallic. Understanding of the bonding, stability and reactions of acetic acid on different surfaces will give an idea as to the nature of the behaviour on Pd/Au. Some of the more common monometallic surfaces studied have included Cu, Ni, and Rh.

1.4.1 Copper

The majority of the work concerning acetate/acetic acid on Cu has been done on the {110} surface. In the late 1970s, Bowker and Madix carried out work on the adsorption of acetic acid (as well as aldehyde) on the Cu{110} surface.³⁵

They used UPS and XPS to show that the behaviour of acetic acid conformed with their previous work on formic acid. The acid was found to adsorb intact at low temperature, with the binding being apparently through the hydroxyl O as in Figure 1.4.1.1 below.

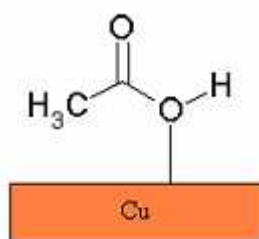


Fig 1.4.1.1 – Monodentate binding of acetate to a Cu surface

They also found that at higher temperatures, there was evidence of a bidentate acetate species formed, a result of which was that the two oxygen atoms became completely equivalent, as in Figure 1.4.1.2.

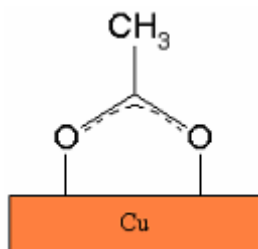


Fig 1.4.1.2 – Bidentate binding of acetate to a Cu surface

They proposed the full mechanism for the adsorption and reaction of acetic acid with Cu{110}, which can be found on the original paper.³⁵

Bowker and Madix's work was used as a basis for some of the work carried out in the late 1980s by Woodruff *et al.*³⁶ who looked at the formation and structure of acetate on Cu{110} using angle-resolved polarised light photoemission. They were able to conclude that Bowker and Madix's³⁵ initial observations were correct. At low temperature, the acid adsorbs in the molecular form, although they found significant dimerisation of the monolayer coverage at 155 K. At temperatures just above 300 K this layer was found to transform into a surface acetate species.

A similar experiment carried out in the presence of pre-absorbed oxygen found a similar effect, but at a much lower temperature. Going to a higher temperature, the acetate species was dissociated and desorbed, although there was evidence of a low coverage of a possible surface intermediate during the heating, which was believed to be acetic anhydride based on the desorption products formed. Another reason for the work done by Goodman *et al.*³⁶ was to try and predict the local structure of acetate on

Cu{110}. They were able to surmise that the structure was very similar to that of formate on the same surface. At the time however, there were problems surrounding the proper identification of the adsorption site of formate. Hence they were unable to provide a definitive answer regarding the adsorption structure of acetate.

In the mid to late 1990s, these questions began to be answered. Haq and Leibsle were investigating the evidence for long-range intermolecular interactions and molecular-induced restructuring of metal surfaces and chose acetate on Cu{110} as the example³⁷.

It had already been shown that metal surfaces could reconstruct as a result of the influence of adsorbates. The most well known of these was the Cu{110}-(2x1) O reconstruction.³⁸

Haq and Leibsle³⁷ presented further evidence in their paper that metal substrates are not rigid templates, as far as adsorbates are concerned. They also managed to report complex molecular-molecular interactions for this system.

Previous photoelectron diffraction studies had recorded the believed dimensions for the adsorbed acetate species to be very similar to the free acetate ion.³⁹ They were also able to determine the Cu-O distance as 1.91Å. Haq and Liebsle's³⁷ work concentrated more on the long-range surface order (if any).

They were able to determine that acetate dosed onto a clean Cu{110} surface yielded the following LEED pattern (Figure 1.4.1.3 overleaf), which is indicative of two reflectionally equivalent domains, (-1 1 | 4 4) and (1 1 | 4 -4).

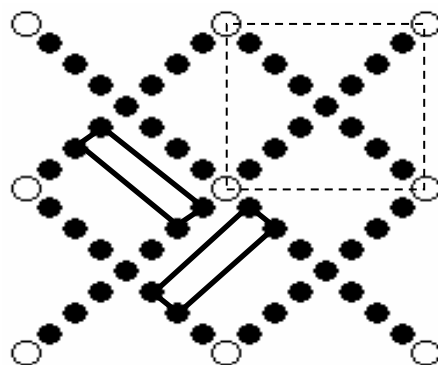


Fig 1.4.1.3 - LEED pattern of acetate on a clean Cu{110} surface. *Adapted from reference*³⁷

The STM images recorded showed terraces separated by single monatomic steps, which were atomically straight and ran along the $\langle 1\bar{1}2 \rangle$ directions. The ability of atomic adsorbates to cause step edges to specifically orient along certain crystallographic directions was not unusual, having been seen many times before.^{38,40,41} The interesting thing about this observation was that mass transport of the substrate atoms was necessary to effect the change. This is believed to be a feature of interactions between carboxylates and Cu{110} as formate and benzoate show a similar effect.⁴² Also acquired were STM images that showed row-like structures on the terraces, which run along the $\langle 1\bar{1}2 \rangle$ as well. The spacing between these “rows” is consistent with the LEED observed periodicity and lead to a model for the structure being suggested (Figure 1.4.1.4),³⁷

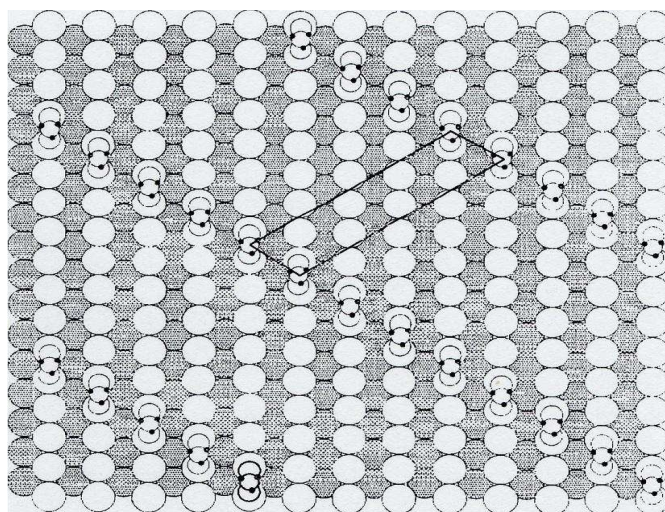


Fig 1.4.1.4 – Proposed structure of acetate on Cu{110} surface. *Taken from reference*³⁷

Despite high saturation levels, the surface coverage never increases higher than when all the terraces are full. This may be a result of some long-range intermolecular interaction existing between rows, but the fact the rows have been observed as long as 570Å indicates that there may be a highly attractive interaction within the rows. The step heights are believed to be monatomic and it has been suggested that the structures are effectively arrays of up-down steps (similar to the ramparts of a castle). This adsorbate induced-surface restructuring may achieve two things;

- i) increase the surface area
- ii) create different adsorption sites.

In this case, the formation of the step edges creates adsorption sites that closely resemble those found on a {111} plane.

Similar studies of acetate on a oxygen pre-adsorbed Cu{110} surface which, undergoes the Cu{110}-(2x1) O rearrangement, results in the formation of c(2x2) overlayer.³⁷ There was no evidence of the up-down steps seen with the clean surface.

The results found for the clean system seem to indicate, quite conclusively, that there are long-range interactions in existence, which may play a significant part in determining saturation coverage. Coupled to that was the proof that metal surfaces can be rearranged and restructured as a result of adsorbate presence, seemingly altering the surface area and the type of adsorption sites available.

Around the same time, Baumann *et al.* were investigating the long range ordered structure of acetate on Cu{110}⁴³. They came to virtually the same conclusions as Haq and Leibsle³⁷ in that Baumann *et al.* found a (4 -4 | 1 1) LEED pattern with acetate on clean Cu{110} at 300K. They produced a structure model for the proposed

structure based on the LEED pattern, which proved almost identical to Haq and Liebsle's. The only new information provided by Baumann's group was that the surface coverage was 0.38 acetate species per Cu atom, which seemed to support the idea of a low saturation coverage, although they provided no explanation for this observation.

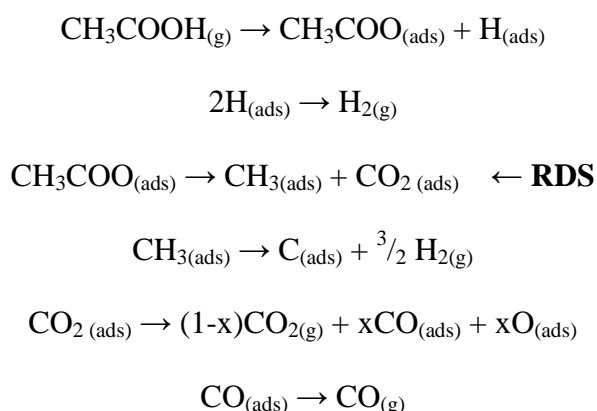
Further studies carried out by Johnston *et al.* in the late 1990s indicated that there was no face dependence on the surface structure of acetate. They found that acetate on Cu{110}, Cu{111} and Cu{100} was equivalent in the way it adsorbed and interacted.⁴⁴

1.4.2 Nickel

Most of the structural work on Nickel has centred around the Ni{110} crystal face. In 1999 Nowicki *et al.* provided the best analysis of acetate and its binding to the Ni{110} face.⁴⁵ They made some interesting comparisons between Ni{110} and Cu{110}, including the fact that acetate binds in the same way to Ni{110} as to Cu{110}, bidentate through the two oxygen atoms. However there were slight differences, one of which was the acetate coverage per metal atom. Ni had a higher coverage (0.48 to 0.37) which may be a direct result of the different electronic structures of Ni and Cu. Ni has a longer C-O bond length in acetate, which could indicate a stronger M-O bond in Ni. This is not unlikely due to Ni's higher affinity for oxygen. This would be a simple explanation for the subsequent increase in surface coverage for the Ni system when compared to Cu. However, this was only a secondary point that was overshadowed by the main difference, the structure of the acetate overlayer. Cu{110} had the (4 -4 | 1 1) structure as detailed above whereas Ni{110} was found to have the c(2x2) overlayer pattern.

We know that the Cu{110} undergoes a serious re-arrangement in the presence of acetate but it appears that Ni {110} does not undergo the same re-arrangement. More detailed study into the system is currently being undertaken by the same group responsible for the initial work.⁴⁵

The rest of the work concerning acetate on Ni concentrated on the decomposition of acetate on the Ni{111} surface. Work carried out by Schoofs and Benziger in the early 1980s seemed to indicate that acetic acid monomer dehydrogenated on the surface to give adsorbed acetate and hydrogen, before decomposing when heated, according to the following scheme,⁴⁶



CO could also be formed by interaction between the adsorbed C and O.

Acetic acid dimers are believed to dehydrate, leaving adsorbed acetate, methyl groups and CO on the surface as Fig 1.4.2.1 below;⁴⁶

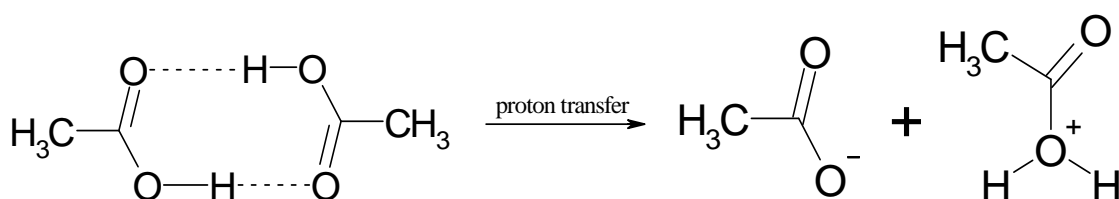


Fig 1.4.2.1 – Suspected mode of dehydration of acetic acid dimers on Ni{111}

The protonated hydroxyl group falls apart to leave H₂O, which desorbs, while CO and CH₃ remain on the surface. The exact method of decomposition of the acetate for both the monomer and dimer is influenced by the presence of other molecules such as CO. Attractive interactions between adsorbed acetate molecules decrease rate of reaction while CO-acetate repulsive interactions help to increase the rate.

Benziger and Scharpf echoed these results, on the Ni{100} face, a few years later.⁴⁷ They found almost the exact same method of decomposition, the monomer adsorbing as acetate before decomposing to the products shown above. The dimer decomposed identically to the Ni{111} system as well which seemed to indicate there was no face dependency in the decomposition of acetate on different Ni surfaces.

In the late 1980s however, Sander and Early produced some results that seemed to contradict all of the Ni{111} work carried out by Schoofs and Benziger⁴⁷ mentioned previously. Sander and Early⁴⁸ group used RAIRS and TPD to reinvestigate the initial research carried out. They did this on the basis of their own work with formic acid on Ni{111}, which seemed to suggest that the main surface intermediate was actually formic anhydride and not formate. After repeating the work of Schoofs and Benziger,⁴⁷ it was found to be the case that acetic anhydride was the main surface intermediate in the decomposition of acetic acid. It has subsequently become apparent that this is a trend of Ni{111} with this class of organic compounds, to form an anhydride on decomposition.⁴⁸

It should be noted that, like Cu{110}, Ni{110} showed acetate as the main intermediate of the decomposition of acetic acid when work was carried out by Madix *et al.*⁴⁹ They were the first to describe the phenomenon of autocatalytic

decomposition, whereby at a high enough temperature, the previously stable acetate will simply decompose, on a metal condition. They explained this by assuming that, at low coverage, the adsorbed species are held in sites quite far apart. As the coverage increases, islands begin to grow and, owing to the anisotropy of the {110} surface, an ordering of the adsorbate molecules takes place. There is now an attractive interaction between the adsorbates which further stabilises them. Free metal sites must be available for decomposition to take place but at high coverage these are not always present, slowing down the decomposition further. Once the first molecules have decomposed, the free sites left behind act as catalytic centres for the further decompositions and hence the reaction becomes self-accelerating. This interesting phenomenon has since been found on numerous other metal surfaces, some of which are mentioned below.

The work done on Ni{100}⁴⁷ has not been challenged since it was done, and this seems to indicate that Ni{111} may behave anomalously in comparison with other transition metal surfaces in promoting anhydride formation ahead of acetate.

1.4.3 Rhodium

The two main areas of study with respect to the Rh/Acetate system centre around the Rh{111} and Rh{110} faces. Li and Bowker did the majority of the early work on Rh{110} in the early late 1980s.⁵⁰

Like the other {110} faces investigated, acetic acid adsorption onto a clean Rh{110} surface results in the breaking of the O-H bond, with the ensuing acetate binding to the surface as a bridging bidentate ligand (between two adjacent Rh atoms). It is

generally accepted in all the cases that the two oxygens are equivalent (see Figure 1.4.3.1 overleaf)

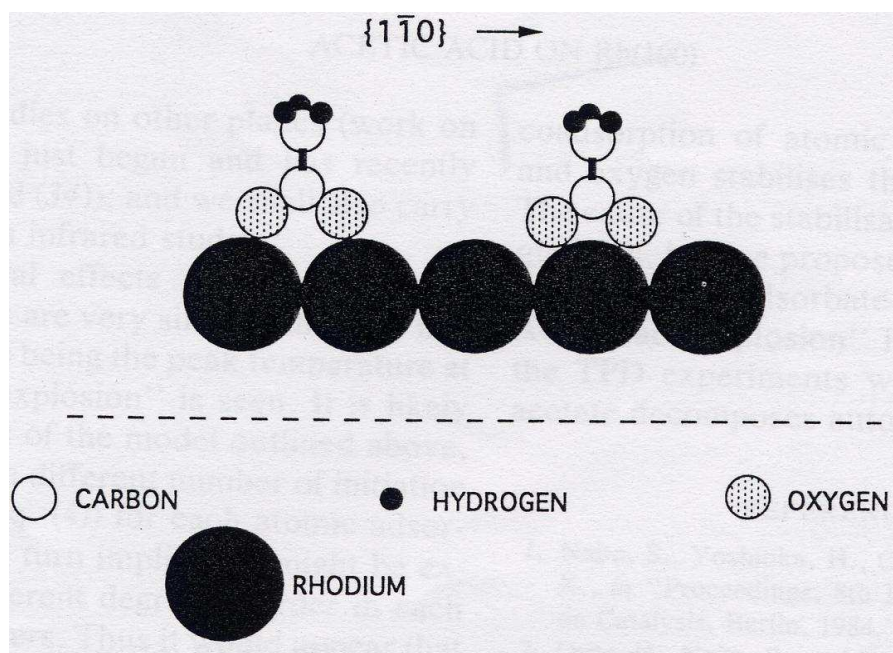


Fig 1.4.3.1 – Mode of binding of acetate to Rh{110}. Taken from reference⁵⁰

It was again found that the co-adsorption of atomic carbon, nitrogen or oxygen resulted in a stabilisation of the surface acetate, by approximately the same amount regardless of which adatom was present.

The exact reasons for this were still unclear but three theories were put forward to try to explain this, expanding on Madix *et al.*'s theory from Ni{110}.⁴⁹ This theory no longer fitted as it only accounted for the phenomenon on {110} surfaces (the anisotropy of the {110} surface was an important part of the theory);

(1) *Surface reconstruction* – A similar effect to the Cu{110}-(2x1)O reconstruction could be taking place, which creates different sites from those found on the clean surface, affecting the available bridging options for the acetate.

(2) *Site blocking* – It is possible that the adatom is simply acting as a poison, blocking sites adjacent to the acetate which are required for decomposition. (see Figure 1.4.3.2 overleaf)

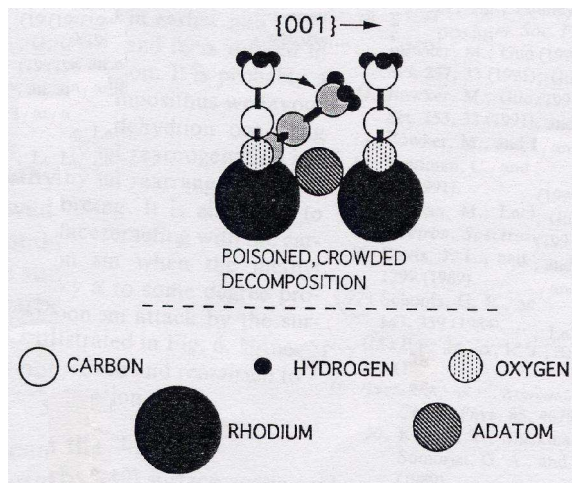


Fig 1.4.3.2 – Mode of acetate site blocking by adatom on Rh{100}. Taken from reference⁵⁰

(3) *Adsorbate-induced ordering* – This concept is shown in Figure 1.4.3.3. It explains the “poisoning” effect that seems to be taking place in an interesting way. The acetate effectively poisons itself as it is forced to arrange in a certain pattern by the presence of the adatoms. On the clean surface the acetate is unstable at room temperature but the adatoms offer stability by being adjacent to the acetate which creates an attractive interaction, and also by the ordering, which puts the acetate onto the active decomposition sites thereby blocking the use of that particular site.

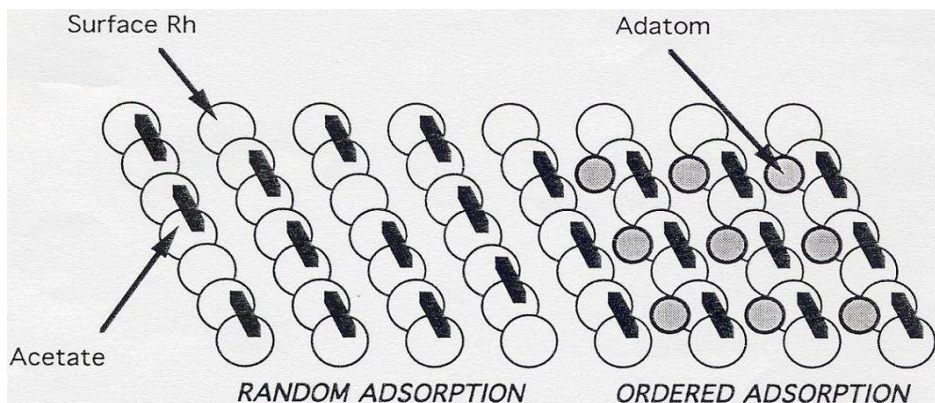


Fig 1.4.3.3 – Induced ordered adsorption on Rh{110} by the presence of pre-adsorbed adatoms. Taken from reference⁵⁰

Bowker and Li⁵⁰ believed the third explanation to be the more likely one on the basis of their results, as it seemed to fit in with the rate equations and other kinetic phenomena they had recorded, such as the “surface explosion” seen during autocatalytic decomposition at higher temperature.

The presence of the co-adsorbed atom enabled the acetate to be kept on the surface in a stable environment before being heated to certain temperature in order to induce the decomposition and desorption. For clean Rh{110} and acetate this is not possible as the acetate decomposes and desorbed during the adsorption process and cannot be isolated.

Around the same time, Bowker and Li were also carrying out work on the Rh{111} surface.⁵⁰ There were very few differences in the general schemes, such as the increased stability of the acetate in the presence of adatoms, although it was a smaller increase for Rh{111}. The same surface explosion (decomposition) was also seen at high temperature. The major difference was that acetate was stable at room temperature on the clean Rh{111} surface, unlike Rh{110}, enabling controlled analysis of its decomposition to be undertaken. The temperature at which the surface explosion occurred was also higher for the Rh{111} pre-adsorbed surfaces, by about 100 K.

The reason for this difference between Rh{110} and Rh{111} is put down to the difference in the structure of the surface. The sites available on {110} are either in a much more reactive configuration, or require less energy in the vibrational mode to access the reactive transition, both effects being due to the lowered steric hindrance.

This means that the acetate is highly reactive when on the clean Rh{110} surface and therefore decomposes instantly. By adsorbing an adatom such as C, N or O, the surface dynamics (available adsorption sites for example) can be altered enough to reduce the reactivity of the surface as a whole, meaning acetate is stable at room temperature.

For the Rh{111} system, the surface reactivity is already low enough for the clean system so as not to require a co-adsorbed atom. Addition of an atom however, would reduce the reactivity even further and mean the temperature of autocatalytic decomposition would be higher still.

Bowker and Li⁵⁰ concluded, amongst other things, that the essential requirement for the autocatalytic decomposition on Rh{111} and Rh{110} was the presence of the co-adsorbed adatom. This ties in with the similar observations they made about Pd{110}, which is covered in Chapter 1.4.5 below and also the work of Madix *et al.* on Ni{110}⁴⁹. This adatom had two probable functions (neither of which could be confirmed at the time); ordering the acetate layer, and acting as a direct poison to “frustrate” the acetate.

Further work was carried out on the Rh{111}/acetate system by Hoogers *et al.*⁵¹ and they came to a number of conclusions based on the results they obtained. Firstly, they showed that the autocatalytic decomposition of acetate on Rh{111} could be induced by saturation exposures to acetic acid at room temperature. This would lead to a crowded acetate adlayer. The driving force for the reaction is the creation of the vacant sites which result from desorption of the decomposition products.

As previously mentioned, Madix *et al.* found some island formation at lower acetate coverage on the surface of Ni{110}⁴⁹ but this was not observed for the clean Rh{111} system. Pre-adsorbed oxygen and potassium ions intermixed with the acetate molecules however, have an influence on the process.

Unlike the clean surface, mixed component dense islands were formed which provides an efficient method of site filling (without the need for any long-range order). This enhances the extent of the autocatalytic decomposition and the proximity of the acetate to the co-adsorbates enables electronic interactions, which themselves modulate the acetate stability. Electron donors, such as K, weaken the intramolecular acetate bonds whilst electron acceptors, like O, have a stabilising effect.

1.4.5 Gold

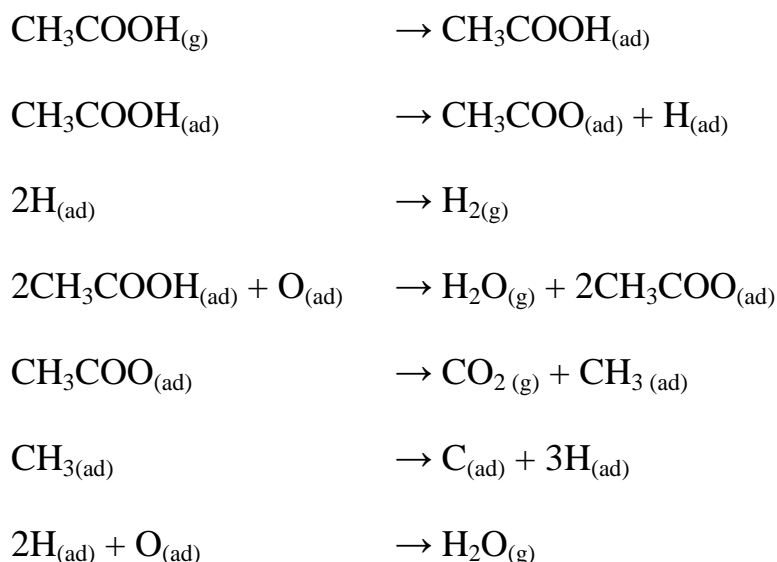
There had been no papers published on the behaviour of acetic acid or acetate on any Au surface when this project was commenced.

1.4.5 Palladium

Pd{110} was first studied in detail by Bowker and Aas,⁵² around the same time Bowker was working on Rh{111} and Rh{110}. In fact, he found that the Pd{110} system was very similar to the Rh{111} system.

The acetic acid was adsorbed onto the surface and the acetate remained stable up to ~350K [vs. 380K for Rh{111}]⁵⁰.

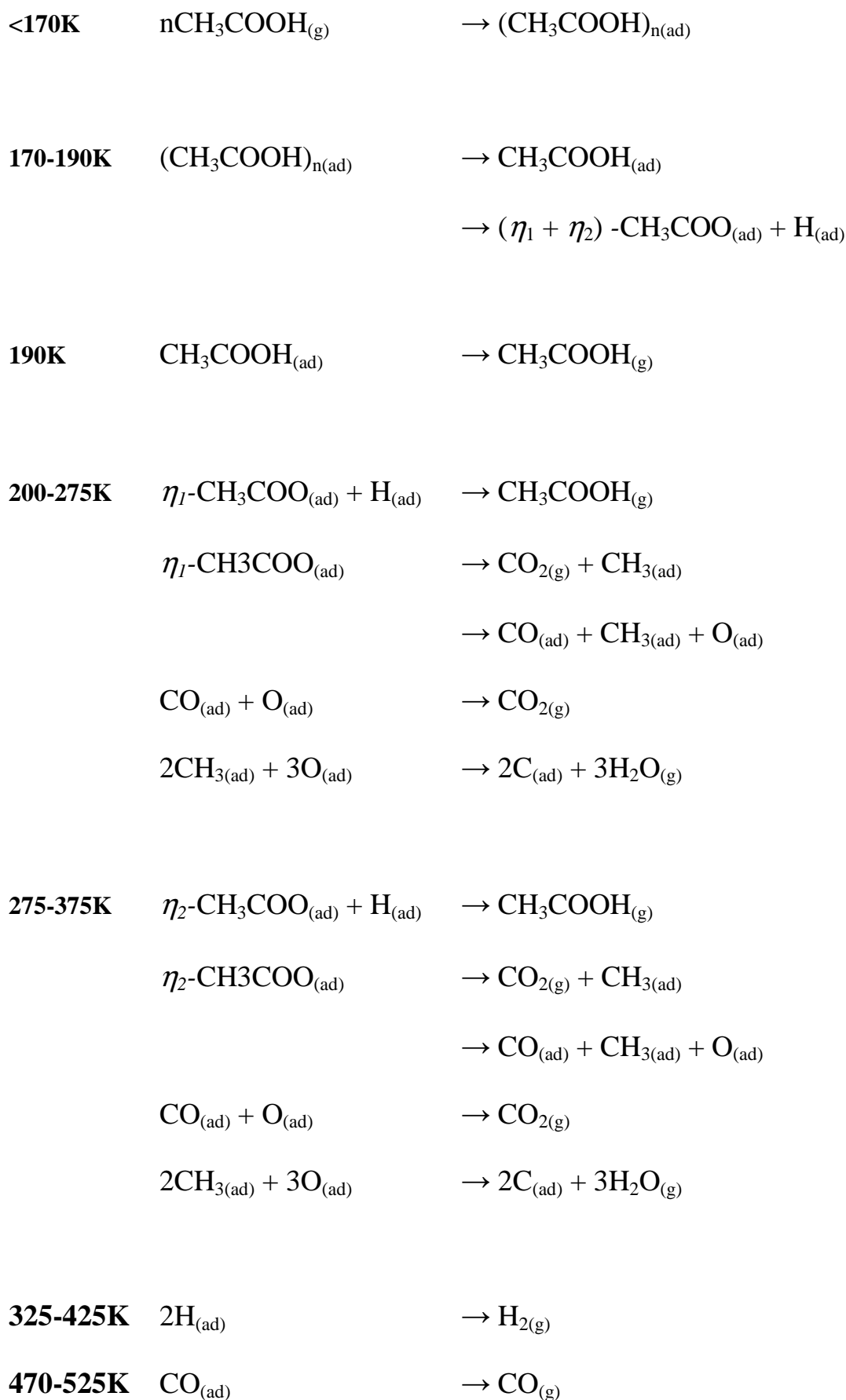
Analysis of the TPD data meant that the mechanism of adsorption, decomposition and desorption was assigned as follows;



The adsorbed C left behind acts as a site-blocking adatom increasing the temperature of some of the decomposition steps by the same method as described in 1.4.3. As can be seen, there is only one route of decomposition for acetate on Pd{110}.

Contrasting that with Pd{111} studies, carried out by Davis and Barteau,⁵³ we find some interesting results. They found that acetic acid on clean Pd{111} decomposes between 350 and 375K to yield CO₂ and H₂, analogous to acetic acid on Rh{110}. The pre-adsorbing of O to form a Pd{111}-(2x2)O structure served the same purpose as previously, enabling the acetate to remain stable up to 400K, which allowed for autocatalytic decomposition at higher temperatures.⁵⁴

Davis and Barteau also found that the mechanism of decomposition was different on Pd{111} compared with Pd{110} and in the late 1990s Haley, Tikhov and Lambert proposed the mechanism for the decomposition of acetate on Pd{111}, which is shown overleaf;⁵⁵



where η_1 – monodentate acetate

η_2 – bidentate acetate

It can be seen that there is more than one method of decomposition of acetate in this scheme, which obviously contributes, in some way, to the differences in the reactivity of the acetate on the two Pd surfaces.

The data in the paper fully supports this mechanism but also corrects some of the erroneous statements that were made in the original papers by Davis and Barteau^{53,54}. Several conclusions were drawn from Haley *et al.*'s⁵⁵ work, of which the most important were;

- At 170K, the first absorbed monolayer of acetic acid on Pd{111} contains molecular and dissociated acetic acid molecules, the dissociated species consisting of a mixture of bidentate and (although this is not clear) suspected monodentate acetates. This is analogous to previous work on the structure of acetate species on Cu{110}.
- Monodentate acetate is believed to form at high coverages. This is consistent with its reduced surface co-ordination. The monodentate species very closely resembles the species identified at the surface of the pure Pd VAM catalyst and therefore could be a key reaction intermediate for the process.
- The thermal decomposition of the adsorbate yields C, CO, CO₂, H₂ and H₂O. The related processes can be rationalised in terms of two reaction routes, corresponding to the mono- and bidentate acetate (shown in the scheme above).

Due to its use as a VAM catalyst, the acetate species on Pd{111} needs to be investigated to the same level as systems such as Ni{110} and Rh{111}, both of

which have been exhaustively researched with respect to acetic acid. Investigating the effect of co-adsorbed species (both stability inducing, such as C, N, O and acetate-bond weakening, such as K) is a key task in understanding how the VAM catalyst systems work fundamentally. Following on from this, an extension of the research into bimetallic systems (particularly Pd/Au) is the next logical step after that and will bring us closer to the current VAM process catalyst.

1.5 Bimetallic Catalysis

1.5.1 Fundamentals of Bimetallic Catalysis

Bimetallic surface science has become an increasingly significant field of study over the last 35 years. It plays a crucial role in a number of technologically important industries, particularly catalysis.⁵⁶ With the advent of UHV vacuum surface analytical techniques and the improvements in surface preparation methods it is becoming increasingly routine to prepare well-defined bimetallic surfaces. These surfaces have provided an opportunity to correlate atomic-level structure with surface reactivity, forming the basis for tailor-made bimetallic surfaces with specific reactivity properties. Subtle changes in bimetallic systems can produce large changes in reactivity and behaviour so a fundamental understanding would be of great use.

Bimetallic catalysts have often been shown to outperform their monometallic counterparts in terms of both activity and selectivity.⁵⁷ Traditionally two reasons have been proposed for the enhancement of a bimetallic catalyst over its monometallic counterparts. These are known as the *ensemble* (structural) and *ligand* (electronic) effects;

- *Ensemble Effects*

The idea of the importance of surface structure in the chemistry of bimetallic surfaces relies largely on the concept of the “active site” for a particular surface chemical reaction. If one reaction requires the presence of three-fold hollow sites on an fcc(111) facet, while a competing reaction requires only single atomic sites, then the random dilution of the active metal by an inert second metal would rapidly deplete the number of active three-fold ensembles. By contrast, the number of single atom sites available would be depleted much

less dramatically as a function of composition. Thus, the selectivity of the catalyst would vary with surface composition.

- *Ligand Effects*

Another factor in the improved performance of bimetallic systems is the so-called “electronic factor”. Here it is presumed that the electronic properties of one element can be modified by the presence of another element and that this in turn can modify the chemisorption and reaction properties of adsorbates. One of the earliest theoretical approaches to explain such effects was the Rigid Band Model.⁵⁸ In this model, it was assumed, for example, that upon dilution of a pure element from Group VIII (e.g. Pd) by an element from Group IB (e.g. Au), the Brillouin Zone* structure of the pure element is preserved.

* *“In mathematics and solid state physics, the first **Brillouin Zone** is the primitive cell in the reciprocal lattice in momentum space. The importance of the Brillouin zone stems from the Bloch wave description of waves in a periodic medium, in which it is found that the solutions can be completely characterized by their behavior in a single Brillouin zone.*

Taking the surfaces at the same distance from one element of the lattice and its neighbours, the volume included is the first Brillouin zone. Another definition is as the set of points in k -space that can be reached from the origin without crossing any Bragg plane.” – Definition of the Brillouin Zone taken directly from the online encyclopedia, Wikipedia.⁵⁹

The net effect would be that 1 extra electron is added to the common band structure for every additional atom of IB element and the consequence of this would be to alter the density of occupied electron states at the Fermi Energy as the composition of the alloy varied. In the case of pure Pd, the d-band is

approximately 95% filled ($4d^8$) giving rise to a high density of states at the Fermi Energy. Using this model, on addition of Au, a dramatic effect on the adsorption properties would be anticipated at the composition where the d-band became filled due to the extra electrons being supplied by Au. Further, more detailed, information regarding ensemble and ligand effects can be found in papers that deal with the more fundamental aspects of bimetallic surface chemistry.^{60,61}

In general, differentiation between ensemble and electronic effects is rarely clear and often there is a contribution from both effects which results in the changing properties of bimetallic systems with changing composition.

The chemistry of bimetallic surfaces is largely controlled by the composition of the outermost surface layer (and to a lesser extent by the immediate sub-surface layers). For many years it was predicted that the composition of the bulk of a bimetallic system will differ from that of the surface.⁶⁰

In general, for an alloy AB, the phenomenon of segregation is controlled by a range of parameters including the differences in bond strengths (A-A, B-B and A-B), atomic size, enthalpies of sublimation and surface energies, temperature, the exposed crystal plane, and metal particle size.

The driving force for segregation is the difference in the binding energies between the two metal atoms, A-B and the binding energies in the pure components, A-A and B-B.⁶² The same change in chemical bonding gives rise to a change in the surface tension of the binary system compared to the surface tension of the pure constituents.

A strong correlation is known to exist for metals between the surface tension and the enthalpy of sublimation, ΔH_{sub} . For atoms at an fcc(111) surface, the coordination number is 9 compared with 12 in the bulk. ΔH_{sub} can be thought of as being proportional to the heat required to convert a 12-coordinate atom into an isolated (gas phase) atom. Thus the difference in energy of atoms in the surface (111) plane relative to that of atoms in the bulk can be considered to be that required to break 3 of the 12 bonds of the bulk metal. Experimentally a value of $0.16.\Delta H_{sub}$ has been obtained.⁶³ Somorjai showed that the ratio of the mole fraction of surface A atoms to surface B atoms can be expressed by the following equation,⁶²

$$\frac{\chi_{B^s}}{\chi_{A^s}} = \frac{\chi_{B^b}}{\chi_{A^b}} \exp \left[\frac{0.16 (\Delta H_{subA} - \Delta H_{subB})}{RT} \right]$$

where x_B^s and x_B^b are the surface and bulk mole fractions of component B respectively.

From this equation, several features emerge;

1. The bulk and surface concentrations of a particular element are generally different.
2. The element with the lower value of heat of sublimation is likely to be the dominant species at the surface.
3. The surface concentration will depend exponentially on temperature.

Part of the derivation of the above equation involved treating the alloy as an ideal solution. However, an alloy has a finite heat of mixing and once this parameter is

incorporated into the model it becomes clear that the surface composition will be strongly dependent on the heat of mixing, its sign and its magnitude.⁶⁴

In terms of thermodynamics, it is also logical that there is some dependence on the adsorbate and it can be assumed that the overriding factor in determining whether and adsorbate, X, induced segregation at a bimetallic surface AB, will be the relative strength of the A-X and B-X bonds. To this end, Tomanek *et al.*⁶⁵ proposed a modified version of the Somorjai's original equation⁶² to take into account the adsorbate effect,

$$\frac{\chi_{B^s}}{\chi_{A^s}} = \frac{\chi_{B^b}}{\chi_{A^b}} \exp \left[\frac{Q_{seg}^{chem}}{RT} \right]$$

where $Q_{seg}^{chem.} = Q_{seg} + (E_A - E_B)/\theta$

Here, Q_{seg} is the work involved in exchanging a surface A atom for a bulk B atom, E_E is the chemisorption energy of the adsorbate on element E and θ is the fractional adsorbate coverage. This equation however, fails to take into account the variation in adsorbate energy as a function of coverage which will have an effect on Q_{seg} .

There is a further consideration in solids, namely that of strain reduction. Solute atoms that differ in size from the solvent lattice will create a strain in the lattice.⁶⁶ Solute atoms may migrate to grain boundaries, where there are open sites with more space available to the atoms, in a bid to reduce strain energy.

As can be seen, even in the relatively simple case of estimating the surface segregation of adsorbate free bimetallic surface problems can be encountered with the calculations,⁶⁷ even before other possible factors *e.g.* face-dependence on behalf of

the segregating species, are considered. However, Mezey *et al.* developed a theory which is known as Modern Thermodynamic Calculation of Interface Properties (MTCIP)^{68,69,70} within which the conditions of the thermodynamic equilibrium state of an interface separating two homogeneous bodies are represented by a system of coupled, non-linear equations. Good agreement was found between this theory and experimental data in all the examined cases (included correct prediction of the face sensitive behaviour of segregation). Further refinements have led to a database of surface compositional predictions for bimetallic systems being established.⁷¹

1.5.2 The Pd/Au bimetallic System

For the production of vinyl acetate in industry, a Pd/Au bimetallic system is used. The exact nature of the system is, of course, covered by confidentiality agreements and patent literature but analysis of the behaviour of acetic acid on differing Pd/Au systems can provide valuable information which can be applied to industrial processes.

There are three ways of creating a Pd/Au bimetallic system on a surface,

- (1) Pd metal deposited on a Au{111} surface
- (2) Au metal deposited on a Pd{111} surface
- (3) Pd-Au single crystals

In practical applications (such as the industrial synthesis of vinyl acetate) Pd/Au bimetallic colloidal particles can also be used but these will not be dealt with in this report, as no measurements were made on such systems in this study. Recent literature indicates that Au is highly active when it is dispersed as nanoparticles^{72,73} The reader

is referred to official *bp* publications in order to learn more about the industrial methods of producing vinyl acetate synthesis.

Pd on Au{111}

Pd on Au{111} is the better researched of the two systems. There are conventionally two ways of depositing Pd onto Au (in fact any metal onto another),

- (1) UHV vapour deposition
- (2) In situ electrochemical deposition

UHV vapour deposition is the older of the two techniques. Shen *et al.*^{74,75} carried out studies on the growth mode and electronic structure of Pd in the mid 1980s and proposed a layer-by layer growth mode for Pd at room temperature. At the time of Shen's work, previous literature reports on the composition and surface segregation at Pd-Au suggested that epitaxial Pd monolayer growth on Au{111} would be thermodynamically unstable, even at moderate temperatures. The reason for this is the greater surface free energy of Pd compared with Au. Pd-Au alloys have been used as catalyst in a number of other systems and several investigations into the surface compositions of these alloys were conducted in the late 1970s and early 1980s, with differing results. Some reports suggested there was no Au enrichment on the surface^{76,77} whilst others reported significant Au enrichment on annealed and sputtered surfaces^{78,79}. Later work by Varga and Hetzendorf⁸⁰ concluded that there was Au segregation in the first layer at room temperature and that annealing to 500 °C causes extensive Au segregation. Poppa *et al.*⁸¹ concluded from their work that Pd-Au alloys formed at room temperature.

All this conflicting information led Koel *et al.*⁸² to carry out a reinvestigation of the system. They concluded that the growth mode of Pd on Au{111} depended strongly on the Pd deposition temperature. At 150 K, the deposition of Pd resulted in a layer-by-layer growth. At 300 K it was not possible to grow a pure Pd monolayer, instead alloying (either by Pd diffusion into the subsurface or Au segregation to the surface) occurred and led to Au substitutionally mixing with the surface Pd. Deposition at 500 K resulted, the Pd/Au mixing was much more substantial, resulting in an Au rich outermost surface layer.

Lambert and his group did further work on the structure of Pd on Au{111} and cyclisation of acetylene to benzene on this system using STM.^{83,84} They made a number of conclusions about the nucleation and growth of Pd on Au{111},

- Nucleation of Pd on Au{111} is preferred at the bulged elbow sites of the well-known reconstructed Au{111}- $22 \times \sqrt{3}$ (herringbone) surface (see Figure 1.4.9).

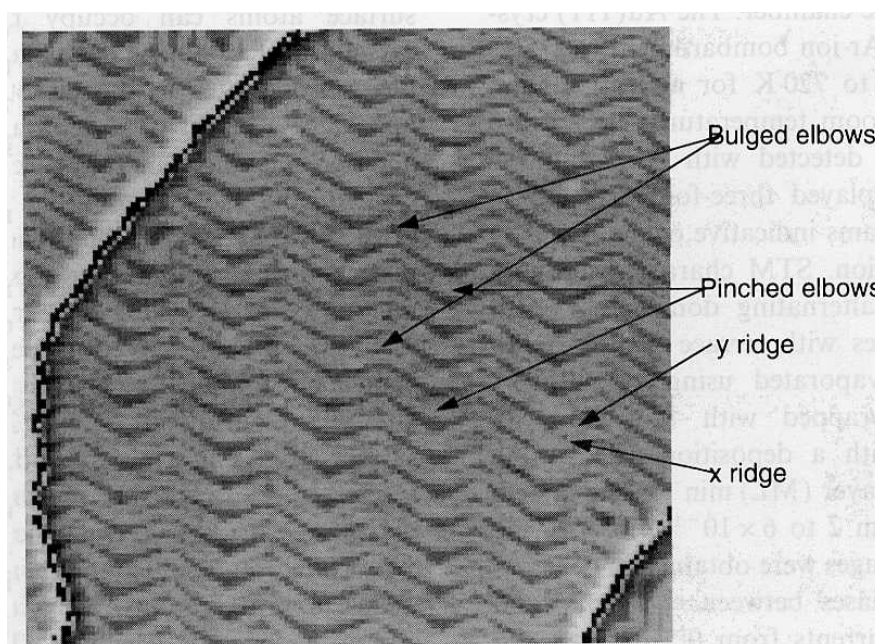


Fig1.4.9 - "Herringbone reconstruction" of Au{111}. Taken from reference⁸³

However, as surface coverage grows, Pd does nucleate at the pinched elbow sites also.

The island size and distribution is similar in both of these cases.

- Sub-monolayer growth of Pd on the reconstructed Au surface is dominated by growth kinetics and island nucleation. The start of the second layer growth commences at around 0.5 ML coverage. The Pd islands formed grow preferentially on FCC regions and are close-packed.
- Higher Pd coverage corresponds with rough multilayers. The morphology of the layers affects the catalytic behaviour in the case of the cyclisation of acetylene to benzene.
- Pd/Au intermixing does not occur at the surface at 300 K.

This final result is in contrast to the work by Koel,⁸² who found Au/Pd intermixing was already present at 300 K. The difference was rationalised as a result of the STM images produced by Lambert and his group in which they showed conclusively that second layer Pd growth commences well before the completion of the first monolayer (see Figure 1.4.10).⁸⁵ A LEIS scattering spectrum for this system would show a persistent Au signal without any intermixing having occurred, hence the reason for the result Koel found and the discrepancy with the actual system.

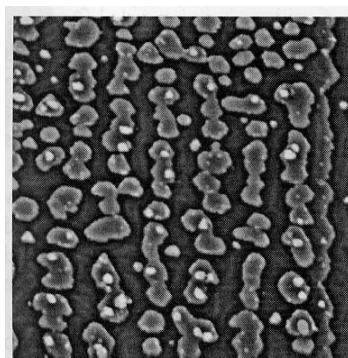


Fig 1.4.10- STM of 0.5 ML Pd on Au{111} at 300 K showing onset of 2nd layer growth before completion of 1st layer. Taken from reference⁸⁵

Previous work by the same group had reported the presence and structure of the Pd₂Au ordered surface alloy that forms at the higher temperature (>400 K), showing that intermixing does take place, but at a higher temperature than Koel.⁸²

Groß and Roudgar recently released some initial work looking into the local reactivity of metal overlayers and he chose the Pd/Au{111} and Pd/Au{100} systems to investigate using DFT^{86,87}. This theoretical study is a good prototype study for investigating the electronic effects and reactivity involved with strained metal overlayers and as such the main conclusion that could be drawn was that the local reactivity of metal overlayers is strongly influenced by a combination of strain, metal-support interaction and bond length effects. The interested reader is directed to the relevant papers but the information contained in the research will not be discussed further as it is not relevant to our work at the early stage of investigation which their study currently exists at.

Groß also carried out some first principles studies into the reactivity of bimetallic systems and included Pd₃ clusters on Au{111}.⁸⁸ He was looking into the electronic structure of the clusters and how they can be altered by and/or alter the surface structure of the Au{111} by using local density of states calculations and his results are reported in his paper. No experiments however were undertaken on these clusters and so there is no more information about the reactions that may take place on these surfaces.

There is another way to synthesise Pd/Au bimetallic systems without the need for vapour metal deposition or cluster creation, namely electrochemical deposition of Pd onto an Au{111} electrode surface. Baldauf and Kolb⁸⁹ carried out the first work on

this electrochemical deposition of Pd onto Au{111} single crystal electrodes and found epitaxial Pd growth.

In the late 1990s, Uosaki *et al.*⁹⁰ investigated the adsorption and electrochemical reduction of PdCl₄²⁻ on Au{111} in H₂SO₄ by in-situ STM. They adsorbed an adlayer of PdCl₄²⁻ with a ($\sqrt{7}\times\sqrt{7}$)R19.1° structure on the unreconstructed Au{111} with the number of adsorbed PdCl₄²⁻ species being *ca.* 15% of that of the Au{111} surface atoms. An alteration in the potential resulted in the deposition of Pd from the adsorbed PdCl₄²⁻. The Pd deposition proceeded by an epitaxial layer-by-layer growth mode, with the adlayer of PdCl₄²⁻ being observed on the Pd thin film with the same structure as on the Au{111} surface.

Following on from the work by Uosaki⁹⁰, Kibler *et al.*⁹¹ carried on similar work investigating the deposition of Pd onto Au(hkl) surfaces, including Au{111}. As a result of the work undertaken, they were able to draw a number of conclusions,

- Au{111} is covered by a distorted hexagonal layer of PdCl₄²⁻ which is similar, but not identical, to the ($\sqrt{7}\times\sqrt{7}$)R19.1° overlayer reported by Uosaki. A similar layer of PdCl₄²⁻ is found on the first Pd layer as well.
- Deposition of the first Pd monolayer starts at underpotentials. Pseudomorphic growth of Pd for the first four monolayers is supported by the appearance of a hexagonal Moiré pattern on the fifth layer. The deposition of the UPD layer starts at steps, before nucleation on terraces occurs at higher overpotentials. Unlike in UHV scenarios, Pd doesn't form a surface alloy with Au{111} in the electrochemical environments.
- The first two layers of Pd grow layer-by-layer, the second starting when the first has been completed. Pd deposition begins exclusively at the surface steps

and the rims of the monatomic high gold islands created by the lifting of the Au herringbone reconstruction.

- There is a slight difference between Au and Pd noted in the STM images obtained during growth of the first Pd layer. Counter-intuitively, Pd appears slightly higher than Au, a fact not explained by Kibler *et al.*⁹¹
- As higher deposition coverage continues, the Pd overlayer acquires a rough appearance, as a result of the next layers growing before the previous ones are completed. Closer examination of the surface morphology reveals flat terraces in the 10nm range, hence terrace atoms far outnumber the step atoms. As a result, Pd overlayers in the 2-10 monolayer thickness in Au{111}, ideally mimics massive Pd{111} crystals.

Monte Carlo simulations carried out by Rojas *et al.*⁹² also concluded that the Pd film grows pseudomorphically on the Au{111} with the same lattice constant and crystallographic orientation as the initial substrate.

The lifting of the herringbone reconstruction in the electrochemical environment is an interesting facet of the Au{111} surface. In the UHV system, the Pd nucleates at the kinks of the reconstruction. In order to lift the reconstruction, the sample can be heated to about 900 K. However, Pd-Au formation is almost guaranteed at this temperature. Looking at the electrochemical scenario however, the reconstruction can be lifted at a potential of +0.35V (versus Ag/AgCl) in H₂SO₄⁹³. In this environment, Pd deposition occurs at +0.58V, which is positive enough (relative to the surface reconstruction transition) to allow Pd to be deposited onto the ideal Au 1x1 surface.

Uosaki *et al.*⁹⁴ confirmed the mechanism for the nucleation and growth proceeded by an instantaneous nucleation and 2D growth in a paper published early last year. However, at slightly higher concentrations of PdCl_4^{2-} , there were slight discrepancies between the experimental results and theoretical models. However, future work is currently ongoing to confirm these findings and, if possible, propose a reason for them.

The difference between the electrochemical and UHV scenarios means that we can create Pd-Au surface alloys by one method and pseudomorphic Pd films by the other. These surfaces will obviously have different surface reactivities and catalytic properties, which can be tailor-made as required.

Au on Pd{111}

Far less is known about the inverse Au/Pd{111} system. Kuk *et al.*⁹⁵ investigated the growth of Au on Pd{111} in the early 1980s and found a transition from the pseudomorphic state to the non-registered state in epitaxial growth. They determined that initially the growth mode was layer-by-layer (*Franck-van der Merwe*) with little to no three dimensional islanding. It was further indicated that inter-diffusion at room temperature was negligible, leading to sharp interface structures. The Au lattice parameter during the initial pseudomorphic growth corresponded to the Pd value. After about 1 monolayer of deposition (discovered to be the “*critical thickness*”)⁹⁵ the lattice parameter slowly increases to the normal Au value. They also discovered that the Pd substrate lattice parameter changed slightly as larger amounts of Au were deposited, an effect not seen by other experiments.

Around the same time, Weissman-Wenocur *et al.* carried out a photoemission study of Au overlayers on Pd{111} and the formation of a Pd-Au alloy surface.⁹⁶ They found that a new structure appeared for Au coverages as low as 0.1 ML, which evolved steadily and smoothly into a structure which was characteristic of bulk Au. They also found similarity in the valence-band electronic structure between a 0.3 ML overlayer of Au on Pd and the ~30% Au alloy which they were able to form. It has been suggested that the alloy is a quasi-random substitutional alloy with a variable composition in the topmost layer.⁶⁰

More recently, Baddeley *et al.*⁹⁷ carried out work on the coupling of acetylene to benzene on the Au/Pd{111} using UHV vapour deposition. They included in their paper a summary of the known facts about the surface structure of the system and it is this summary that is recreated here. Ordered surface alloys were not found, instead a range of disordered Pd/Au alloys with continuously varying compositions are generated. They found that the Au overlayers began to intermix with Pd substrate at 200 K higher than for the inverse Pd/Au{111} system (i.e. about 600 K). Another difference in the two systems comes when comparing the idea of composition stability. For the Pd/Au{111} case we have already seen that system forms a stable, crystalline surface alloy of composition Pd₂Au in the range 450-700 K. In the Au/Pd{111} case there is no temperature regime over which there is a surface of constant composition. The difference between these has been put down to the different mobilities of Au in Pd⁹⁵ and Pd in Au.⁵³ The surface lattice parameter for a 4 ML Au film deposited at 300 K is 4.8% larger than that of Pd{111} and corresponds exactly to the value for Au{111}.⁹⁷ Annealing at 600 K resulted in a small contraction (corresponding to marginal intermixing), whilst there is a linear decrease from 600-900 K to a value just above the Pd{111} clean value. Between 900-1200 K there is a

return to the Pd{111} surface value. This trend is characteristic of the formation of random Pd/Au surface alloys with increasing Pd content as we increase anneal temperature.

Behm and his group created three distinct surface configurations during their work investigating CO adsorption on well-defined bimetallic Au/Pd{111} surfaces in the mid-late 1990s.⁹⁸ The first configuration was prepared by deposition of a sub-monolayer (~ 0.25) of Au at low temperatures (100 K). They found that the substrate terraces were covered in islands with an average size of *ca.* 20Å and a density of *ca.* $9 \times 10^{12} \text{ cm}^{-2}$ and were able to determine that the islands exhibited a structured shape which they described as reminiscent of a relaxed dendritic shape.

Further investigations led them to determine that the islands consisted of Au adatoms and also that the exchange of Au adatoms and Pd surface atoms or the dissolution of Au into the bulk was inhibited under the conditions they were using. From other experiments, it was found that the island density and size did not change drastically upon annealing to 300 K.⁹⁹

Behm and his group also calculated that the relative amount of Au island edge atoms with respect to the total number of Au atoms deposited was *ca.* 40% and about 14% of the available Pd surface atoms were adjacent to island edges. The second bimetallic surface was created by Au deposition (*ca.* 0.2ML) at a higher temperature (300 K). Once again it was discovered that the Au atoms assembled exclusively in adlayer islands on the Pd terraces or as narrow Au structures that extended from the steps on the lower Pd terraces. The island density was found to drop by two orders to $\sim 6 \times 10^{10}$

cm^{-2} , due to the higher mobility of Au adatoms as the temperature is increased, and the average diameter of the island envelope was measured at *ca.* 300Å.

The Au islands now developed a characteristic, partly relaxed dendritic shape but the mobility of the Au adatoms along the island edges was not sufficient for the islands to assume their thermodynamically stable shape. Once again, the group calculated that the relative amount of Au island edge atoms with respect to the total number of Au atoms deposited and the amount of the available Pd surface atoms that were adjacent to island edges, calculating values of 7% and 2% respectively.

The third bimetallic surface was created by the step-wise annealing of a 1.3ML film of Au, deposited at 300 K, to 925 K. Au dissolution was found to commence at about 450 K (slightly lower than that found by Baddeley *et al.*⁹⁷) although the process became much more pronounced as anneal temperatures rose above 650 K, which is in agreement with the previous study. The Au intensity, measured by AES, had dropped to 11% of its original value and the surface exhibited a flat step-terrace morphology with no islands on the terraces and no additional material nucleated at the step-edges. Behm and his group used quantitative evaluation of STM images to determine that the surface concentration was *ca.* 17% Au but they were unable to probe the sub-surface regions.^{98,99}

There has been very little groundbreaking work on this system since the work detailed above and this author has been unable to find any papers dealing with the electrochemical deposition of Au onto Pd{111}.

Pd-Au Single Crystals

There has been very little work carried out on Pd-Au single crystals in the literature. Heiland and his co-workers did carry out some work concerning structural studies of the $\text{Au}_3\text{Pd}\{100\}$ ¹⁰⁰ and $\{113\}$ ¹⁰¹ surfaces, in the mid-1990s, and found that both surfaces are 100% Au-terminated. Early work in the 1970s and 1980s reported Au segregation from experimental studies of Pd-Au polycrystals^{102,103,104}. Piccolo *et al.* recently looked at the selective hydrogenation of 1,3-butadiene on Pd-Au single crystal surfaces.¹⁰⁵ The surfaces they investigated were the $\text{Pd}_{70}\text{Au}_{30}\{111\}$ and $\{110\}$ ones and both exhibited a (1x1) structure. Strong surface segregation of Au was activated when the samples were heated above *ca.* 250°C and annealing to 450°C led to Au concentrations of 75% and 85% in the top layers for the $\{111\}$ and $\{110\}$ surfaces respectively.

1.6 K as a promoter on Pd and Au surfaces

The effect of alkali metal promoters in catalytic reactions has been subject to rigorous study because of their use in important industrial reactions such as CO hydrogenation, methanol synthesis, coal gasification, ammonia synthesis and vinyl acetate monomer production. In depth surface science studies have been able to demonstrate that alkali metals can alter the electronic structure of the underlying metal substrate which can modify the metal-adsorbate bond of a chemisorbed molecule and lead to a weakening of the bonds within the molecule.¹⁰⁶ This would, of course, promote the dissociation of the adsorbate on the metal surface. Another wholly different effect of alkali metal promoters concerns their participation in the reaction. Alkali metals are generally highly reactive and have a tendency to form compounds with a large number of molecules (mostly oxygen containing). The reactivity of an alkali metal atom with co-adsorbed molecules had been found to be a strong function of alkali coverage and usually dominated at high alkali coverage (i.e. a near saturation coverage of the first layer) where the alkali atoms exhibit “metallic behaviour”.¹⁰⁷ This idea was originally discussed in the 1930s by Langmuir¹⁰⁸ and Gurney¹⁰⁹ in which the behaviour of alkali adsorption on transition metals was described as “ionic” at low coverages with a gradual transition towards “metallic” at saturation. The initial adsorption of alkali metals onto metal surfaces was regarded to proceed via a charge transfer mechanism from the valence s-electrons of the adsorbate (which are loosely bound) to the substrate, in other words, the alkali metal and metal substrate form an “ionic” bond. Langmuir¹⁰⁸ and Gurney¹⁰⁹ surmised that the alkali metal to substrate bond was the stronger (*i.e.* the charge flow from alkali metal to metal is the more efficient) resulting in the creation of a slightly positively charged alkali metal. This now positively charged alkali metal would induce a screening charge in the metal surface, creating an electric dipole moment.

As the coverage increases, the alkali metal begins to depolarize and eventually the adsorbed alkali metal atoms become neutral and the binding is “metallic”. This picture was generally accepted up until the last twenty years or so where certain practical and numerical experiments have highlighted phenomena that were not predicted by the Langmuir-Gurney model, a succinct summary and analysis of some of these systems is presented by Diehl and McGrath.¹¹⁰ Evidence of these phenomena has led to a renewed interest in the Langmuir-Gurney model as it is somewhat deficient. For example, studies examining the electron density using density-functional theory (DFT) have provided more in-depth insight into the complex adsorbate-substrate interaction, and in the case of Co{10 $\bar{1}$ 0}-c(2x2)-K, the bonding has been shown to have both ionic and metallic contributions, not predicted by the original model.¹¹¹ Returning to the initial work on this topic by Langmuir¹⁰⁸ and Gurney¹⁰⁹, they predicted drastic changes in the adsorption geometry as the alkali metal coverage increases due to the differences in Pauling radii between alkali metals when in their ionic and metallic states (see Table 1.6.1).

Alkali Metal	Pauling radii / Å		
	Ionic	Covalent	Metallic
Li	0.60	1.23	1.55
Na	0.95	1.54	1.90
K	1.33	2.03	2.35
Rb	1.48	2.16	2.48
Cs	1.69	2.35	2.67

Table 1.6.1 – The hard-sphere radii of alkali metals in ionic, covalent and metallic bonding.

Adapted from reference¹¹²

As a result of this belief, the initial method of study for these alkali metal on metal substrate systems was to identify bond length variations with coverages. However, very little compelling evidence has been provided to support that expectation and, in fact, the variation of the alkali metal – metal bond length as a function of alkali metal coverage has not been found to be significant for a particular adsorption system.¹¹³

There have been difficulties, however, in the structural investigations carried out on these systems as it has been found that in a large number of cases the alkali metal coverages were too high for them to be treated as isolated alkali metal atoms on the surface, making the transition from ionic to metallic bonding difficult to probe.

The study of alkali metal structures on metal substrates is still a very important topic as the previous work has revealed a particularly complex behaviour which has resulted in the mechanism of alkali promotion remaining somewhat of a mystery, with the possible exception of the ammonia synthesis reaction.¹¹⁴

As a result of these mysteries, alkali metal promoters have been studied for many years on a variety of metal surfaces such as Ni{110}¹¹⁵, Ru{001}¹¹⁶, Cu{110}^{117,118}, Cu{111}¹¹⁹, Co{10 $\bar{1}$ 0}¹²⁰, Ag{111}¹²¹ and Pt{111}¹²² as well as on Pd and Au surfaces.

Currently there have been no reports done on the Pd/K/AcOH or Pd/Au/K/AcOH systems, which will be critical in the final understanding of the process of vinyl acetate monomer synthesis, and we present data on these two systems at a later point in this thesis. Research has been carried out previously on the K/Pd{111} system and it is prudent to investigate these results prior to commencing our own investigations.

The main work of interest to us concerns the orientation and geometry of K as it is adsorbed on a Pd{111} surface as this will help us to analyse our work on the industrially relevant systems mentioned above.

Over and his group carried out investigations into the atomic geometries of Cs and K on Pd{111} and discussed the role of the ionization potential of the substrate on the results.¹²³ The reader is directed to the original paper for analysis of the ionization potential as only the basic geometric work will be recreated here.

They found that K (and Cs) were both able to form (2x2) and ($\sqrt{3}\times\sqrt{3}$)R30° overlayers on the Pd{111} surface. In both cases K adsorbs in the threefold co-ordinated *hcp* site on Pd{111} and the alkali metal radii is close to the covalent Pauling radii independent of the coverage (see Figures 1.6.1 and 1.6.2 below).

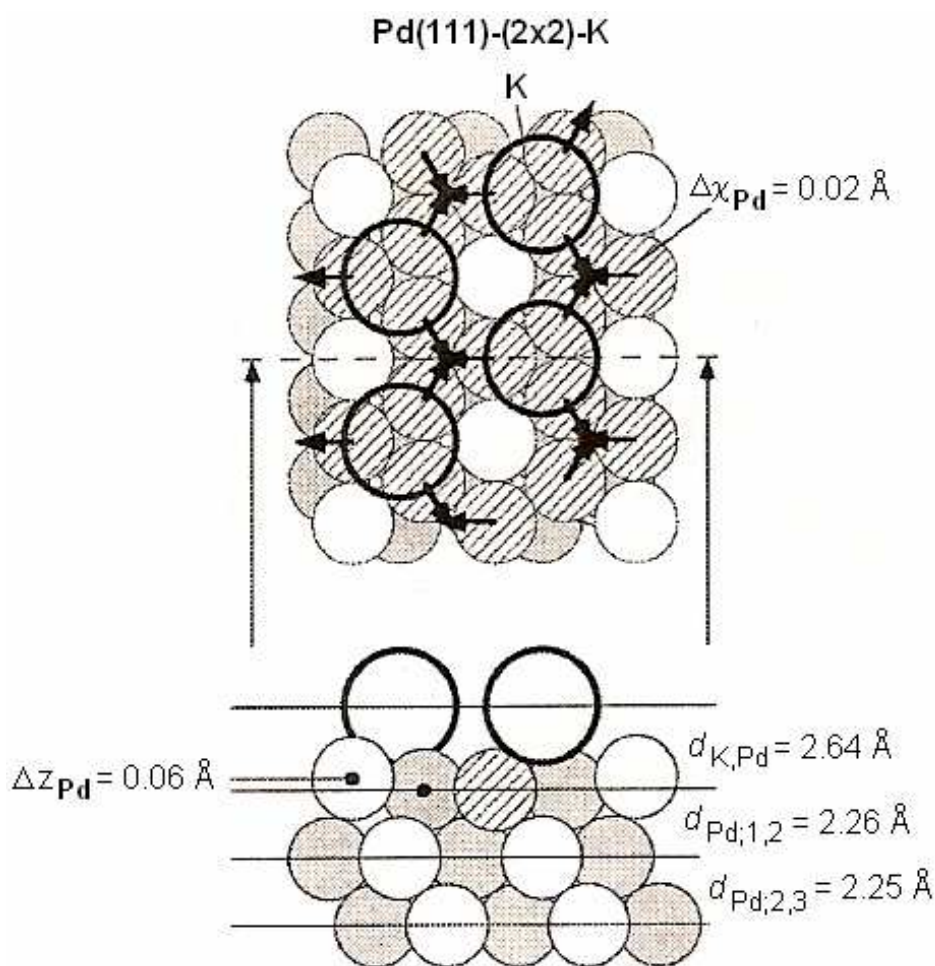


Fig 1.6.1 – Hard-sphere model of the K(2x2) structure on Pd{111}. K sits in the *hcp* position and the Pd-K bond length is 3.10Å. Adapted from reference¹²³

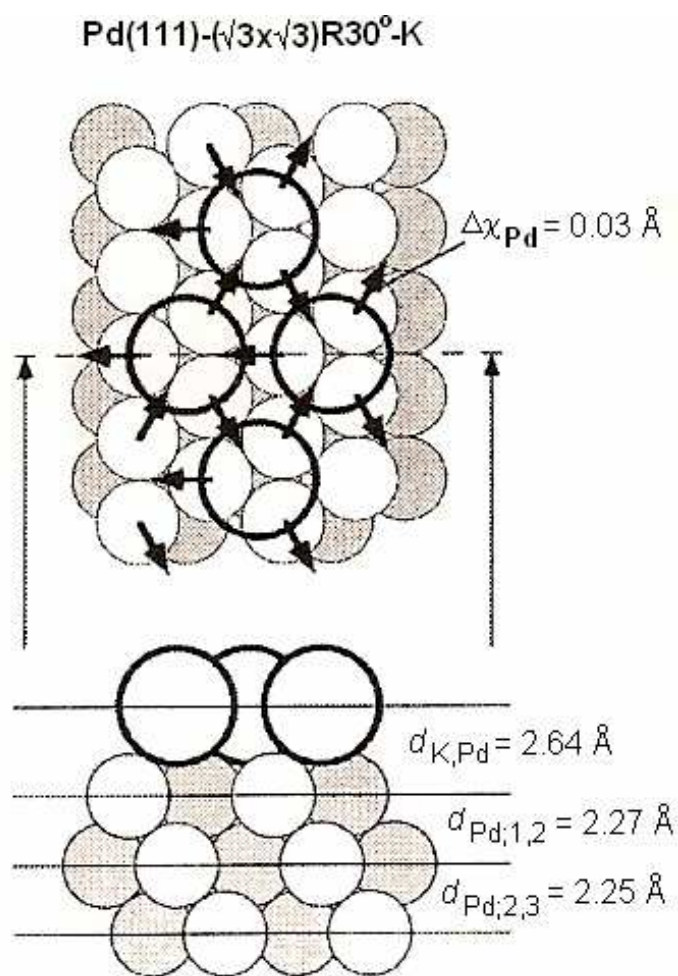


Fig 1.6.2 – Hard-sphere model of the $\text{K}(\sqrt{3}\times\sqrt{3})R30^\circ$ structure on $\text{Pd}\{111\}$. The K resides in the *hcp* position and the Pd-K bond length is 3.10\AA . Adapted from reference¹²³

Over and his group created their sub-monolayer coverages of K and Cs by first depositing a *ca.* 2ML alkali metal film followed by a flash anneal to a specific temperature in order to remove excess alkali metal. They recorded that an anneal to 470 K produced the $(\sqrt{3}\times\sqrt{3})R30^\circ$ overlayer whilst in order to produce the (2x2) overlayer an anneal to 604 K was required – indicating as expected that a lower coverage of K produces the (2x2) surface whilst a slightly higher coverage results in the $(\sqrt{3}\times\sqrt{3})R30^\circ$ K overlayer. They also made comparison with other transition metal-alkali metal systems and the reader is referred to the original paper for their discussion on this topic.¹²³

Work has been carried out on the other Pd systems as well as the Pd{111} surface and papers concerning K behaviour on Pd{110}¹²⁴ and Pd{100}^{125,126} can be found in the literature.

K studies on a variety of Au surfaces have also been undertaken. Au{100}^{127,128,129} and Au{110}^{130,131,132} have been studied more thoroughly than Au{111} and in those cases it has been demonstrated that mixed KAu surface layers are formed (irreversibly) upon thermal annealing at intermediate sub-monolayer coverages of 0.25 – 0.5 ML. The high reactivity of Au surfaces closely relates to the existence of alkali metal Au alloys. Other early studies have shown that low-index Au surfaces are very reactive towards adsorbed alkali metal atoms.^{133,134}

K on Au{111} has been investigated very sparingly and the majority of the work was carried out by Barth *et al.* in the mid 1990s.¹³⁵ They carried out LEED, STM and AES experiments on a range of different K coverages on Au and found varying results. When dosed at 300 K, they saw no LEED pattern until a coverage of *ca.* 0.33 ML when a $(\sqrt{3}\times\sqrt{3})R30^\circ$ pattern was observed. Between 0.35 ML and 0.45 ML this $(\sqrt{3}\times\sqrt{3})R30^\circ$ pattern co-existed with a (2x2) diffraction pattern, whilst above 0.45 ML the (2x2) pattern is uniquely visible. This (2x2) pattern was initially assigned to either a p(2x2) or a superposition of three 120° rotational domains of a (1x2) surface structure and STM studies confirmed the presence of the former and not the latter. At coverages exceeding 0.6 ML the pattern became more and more diffuse until, by 0.9 ML, the spots were hardly visible. When K dosing is carried out at 400 K, the $(\sqrt{3}\times\sqrt{3})R30^\circ$ pattern is not observed but the (2x2) pattern is seen, analogous to adsorption at 300 K. This $(\sqrt{3}\times\sqrt{3})R30^\circ$ pattern has been seen on other systems but the (2x2) phase for higher coverages, and the wide range of coverages over which it is

seen, is untypical for alkali metal adsorption on fcc{111} surfaces.¹³⁶ It is not unique however, as Na adsorption on Al{111} shows analogous behaviour¹³⁷

Na adsorption on Au{111} has been investigated by the same group and they found that a NaAu₂ surface layer was formed, which is considered to be a two-dimensional alloy.¹³⁸ In this case it was also found that the alloy layer is covered by an overlayer of Na. Evidence of alloying in the KAu case is now presented by Barth *et al.*¹³⁵ as well when they discuss the fact that a coverage in excess of 0.5 ML K can be obtained on the Au substrate at 300 K. They calculated that a coverage of 0.45 ML K would correspond to a physical K monolayer (due to the atomic radius of K) and that a second layer must be formed for the higher K coverages, which would not be expected at 300 K. They concluded from the LEED that an intermixed KAu is formed, at higher coverages, which can accommodate the additional adsorption of further K layers on top.

The STM data provided seemed to confirm this theory. In the low coverage cases, the Au “herring-bone” reconstruction (see Figure 1.4.9 earlier) has not been lifted with the addition of K although it has been slightly modified; the periodicity of the zig-zag pattern on the surface is reduced (from 250Å for the clean surface to 150Å at *ca.* 0.33 ML) and the atomic steps appear “fringed” as the motion of the step atoms is much faster than the STM measurements.¹³⁹ The continuing existence of the zig-zag reconstruction for coverages up to *ca.* 0.33 ML is strong evidence that the ($\sqrt{3}\times\sqrt{3}$)R30° LEED pattern corresponds to simply a K overlayer on the reconstructed Au{111} surface. On further dosing of K to coverages above 0.35 ML, the surface begins to lose its herring-bone reconstruction and islands begin to be formed on the surface. The conclusion was drawn that the Au{111} reconstruction was being lifted

and that a K induced reconstruction was being formed with an intermixed KAu surface layer (of unknown K:Au stoichiometry) as predicted by the LEED experiments. They concluded that the Au{111} surface is reactive towards K atoms and forms mixed KAu surface layers at K coverages greater than 0.33 ML.¹³⁵

No work has yet been published on the behaviour of Pd/Au surfaces upon adsorption of alkali metals (and in particular K) and this seems to be a sensible study to undertake given the, as yet unknown, relationship between K, Pd and Au in the synthesis of VAM industrially.

1.7 Thesis Synopsis

This project will deal initially with the Au/Pd{111} bimetallic system as the synthesis of VAM started with a Pd{111} clean surface and has progressed to a Pd/Au system. There is also less work on this system in the literature, allowing us a bigger scope for experiments. Characterisation of the different bimetallic surfaces is a key goal for this work, as is the difference these subtle changes have on reactivity and surface behaviour with respect to acetic acid. MEIS analysis coupled with STM imagery will hopefully give us an excellent understanding of the behaviour of the bimetallic surface.

Analysis of the behaviour of AcOH on the Au/Pd{111} bimetallic system will give us an idea of how the changing surface structure and composition affects the binding and reactivity of AcOH. Addition of pre-adsorbed C and K (separately) will help to look at the system in a more industrially relevant manner as ultimately the aim is to understand the full-scale industrial catalytic process. TPD and RAIRS will be used in conjunction with STM and MEIS experiments and LEED and AES will assist with surface characterisation.

1.8 References for Chapter 1

- ¹ F.Zaera, *Surf. Sci.*, **500**, 947-965 (2002)
- ² G.A.Somorjai, “*Chemistry in 2D: Surfaces*”, Cornell University Press (1981)
- ³ Report acquired from Tecnon OrbiChem at <http://www.tecnon.co.uk/gen>
- ⁴ I.I.Mosieev, M.N.Vargaftic and Ya.K.Syrkin, *Dokl. Akad. Nauk. USSR*, **133**, 377 (1960)
- ⁵ D.Lark, P.Hayden and R.D.Smith, “*Oxidation of Olefins by Palladium Salts in Non-Aqueous solvents*”, August 1968
- ⁶ *Eur. Chem. News*, **11(272)**, 40 (1967)
- ⁷ *World. Pet. Cong. Proc.*, **5**, 41 (1968)
- ⁸ B.T.Charles, *US Patent 4048096* (1977)
- ⁹ B.Samanos, P.Boutry and R.Montarnal, *J. Catal.*, **23**, 19-30 (1971)
- ¹⁰ T.Kunigi and K.Fuzimoto, *Kogyo Kagaku Zashi*, **72**, 1760 (1969)
- ¹¹ S.Nakamura and T.Yasui, *J. Catal.*, **23**, 315-320 (1971)
- ¹² R.S.Shetty, D.H.Kashyap and S.B.Chandalia, *Ind. J. Technol.*, **11**, 170-173 (1973)
- ¹³ H.Debellefontaine and J.Besombes-Vailhe, *J. de Chim. Phys.*, **75(9)**, 801-809 (1978)
- ¹⁴ S.Zaidi, *Appl. Catal.*, **38**, 353-358 (1988)
- ¹⁵ (a) S.Zaidi, *Zh. Obshchei. Khimii*, **51**, 518 (1981) (b) S.Zaidi, *J. Catal.*, **68**, 255 (1981)
- ¹⁶ P.R.Roney, *J. Catal.*, **14**, 142 (1969)
- ¹⁷ C.R.Reilly and J.J.Lerou, *Catal. Today*, **41**, 433-441 (1998)
- ¹⁸ R.E.Robinson, U.S. Patent No. 3,190,912 (1965)
- ¹⁹ J.H.Wieland, G.Prauser and K.Dialer, *Chem. Ing. Technol.*, **54**, 605 (1982)
- ²⁰ S.Nakamura and T.Yasui, *J. Catal.*, **17**, 366 (1970)
- ²¹ S.M.Augustine and J.P.Blitz, *J. Catal.*, **142**, 312-324 (1993)
- ²² E.A.Crathorne, D.MacGowan, S.R.Morris and A.P.Rawlinson, *J. Catal.*, **149**, 254-267 (1994)
- ²³ R.G.Brown, J.M.Davidson and C.Triggs, *Am. Chem. Soc. Div. Petrol. Chem. Prep.*, **14**, B23 (1969)
- ²⁴ D.D.Kragten and R.A.van Santen, *Inorg. Chem.*, **38**, 331-339 (1999)
- ²⁵ P.M.Henry and R.N.Pandry, “*Homogeneous Catalysis II; Advances in Chemistry Series 132*”, American Chemical Society, Washington, p33 (1973)
- ²⁶ P.M.Henry and R.N.Pandry, *Can. J. Chem.*, **53**, 1833 (1975)
- ²⁷ Y.-F.Han, D.Kumar, C.Sivadinarayana, and D.W.Goodman, *J. Catal.*, **224**, 60-68 (2004)
- ²⁸ Y.-F.Han, D.Kumar, and D.W.Goodman, *J. Catal.*, **230**, 353-358 (2005)
- ²⁹ Y.-F.Han, D.Kumar, C.Sivadinarayana, A.Clearfield and D.W.Goodman, *Catal. Lett.*, **94(3-4)**, 131-134 (2004)
- ³⁰ W.T.Tysoe, L.Burkholder, D.Stacchiola and F.Calaza, *J. Am. Chem. Soc.*, **126**, 15384 (2004)
- ³¹ W.T.Tysoe, L.Burkholder, D.Stacchiola, F.Calaza, M.Neurock and A.W.Schwabacher., *Angew. Chem. Int. Ed.*, **44**, 4572 (2005)
- ³² J.R.Zoeller, G.C.Tustin and R.D.Colberg, *Catal. Today*, **58(4)**, 281-291 (2000)
- ³³ W.D.Provine, P.L.Mills, and J.J.Lerou, *Stud. Surf. Sci. Catal.*, **101**, 191 (1996)
- ³⁴ M.Neurock, *J. Catal.*, **216**, 73 (2003)
- ³⁵ M.Bowker and R.J.Madix, *Appl. of Surf. Sci.*, **8**, 299-317 (1981)
- ³⁶ S.Bao, G.Liu and D.P.Woodruff, *Surf. Sci.*, **203**, 89-100 (1988)
- ³⁷ S.Haq and F.M.Liebsle, *Surf. Sci.*, **355**, L345-L349 (1996)
- ³⁸ D.J.Coulman, J.Wintterlin, R.J.Behm and G.Ertl, *Phys. Rev. Lett.*, **64**, 1761 (1990)
- ³⁹ K.-U.Weiss, R.Dippel, K.-M.Schneider, P.Gardner, V.Fritzsche, A.M.Bradshaw, A.L.D.Kilcoyne and D.P.Woodruff, *Phys. Rev. Lett.*, **69**, 3196 (1992)
- ⁴⁰ F.Jenson, F.Besenbacher, E.Laegsgaard and I.Stensgaard, *Phys. Rev. B.*, **42**, 9206 (1990)
- ⁴¹ E.Kopatzki and R.J.Behm, *Phys. Rev. Lett.*, **74**, 1399 (1995)
- ⁴² F.M.Liebsle, S.Haq, B.Frederick, N.V.Richardson and M.Bowker, *Surf. Sci.*, **343**, L1175 (1995)
- ⁴³ P.Baumann, H.P.Bonzel, G.Pirug and J.Werner, *Chem. Phys. Lett.*, **260** 215-222 (1996)
- ⁴⁴ S.M.Johnston, G.Rousseau, V.Dhanak and M.Kadodwala, *Surf. Sci.*, **477** 163-173 (2001)
- ⁴⁵ M.Nowicki, A.Emundts, J.Werner, G.Pirug and H.P.Bonzel, *Surf. Rev. and Lett.*, **7(1&2)**, 25-36 (2000)
- ⁴⁶ G.R.Schoofs and J.B.Benziger, *Surf. Sci.*, **143**, 359-368 (1984)
- ⁴⁷ J.B.Benziger and E.W.Scharpf, *J. Phys. Chem.*, **91**, 5531-5534 (1987)
- ⁴⁸ D.Sander and W.Erley, *J. Vac. Sci. Technol.*, **7(3)**, 2238 (1989)
- ⁴⁹ R.J.Madix, J.L.Falconer and A.M.Suszko, *Surf. Sci.*, **54**, 6 (1976)
- ⁵⁰ M.Bowker and Y.Li, *J. Catal.*, **142**, 630-640 (1993)
- ⁵¹ G.Hoogers, D.C.Papageorgopoulos, Q.Ge and D.A.King, *Surf. Sci.*, **340**, 23-35 (1995)
- ⁵² M.Bowker and N.Aas, *J. Chem. Soc. Farad. Trans.*, **89(8)**, 1249-1255 (1993)
- ⁵³ J.L.Davis and M.A.Barreau, *Langmuir*, **5**, 1299 (1989)

- ⁵⁴ (a) J.L.Davis and M.A.Barteau, *Surf. Sci.*, **256**, 50 (1991) (b) J.L.Davis and M.A.Barteau, *Surf. Sci.* **260**, 215 (1996)
- ⁵⁵ R.D.Haley, M.S.Tikhov and R.M.Lambert, *Catal. Lett.*, **76(3-4)**, 125 (2001)
- ⁵⁶ G.R.Rao, *Curr. Science.*, **75**, 901 (1998)
- ⁵⁷ J.H.Sinfelt, *Acc. Chem. Research*, **20**, 134 (1987)
- ⁵⁸ E.A.Stern, *Phys. Rev.*, **157**, 544 (1967)
- ⁵⁹ http://en.wikipedia.org/wiki/Main_Page
- ⁶⁰ C.T.Campbell, *Annu. Rev. Phys. Chem.*, **41**, 775 (1990)
- ⁶¹ J.A.Rodriguez, *Surf. Sci. Rep.*, **24**, 223 (1996)
- ⁶² G.A.Somorjai, "Introduction to surface chemistry and catalysis", John Wiley and Sons, New York, chpt. 3 (1994)
- ⁶³ S.Overbury, P.Bertrand and G.A.Somorjai, *Chem. Rev.*, **75**, 547 (1995)
- ⁶⁴ P.Wynblatt and R.C.Ku, *Surf. Sci.*, **65**, 511 (1977)
- ⁶⁵ D.Tomanek, S.Mukherjee, V.Kumar and K.H.Bennemann, *Surf. Sci.*, **114**, 11 (1982)
- ⁶⁶ D.McLean, "Grain Boundaries in Metals", Oxford University Press, London (1957)
- ⁶⁷ L.Z.Mezey and W.Hofer, *Surf. Sci.*, **65**, 511 (1977)
- ⁶⁸ L.Z.Mezey, *Surf. Sci.*, **162**, 510 (1985)
- ⁶⁹ L.Z.Mezey and J.Giber, *Acta Phys. Hung.*, **66**, 309 (1989)
- ⁷⁰ L.Z.Mezey and J.Giber, *Surf. Sci.*, **234**, 210 (1990)
- ⁷¹ P.Weigand, B.Jelinek, W.Hofer and P.Varga, *Surf. Sci.*, **269-270**, 1129 (1992)
- ⁷² M.Haruta, *Catal. Today*, **36**, 153 (1997)
- ⁷³ M.Valden, X.Lai and D.W.Goodman, *Science*, **281**, 1647 (1998)
- ⁷⁴ X.Y.Shen, D.J.Frankel, J.C.Hermanson, R.J.Smith and G.J.Lapeyre, *Phys. Rev. B*, **32**, 2120 (1985)
- ⁷⁵ X.Y.Shen, D.J.Frankel, J.C.Hermanson, R.J.Smith and G.J.Lapeyre, *Phys. Rev. B*, **33**, 5372 (1986)
- ⁷⁶ B.J.Wood and H.Wise, *Surf. Sci.*, **52**, 151 (1975)
- ⁷⁷ L.Hilaire, P.Legare, Y.Hull and G.Maire, *Surf. Sci.*, **103**, 125 (1981)
- ⁷⁸ A.Jablonski, S.H.Overbury and G.A.Somorjai, *Surf. Sci.*, **65**, 578 (1977)
- ⁷⁹ M.J.Kelley, S.B.Ziemaeki and D.G.Swartzfager, *J. Vac. Sci. Technol.*, **19**, 185 (1981)
- ⁸⁰ P.Varga and G.Hetzendorf, *Surf. Sci.*, **162**, 544 (1985)
- ⁸¹ H.Poppa, E.Bauer and H.D.Shih, *Surf. Thin Solid Films*, **88**, L21 (1982)
- ⁸² B.E.Koel, A.Sellidj and M.T.Paffett, *Phys. Rev. B*, **46(12)**, 7846 (1992)
- ⁸³ C.J.Baddeley, R.M.Lambert, A.W.Stephenson and M.S.Tikhov, *Surf. Sci.*, **398**, 172-183 (1998)
- ⁸⁴ C.J.Baddeley, R.M.Lambert, A.W.Stephenson and R.M.Ormerod, *J. Phys. Chem.*, **99(14)**, 5148 (1995)
- ⁸⁵ R.M.Lambert, D.A.King, C.J.Baddeley, R.M.Ormerod, C.J.Barnes and A.Wander, *Surf. Sci.*, **314**, 1 (1994)
- ⁸⁶ A.Roudgar and A.Groß, *J. Electroanal. Chem.*, **548**, 121 (2003)
- ⁸⁷ A.Roudgar and A.Groß, *Phys. Rev. B*, **67**, 033409 (2003)
- ⁸⁸ A.Groß, *Topics in Catalysis*, **37(1)**, 29 (2006)
- ⁸⁹ M.Baldauf and D.M.Kolb, *J. Phys. Chem.*, **38**, 2145 (1993)
- ⁹⁰ K.Uosaki, H.Naohara and S. Ye, *J. Phys. Chem. B*, **102**, 4366-4373 (1998)
- ⁹¹ L.A.Kibler, M.Kleinert, R.Randler and D.M.Kolb, *Surf. Sci.*, **443**, 19-30 (1999)
- ⁹² M.I.Rojas, M.G.Del Pópolo and E.P.Leiva, *Langmuir*, **16**, 9539-9546 (2000)
- ⁹³ M.Takahasi, Y.Hayashi, J.Mizuki, K.Tamura, T.Kondo, H.Naohara and K.Uosaki, *Surf. Sci.*, **461**, 213-218 (2000)
- ⁹⁴ K.Uosaki, M.E.Quayum and S. Ye, *J. Electroanal. Chem.*, **520**, 126-132 (2002)
- ⁹⁵ Y.Kuk, L.C.Feldman and P.J.Silverman, *Phys. Rev. Lett.*, **50(7)**, 511-514 (1982)
- ⁹⁶ D.L.Weissman-Wenocur, P.M.Stefan, B.B.Pate, M.L.Shek, I.Lindau and W.E.Spicer, *Phys. Rev. B*, **27(6)**, 3308 (1983)
- ⁹⁷ C.J.Baddeley, R.M.Lambert, M.S.Tikhov, C.Hardacre and J.R.Lomas, *J. Phys. Chem.*, **100**, 2189 (1996)
- ⁹⁸ B.Gleich, M.Ruff and R.J.Behm, *Surf. Sci.*, **386**, 48-55 (1997)
- ⁹⁹ B.Gleich, *Diploma Thesis: University of Ulm*, 1996
- ¹⁰⁰ M.Aschoff, S.Speller, J.Kuntze, W.Heiland, E.Platzgummer, M.Schmid, P.Varga and B.Baretzky, *Surf. Sci.*, **415**, L1051 (1998)
- ¹⁰¹ M.Aschoff, G.Piaszenski, S.Speller and W.Heiland, *Surf. Sci.*, **402**, 770 (1998)
- ¹⁰² A.Jablonski, S.H.Overbury and G.A.Somorjai, *Surf. Sci.*, **65**, 57 (1977)
- ¹⁰³ D.G.Swartzfager, S.B.Ziemaeki and M.J.Kelly, *J. Vac. Sci. Technol.*, **19**, 185 (1981)
- ¹⁰⁴ G.Hetzendorf and P.Varga, *Nucl. Instr. Meth. Phys. Rev. B*, **18**, 501 (1987)
- ¹⁰⁵ L.Piccolo, A.Piednor and J-C.Bertolini, *Surf. Sci.*, **592**, 169 (2005)
- ¹⁰⁶ H.P.Bonzel, *Surf. Sci. Rep.*, **8**, 43 (1987)

-
- ¹⁰⁷ J.Paul, R.A.de Paola and F.M.Hoffman, “*Materials Science Monographs; Physics and Chemistry of Alkali Adsorption*”, Eds.; H.P.Bonzel, G.Broden and H.J.Krebs, Elsevier, New York, **57**, p213 (1989)
- ¹⁰⁸ I.Langmuir, *J. Am. Chem. Soc.*, **54**, 2798 (1932)
- ¹⁰⁹ R.W.Gurney, *Phys. Rev.*, **47**, 479 (1935)
- ¹¹⁰ R.D.Diehl and R.McGrath, *J. Phys.: Condens. Matter*, **9**, 951 (1997)
- ¹¹¹ S.J.Jenkins and D.A.King, *Chem. Phys. Lett.*, **317**, 372 (2000)
- ¹¹² C.Kittel, “*Introduction to Solid State Physics*”, Wiley, New York, 5th Edn. (1976)
- ¹¹³ R.Diehl and R.McGrath, *Surf. Sci. Rep.*, **23**, 43 (1996)
- ¹¹⁴ G.Ertl, M.Weiss and S.B.Lee, *Chem. Phys. Lett.*, **109**, 51 (1988)
- ¹¹⁵ J.Wambach, G.Iling and H.J.Freund, *Chem. Phys. Lett.*, **184**, 239 (1991)
- ¹¹⁶ M.D.Weisel, J.L.Robbins and F.M.Hoffmann, *J. Phys. Chem.*, **97**, 9441 (1993)
- ¹¹⁷ P.M.Møller, P.J.Godowski and L.Onsgaard, *Vacuum*, **54**, 31 (1999)
- ¹¹⁸ P.M.Møller, P.J.Godowski, S.V.Christensen, J.Nerlov and S.Quist, *Surf. Sci.*, **370**, L137 (1997)
- ¹¹⁹ J.Nakamura, Y.Kushida, Y.Choi, T.Uchijima and T.J.Fujitani, *J. Vac. Sci. Technol. A*, **15**, 1568 (1997)
- ¹²⁰ D.A.King and R.L.Toomes, *Surf. Sci.*, **349**, 19-42; 43-64; 65-80 (1996)
- ¹²¹ P.Herrera-Fierro, K.Wang, F.T.Wagner, T.E.Moylan, G.S.Chottiner and D.A.Scherson, *J. Phys. Chem*, **96**, 3788 (1992)
- ¹²² Z.M.Liu, Y.Zhou, F.Solymosi and J.M.White, *J. Phys. Chem.*, **93(11)**, 4383 (1989)
P. M.Henry and R.N.Pandry, “*Homogeneous Catalysis II; Advances in Chemistry Series 132*”, American Chemical Society, Washington, p33 (1973)
- ¹²³ H.Over, Y.D.Kim and S.Schwegmann, *Phys. Chem. Chem. Phys.* **1**, 2001 (1995)
- ¹²⁴ S.J.Pratt, D.K.Escott and D.A.King, *Phys. Rev. B*, **68**, 235406 (2003)
- ¹²⁵ A.Berkó and F.Solymosi, *Surf. Sci.*, **187**, 359 (1987)
- ¹²⁶ S.J.Jenkins and D.A.King, *Chem. Phys. Lett.*, **317**, 372 (2000)
- ¹²⁷ M.Okada, H.Iwai, R.Klauser and Y.Murata, *J. Phys. Condens. Matt.*, **4**, L593 (1992)
- ¹²⁸ A.Neumann, S.L.M.Schröder and K.Christmann, *Phys. Rev. B*, **51**, 17007 (1995)
- ¹²⁹ S.L.M.Schröder, A.Neumann, T.Solomon, P.Lenz-Solomon and K.Christmann, *Surf. Sci.*, **337**, 285 (1995)
- ¹³⁰ P.Häberle and T.Gustafsson, *Phys. Rev. B*, **40**, 8218 (1989)
- ¹³¹ K.M.Ho, C.T.Chan and K.P.Bohnen, *Phys. Rev. B*, **40**, 9978 (1989)
- ¹³² J.V.Barth, R.Schuster, J.Winterlin, R.J.Behm and G.Ertl, *Phys. Rev. B*, **51**, 4402 (1995)
- ¹³³ P.Häberle, P.Fenter and T.Gustafsson, *Phys. Rev. B*, **39**, 5810 (1989)
- ¹³⁴ D.K.Flynn-Saunders, K.D.Jamison, J.V.Barth, J.Winterlin, P.A.Thiel, G.Ertl and R.J.Behm, *Surf. Sci.*, **253**, 270 (1991)
- ¹³⁵ J.V.Barth, R.Schuster, R.J.Behm and G.Ertl, *Surf. Sci.*, **348**, 280 (1996)
- ¹³⁶ K.Müller, G.Besold and K.Heinz, “*Physics and Chemistry of Alkali Metal Adsorption*”, Eds.; H.P.Bonzel, A.M.Bradshaw and G.Ertl, Elsevier, Amsterdam, p65 (1989)
- ¹³⁷ J.O.Porteus, *Surf. Sci.*, **41**, 515 (1974)
- ¹³⁸ J.V.Barth, H.Brune, R.Schuster, G.Ertl and R.J.Behm, *Surf. Sci.*, **292**, L769 (1993)
- ¹³⁹ M.Poensgen, J.F.Wolf, J.Frohn, M.Giesen and H.Ibach, *Surf. Sci.*, **274**, 430 (1992)

CHAPTER 2: Experimental Techniques

2.1 Temperature Programmed Desorption (TPD)

Temperature Programmed Desorption (TPD) is a relatively straightforward technique for measuring the surface coverage and bonding energies of adsorbates. When dealing with simple molecules, information on the kinetics of desorption can also be determined.

The basic experimental technique essentially involves two steps. First of all is the adsorption of molecules onto the sample surface at low T (frequently room temperature but sometimes sub-ambient temperatures are also used). The sample is then heated in a controlled manner (a linear temperature ramp is desirable) whilst monitoring the evolution of species into the gas phase from the surface.

The detector used is generally a small, quadrupole mass spectrometer with the whole process being carried out using computer control enabling the simultaneous monitoring of a number of different products.

The data that are obtained from such an experiment consists of the variation in partial pressure of each mass fragment measured as a function of temperature. Study of the shape and position of the peaks yields information about the type of bonding to the surface and also the desorption energies of the adsorbate.

There are several key features of this experiment. Firstly, the area under a peak is proportional to the amount of adsorbate originally adsorbed (i.e. surface coverage). However, absolute surface coverage can only be determined (in moles per unit area) if the pumping speed of the vacuum is known and provided this pumping speed remains

constant or by carrying out calibration experiments e.g. by dosing a known quantity of CO which gives a monolayer etc. In this case you don't need to know the absolute pumping speed, but it does need to be constant. The position of the peak (the temperature at the peak maximum) is related to the enthalpy of adsorption, which in turn provides information on the strength of the surface binding. The kinetics of desorption give information on the state of aggregation of the adsorbed species (e.g. molecular or dissociative). These kinetics can be obtained from the peak profile and also the coverage dependence of the desorption characteristics.

The rate of desorption of an adsorbate follows an Arrhenius-type behaviour known as the **Polanyi-Wigner** equation¹,

$$I(T) \propto \frac{dM}{dt} = -\frac{d\theta_M}{dt} = \nu(\theta_M) \cdot \theta_M^n \cdot \exp\left(\frac{-E_{des}(\theta_M)}{R.T}\right)$$

where,

$\nu(\theta_M)$ = frequency factor

θ_M = instantaneous coverage

n = kinetic order or desorption order

$E_{des}(\theta_M)$ = activation energy to desorption

During a TPD experiment, the sample is heated in a linear fashion with a heating rate of α Ks⁻¹. As a result of this, the Polanyi-Wigner equation becomes,

$$-\frac{d\theta_M}{dt} = \frac{\nu \cdot \theta_M^n}{\alpha} \cdot \exp\left(\frac{-E_{des}}{R.T}\right)$$

In the simplest scenario, where E_{des} is coverage independent, a single adsorption peak will be seen and the temperature at which the maximum occurs relates to the

maximum desorption rate. When this is observed, E_{des} can be given by the Redhead equation¹,

$$E_{des} = R.T_{max} \left[\ln \left(\frac{\nu.T_{max}}{\alpha} \right) \times 3.64 \right]$$

This equation holds best for first order desorption kinetics ($n=1$) in which T_{max} is constant for increasing coverage.

Information can be gleaned on the order of desorption from the peak shape and behaviour with varying coverage. However, in this work, TPD experiments were used primarily to determine desorption features that indicate how tightly bound acetate is to the surface and not for extensively interpreting desorption behaviour. Hence further analysis of this method will not be carried out here.

It is important to remember that desorption of certain molecules can occur from other surfaces as well as the one we are measuring (e.g. heating filament, inside of chamber) meaning the technique is not exact. Another problem with the kinetics may occur if we have two molecules with the same m/z as the detector is unable to differentiate between them, possibly leading to ambiguous results. The temperature dependence of ν , E_{des} and n is also a problematic factor and it is often the case that a mathematical treatment of the data results in very complex desorption kinetics being found for what are actually relatively simple systems.

2.2 Low Energy Electron Diffraction (LEED)

LEED is the main technique used for the determination of surface structures. It can be used both **qualitatively** (where the pattern is recorded and the spot positions can be used to yield information on both the clean substrate and the adsorbate unit cells), or **quantitatively** (where the intensities of the various diffracted beams are recorded as a function of beam energy to generate I-V curves. These curves can be compared with theoretical curves to provide accurate information on atomic positioning). The work discussed here features only qualitative LEED experiments.

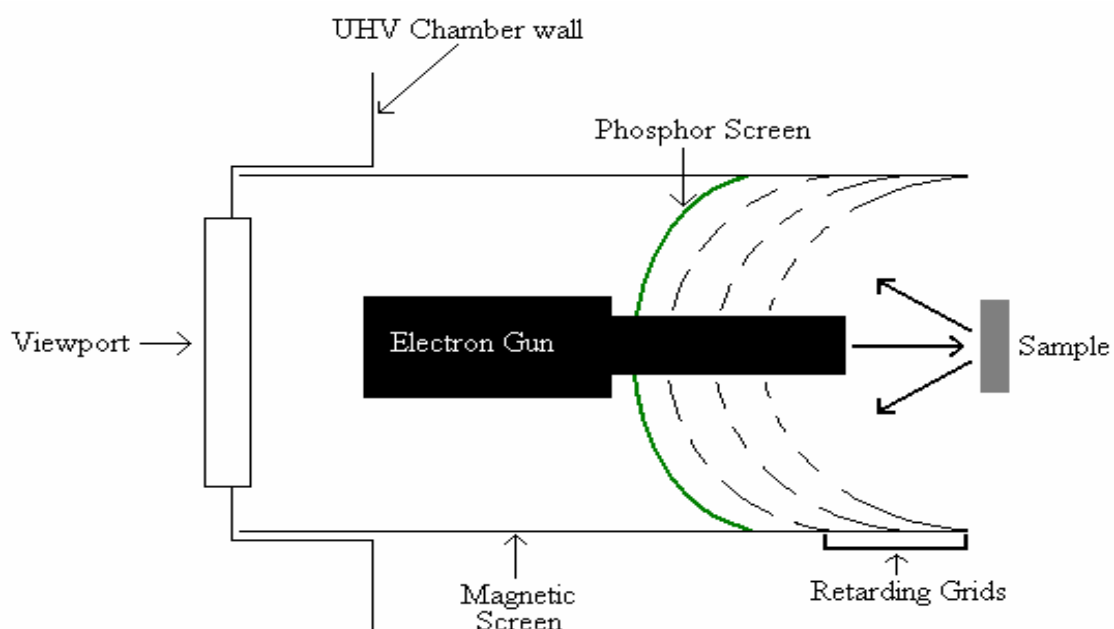


Fig 2.2.1 - A typical LEED apparatus schematic

The electrons are produced by the hot filament as a result of thermionic emission. They are then accelerated down a drift tube and impinge on the surface at the required energy and a well-defined angle (usually 90° to the surface plane). Electrons are back scattered if the desirable conditions are met and these pass through a field free region around the sample towards a series of three concentric hemispherical grids. The first and third are charged to sample potential in order to create the field-free region around the sample and also to ensure that any electrons leaving the sample maintain

their radial geometry. The middle grid is charged to 97% of the potential of the initial source electrons to ensure that only elastically scattered electrons are allowed through. Any electrons passing through these grids are then accelerated to a highly charged (5keV) phosphor-coated screen. Bright spots on the screen indicate places of constructive interference and the pattern produced can be viewed instantly through the viewport, leading to a quick structure determination.

The theory of LEED is based on the principles of wave-particle duality, whereby it becomes possible to regard a beam of electrons as a succession of electron waves incident normally on the sample. These waves can be scattered by regions of high, localised electron density, such as surface atoms, which can be considered to be acting as point scatterers.

The electron wavelength can be given by the de Broglie relationship

$$\lambda = h / p \quad \text{where } p = \text{momentum}$$

Now, $m = \text{mass of electron (kg)}$

$$p = mv \quad v = \text{velocity (ms}^{-1}\text{)}$$

and, $e = \text{electronic charge}$

$$E_k = mv^2/2 \quad E_k = \text{kinetic energy}$$

So, $V = \text{acceleration voltage (in eV)}$

$$p = \sqrt{2m(E_K)} = \sqrt{2meV}$$

and therefore

$$\text{Wavelength, } \lambda = \frac{h}{\sqrt{2meV}}$$

One may calculate, for example, that electrons of 20eV have a wavelength of 2.74Å and electrons of 200eV have a wavelength of 0.87Å. It is immediately obvious that these electrons employed in LEED experiments have wavelengths that are comparable with atomic spacing distances. This is the necessary condition for diffraction effects associated with surface atomic structure to be observed.

The simplest way to model the scattering of electrons by the topmost layer of a surface is to imagine a 1D chain of atoms (with atomic separation d). The incoming electron beam is aligned along the normal to the chain (see Figure 2.2.2)

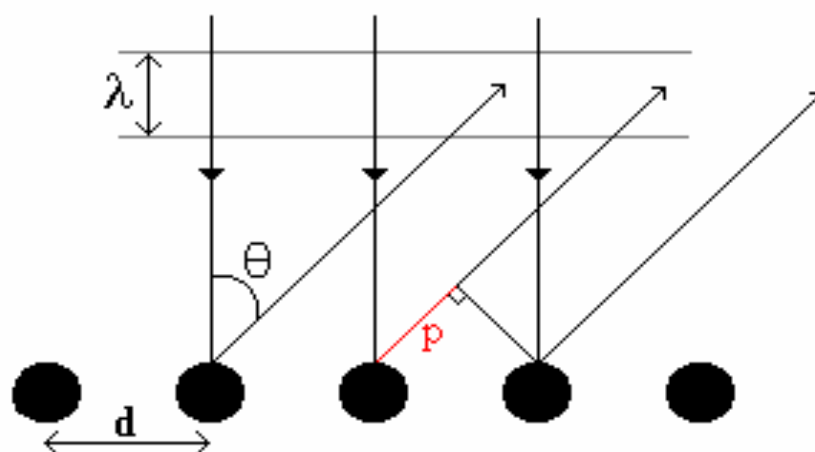


Fig 2.2.2 – Model depicting the scattering of electrons by the topmost layer in a surface

If you considered the back scattering of a wavefront from two adjacent atoms at a defined angle θ to the surface normal (Fig 2.2.2) it is clear that there is a path difference (p). This corresponds to the difference in the distance the radiation has to travel from the scattering centres to the detector (placed effectively at infinity).

The length of this path difference is $d \sin \theta$, which must be equal to an integer number of wavelengths to enable constructive interference to occur when the scattered beams eventually meet at the detector.

In other words,

$$p = d \sin \theta = n \cdot \lambda$$

where $n = \text{integer}$

$\lambda = \text{wavelength}$

When there are two isolated scatterers, the diffracted intensity varies between zero (this is completely destructive interference, $p = (n+1/2)\lambda$) and a maximum value (completely constructive interference, $p = n\lambda$). If dealing with a periodic, large array of scatterers then the diffracted intensity only becomes significant when

$$d \sin \theta = n\lambda$$

is exactly satisfied. A typical intensity profile for this case is reproduced below (Figure 2.2.3).

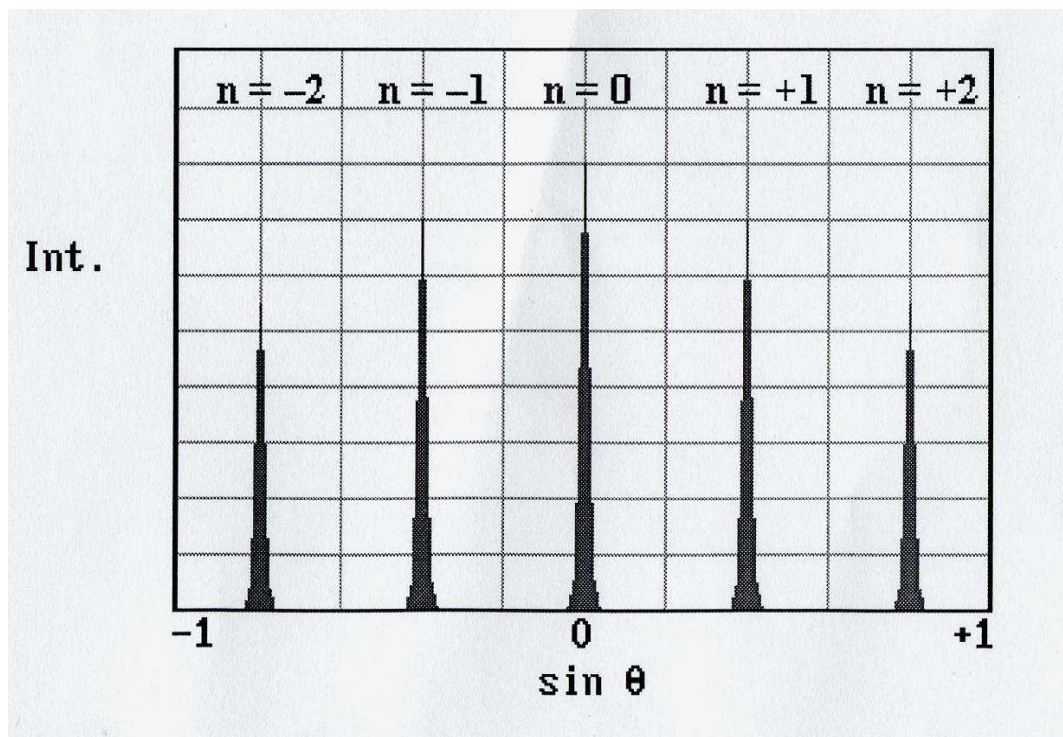


Fig 2.2.3 – Typical intensity profile for two, isolated electron scatterers showing destructive and constructive interference regions. *Taken from reference²*

There are several points that it is worth noticing from this model:

- 1) The pattern is symmetric about $\sin \theta$ (or θ) = 0 – meaning $n=1$ and $n=-1$ produce the same diffraction result.
- 2) $\sin \theta$ is inversely proportional to $V^{1/2}$ – as the energy increases, the diffraction angle decreases.
- 3) $\sin \theta$ is inversely proportional to d – as the lattice parameter increases the diffraction angle decreases.

When it comes to looking at real LEED patterns we notice a strange effect when compared to the surface structure being investigated. Take for example a typical fcc(110) surface and its LEED pattern (Figure 2.2.4),

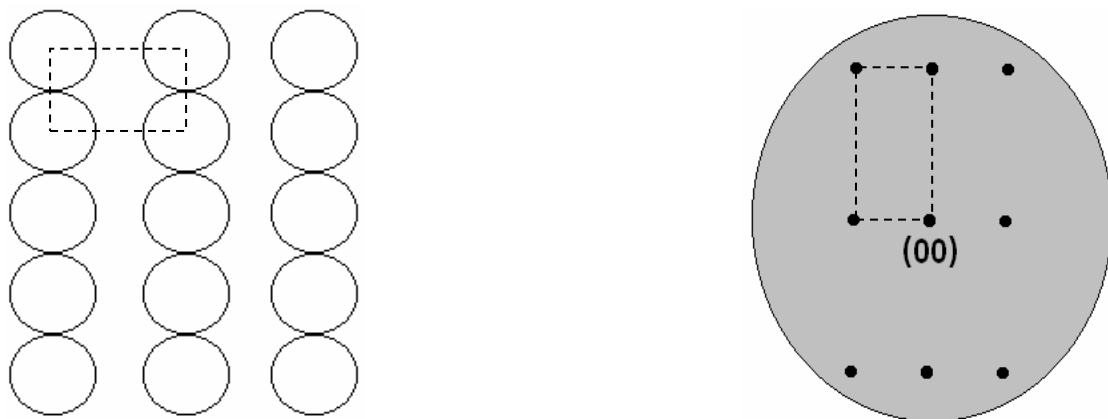


Fig 2.2.4 – An fcc(110) surface and its associated LEED pattern

The pattern shows exactly the same rectangular shape and symmetry as the substrate surface but appears to be longer in the horizontal plane rather than the vertical plane.

Fig 2.2.4 shows only the first-order beams, i.e. it is representative of the diffraction pattern when viewed at low energies when only for $n=\pm 1$ is the angle of diffraction small enough to allow the diffracted beam to hit the display surface.

By doubling the energy of the incident electrons it becomes possible to see some of the second-order ($n=\pm 2$) spots as well as an overall contraction of the pattern (see Figure 2.2.5 overleaf).

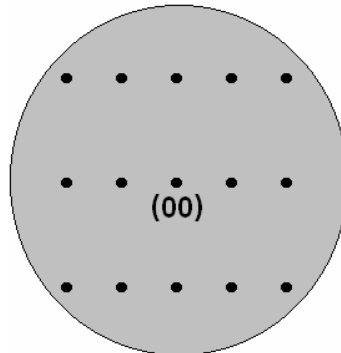
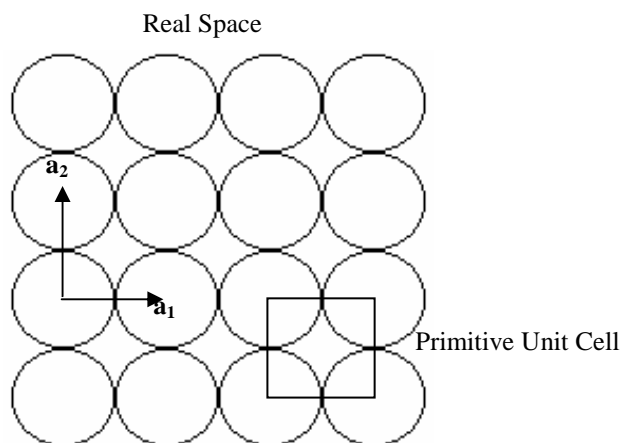


Fig 2.2.5 – LEED pattern for a clean fcc(110) surface showing the presence of 2nd order spots

There are a few simple explanations for these effects but a much better method of looking at LEED diffraction patterns involves the concept of “*reciprocal space*”. It can be readily shown that,

*“The observed LEED pattern is a (scaled) representation of the **reciprocal net** of the pseudo-2D surface structure”¹*

We can define a real space lattice by lattice vectors \mathbf{a}_1 and \mathbf{a}_2 ,



Reciprocal surface space is defined by the vectors \mathbf{a}'_1 and \mathbf{a}'_2 . These reciprocal vectors are related to the real space vectors by the scalar product relationships:

$$\mathbf{a}_1 \cdot \mathbf{a}'_2 = \mathbf{a}'_1 \cdot \mathbf{a}_2 = 0 \quad \text{and} \quad \mathbf{a}_1 \cdot \mathbf{a}'_1 = \mathbf{a}_2 \cdot \mathbf{a}'_2 = 1$$

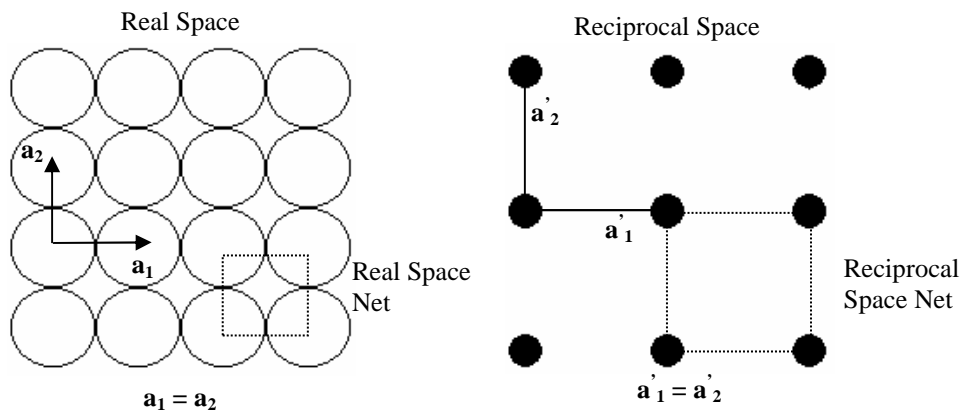
The physical meanings of these relationships can be summarised as follows ;

- \mathbf{a}_1 is perpendicular to \mathbf{a}'_2 , and \mathbf{a}'_1 is perpendicular to \mathbf{a}_2 .
- There is an inverse relationship between the lengths of \mathbf{a}_1 and \mathbf{a}'_1 (and also \mathbf{a}_2 and \mathbf{a}'_2):

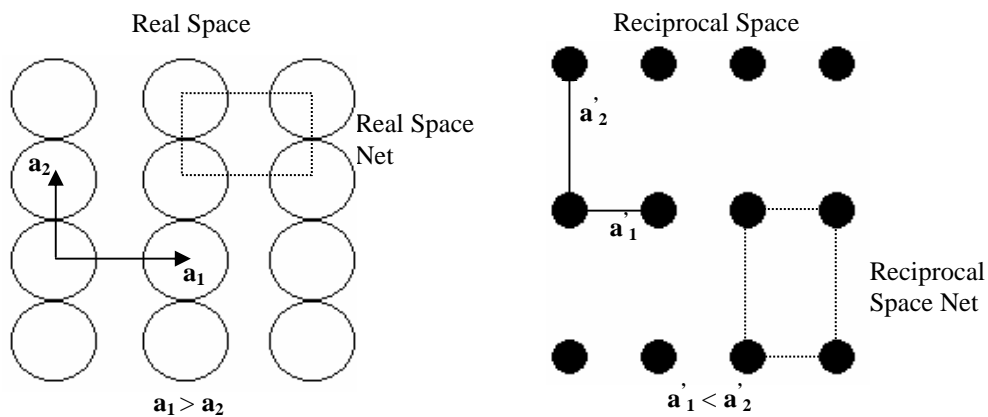
$$|\underline{a}_1| = \frac{1}{|\underline{a}'_1| \cos \gamma} \quad \text{where } \gamma \text{ is the angle between the two vectors}$$

We can now predict LEED patterns for the (100), (110) and (111) faces of fcc crystals using the above method;

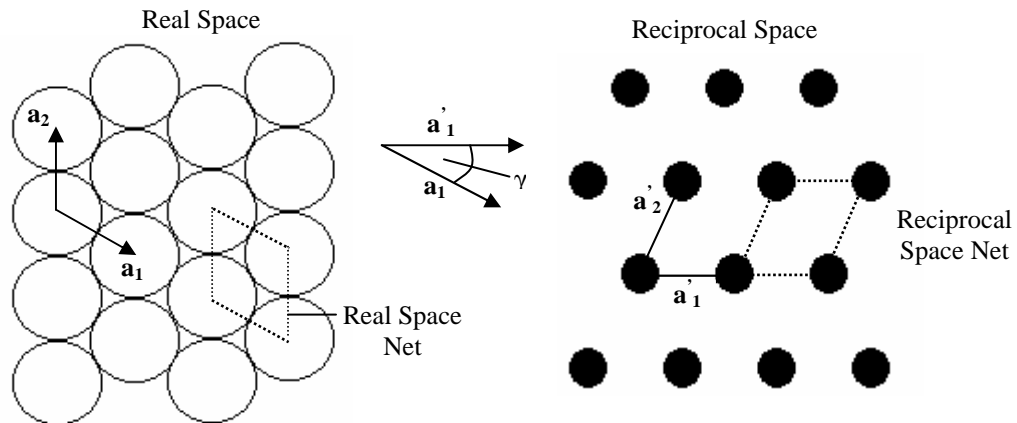
1) fcc(100)



2) fcc(110)



3) fcc(111)



Note that, due to the fact that \mathbf{a}_1 is not perpendicular to \mathbf{a}'_1 , $\cos. \gamma = \sqrt{3}/2$ and so

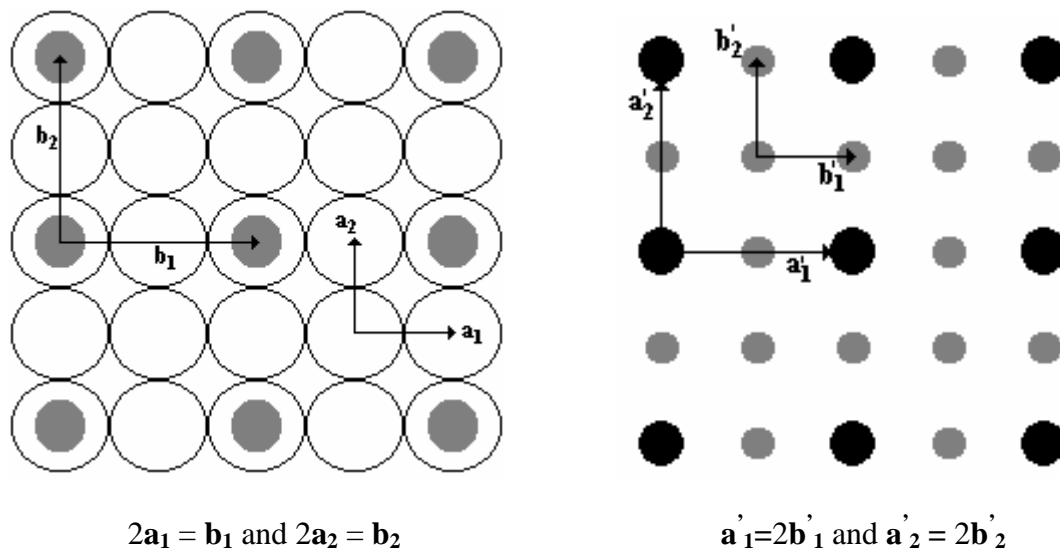
$$\text{therefore } |\underline{a}_1| = \frac{2}{|\underline{a}'_1| \sqrt{3}}.$$

When considering fcc(100) and fcc(110), $\cos. \gamma = 1$ and hence $|\underline{a}_1| = \frac{1}{|\underline{a}'_1|}$.

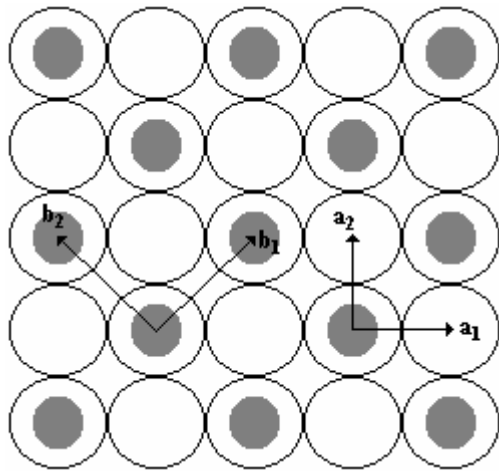
Another useful aspect of LEED is that it can also be used to detect adsorbate overlayers on top of metal surfaces. These overlayers can often be quite complex and LEED gives a good starting point as to the kind of structure being adopted. In some simple cases LEED is in fact all that is needed to establish an overlayer structure.

Two simple overlayer structures are shown here,

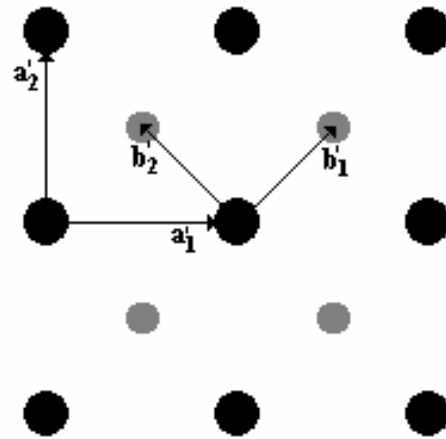
i) primitive (2x2) structure on fcc(100) with the adsorbate in on-top sites



ii) c(2x2) structure on the same fcc(100) surface



$$a_1\sqrt{2} = b_1 \text{ and } a_2\sqrt{2} = b_2$$



$$a'_1 = b'_1\sqrt{2} \text{ and } a'_2 = b'_2\sqrt{2}$$

The technique of LEED allows the arrangement of atoms at the surface to be established and is also used to give information on overlayer structures, defects and step morphology. The main inherent weakness of LEED is the requirement that the sample must be crystalline as the electron diffraction requires long-range order to be present on the surface.

2.3 Auger Electron Spectroscopy (AES)

Auger Electron Spectroscopy (AES) is a surface composition analysis technique, which utilises the low energy emission of electrons via the *Auger Process*. It is very simple to use and is consequently one of the most commonly used techniques for measuring the surface composition of a sample.

AES has been used throughout this work to check the cleanliness of the sample prior to experimentation but more importantly to measure the thickness of the Au overlayer on Pd prior to bimetallic experiments.

Theoretically, AES shares a common start point with XPS (X-Ray Photoelectron Spectroscopy) but since no XPS work has been carried out the theory behind this technique will not be explained in this project. Instead AES will be treated from a first principles perspective.

AES is generally considered to involve three basic steps;

- i) Atomic Ionisation (involves removal of a core electron)
- ii) Electron Emission (Auger process)
- iii) Analysis (this involves detecting the charged particles with a high enough sensitivity and also the calculation of the E_K of the emitted electrons.

Ionisation

The initial process is the creation of a core hole, in AES this is typically done by exposing the sample to a beam of high-energy electrons (with a primary energy in the range 1-10 keV). Figure 2.3.1 (overleaf) shows a schematic of how this is achieved.

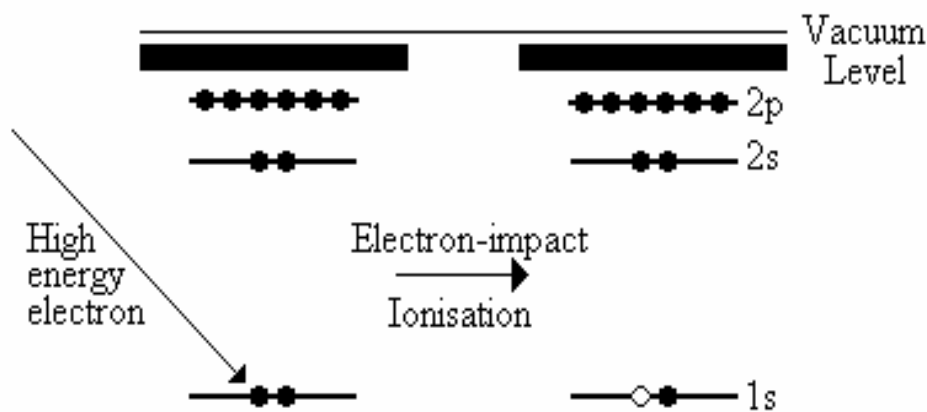


Fig 2.3.1 – The ionisation procedure for Auger Electron Spectroscopy (common with X-ray Photoelectron Spectroscopy – XPS)

Although the above diagram shows the ionisation to occur by removal of a 1s (K-shell) electron, the method of ionisation is actually quite crude and so a variety of different ions with holes in different inner shell levels are formed. After the removal of the core electron, the ionised atom remaining is in a highly excited state and will endeavour to relax back to a lower energy state rapidly. There are two general ways for this to occur:

- a) Auger Emission (AES)
- b) X-ray fluorescence (not important here)

The Auger Emission takes place as shown in Figure 2.3.2

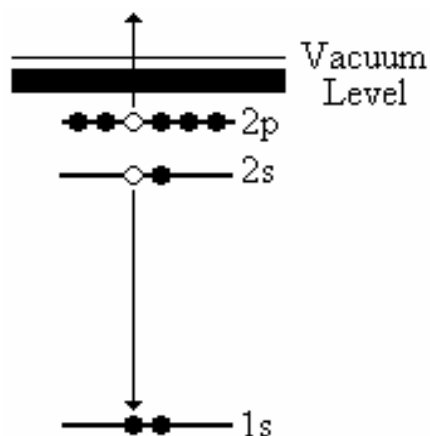


Fig 2.3.2 – The process by which an Auger electron is emitted

One electron falls from a higher energy level in order to fill the core hole created by the loss of the electron. This releases energy, which is transferred simultaneously to a second electron. Generally, this energy is more than sufficient (>10x) to overcome the binding energy of the second electron, the remainder is exhibited by the escaping Auger electron as kinetic energy. It can be seen that the Auger process involves three electrons, which leaves a doubly ionised atom. We can make a rough estimate of the E_K of the emitted Auger electron, assuming we know the binding energies of the levels involved. For the above example this would correspond to:

$$E_K = (B_K - B_{L1}) - B_{L2,3}$$

which can be rearranged to give;

$$E_K = B_K - (B_{L1} + B_{L2,3})$$

It becomes obvious from this equation that the latter two terms are interchangeable.

Physically this means that it is impossible to say which electron drops down to fill the hole and which is eventually emitted as the Auger electron. For this reason, an Auger transition is characterised by (i) the initial hole location and (ii) the location of the final two holes.

Auger transitions have a defined nomenclature in which the initial hole location is given first, followed by the two final hole locations, usually in order of decreasing binding energy. In the above example we are looking at a **KL₁L_{2,3}** transition.

Another aspect of Auger is that the initial ionisation is non-selective meaning the initial hole may be situated in any number of shells. As a result there will be many possible Auger transitions for each given element (varying in intensity) and therefore

each element has a characteristic set of peaks at various kinetic energies (the variable the Auger detectors measure). Figure 2.3.3a shows a typical Pd Auger spectrum.

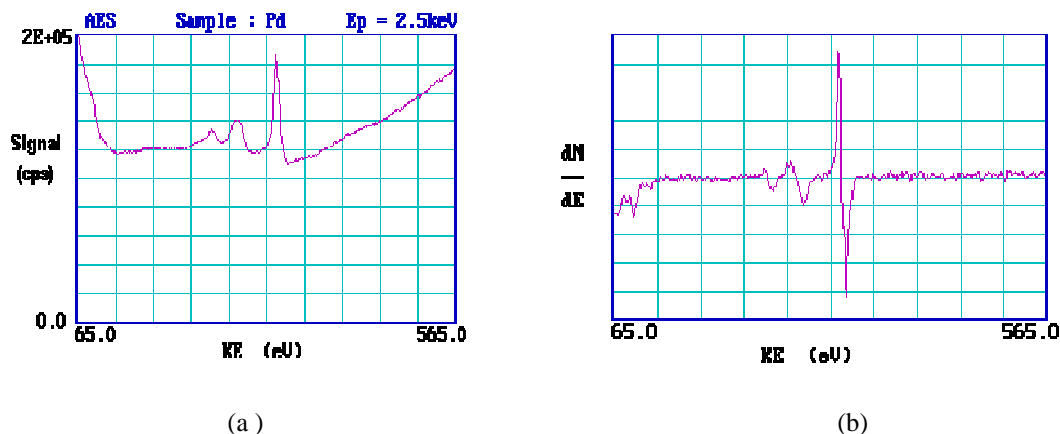


Fig 2.3.3 – Auger spectra for Pd metal in a) standard form b) derivative form. Taken from reference³

Auger spectra are frequently shown in a differentiated form, mainly because this form of spectra leads to a greater sensitivity due to the differentiation removing most of the background contribution. (see Figure 2.3.3b). This comes in very useful for overlayer measurements as the change in height of a main peak (e.g. Pd at 340eV) can be used to calculate the amount of that element in the surface. The high sensitivity of AES (to all elements except H and He) means that the technique provides a very accurate way to quantitatively determine the surface composition of bimetallic samples such as Au/Pd(111) used extensively during this work.

It should be mentioned that AES has been adapted for use in other techniques that have more specific uses. These include Auger Depth Profiling (which provides quantitative compositional information as a function of depth below the surface) and Scanning Auger Microscopy (which is capable of providing spatially resolved compositional information on heterogeneous samples)⁴.

2.4 Scanning Tunnelling Microscopy

Developed in the early 1980s by two IBM scientists, Binnig & Rohrer, Scanning Tunnelling Microscopy (STM) is a relatively new technique for accurately studying the atomic structure of a surface. The technique is based on the phenomenon of “tunnelling” but before we can look at this effect we need to look at the basics of the electronic structure of solids.

Moving from $\boxed{\textit{single atom} \rightarrow \textit{multiple atoms} \rightarrow \textit{solid}}$ we have a change in the electronic properties as we go from $\boxed{\textit{atomic orbitals} \rightarrow \textit{molecular orbitals} \rightarrow \textit{bands}}$

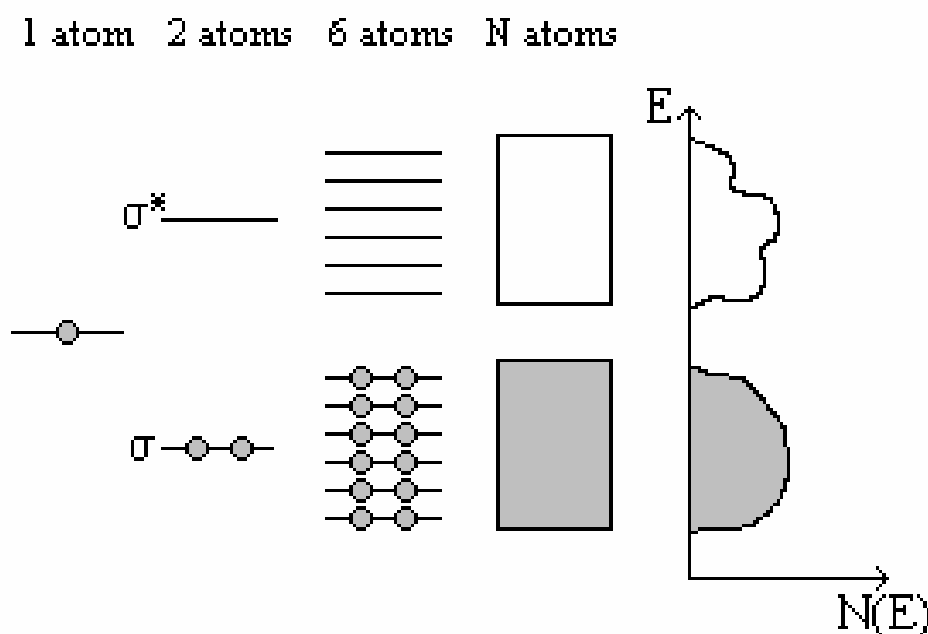


Fig 2.4.1 – The transition from atomic orbitals to a band structure as we increase the number of atoms from $1 \rightarrow N$. Also included is a typical DOS plot for a N atom system

The band is effectively continuous (energy change from one level to the next is negligible) and is delocalised over the solid. Density of States (DOS) is the number of energy levels per unit energy (usually states. eV^{-1}). The states themselves may have s, p, d, f or mixed (hybrid) character depending on the character of the parent atomic orbitals.

The type of material depends on the position and overlap of the bands. Depending on the DOS and the number of electrons, the bands may be filled, partially filled or empty.

In insulators (and semi-conductors) there is a gap (Band gap, E_g) between the filled conduction band and the empty valence band whereas in metals the topmost band is only partially filled and there is no band gap. The energy level dividing the filled and empty bands is known as the *Fermi Level*, E_F .

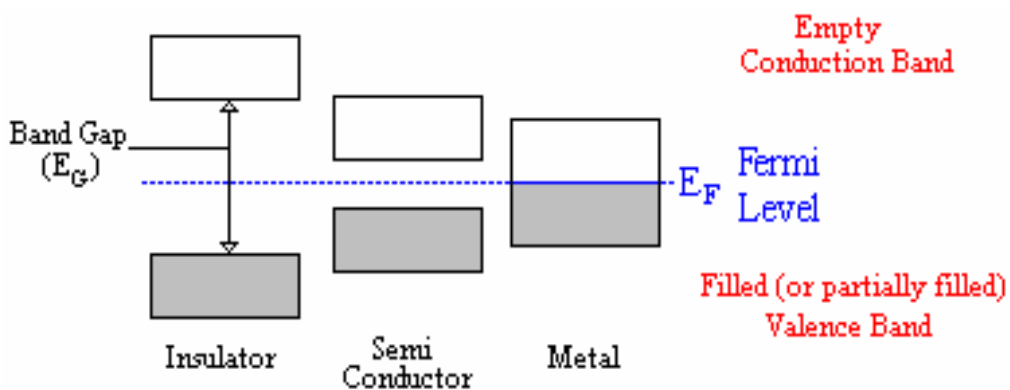


Fig 2.4.2 – An insulator, a semi-conductor and a metal expressed by means of energy band gaps

Now, if we look more specifically at the electronic structure of a surface we see slight differences. The energy required to move an electron from E_F to E_v (where it is effectively a free electron) is known as the workfunction, ϕ .

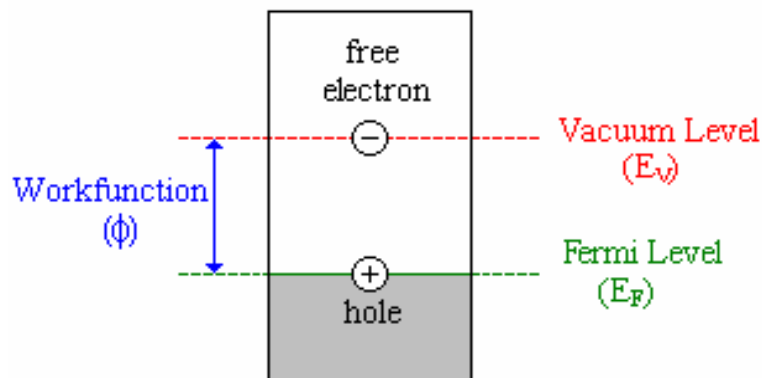


Fig 2.4.3 – Definition of the workfunction (ϕ) associated with a surface

This workfunction is sensitive to adsorbates, reconstructions and external fields and also varies between different materials. Different faces of the same crystal also have different workfunctions.

In order to explain the phenomenon of tunnelling we need to go back to the basics of quantum mechanics and in particular to the solution to Schrödinger equation inside and outside a solid that has non-infinite walls.

$$H\Psi = E\Psi$$

$$-\left(\frac{h}{2m}\right)\frac{d^2\Psi}{dx^2} = E\Psi \quad \text{inside solid}$$

$$-\left(\frac{h}{2m}\right)\frac{d^2\Psi}{dx^2} + V\Psi = E\Psi \quad \text{outside solid (V=}\phi\text{)}$$

The solutions to these equations are

$$\Psi_{in} = Ae^{i.k.x} + A'e^{-i.k.x} \quad k = \sqrt{\frac{2.m.E}{h^2}}$$

$$\Psi_{out} = \underset{\text{(I)}}{Be^{i.k.x}} + \underset{\text{(II)}}{B'e^{-i.k.x}} \quad k = \sqrt{\frac{2.m.(V-E)}{h^2}}$$

It can be seen that the wavefunction outside of the solid has two parts,

(I) is a complex number (imaginary) when $E < \phi$.

(II) is an exponential decay curve leading to the following wavefunction being found,

As can be seen in Figure 2.4.4 electron density decays exponentially away from the surface. There is a property used to measure the rate of decay. The inverse decay length (K) is the reciprocal of distance for density to fall to e^{-1} .

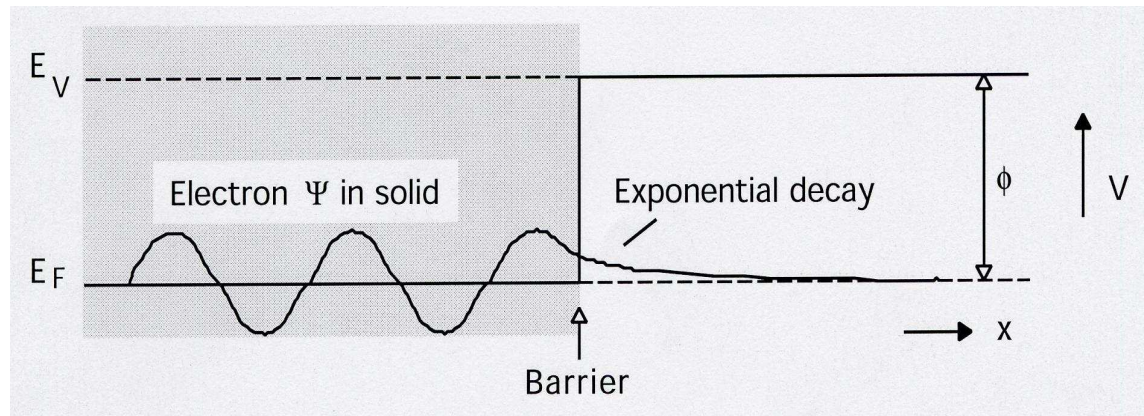


Fig 2.4.4 – Wavefunction produced as a result of solving the Schrödinger equation inside and outside a solid that has non-infinite walls. *Taken from reference⁵*

The value of K is typically $1-2\text{\AA}^{-1}$ for a metal. If two metals are brought into close enough proximity so that their electron density overlaps then electrons can be made to “tunnel” between the two metals. However, the current flow is equal in both directions (see Figure 2.4.5)

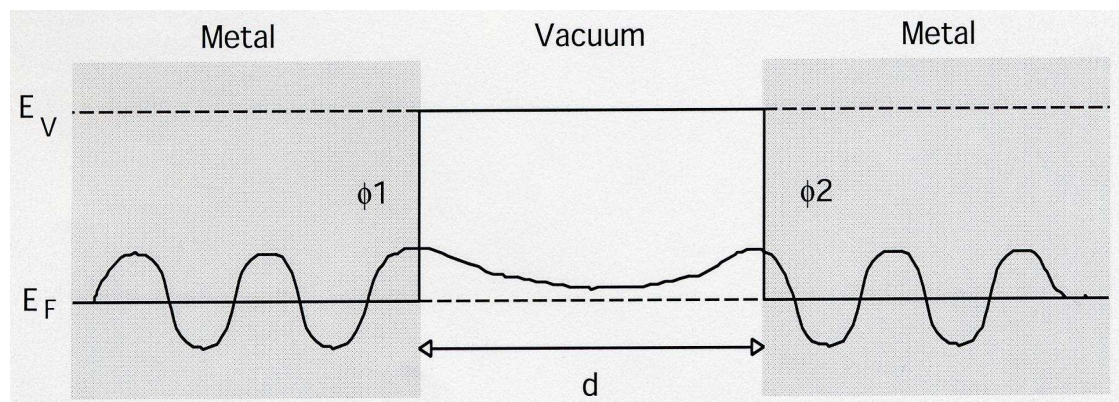


Fig 2.4.5 – The physical phenomenon of tunnelling between two metals in close proximity. In this example, both metals have the same workfunction (ϕ) *Taken from reference⁵*

By applying an external potential, or bias, (V_{ext}) to one metal (the electrons can be driven either way). Tunnelling always occurs from the filled states within V_{ext} of E_F in

the negative metal (the one with the bias across it) and travels to the empty states just above E_F in the second metal (see Figure 2.4.6).

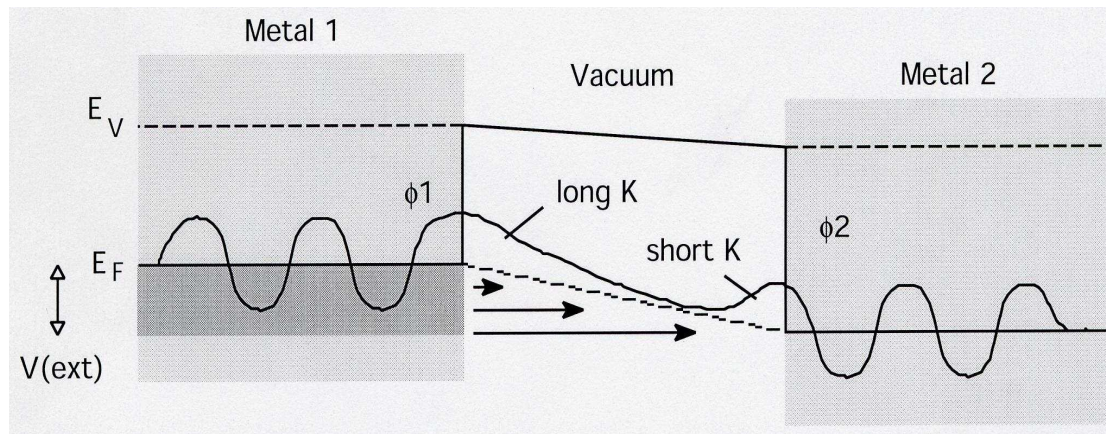
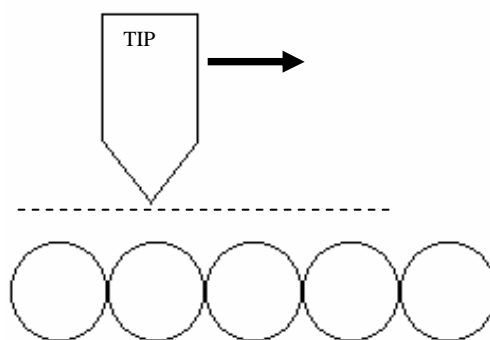


Fig 2.4.6 – The physical result of applying a small potential bias (V_{ext}) across one metal to precipitate one directional tunnelling between two conducting samples. Taken from reference⁶

The tunnelling current between the two metals can then be measured using computer software. It is this tunnelling current that STM relies on and is designed to measure, meaning that it can obviously only be used with a conducting surface.

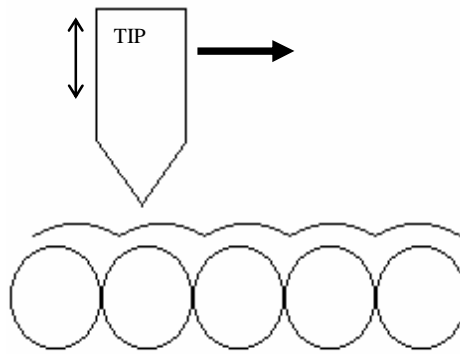
There are two methods of operation for a basic STM:

- Constant Height Mode



Tip-sample distance is fixed and the variation in tunnelling current (I_T) forms the image. This method works best for atomically flat samples and is a relatively rapid method of scanning.

- Constant Current Mode



I_T is kept constant by moving the tip up and down (controlled automatically by a feedback circuit). The tip's Z-movement is recorded and gives rise to the image (topography). This is a slower method but works successfully for rough surfaces and consequently is the more common method of operation.

As can be seen, there are two factors that are vital for a successful STM experiment. Firstly, we must be able to very accurately position the tip with respect to the surface (need $<0.5\text{\AA}$ control) as the technique is very sensitive to tunnelling distance. This is a success of engineering as we are able to do this using a piezoelectric drive with very high sensitivity and obviously by minimising any external vibrational influences.

The other important aspect over which there is more chemical control is the tip itself. The tip can be made with a variety of materials but the most common are W or Pt/Ir. A monatomic tip is desirable and is usually achieved as a result of the naturally sharp edge of the real metal combined with knowledge of how the tip behaves when cut or electrochemically etched.

If an atomically sharp tip can be achieved, then I_T will be dominated by the contribution from the end of the tip, meaning a good lateral resolution can be achieved (see Figure 2.4.7 overleaf)

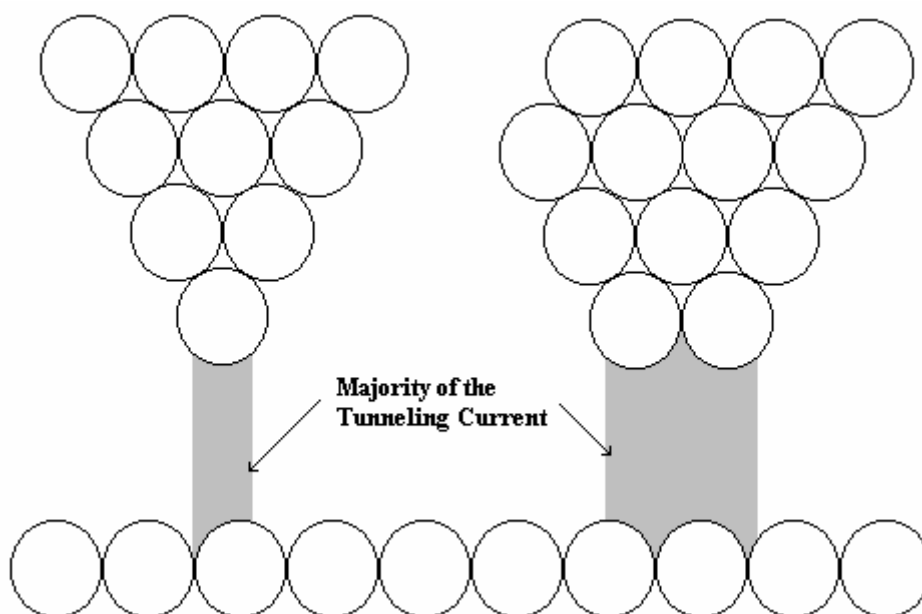


Fig 2.4.7 – Schematic indicating the approximate difference in lateral resolution between a monatomic STM tip and a diatomic STM tip

STM is obviously a very useful technique for flat, conducting surfaces, as it can give an accurate picture of the topography, down to atomic resolution under optimised conditions. In conjunction with LEED we can also get a picture of the structures of adsorbate overlayers and surface reconstructions. STM has the added advantage that it does not require UHV conditions and in fact can be carried out in air and liquid regimes as well as under UHV. As more and more is being understood about STM, other scanning probe techniques have been developed alongside. The most common of these is AFM (Atomic Force Microscopy) which can be used on non-conducting surfaces. Since no AFM has been carried out during this project, this technique will not be discussed here.

2.5 Medium Energy Ion Scattering (MEIS)

2.5.1 Theoretical Basis

Ion scattering has become a very important surface analytical technique during the last twenty years or so. The main reason is the quantitative nature of the results that can be produced. Medium Energy Ion Scattering (MEIS) is one of these new, innovative techniques. It is capable of determining the positions of the surface and near-surface atoms in real space and is also capable of distinguishing between atom types. This makes it ideally suited for analysing both the structure and composition of surface alloys, in our particularly case, Au/Pd(111). MEIS is a close relative of two other important ion scattering techniques, namely Rutherford Backscattering Spectroscopy (RBS) and Low Energy Ion Scattering (LEIS). The main difference is in the energy of the ions and the nature of the data obtained. RBS employs ions of $>0.5\text{MeV}$ and is mainly used as a depth profiling technique whilst LEIS can obtain structural information on the top layer of the sample only as it uses ions of energy 1-10keV. MEIS fits nicely in-between these two, using ions (typically H^+ and He^+) of an energy between 50 and 500keV.⁷

The ions in this energy range are particularly useful for two main reasons,

- Firstly, MEIS has a very high surface sensitivity compared with RBS. LEIS is, in fact, the most surface sensitive of these techniques. This is due to the large shadow cone associated with LEIS meaning that only the surface layer can be seen. For MEIS, the width of the shadow cone is of the correct size to enable selective illumination of the surface and sub-surface layers, with resolution close to an atomic layer. Shadow cones will be discussed later in the Chapter.

- Secondly the solid state detectors that are used in RBS for detecting high-energy ions have a depth resolution of 50-100Å. These detectors can be replaced by electrostatic analysers with depth resolutions of atomic dimensions for the ions used in MEIS.

The basic physical principle of MEIS is to fire a monochromatic beam of ions onto the surface of a single crystal and then analyse the scattered ions as a function of both energy and scattering angle. Analysis of the energy and direction of these scattered ions can yield information about the mass of the atom they collide with in the crystal lattice. This can lead to accurate elemental identification and provides a step on the road to establishing alloy compositions.

There are two types of energy loss mechanism possible. Ions colliding with the surface atoms do so in an *elastic* fashion and hence will yield information on the top-most layers and their composition. However, some ions are capable of travelling deeper into the crystal bulk where they undergo *inelastic* energy losses as they pass through. MEIS is able to distinguish elastically and inelastically scattered ions due to its high energy resolution.

Inelastically scattered ions suffer energy losses proportional to their penetration depth but this energy loss is also dependent on the nature of the sub-surface atoms encountered and can therefore provide a depth profile of the sample composition.

It is possible to obtain the relative atomic positions of the near surface atoms by investigating the variation of scattered ion intensity with scattering angle.

The physics involved in ion scattering in general can be explained using classical mechanics and is reproduced here from reference².

First of all we will look at the elastic collisions;

Consider two masses m_1 and m_2 (atomic number z_1 and z_2 respectively), with m_1 moving with velocity v_0 and m_2 stationary. As the collision is elastic it can be described uniquely and completely by the principles of conservation of total energy and momentum.

If m_1 is deflected by an angle θ (as in Figure 2.5.1.1) then its kinetic energy after collision will be;

$$E_1 = k^2 E_0$$

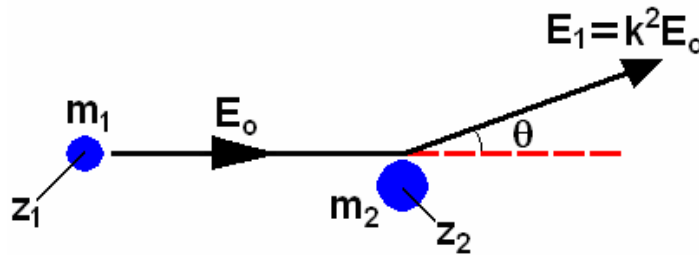


Fig 2.5.1.1 –The physics behind atom scattering in a two-body collision

Where k^2 is the kinetic scattering factor and is given by;

$$k^2 = \left[\frac{(m_2^2 - m_1^2 \sin^2 \theta)^{1/2} + m_1 \cos \theta}{m_1 + m_2} \right]$$

For the simple case where $\theta = 90^\circ$ we find that $k^2 = (m_2 - m_1)/(m_2 + m_1)$ but for more complex cases it can be seen in Figure 2.5.1.2 that k^2 is a complex function of both scattering angle (θ) and mass ratio (m_2/m_1).

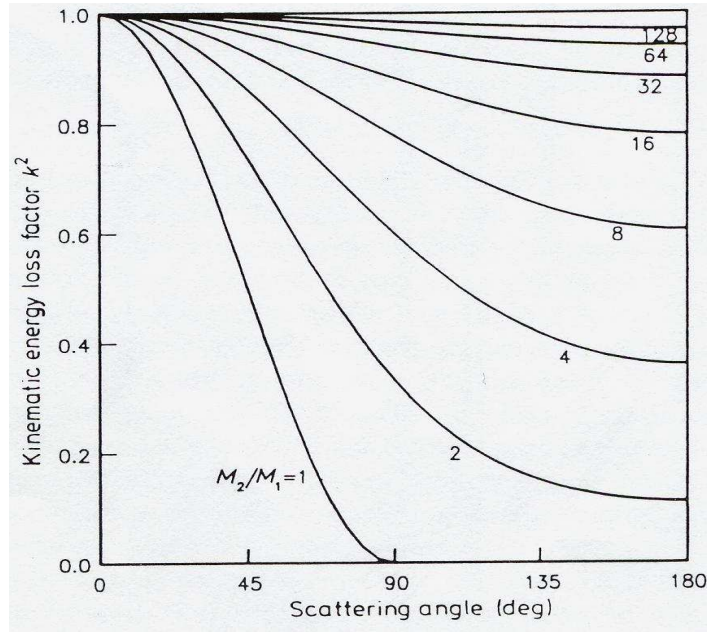


Fig 2.5.1.2 – Variation of the kinematic scattering factor (k^2) with scattering angle ($^\circ$) and mass ratio.

Taken from reference⁵

The probability density that an ion is scattered over a certain scattering angle can be represented by;

$$\frac{d\sigma}{d\Omega} = F \left[\frac{z_1 z_2 e^2}{4E \sin^2(\theta/2)} \right]^2 g(\theta, m_1, m_2)$$

F is called the screening factor and is given by

$$F = 1 - \frac{(0.042 z_1 z_2)^{4/3}}{E}$$

according to the Moliere approximation.

The multiplication factor $g(\theta, m_1, m_2)$ arises as a result of the transformation from centre of mass to lab frame and can be represented by;

$$g(\theta, m_1, m_2) \approx 1 - \left[2 \left(\frac{m_1}{m_2} \right) \sin^4(\theta/2) \right] \quad \text{for } m_2 \gg m_1$$

Two important features of the cross section of ion scattering can be seen from the above equations,

- (i) The cross-section is proportional to the square of z_1 and z_2 , meaning that if the ion species is changed from H^+ to He^+ there is a four-fold increase in scattering intensity.
- (ii) The cross-section is a strong function of the scattering angle (θ), being proportional to $1/\sin^4(\theta/2)$. The scattering cross-section for $\theta=90^\circ$ is 4 times larger than from $\theta=180^\circ$. This would imply that lower scattering angles would be more advantageous than higher ones due to the larger scattering cross-sections. However, a glance at Fig 2.5.2 shows that, at low scattering cross-section, the mass separation in the energy spectrum is small. This was the reason RBS experiments used to be carried out at $\theta=170^\circ$, the detectors could only detect different masses when the separation was high. MEIS detectors however are capable of distinguishing between different masses even at low separation and hence most experiments are done at $\theta < 90^\circ$ to take advantage of the higher scattering cross-section.

The above equations show that the ion scattering cross-section is known with a high precision. This becomes extremely important because it enables ion scattering to be a truly quantitative surface analytical technique. A further discussion of this will be undertaken later when considering data processing methods.

Moving onto inelastic collisions and scattering, we know that as an ion moves through a solid it can lose energy, even if it undergoes no elastic collisions. This energy loss is a result of inelastic interactions with the electrons present in the bulk solid. The rate of energy loss is known as the 'stopping power' and is unique for each element.⁸ This

stopping power depends upon the composition of the sample and also on the energy and species of the ion. When an ion is moving through a solid, its energy is decreasing constantly and hence the inelastic energy loss per unit length is not a constant value.

However, in MEIS we are usually dealing with layers that are thin enough and inelastic losses that are small enough to treat the stopping power as one constant value before the scattering and another constant value after the scattering. If we look at a schematic of an ion beam impinging on the surface at angle θ_1 and leaving at θ_2 it is possible to calculate the energy loss per unit length (see Figure 2.5.1.3)

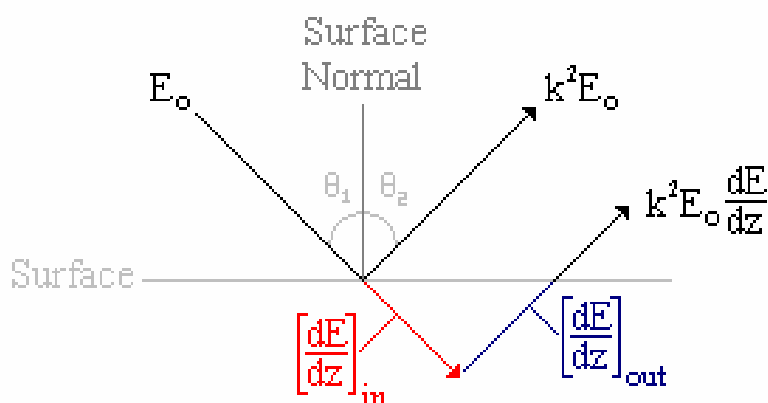


Fig 2.5.1.3 – Schematic of energy loss of an ion beam as it is scattered from below the surface

By employing the surface approximation (i.e. the scattering occurs close to the surface) it is possible to assume that the stopping power on approach $(dE/dz)_{Ein}$ equals $(dE/dz)_{E_0}$ and the stopping power on exit $(dE/dz)_{Eout}$ equals $(dE/dz)_{k^2 E_0}$. Hence the inelastic energy loss (incoming plus outgoing) per unit length (as measured along the surface normal) can be calculated as;

$$\frac{dE}{dz} = \frac{k^2}{\cos \theta_1} \left(\frac{dE}{dz} \right)_{E_0} + \frac{1}{\cos \theta_2} \left(\frac{dE}{dz} \right)_{k^2 E_0}$$

From this it is possible to see that an ion scattered from a depth of \underline{a} will suffer an inelastic energy loss of,

$$E_{loss} = a \frac{dE}{dz}$$

Having explained the basic physics of ion scattering, it is important to understand the two fundamental effects that MEIS makes use of to obtain accurate structural information, “shadowing” and “blocking”.

Shadowing is a phenomenon associated with the incident ions impacting on the surface. If the beam is aligned along a low-index crystallographic plane then it will only strike the first atom in every row. This first atom will then cast a kind of shadow over the other atoms in the row, so the atoms effectively do not see the beam and the ions are no longer able to backscatter (see Figure 2.5.1.4).

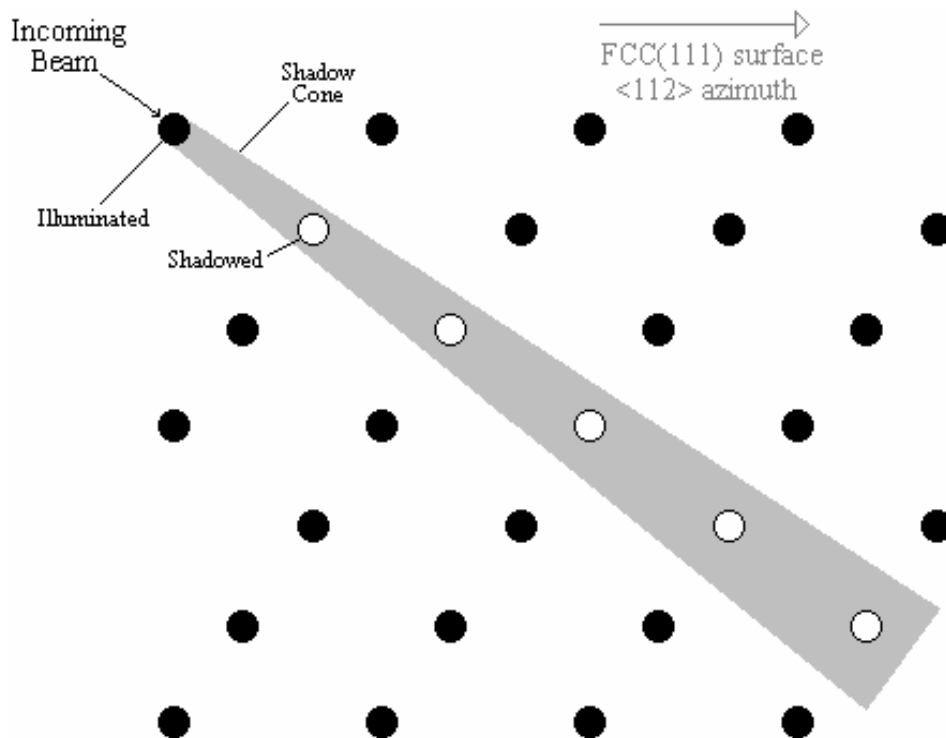


Fig 2.5.1.4 – Illustration of the phenomenon of shadowing and shadow cones employed by MEIS

This shadow is known as a “shadow cone” and results from the Coulombic interaction that takes place between the ion cores of the lattice atoms and the incident ions.

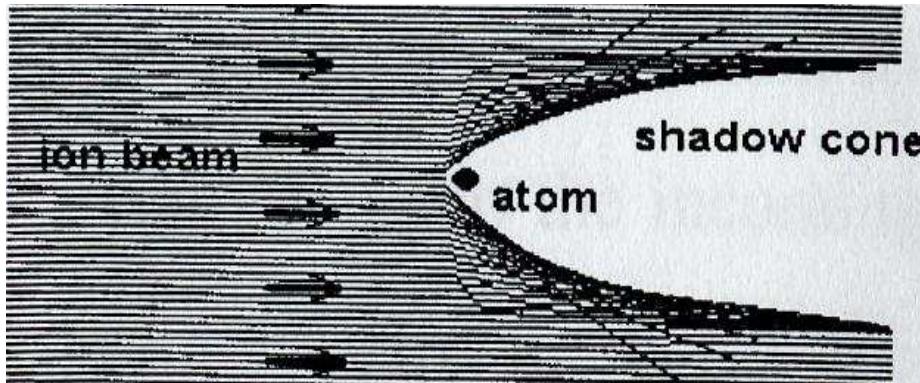


Fig 2.5.1.5 – Illustration of the shape of a shadow cone, showing its distance dependent radius. Taken from reference⁵

The radius of the shadow cone can be calculated for Coulombic scattering potentials, which neglect the nuclear charge screening, and is a function of atomic number and incident ion energy,

$$r_{sc} = 2 \sqrt{\frac{dz_1 z_2 e^2}{4\pi\epsilon_0 E}}$$

where d = distance of shadow cone from atom

E = energy of incident ions

The shadow cone is larger for higher atomic number lattice atoms but decreases as the incident energy increases.

Of course, Figure 2.5.1.4 shows an ideal situation, which would result from a bulk terminated uniform surface of a crystal. There are two main effects that disrupt this ideal surface and as a result perfect shadowing is not achieved.

i) *Surface Relaxation*: The top-most layer of the sample will either contract or relax relative to the bulk meaning the shadow cone is displaced slightly. As a result of this, the underlying atoms may be exposed to the incoming beam. The causes as increased ion yield at the detector, particularly in the first layer. This can be seen in Fig 2.5.1.6

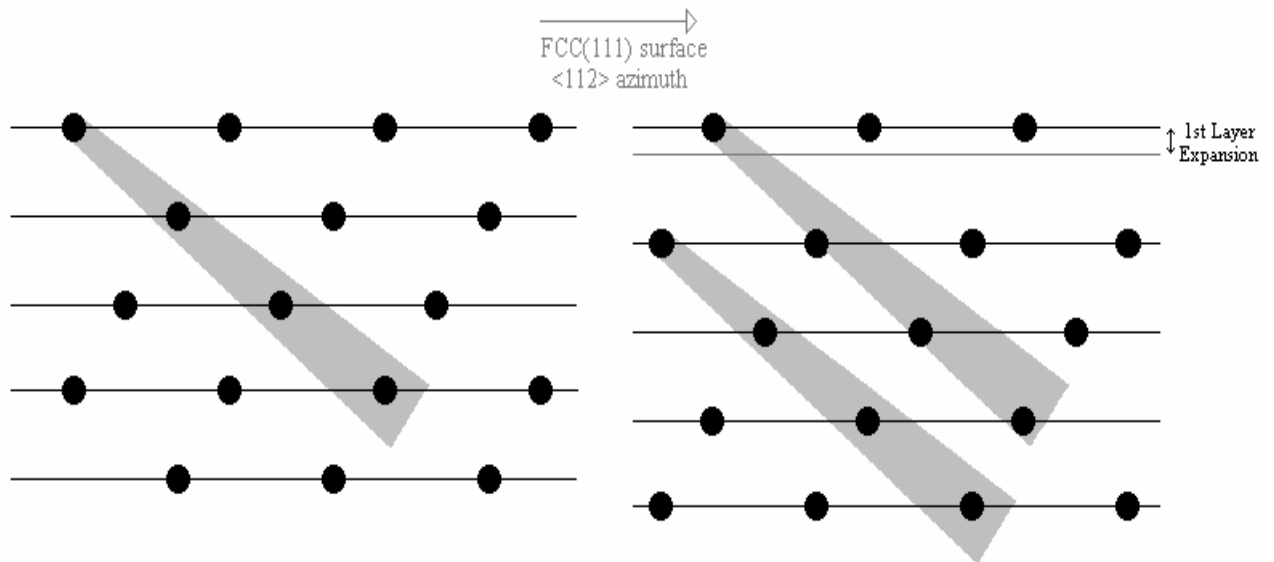


Fig 2.5.1.6 – Illustration of a surface relaxation (and the subsequent effect on the shadow cone) showing how lower-lying, supposedly hidden, atoms may contribute to the scattering of incident ions

ii) *Thermal vibrations*: The lattice atoms are not fixed in space and vibrate with amplitude that is related to the Debye temperature of the surface. The thermal vibrations blur the shadowing effect slightly, which introduces scattering contributions from the lower levels. Surface atoms vibrate more freely than bulk atoms and so the effect is amplified further.

It should also be mentioned that the presence of adsorbate atoms could lead to a surface losing its uniform structure, which in turn will lead to imperfect shadowing and blocking. This will be dealt with later in the section on compositional information.

In order to minimise the contribution of lower lying atoms to the scattering, the ion yield can be measured along specific exit directions. This is the phenomenon of “blocking”, which concerns the outgoing path of the scattered ions. Ions that are scattered from deeper layers and try to escape through the crystal can have their paths blocked by higher lying atoms.

If this is the case, the detector will pick up a region of low ion count at a particular scattering angle, which will lead to a “blocking dip” in the spectrum of intensity versus scattering angle. The theory behind blocking is analogous to the theory of shadowing. The blocking cone can be displaced in exactly the same way as a shadow cone, for example by a surface contraction or relaxation. This will lead to a shift in the surface blocking dip when compared to the bulk blocking dip and this shift can be used to calculate the surface alteration if required.

Shifts in blocking dips can also be used to recognise surface reconstructions (including adsorbate induced restructuring, which is done by comparison of the surface and bulk blocking spectra) as well as spotting changes in the surface composition and structure of a bimetallic species.

By combining both the shadowing and blocking effects, the surface specificity of MEIS can be maximised. Careful alignment of the incident ion beam and the analyser to the sample can be used to illuminate the desired layers, while excluding any contribution from deeper scattered ions. This technique will be dealt with further in section 2.5.3.

2.5.2 Experimental Details

The ion scattering experiments were carried out at the MEIS facility based at the CCLRC Laboratory in Daresbury, which uses a duo-plasmatron ion source and accelerator capable of producing H^+ and He^+ ions with energies up to 400 keV. Figure 2.5.2.1 shows a schematic of the facility.

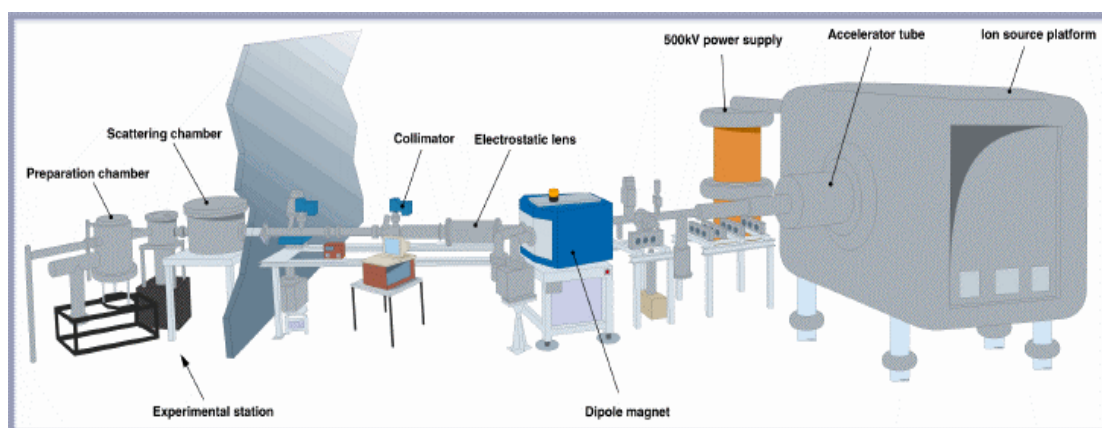


Fig 2.5.2.1 – Schematic of the MEIS facility at Daresbury. Taken from reference⁹

The facility consists of three main sections,

- i) The ion source and accelerating lens - capable of producing H^+ or He^+ ions at energies up to 270 keV (in our case 100 keV He^+ ions)
- ii) The transfer beam line for transport of the ions with a well-defined energy ($<0.15\%$) and low angular divergence ($<0.1^\circ$)
- iii) The experimental multi-chamber UHV end station.

The system is pumped with a combination of titanium sublimation and turbo molecular (500 l s^{-1}) pumps. The ion beam is produced in the duo-plasmatron source but its operation is controlled from a computer console situated in the end station. Once the beam is formed, it is accelerated to a high potential ($\sim 100 \text{ kV}$) and is focused using a quadrupole triplet lens. A series of apertures is used to collimate the beam and it is then steered with a magnet to produce a mono-energetic beam

(tolerance $<0.1\%$) of 1×0.5 mm with angular divergence of less than 0.1° . Effort is taken to obtain a well-collimated incident beam as this reduces the energy width of the scattered peaks, leading to good mass resolution. This is particularly important at the lower scattering angles where the energy loss is low.

The beam is introduced to the scattering chamber via a differential pumping section and a final aperture to produce a current of $\sim 0.5\mu\text{A}$ on the sample, which is electronically isolated and biased to a positive potential. This is to prevent secondary electron emission, which can affect the beam current measurement.

The sample itself is clipped into a sample holder that is mounted on a goniometer possessing three dimensions of freedom; allowing very precise movement and hence accurate beam alignment (see Figure 2.5.2.2). The sample is held approximately 30-35cm from the final aperture.

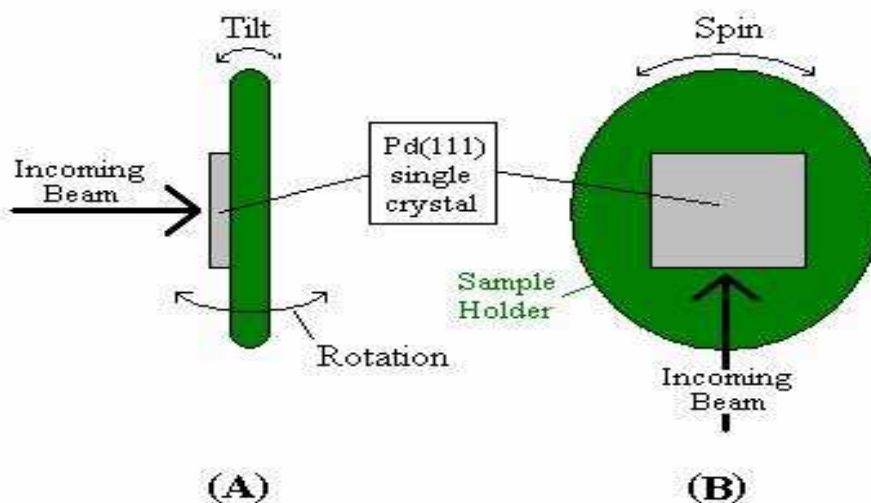


Fig 2.5.2.2 – Representation of the goniometer used in the facility at Daresbury from (a) 90° to the beam and (b) parallel to the beam, detailing the three degrees of freedom the sample holder has.

Scattered ions are analysed as a function of both energy and scattering angle and are detected using a two-dimensional Toroidal Electrostatic Analyser (TEA) which has a

precision sensitive detector (energy resolution $\Delta E/E = 2.4 \times 10^{-3}$). The TEA can detect ions over a range of 24° with an angular resolution of $<0.5^\circ$ and is rotatable by 140° around the sample in a horizontal plane. Actual ion detection is achieved by channel plates and a position sensitive detector. This multi-channel detection set-up leads to good, high quality data with a low signal to noise ratio.

Located in the experimental end-station are four vacuum linked chambers; a storage chamber, a fast entry sample introduction load lock chamber, a sample preparation chamber. The preparation chamber is used for sample cleaning and characterisation (LEED/AES). The scattering chamber contains a precision six-axis goniometer to allow accurate alignment with the beam and a toroidal electrostatic energy analyser with position sensitive detector to measure the scattered ion intensities as functions of scattering angle and ion energy.

2.5.3 Data Collection

Coherent spectra are only produced if the beam is aligned properly with the bulk of the sample, a process known as “channelling”. Alignment is achieved through a series of scans of each goniometer axis in turn. These alignment scans simply count the scattered ions for a certain length of time at each scattering angle. This produces a plot of integrated ion counts, showing a minimum at a particular scattering angle if the alignment is correct.

The minimum corresponds to the blocking channel for the particular layer being studied. Stereographic projections, such as the one shown in Fig 2.5.3.1, can be used to assist in the determination of blocking axis.

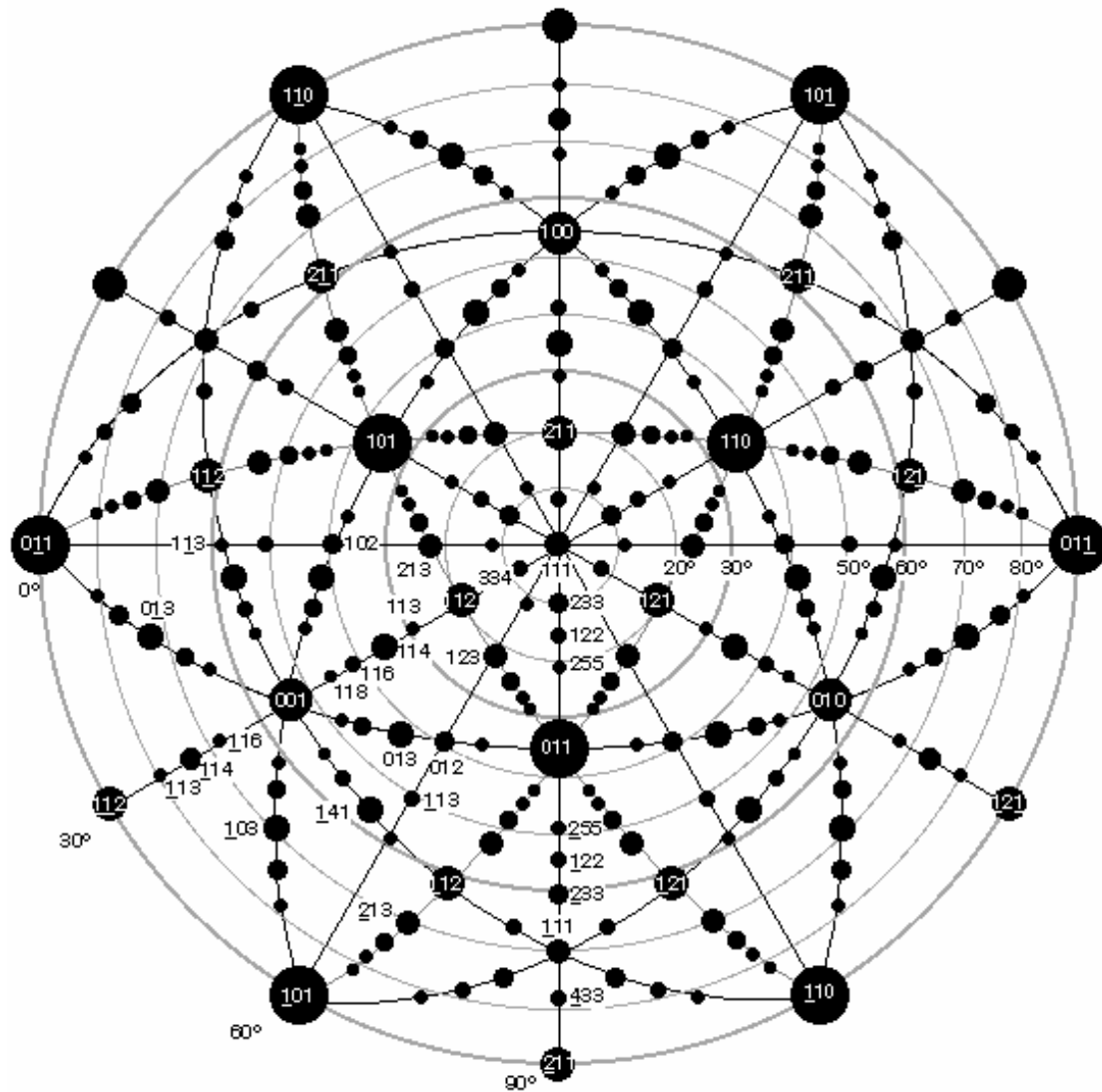


Fig 2.5.3.1 -fcc(111) stereographic projection used to assist in the determination of blocking access.

Taken from reference¹⁰

The positions of the circles indicate the positions of the channels for an fcc(111) oriented crystal and the size of the circles gives an indication of the size and intensity of the channel. This is determined primarily by the interaction of the shadow cone and the distance between the atoms in that particular direction.

More intense channelling results in a greater shadowing of sub-surface atoms, producing more prominent blocking dips.

For our experiments (fcc(111) crystal using He⁺ ions) it is possible to use only one incident angle to look at the 1st, 2nd and 3rd layer geometries. This significantly reduces experimental time, as there is less need to spend time aligning the beam for different incoming geometries (see Figure 2.5.3.2)

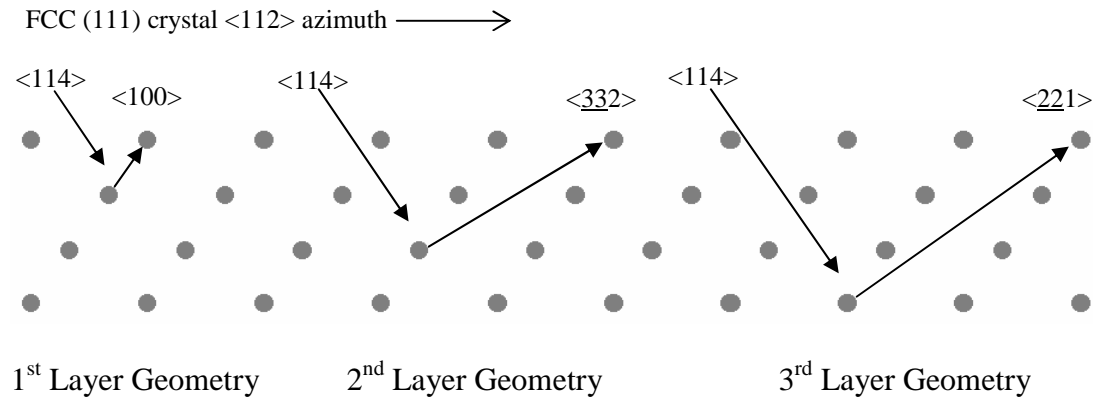


Fig 2.5.3.2 - Schematic diagrams showing the ion beam trajectories utilised to achieve 1-, 2- and 3-layer specific alignments in the $\langle 112 \rangle$ azimuth of the fcc {111} surface.

Compositional information from the first layer of the sample can be obtained by aligning the beam along the $\langle 114 \rangle$ channel and detecting along the $\langle 100 \rangle$ channel. This is known as the 1st layer geometry. Information for the first and second layers can be obtained by aligning along the same $\langle 114 \rangle$ channel but this time detecting along the $\langle 332 \rangle$ channel, blocking the path of any ions that may be scattered from the third layer. The 3rd layer geometry was obtained in a similar manner, picking an azimuth that will block ions scattered from lower atoms.

Table 2.5.3.1 below shows the scattering angles for the respective geometries,

Layer	Incident	Exit	Rotation	Scat. Angle
1	$\langle 114 \rangle$	$\langle 100 \rangle$	35.26°	109.5°
2	$\langle 114 \rangle$	$\langle 332 \rangle$	35.26°	84.24°
3	$\langle 114 \rangle$	$\langle 221 \rangle$	35.26°	90.00°

Table 2.5.3.1 – Summary of blocking direction investigated during our calculations and the respective scattering angle they relate to.

Once the beam is aligned along the $\langle 114 \rangle$ direction, the analyser is placed in one of two positions (one can detect 2nd and 3rd layer geometries from a single place whilst the other can detect the 1st layer geometry) and the data acquisition can begin. Once the data plots are obtained, it is simply a case of looking along each of the three main blocking dips to obtain the required information.

Unlike during alignment, when ions are collected over a certain period of time, during actual data collection, ions are collected for a pre-set integrated current. This allows direct comparison of each data set in terms of the number of counts each contains. The analyser is then cleared, the pass energy is lowered and a new measurement is started. This procedure is continued until the energy range covering the desired peaks has been completed.

The detector system produces two dimensional intensity maps of the ion intensity over a 1.5% range of pass energy and a scattering angle range of 24° with a resolution of 0.3% and 0.3° respectively.

Full two-dimensional data sets are accumulated by taking a series of 'tiles' which cover the required angle/energy range and joining them together electronically to produce a single scattered ion intensity map. (see Figure 2.5.3.3 overleaf for a typical image).

The image produced is a plot of ion count intensity (indicated by the colour) as a function of scattering angle (x-axis) and scattered ion energy (y-axis). Areas of high ion intensity, caused by the presence of Pd and Au atoms are represented by the bright patches going diagonally from left to right.

The raw data is always presented as a three-dimensional topographic map with Beam Energy versus Scattering Angle on the 2-D x- and y- axes and Ion Intensity along the z-axis

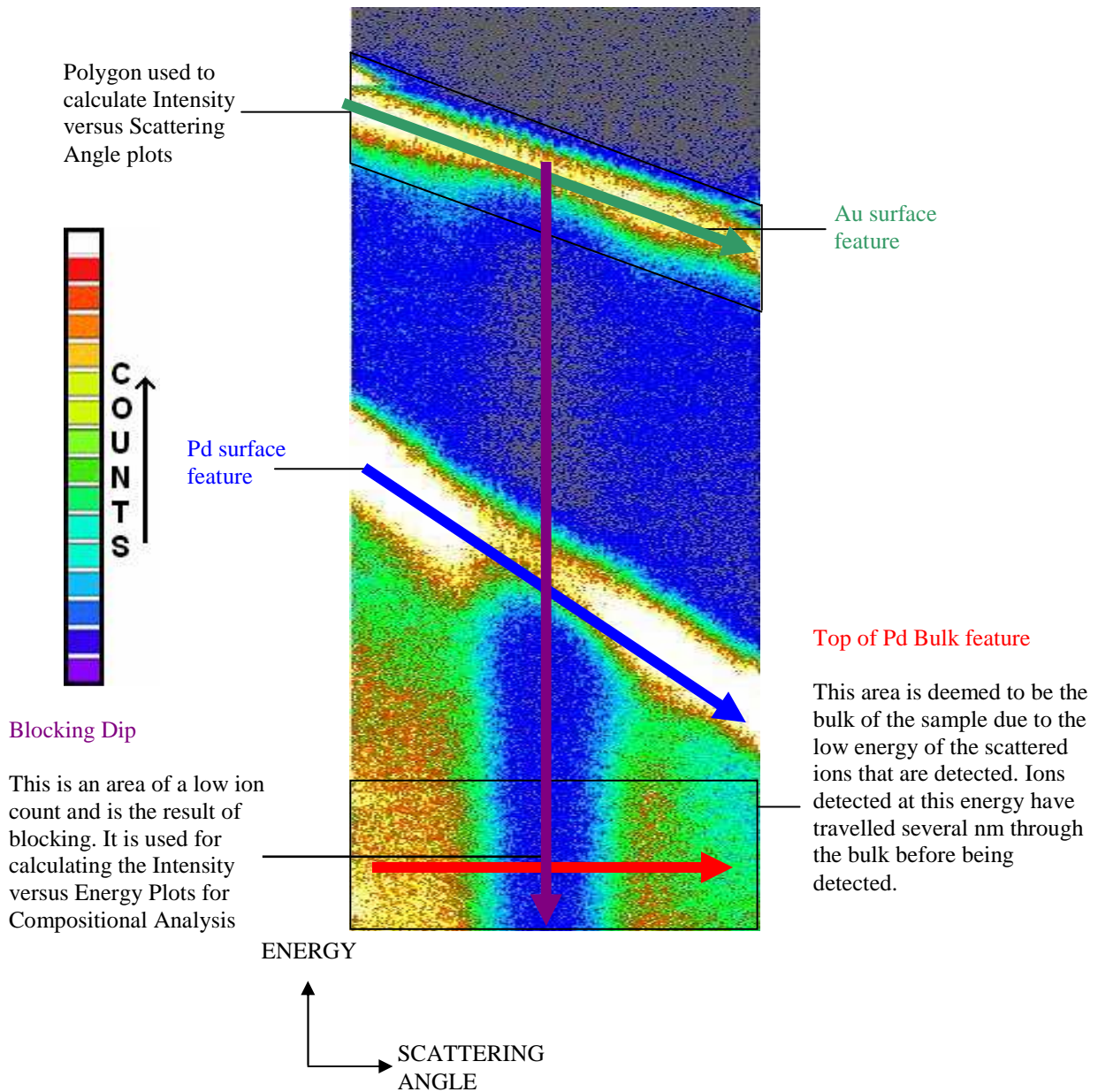


Fig 2.5.3.3 – A typical raw MEIS data spectrum. The coloured arrows correspond to the Intensity vs. Scattering Angle Plots shown below in Figure 2.5.4.1 and the Intensity vs. Energy Plot shown in Figure 2.5.4.3.

The sloping is a direct result of the kinematic factor's dependence on scattering angle and can be corrected for using the computer software. The peaks themselves can be identified using the following equation (assuming conservation of energy and momentum in a two-body collision),

$$\frac{E_1}{E_0} = \frac{1}{(1+A)^2 \cdot [\cos\theta_1 \pm (A^2 - \sin^2\theta_1)^{1/2}]^2}$$

where, E_1 = energy of the peak

m_2 = mass of surface atom

E_0 = incident beam energy

m_1 = mass of incident projectile

$A = m_2/m_1$

θ_1 = scattering angle

Whilst two-dimensional data sets provide a complete picture of the scattering behaviour it is normal to process the data by integrating over a range of angles or energies to produce one-dimensional plots. Plots of scattered ion intensity versus scattering angle provide structural information that can be used to calculate parameters such as surface layer relaxation and to verify the alignment of the sample with respect to the beam.

2.5.4 Data Interpretation

There are two types of data that can be taken from the raw MEIS plots,

- 1) Structural information can come from Ion Intensity versus Scattering angle curves
- 2) Compositional information can come from Ion Intensity versus Energy curves

Structural Information

If we look at the 2D raw plot produced by the MEIS experiment then we can determine three areas of note,

- (A) The Au surface feature
- (B) The Pd surface feature
- (C) The Pd bulk feature

By taking a “cut” through each of the features it is possible to produce a 1D plot of Ion intensity versus Scattering angle as shown in Figure 2.5.4.1 below,

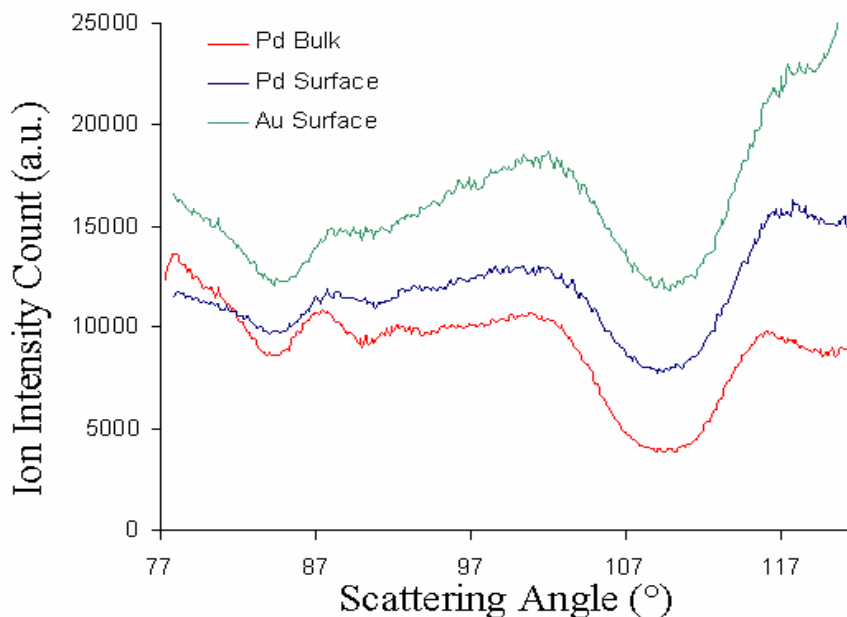


Fig 2.5.4.1 – Typical ion intensity vs. scattering angle plots produced from raw data for a Pd/Au bimetallic surface

The cuts are achieved by superimposing polygons onto the raw data tile and then projecting the intensity contained within the polygon onto a scattering angle vs. ion intensity plot. The polygons themselves are created in the Igor Pro program by calculating the energy loss experience by the ion beam as it passes through a certain number of atomic layers (usually 6 is chosen from convention). The calculation itself utilises the stopping power of the ion beam in the Au or Pd surface, the mass of both incident ion and target atom and the incident angle of the beam using the SRIM code.¹¹

The plots show the positions of the 1st, 2nd and 3rd layer geometry blocking dips and they have many uses in structure determination. If there is a slight shift in the blocking curve between the bulk spectrum and the surface spectrum then this is evidence of a surface relaxation. Calculations can be done to determine the exact

value of the surface relaxation if required. Differences in blocking curves between two metals of a bimetallic system can give an idea of how well the two metals sit together and a change in blocking curve corresponding to an anneal could be the result of a surface reconstruction or change in composition.

There are three generally accepted common methods of growth of a metal on a metal substrate (Figure 2.5.4.2),

- i) **Franck – van der Merwe (F-vdM)**: Second metal grows monolayer by monolayer directly on top of substrate metal in a pseudomorphic fashion
- ii) **Stranski – Krastanov (S-K)**: Second metal begins to grow homogeneous to the first metal but after a while begins to growth as islands on the surface
- iii) **Volmer – Weber (V-W)**: Second metal grows on the substrate metal as islands

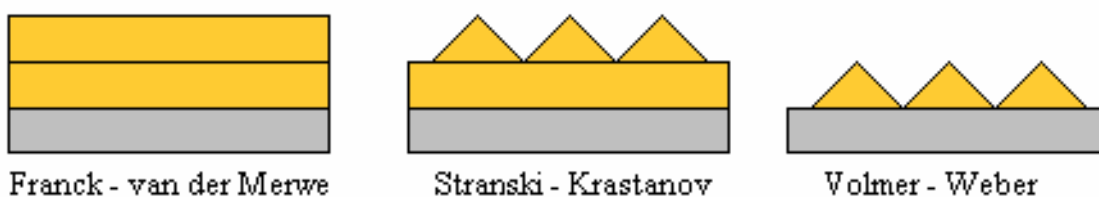


Fig 2.5.4.2- Growth methods of a metal overlayer on a metal substrate

MEIS structural analysis can give an idea as to which method is the more likely by looking at the blocking dip shifts. Obviously, there will be a pronounced difference in bulk and surface blocking dips for both the V-W and the S-K method (more obvious in V-W) whereas the F-vdM growth mode will show a very small blocking dip shift (if any). Simulations can also be carried out on “suspected” structures and these simulated spectra can be compared with real data to try and fit real systems. More about these simulations will be mentioned in the following section on compositional information.

Compositional Information

Going back to the 2D plots and the blocking dip we can observe at $\sim 110^\circ$. In our system this corresponds to the exit blocking direction in the 1st layer geometry. By summing the ion intensity over a small angular range at the base of this dip it is possible to produce a 1D plot of ion intensity versus energy of the scattered ions (an example is shown in Figure 2.5.4.3).

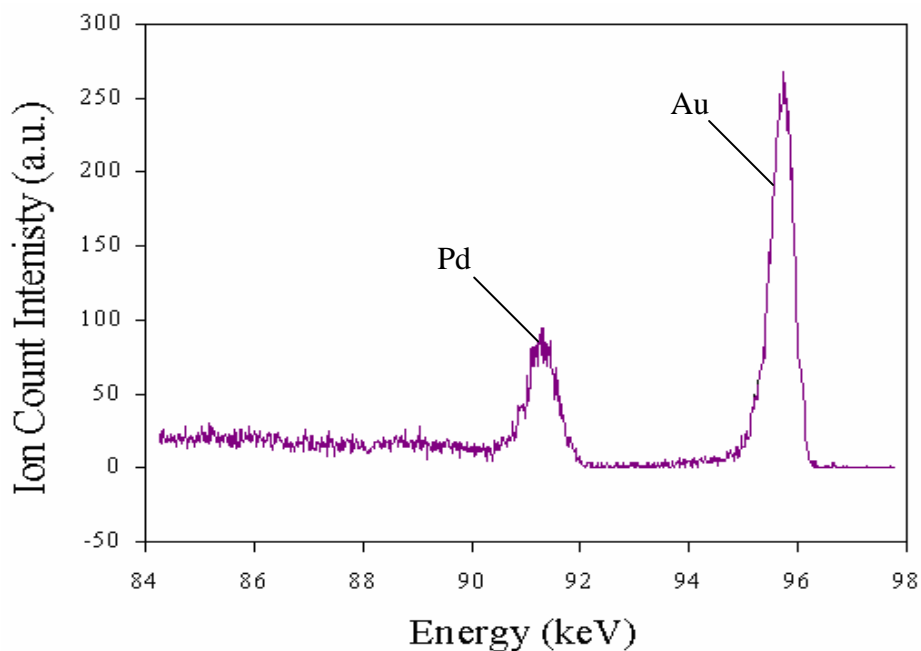


Fig 2.5.4.3 – Typical ion intensity vs. energy plot produced from raw data of a Pd/Au bimetallic system

As this spectrum is produced from the least intense portion of the blocking curve, it is a fair assumption that it contains information dominated by the first layer. Calculation of the peak areas can be calculated via a background subtraction (usually linear or quadratic) and a subsequent integration. There are peak normalisation calculations that need to be done however. As noted previously, the probability density that an ion is scattered over a certain scattering angle can be represented by,

$$\frac{d\sigma}{d\Omega} = F \left[\frac{z_1 z_2 e^2}{4E \sin^2(\theta/2)} \right]^2 g(\theta, m_1, m_2)$$

In order to compare the peak areas on the integrated spectrum directly, they must be corrected in line with this equation. The result is peak areas that are proportional to the number of atoms of each metal in the particular layer of the sample. In all MEIS experiments $g(\theta, \mathbf{m}_1, \mathbf{m}_2)$ has a value close to 1 and hence is ignored. There are up to six further corrections that must be carried out,

- i) The peak area is strongly dependent upon the scattering cross-section of each element. Therefore, each peak area must be divided by the square of the relative **atomic number**, z^2 .
- ii) Since ion intensity is proportional to $1/(\sin^4(\theta/2))$, the peak areas must be multiplied by $\sin^4(\theta/2)$ where θ is the scattering angle for the particular alignment (as found in Table 2.5.1).
- iii) The value of **F** can be calculated for each target ion/incident ion pair from the equation detailed in 2.5.1. For all our experiments done with 100keV He⁺, F=0.86 for Pd and F=0.72 for Au.
- iv) During the initial integration of the raw data, the number of channels used to produce the 1D plot may vary depending on peak shape and width. It is therefore necessary to divide each peak area by the number of channels taken. *This correction was not done for our data as all raw data integrations were performed with the same number of channels.*
- v) The standard dose used in our MEIS experiments is 1500nC. However, from time to time it may be necessary to use a high or lower dose. This dose must be taken into account when calculating the peak areas. *This correction was not performed for our data, as all doses were equal at 1500nC.*
- iv) Figure 2.5.4.4 shows the difference in “beam footprint” (area of the ion beam on the surface) when the incident angle is not 0°. Simple trigonometry tells us that the width of the beam is equal to $a/(\cos \phi)$ where ϕ is the angle the beam

makes with the surface normal and a is the beam width. If the sample is tilted by ϕ then the beam is wider by a factor of $\cos. \phi$ and hence all peak areas must be divided by $\cos. \phi$. *In the majority of our experiments, the layer specific geometry was acquired from a constant incident angle – hence, the footprint correction was normally not required in this work.*

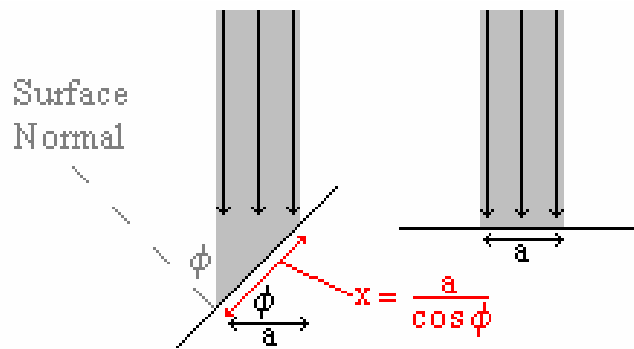


Fig 2.5.4.4 – Schematic of the changing “beam footprint” at non-normal incident angles.

Despite all these corrections, it is still not the case that we take the ratio of Pd to Au as the composition for each layer because, as mentioned previously, the shadowing and blocking are not perfect. This can be shown by summing the two normalised peak areas for each layer geometry to give an idea of the number of ions scattered. This value is known as the *normalised illumination*, or n_{Au+Pd} . By taking the ratio of the three normalised illuminations we can get an idea of how bad the over-illumination is. We are obviously expecting the ratio to be 1:2:3.

Previously, we discussed some of the possible reasons for imperfect scattering that could lead to an over-illumination such as,

- i) the shadow cone radius of the lattice atoms
- ii) the surface relaxation of the sample
- iii) the presence of adsorbate molecules
- iv) the enhanced vibrations of the surface atoms

It is possible to calculate the contribution each of these will have to the over-illumination of a particular system. However, as we are using a relatively simple system in which we are illuminating the top three layers with the incident beam and analysing the 1st, 2nd and 3rd layer geometries simply by looking along the blocking dips, the over-illumination effect will be quite small.

We simply need a method for estimating the number of layers contributing to the ion intensity for each scattering geometry. This is achieved by carrying out computer simulations using the VEGAS code.¹² This simulation is able to estimate the contribution of each layer to the ion scattering signal, however, there are several parameters and assumptions that need to be addressed,

- 1) a lattice structure needs to be provided (or a starting one if the actual structure is in doubt)
- 2) values for the both the bulk and surface vibrations
- 3) a value for the surface relaxation (if relevant)

The details of the VEGAS simulation carried out for these MEIS results are contained in Chapter 3.2. Once VEGAS has estimated the actual number of layers contributing to the illumination for each geometry, the corrections to compensate for the over-illumination can be carried out and only a few simple computer steps are needed to calculate the composition of the required layers.

2.6 Reflection-Absorption Infrared Spectroscopy (RAIRS)

One of the most powerful methods for surface compositional analysis is Vibrational Surface Spectroscopy. It can fingerprint adsorbed species and we can use selection rules to deduce bonding orientations.

It is based on the absorption of energy from the incident particle (i.e. electron – EELS, IR; photon – RAIRS) and is carried out by measuring the intensity vs. energy distribution of the particle following absorption;

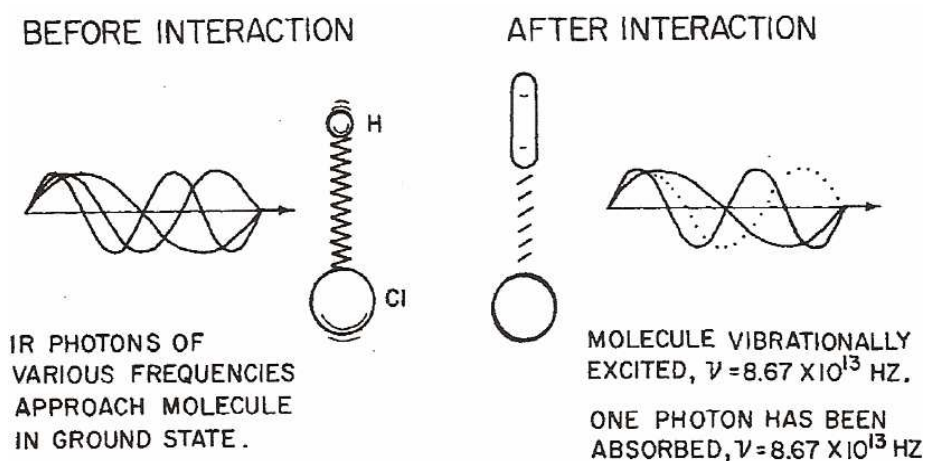


Fig 2.6.1 – Schematic illustration of infrared absorption. The HCl molecule, whose vibrational frequency is 8.67×10^{13} Hz, increases its vibrational energy by absorbing the energy of an infrared photon which has this same frequency. *Taken from reference¹¹*

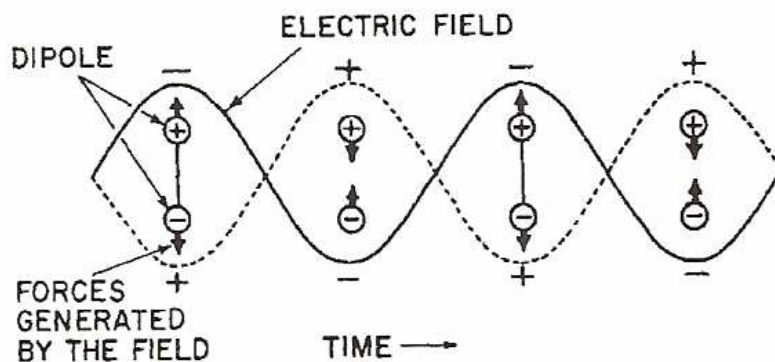


Fig 2.6.2 – Forces generate on a dipole by an oscillating electric field. These forces tend to alternately increase and decrease the dipole spacing. *Taken from reference¹¹*

Infrared methods can be performed using conventional (non-dispersive) FTIR instrumentation in *transmission* or *reflectance* mode.

In transmission mode,

$$I = I_o \exp(k.c.l) \quad \frac{I}{I_o} = T = \exp(k.c.l) \quad \text{Transmittance}$$

$$\ln \frac{I}{I_o} = k.c.l \quad A = \epsilon.c.l \quad \text{Absorbance}$$

where k = absorption coefficient, ϵ = absorptivity, c = surface concentration and l = path length

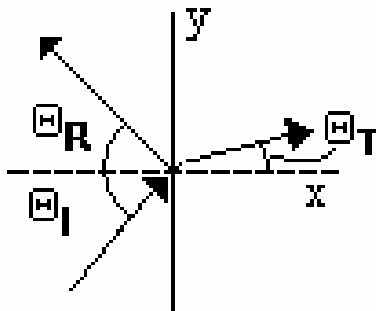
It can be shown that k is also the *imaginary* part of the *refractive index*

$$\mathbf{n} = n + ik$$

In a non-absorbing (dielectric) medium the refractive index, $\mathbf{n} = n$. In an absorbing medium, the refractive index contains a portion corresponding to the absorption, k .

Reflection, refraction and absorption are all related through Maxwell's equations for electromagnetic radiation for interfaces of different \mathbf{n} .

The *reflection* and *refraction* angles are given by Snell's Law;



$$\Theta_I = \Theta_R \text{ and } \frac{n_1}{n_2} = \frac{\sin \Theta_I}{\sin \Theta_T}$$

for $\Theta_I < \Theta_{crit} = \sin^{-1} \frac{n_2}{n_1}$

where the plane containing the incident and reflected (and transmitted) waves is called the *plane of incidence*.

The intensities of the reflected waves are given by the **Fresnel equations** and are dependent on their polarisations.

When $\mathbf{n}_1 = 1.00$ (vacuum/air) and $\mathbf{n}_2 = n + ik$;

For p -polarised light (E-field \parallel to plane of incidence)

$$R_p = \frac{\cos^2 \Theta_T - 2n \cos \Theta_I \Theta_T + (n^2 + k^2) \cos^2 \Theta_I}{\cos^2 \Theta_T + 2n \cos \Theta_I \Theta_T + (n^2 + k^2) \cos^2 \Theta_I}$$

and for s -polarised light (E-field \perp to plane of incidence)

$$R_s = \frac{\cos^2 \Theta_I - 2n \cos \Theta_I \Theta_T + (n^2 + k^2) \cos^2 \Theta_2}{\cos^2 \Theta_I + 2n \cos \Theta_I \Theta_T + (n^2 + k^2) \cos^2 \Theta_2}$$

These equations allow us to predict the reflectivity of materials (\mathbf{n}_2) with incidence angle. For very thin surfaces on reflective materials (e.g. single crystals) it can be calculated that Θ_I should be large ($\sim 75^\circ$ - 85°) in order to maximise sensitivity. This is employed in the grazing incidence experiment known as RAIRS which is used to study adsorbates on metallic surfaces.

RAIRS uses photons as the incident particle and because it is an optical technique it is not necessary for such studies to be carried out in a vacuum. However, the RAIRS experiments all contained within this piece of work are carried out in the UHV system at the University of St. Andrews. The technique is not inherently surface-specific but;

- there is no bulk signal to interfere with the surface signal
- the surface signal is readily distinguishable from gas-phase absorptions using polarization effects.

The intensity of the light reflected from the surface is related to the phase shift (δ) upon reflection;

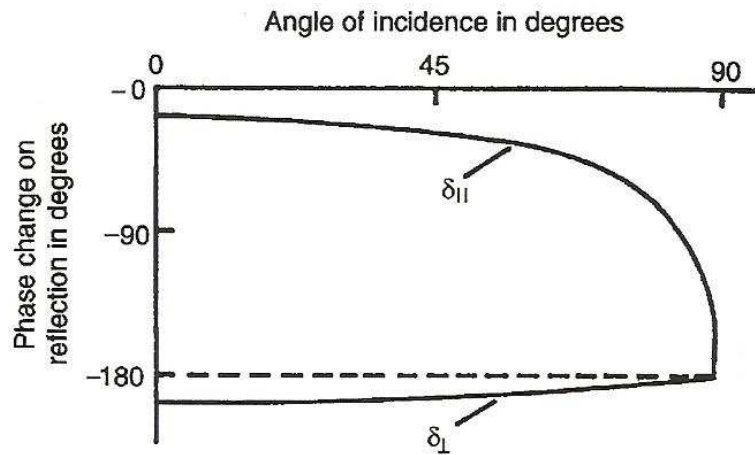


Fig 2.6.3 – The phase shift for light reflected from a metal surface as calculated for light polarised both parallel ($\delta_{||}$ - p-polarised) and perpendicular (δ_{\perp} - s-polarised) to the plane of incidence. Taken from reference¹³

The Fresnel equations show that **s-polarised light** is almost cancelled by reflection at grazing incidence and **p-polarised light** is almost doubled by reflection at grazing incidence (until we reach very grazing situations).

Only p-polarised component light can be reflected from the surface at high incidence angles.

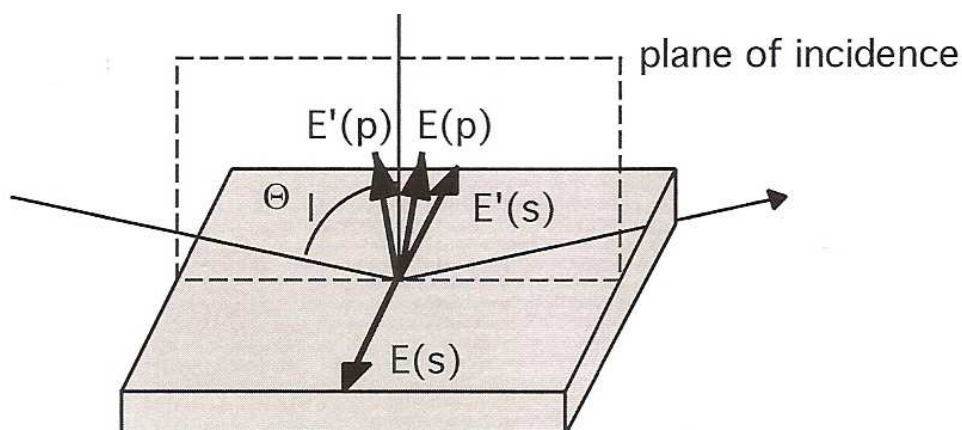


Fig 2.6.4 – Schematic showing the reflection from the surface of p- and s-polarised component light for high incidence angles. Taken from reference¹¹

The observation of vibrational modes of surface bound adsorbates is subject to the *surface dipole selection rule* which states basically that, only vibrations which give rise to an oscillating dipole aligned perpendicular to the surface plane can interact with the incident light”.

Practically this means that only vibrations whose dipole moment is perpendicular to the surface are IR active and give rise to an observable adsorption band. Group theory can be used to tell us which vibrations have components in the x, y and z directions. This can enable us to predict IR active bands for known adsorbates and to assign IR bands produced from RAIRS spectra of single crystal metal surfaces. Further information on the surface selection rules for RAIRS can be found in the review by Sheppard & Erkelens¹⁴ and it is also worth noting that even if a transition is allowed, it may still be very weak if the change in dipole moment is small.

One of the potential problems of RAIRS is that of sensitivity, the signal is usually very weak owing to the small number of adsorbing molecules. Typically, the sampled area is ca. 1cm^2 with less than 10^{15} adsorbed molecules (i.e. about 1 nanomole). With modern FTIR spectrometers, however, such small signals (0.01% - 2% absorption) can still be recorded at relatively high resolution (ca. 1cm^{-1}). Since absorbance A is proportional to E^2 and the area of the surface sampled is inversely proportional to $\cos \Theta_1$ it follows that the sensitivity of RAIRS is proportional to $E^2/\cos \Theta_1$.

For a number of practical reasons, low frequency modes ($<600\text{cm}^{-1}$) are not generally observable and it is therefore not usually possible to see the vibration modes of the metal-adsorbate bond. For this reason, attention is concentrated on the intrinsic vibrations of any adsorbate species which are found in the range $600 - 3600\text{cm}^{-1}$.

2.7 Experimental Set-up and Sample Preparation

Three ultrahigh vacuum (UHV) systems were used in this study, two in St. Andrews and one at the MEIS facility at CCLRC Daresbury Laboratory.

The first system consists of an Omicron variable temperature-STM chamber (base pressure 1×10^{-10} mbar) which has facilities for sample cleaning, STM and LEED/AES experiments. Interfaced to this UHV system is an auxiliary chamber for RAIRS experiments using a Nicolet Nexus spectrometer with a mercury cadmium telluride detector. RAIRS data correspond to 512 scans at a resolution of 8 cm^{-1} . A typical experiment would involve the characterisation of the adsorbate with RAIRS followed by UHV sample transfer for STM measurements.

The second UHV chamber (base pressure 1×10^{-10} mbar) contains facilities for Ar^+ bombardment, LEED, Auger spectroscopy and a mass spectrometer for TPD experiments. The sample temperature was measured by means of a K-type thermocouple whose junction was directly attached to the Pd{111} sample.

The third UHV system is the MEIS facility at CCLRC Daresbury Laboratory²³ which has been detailed in Section 2.5.2.

In all experiments, the Pd{111} sample was cleaned by cycles of sputtering (Ar^+ , 1.0 keV, 40mA) and annealing to 1000 K until a sharp (1x1) LEED pattern was obtained and no impurities were observed by AES. Since the C (KLL) Auger transition at 270 eV overlaps with a Pd ($\text{M}_{45}\text{N}_{23}\text{N}_{45}$) feature, the detection of surface carbon with AES is problematic. However, by monitoring the ratio of the Pd ($\text{M}_5\text{N}_{45}\text{N}_{45}$) transition at

330 eV to the 270 eV peak, one is able to detect when the level of surface C has been minimized.

In each chamber, Au deposition was achieved via a resistively heated Au droplet wound around W wire, except in the case of the MEIS experiments where it was deposited from a Au K-cell. Initial deposition rate calibration experiments were carried out via Auger measurements monitoring the attenuation of the Pd (330 eV) Auger signal.

The Au/Pd{111} surfaces were annealed to a specified temperature for 5 minutes and then cooled to room temperature before either analysis, exposure to K (dosed via an SAES getter source) or exposure to acetic acid (AcOH, dosed via a leak valve). AcOH (Aldrich, 99.9%) had been purified by successive freeze-pump-thaw cycles.

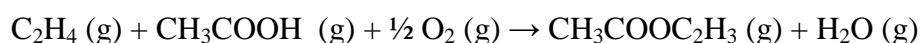
2.8 Chapter 2 References

- ¹ S.J. Garrett, CEM924 course notes, Michigan Sate University, Spring, **6.1**, 13.5 (2001)
- ² http://www.chem.qmw.ac.uk/surfaces/scc/scat6_2.htm
- ³ http://www.chem.qmw.ac.uk/surfaces/scc/scat5_2.htm
- ⁴ http://www.chem.qmul.ac.uk/surfaces/scc/scat7_2.htm
- ⁵ S.J. Garrett, CEM924 course notes, Michigan Sate University, Spring **4.9**, 8.4 (2001)
- ⁶ S.J. Garrett, CEM924 course notes, Michigan Sate University, Spring **4.9**, 8.4 (2001)
- ⁷ R.M.Tromp, *Practical Surface Analysis, Vol. 2: Ion and Neutron Spectroscopy*, 2nd Ed., D. Briggs and M. Seah (Eds.), John Wiley and Sons, New York (1973)
- ⁸ <http://www.srim.org/SRIM/SRIM2003.htm>
- ⁹ <http://www.dl.ac.uk/MEIS/facility/index.htm>
- ¹⁰ <http://www.dl.ac.uk/MEIS/stereographs/sp.fcc.111.html>
- ¹¹ P. Bailey; T.C.Q Noakes; S.P.Tear; D.P.Woodruff and C.J.Baddeley, *Nuc. Ins. Meth. B*, **183**, 62 (2001)
- ¹² J.W.M. Frenken, J.F. van der Veen, and R.M.Tromp, *Nuc. Ins. Meth. B*, **17**, 334 (1986)
- ¹³ S.J. Garrett, CEM924 course notes, Michigan Sate University, Spring, **5.7**, 11.6 (2001)
- ¹⁴ N. Sheppard and J. Erkelens, *Appl. Spec.*, **38**, 471 (1984)

CHAPTER 3: Au/Pd{111}

3.1 Introduction

Vinyl acetate is currently synthesised industrially by a catalytic process involving a silica supported Pd/Au bimetallic catalyst.



The Pd/Au{111} system has been studied in detail (see Chapter 1.5) but far less is known about the inverse Au/Pd{111} system. The little that is contained in the literature has been recreated in Chapter 1.5 and will not be revisited here. Despite this research, there is still a distinct lack of fundamental understanding of the behaviour of the Pd/Au system. In order to understand how the reaction proceeds on an industrial scale it is critical to have a thorough knowledge of the bimetallic surface on which the reaction takes place. Currently the industrial process involves the use of silica supported Pd/Au bimetallic colloidal particles, the composition and structure of which can be found in a patent, which allows details some of the synthetic steps.¹ Surface science studies on a variety of Pd/Au bimetallic surfaces should provide an in-depth understanding of the properties and behaviour of the system which, in turn, can be applied to the industrial process.

In this chapter STM experiments have been used to investigate the growth mode of Au on Pd{111} at 300 K and to investigate the surface morphology at a variety of pre-annealing temperatures between 600 K and 975 K. MEIS work has yielded compositional behaviour of the surface and sub-surface as a function of anneal temperature and a qualitative structural study has also been used as to reinforce the findings.. LEED and AES have been used to assist with surface characterisation.

3.2 Experimental section

Experimental and sample preparation procedures were carried out as detailed in Chapter 2.7. The STM and MEIS experiments were carried out in separate chambers at different facilities and therefore on slightly different pre-annealed surfaces.

STM experiments followed the pattern:

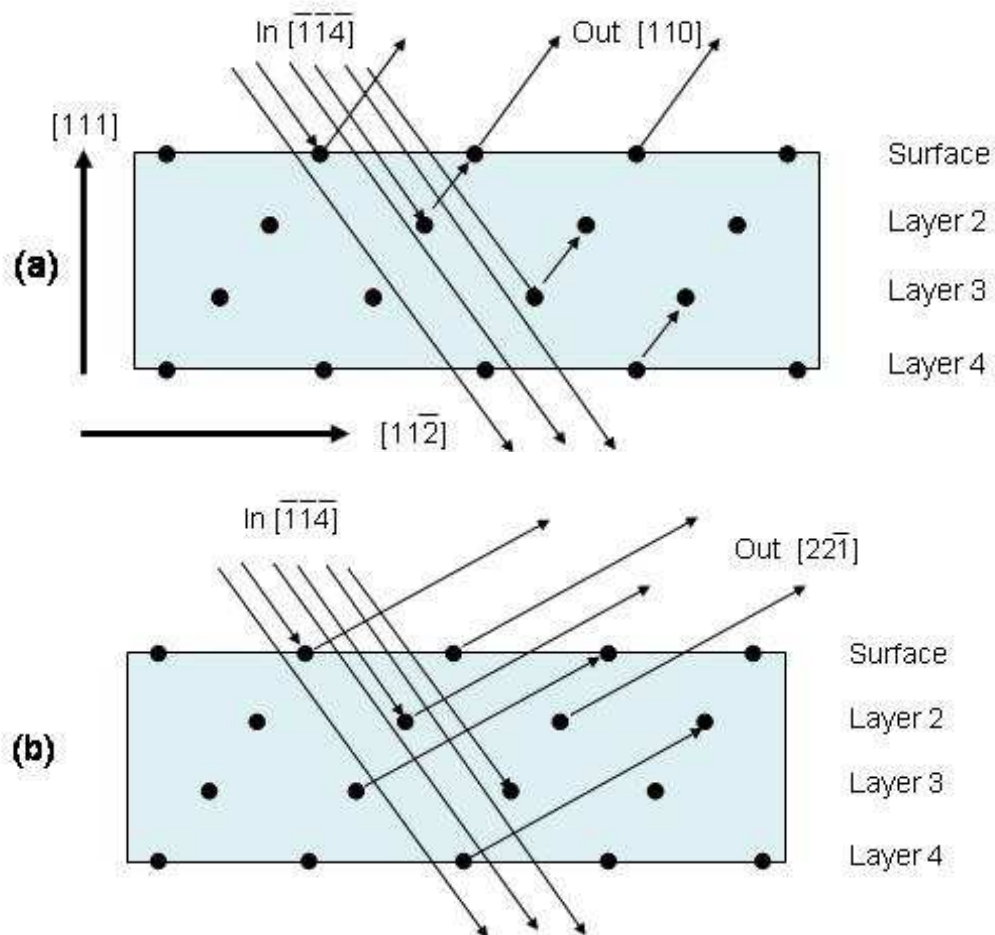
- Pd{111} single-crystal cleaned by Argon bombardment and high temperature (1000 K) annealing cycles and checked for impurities by LEED and STM.
- Once cleaned; Au deposited at room temperature by vapour deposition (5 min cycles) and checked by STM during the growth process until Au layer became significant (>10 ML).
- Pd{111} single-crystal cleaned.
- 1-2 monolayers of Au deposited onto the surface.
- Pd/Au surface annealed to the lowest pre-annealing temperature for 5 minutes and allowed to cool to room temperature.
- Pd/Au annealed surface analysed by STM.
- Pd/Au surface annealed to the next pre-annealing temperature for 5 minutes and allowed to cool to room temperature.
- Process repeated until the final anneal temperature (950 K) has been analysed.
- Sample cleaned ready for next experiment

MEIS experiments followed the sequence:

- Pd{111} single-crystal cleaned by argon ion bombardment and high temperature (1000 K) annealing cycles and checked for impurities by AES and LEED.

- Once cleaned; Au deposited at room temperature from a K-cell and the amount verified on completion by AES Pd/Au surface annealed to the required pre-annealing temperature for 5 minutes and allowed to cool to room temperature.
- Pd/Au annealed surface transferred to scattering chamber and analysed by MEIS.
- Sample returned to preparation chamber.
- Pd {111} crystal cleaned in preparation for next experiment.

The theory of MEIS is explained in detail in Chapter 2.5. The MEIS experiments described in this chapter use layer specific experimental geometries as shown in Figure 3.2.1.



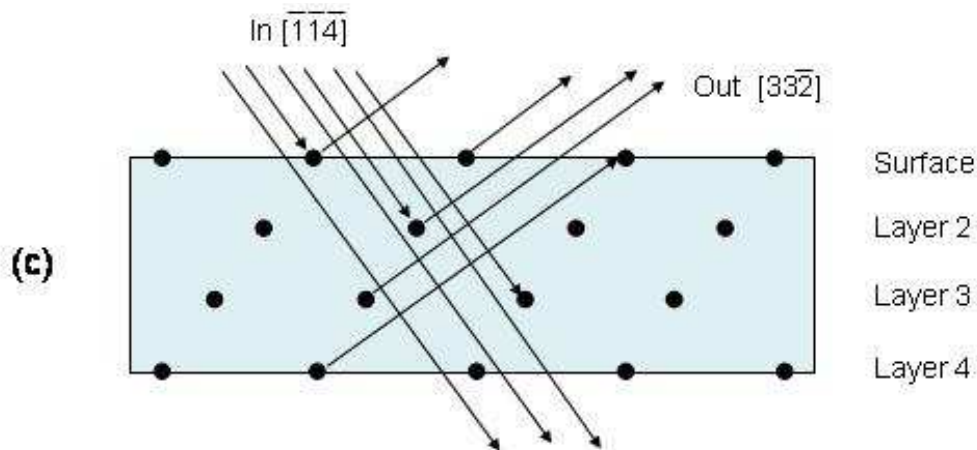


Figure 3.2.1 - : Schematic diagrams showing the ion beam trajectories utilised to achieve (a) 1-, (b) 2- and (c) 3-layer specific alignments in the $\langle 11\text{-}2 \rangle$ azimuth of the fcc $\{111\}$ surface. The arrows represent ion trajectories and show, for example, how the 1st, 2nd and 3rd layer atoms are visible to the incident beam while, by contrast, the 4th layer atoms are shadowed. Similarly, outgoing trajectories show how the phenomenon of blocking can be utilised to achieve layer specific information.

At the ion energies employed in MEIS, a randomly directed ion beam is able to penetrate deep into the Pd sample. However, aligning the Pd $\{111\}$ sample along the incident direction shown in Figure 3.2.1 results in the ion beam striking the top, second and third Pd layers.

Deeper lying Pd layers are, to a good first approximation, shadowed from the incident beam. Using the outgoing trajectories shown in Figure 3.2.1, we can extract data specifically from the top, top two and top three layers of the surface by utilising the phenomenon of blocking. Ion intensity versus scattered ion energy plots are achieved by integrating the measured ion counts over a narrow scattering angle range ($\sim 0.6^\circ$) at the bottom of the relevant blocking dip.

The peak areas corresponding to near-surface Pd and near-surface Au are then measured. To achieve a direct molar ratio between Pd and Au, the peak areas must be

corrected for the scattered ion cross-section. The differential scattering cross section is given by the following equation;

$$\frac{d\sigma}{d\Omega} \propto F \left[\frac{z_1 z_2 e^2}{4E \sin^2\left(\frac{\theta}{2}\right)} \right]^2$$

Where $F = 1 - (0.042z_1z_2^{4/3}/E)$; z_1 and z_2 are the atomic numbers of the incident ion and the target ion respectively and E is the beam energy in keV ²². For Pd, $F = 0.86$ and for Au, $F = 0.72$. These corrections are discussed in more depth during Chapter 2.5.4 and the reader is directed to this discussion for further information.

In order to quantify the composition of each surface layer, Monte Carlo simulations using the VEGAS code² are undertaken to estimate to what extent the scattered ion yield from (say) the one layer geometry is specific to the surface layer. Since the shadow cones produced by impinging 100 keV He⁺ ions are relatively narrow, there is a finite probability of some unwanted contributions from atoms in deeper lying layers to the scattered ion signal due to;

- (i) the surface layer relaxation,
 - (ii) thermal vibrations of lattice atoms
- and (iii) rumpling due to differences in atomic sizes of Au and Pd.

For clean Pd{111}, VEGAS simulations predict that *ca.* 15% of the second layer Pd contributes to the scattered ion signal in the 1-layer geometry at 300 K. Similarly, in the 2-layer geometry a contribution is predicted from about 10% of the third layer. However, in the 3-layer geometry, simulations predict that one can neglect the contribution from deeper lying layers. There is a degree of uncertainty in the contribution of underlying layers to the MEIS signal, hence we decided to calculate

the layer compositions using a range of 1-layer illuminations from **1.0** to **1.3** to give an indication of the magnitude of the error in our calculations.

Consequently, the measured compositions are accurate to $\sim\pm 3\%$. However, it is important to note that the error in calculating the Pd and Au peak areas is extremely small, so we have a very high degree of confidence in the calculation of the Au:Pd molar ratio in a given experimental geometry. In addition, we are able to neglect the influence of light adsorbate atoms on the number of visible metal atoms.³

3.3 Results

3.3.1 Surface Morphology (STM)

Au was deposited onto a clean Pd{111} single-crystal and the surface morphology was observed using STM. Figures 3.3.1.1 and 3.3.1.2 show STM data following the deposition of 1-2 ML of Au on Pd {111} at 300 K. Initially the growth is dendritic, nucleated at the step-edges.

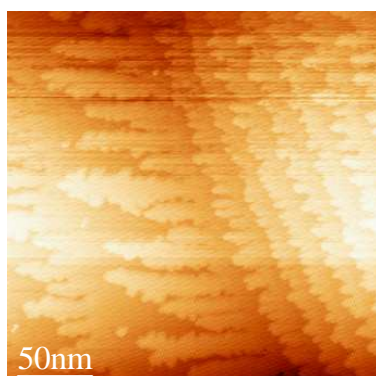


Figure 3.3.1.1 - STM image (250 nm x 250 nm) following the deposition of 1-2 ML of Au on Pd{111} at 300 K

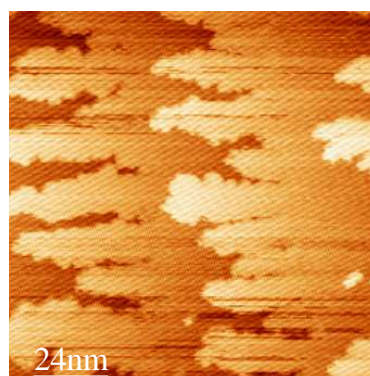


Figure 3.3.1.2 - STM image (122 nm x 122 nm) following the deposition of 1-2 ML of Au on Pd{111} at 300 K

Au can also grow as islands on top of the Pd{111} crystal, as in Figure 3.3.1.3. As the coverage is increased, there is evidence of second layer Au growth prior to the completion of the monolayer.

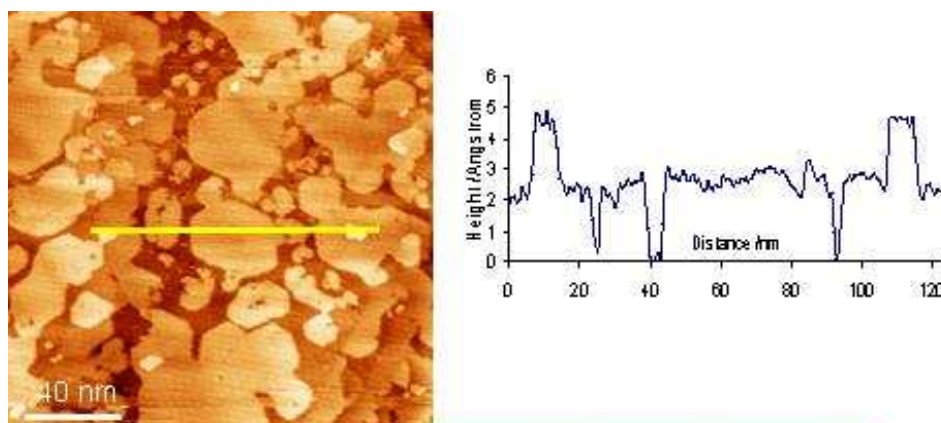


Figure 3.3.1.3 - STM image (180 nm x 180 nm) following the deposition of ~2 ML of Au on Pd{111} at 300 K (inset shows a line profile displaying the onset of 2nd layer Au growth prior to the completion of the first monolayer).

Evidence for this phenomenon is provided in the line image shown in Figure 3.3.1.3 in which the step heights measured are ~ 2 to 2.5 \AA (i.e. consistent with a Au step height).

A Moiré structure has also been seen when multi-layers of Au are deposited on Pd{111}. An example of this can be seen in Figure 3.3.1.4.

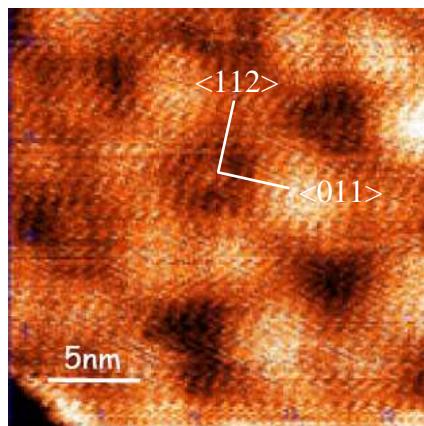
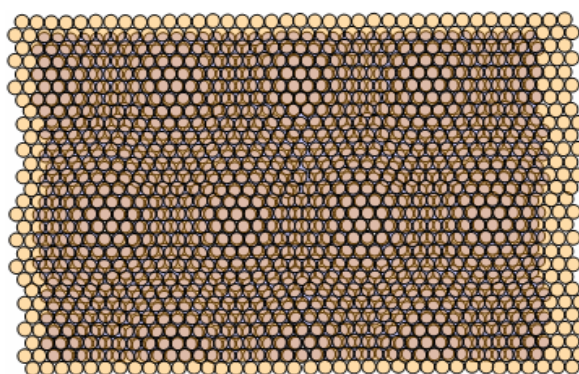


Fig 3.3.1.4 - STM image (22 nm x 22 nm) following the deposition of ~ 1 -2 ML of Au on Pd{111} at 300 K showing the presence of a hexagonal overlayer structure with 80 \AA periodicity.

The periodicity of $\sim 80 \text{ \AA}$ is equivalent to ~ 29 Pd-Pd spacings. The most likely scenario is that 28 overlayer atoms cover 29 underlying atoms. If so, then the nearest neighbour spacing of the overlayer is $\sim 2.85 \text{ \AA}$. Hence the overlayer is either a Au overlayer with a contracted Au-Au spacing or a Au rich Au/Pd alloy.

This kind of lattice mismatch has been seen before on different systems. Jones *et al.* reported an Au/Ni{111} Moiré structure with a periodicity of 22 \AA .⁴ Figure 3.3.1.5 shows a schematic of how the lattice mismatch between Au and Ni{111} creates the Moiré structure. The Au on Pd{111} lattice mismatch has a much larger unit cell (29 atoms rather than 9) and is harder to reproduce diagrammatically. However, a similar effect is responsible for the structure seen in Figure 3.3.1.4 above.



Ni {111} -(9x9)-Au (Moiré structure)

**Ni{111} - nearest neighbour spacing 2.49Å
mismatch with Au-Au bulking spacing = 16%
Au spacing contracted from 2.89 to ~ 2.80Å**

Fig 3.3.1.5 – Schematic showing Au on Ni{111} which forms a Moiré structure resulting from the 16% lattice mismatch which causes the two metals to go in and out of registry. *Adapted from reference⁴*

As the Pd/Au bimetallic sample is annealed up to temperatures of 750 K, the average size of the overlayer islands becomes larger (Figures 3.3.1.6 - 3.3.1.8).

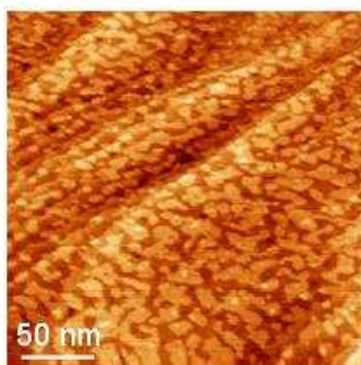


Figure 3.3.1.6 - STM image (250 nm x 250 nm) following the deposition of 1-2 ML of Au on Pd{111} at 300K and subsequently anneal to 570K

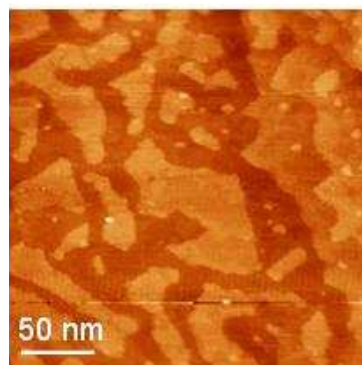


Figure 3.3.1.7 - STM image (250 nm x 250 nm) following the deposition of 1-2 ML of Au on Pd{111} at 300K and subsequently anneal to 650K

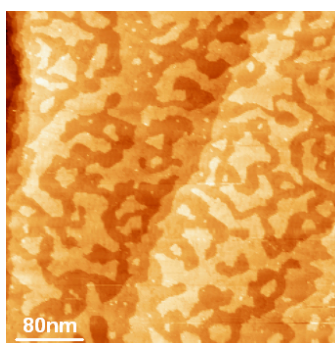


Figure 3.3.1.8 - STM image (400 nm x 400 nm) following the deposition of 1-2 ML of Au on Pd{111} at 300K and subsequently anneal to 730K

The surface begins to flatten when annealed in the range 750 K – 900 K and the terraces become larger and less jagged at their edges (Figures 3.3.1.9 - 3.3.1.11)

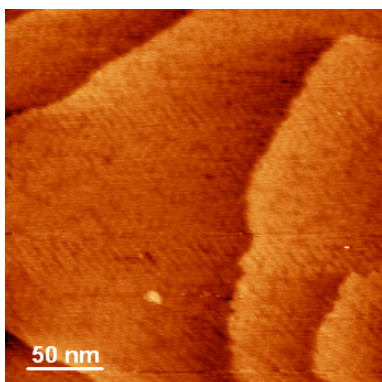


Figure 3.3.1.9 - STM image (250 nm x 250 nm) following the deposition of 1-2 ML of Au on Pd{111} at 300K and subsequently anneal to 775K

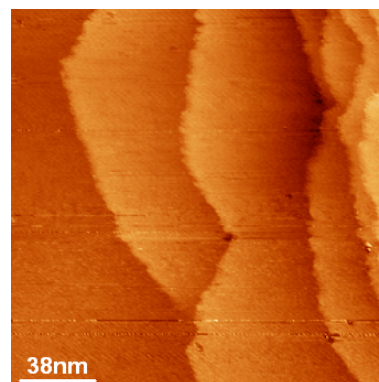


Figure 3.3.1.10 - STM image (190 nm x 190 nm) following the deposition of 1-2 ML of Au on Pd{111} at 300K and subsequently anneal to 820K

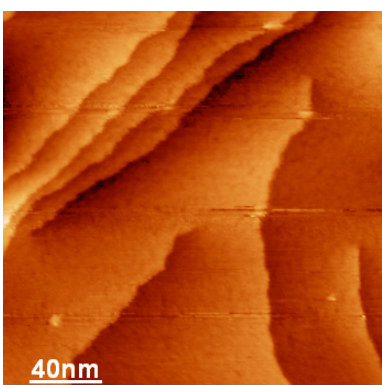


Figure 3.3.1.11 - STM image (220 nm x 220 nm) following the deposition of 1-2 ML of Au on Pd{111} at 300K and subsequently anneal to 900K

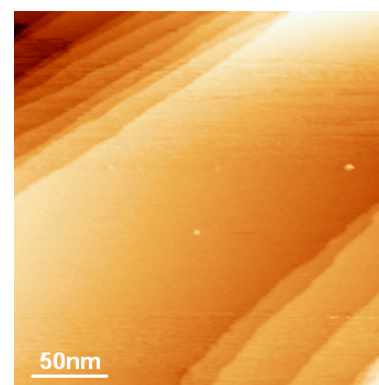


Figure 3.3.1.12 - STM image (250 nm x 250 nm) following the deposition of 1-2 ML of Au on Pd{111} at 300K and subsequently anneal to 950K

By the highest pre-annealing treatment of 950 K, the surface essentially appears flat (Figure 3.3.1.12) exhibiting extensive flat terraces separated by well-defined steps.

This changing morphology can roughly be grouped into two regions. “Low-T” pre-annealing temperatures (<750 K) show distinct Au islands growing on the Pd{111} crystal surface whereas the “High-T” pre-annealing temperatures (>825K) show that the Au overlayer is being flattened to more closely resemble the clean Pd{111}

surface. These two different regimes have different MEIS characteristics, as can be seen in the later discussions in this chapter.

3.3.2 Surface and Sub-Surface Composition

MEIS can be used to probe the surface and sub-surface regions of a bimetallic such as Pd/Au in a bid to determine the composition and also the structure of these areas. 3-4 ML Au was deposited on a clean Pd{111} and analysed using the MEIS facility at CCLRC Daresbury.

The energy loss of the helium ion in the “billiard-ball” like collision with Pd and Au target atoms is readily calculated enabling the assignment of the Pd and Au related peaks. Figures 3.3.2.1 – 3.3.2.3 show plots of scattered ion intensity versus ion energy for the 1-, 2- and 3-layer geometries as a function of pre-annealing temperature.

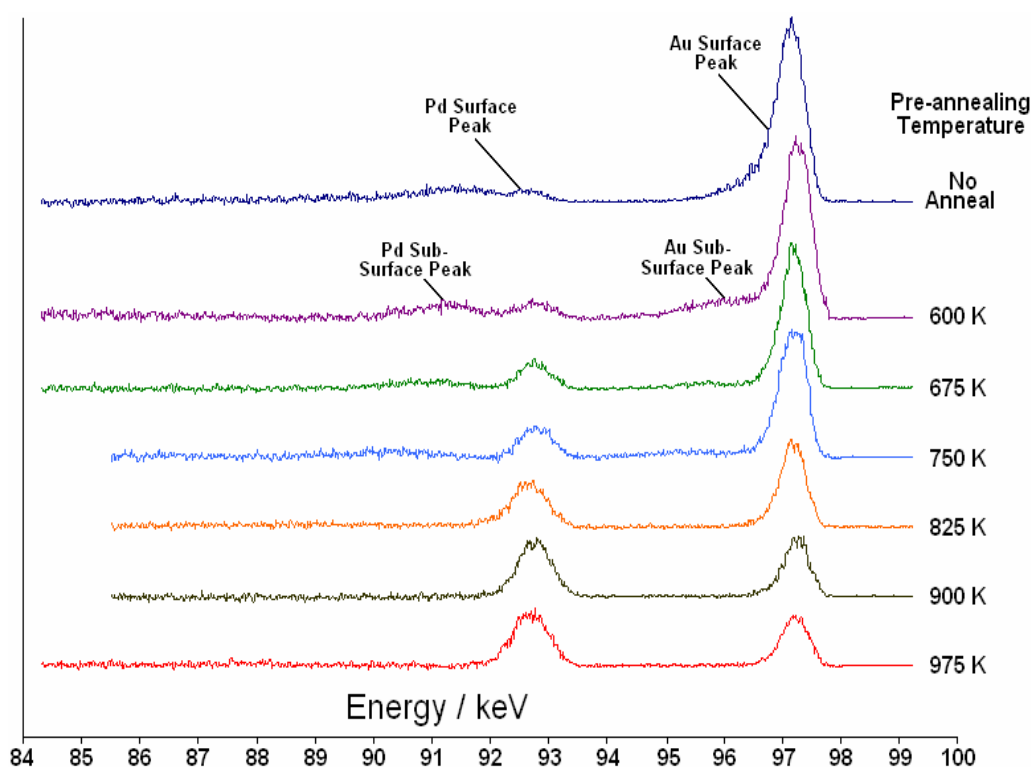


Fig 3.3.2.1 – MEIS Plot of Intensity vs. Energy as a function of annealing temperature. Cut was taken along the (110) out channel which corresponds to the 1-Layer specific alignment.

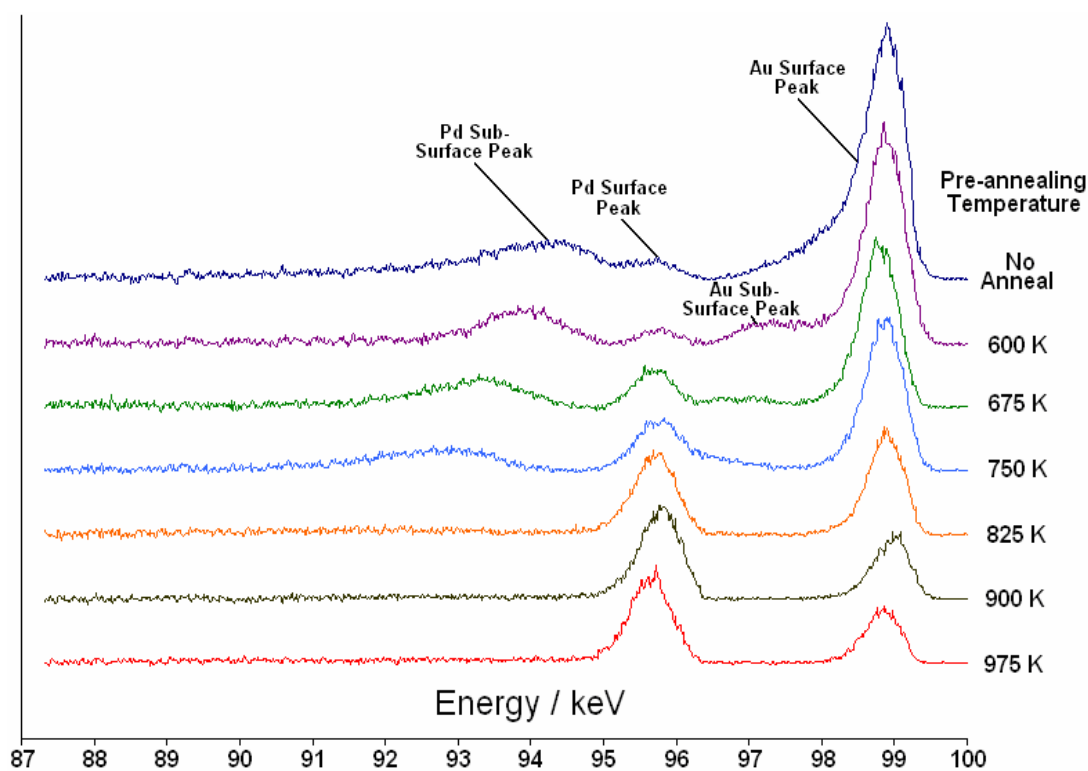


Fig 3.3.2.2 – MEIS Plot of Intensity vs. Energy as a function of annealing temperature. Cut was taken along the $(22\bar{1})$ out channel which corresponds to the 2-Layer specific alignment.

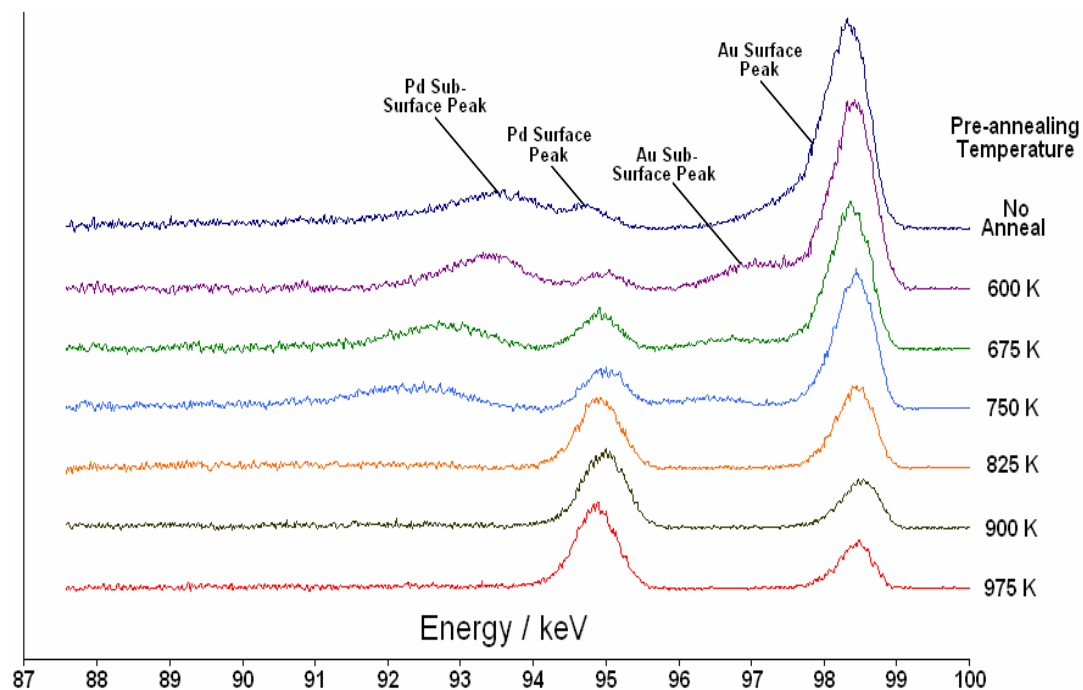


Fig 3.3.2.3 – MEIS Plot of Intensity vs. Energy as a function of annealing temperature. Cut was taken along the $(33\bar{2})$ out channel which corresponds to the 3-Layer specific alignment.

It can be seen that following deposition of 3-4 ML Au on Pd{111}, the Au peak is the dominant feature in the spectrum. As the surface is annealed to higher temperatures,

the Pd peak increases intensity while the Au peak becomes smaller. The amount of Au in the top two layers (by atom %) is shown in Figs 3.3.2.4a and 3.3.2.4b.

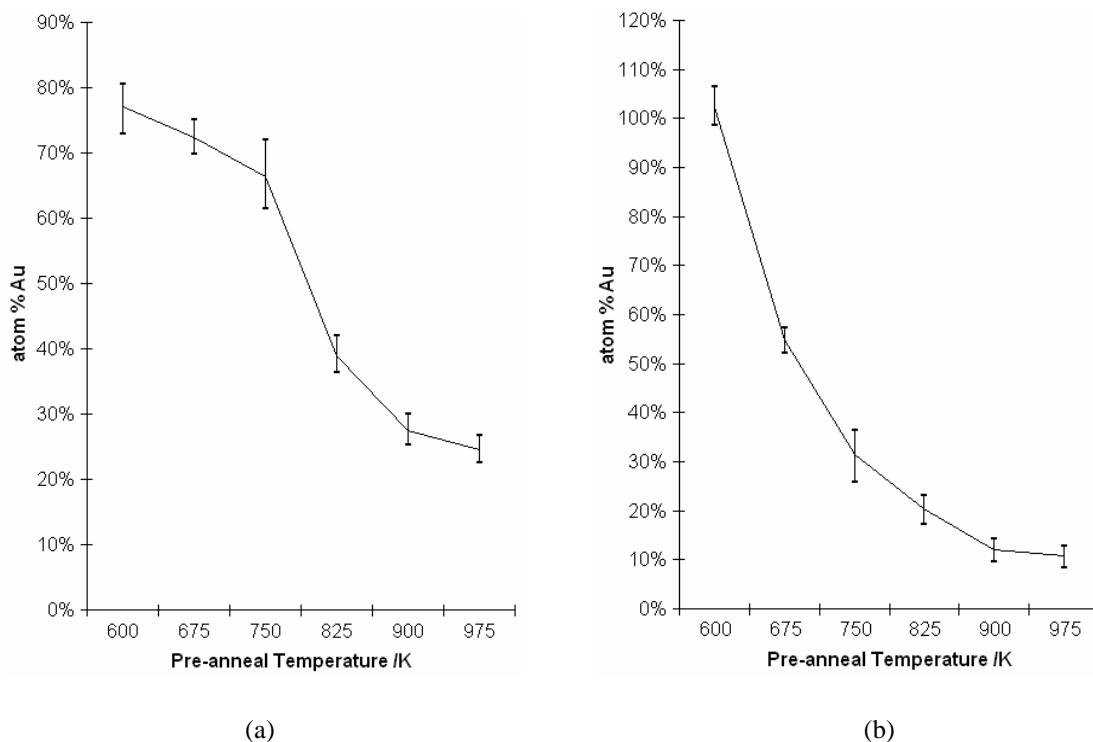


Fig 3.3.2.4 - Concentration of Au (in atom %) of (a) the top layer and (b) the second layer of the bimetallic surface as a function of pre-annealing temperature. Error bars indicate extreme values of calculation and the line indicates the mid-point at each temperature

In addition to the two surface peaks, there are broader peaks on the low energy side of the surface peaks for samples annealed up to and including 750 K. We can assign these features to sub-surface Au and Pd atoms.

It is interesting to note that there is the largest change in atom %Au in the top layer between the anneal temperatures of 750 K and 825K and this corresponds to the changeover between the four-peak system at low T (<750K) and the two-peak system at high T (>825K) in the Intensity vs. Energy plots shown in Figures 3.3.2.1 – 3.3.2.3.

These two regimes also exhibit different surface morphologies as has been discussed previously in Chapter 3.3.1.

The raw data shows a difference across the two regions as well;

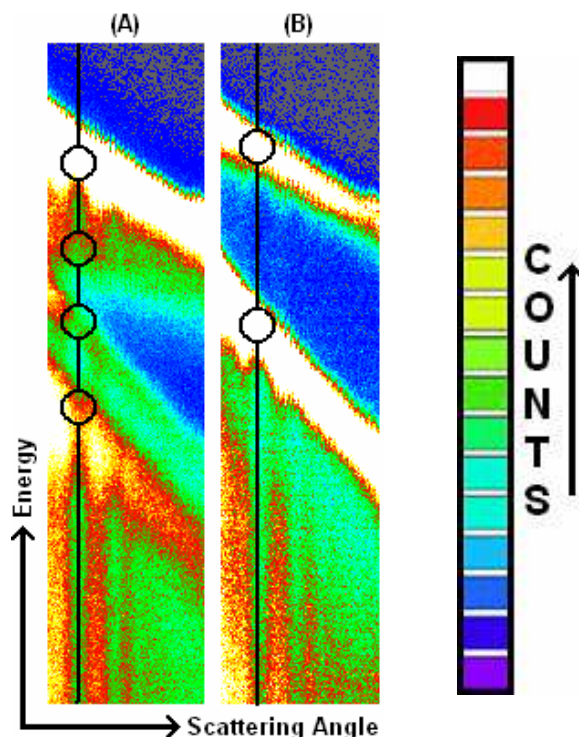


Fig 3.3.2.5 – Raw MEIS data showing (A) a Pd{111}/Au sample pre-annealed to 675 K and (B) a Pd{111}/Au sample pre-annealed to 975 K. The line is the position of the Intensity vs. Energy “cut” which is taken down the centre of (in this case) the 2-layer channel and the circles indicate the positions of higher intensity which will show up as peaks on the Intensity vs. Energy plot.

The two different regimes will be known as the “Pd-rich” and “Au-rich” regimes corresponding to pre-anneal temperatures >825 K and <750 K respectively and can be dealt with separately;

At higher pre-annealing temperatures (>825 K) there are two peaks in the Intensity versus Ion Energy spectra (Figure 3.3.2.6 overleaf) corresponding to surface Pd and surface Au in all three layer alignments (1, 2 and 3 layers).

There is an obvious decrease in the %Au in top two layers as anneal temperature is increased from 825 K to 975 K due to the surface and sub-surface becoming more and more Pd rich (as can be seen in Figure 3.3.2.4 above)

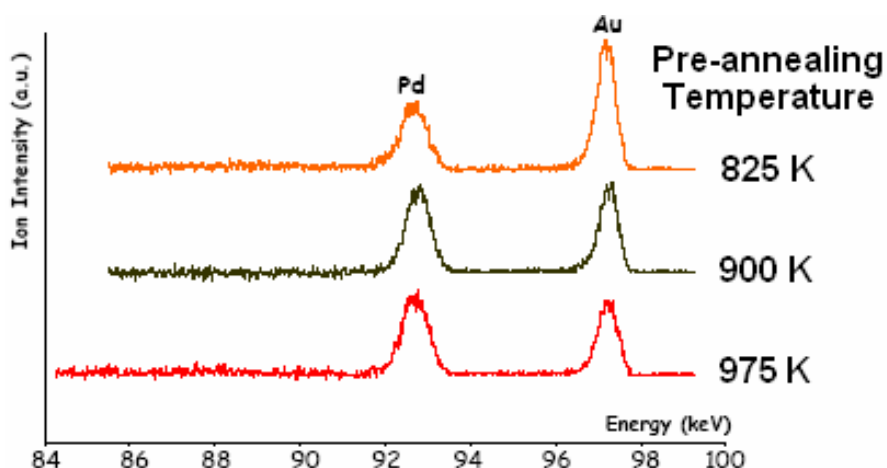


Fig 3.3.2.6 - MEIS Plot of Intensity vs. Energy as a function of annealing temperature for the high pre-annealing temperature (<750 K) range. The cuts were taken along the (110) out channel which corresponds to the 1-Layer specific alignment.

At lower pre-annealing temperatures (<750 K) there are four peaks in the plots of intensity v energy (Figure 3.3.2.7), two of which can be assigned to the Pd surface and Au surface as with the higher pre-annealing temperatures. As previously discussed, the other two peaks can be assigned to Pd and Au subsurface atoms in a sub-surface Pd/Au alloy sitting below 1 or 2 crystalline Au layers. Since the sub-surface peaks are visible even using double alignment geometries, the lattice parameter of the alloy must be different to bulk Pd{111}.

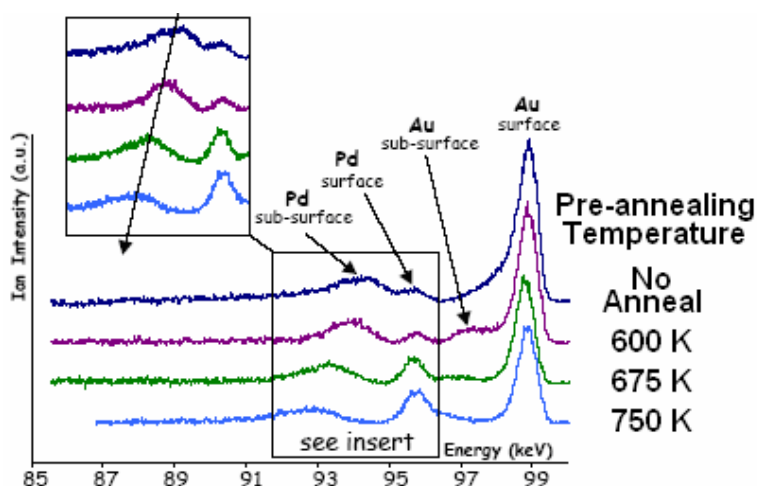


Fig 3.3.2.7 - MEIS Plot of Intensity vs. Energy as a function of annealing temperature for the low pre-annealing temperature (<750 K) range. The cuts were taken along the (22 $\bar{1}$) out channel which corresponds to the 2-Layer specific alignment as this shows the effect best.

The trend line shown on the inset shows a shift in the position and shape of the Pd sub-surface peak. The trend indicated is due to Au diffusing down into the bulk as pre-annealing temperature is increased and this is shown by the increase in the energy range of the sub-surface peak (the alloy is present in a greater number of sub-surface layers).

Measurement of the width of the sub-surface peak (in keV) gives an indication of the thickness of the alloy. This value is the difference in energy loss between ions scattered at the top of the alloy and those at the bottom. Using the SRIM code⁵, the stopping power of 100 keV helium ions in Au is 284 eV/nm and in Pd is 384 eV/nm.

Taking into account the difference in energy between the surface and sub-surface features, one may attempt to ascertain the depth of the sub-surface features.

Assuming in the low temperature case that the buried Au and Pd atoms giving rise to these features are covered in a mixture of 3-4 ML Au and the remainder Pd, it is clear that one cannot use either the pure Au or pure Pd stopping power to estimate depth. Hence choosing an intermediate value of the stopping power of 330 eV/nm, the depth of the Pd feature can be estimated to be ~1.5-3.0nm below the surface or ~ 7-13 layers.

Interestingly, the depth of the Au sub-surface feature is systematically shallower (by a factor of approximately 1.5 to 2.0) than the Pd related feature. In these estimates, we have assumed that the inelastic energy loss is directly proportional to the path length of the ion beam within the sample and does not depend on the scattering geometry.

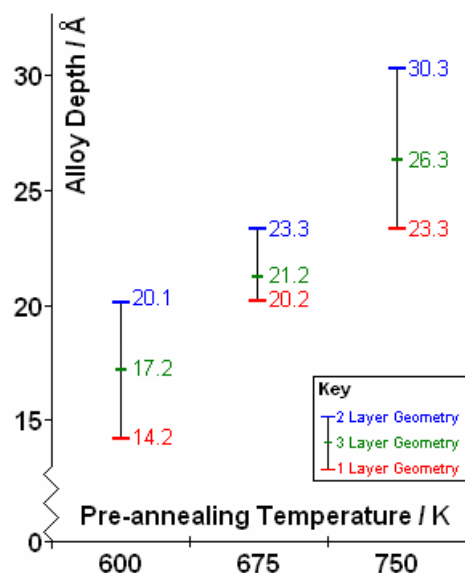


Fig 3.3.2.8 – Depth of the Pd sub-surface feature as a function of pre-annealing temperature calculated from the position of the Pd sub-surface peak in the 1-, 2- and 3-layer alignment Intensity vs. Energy MEIS plots. There are no values for High T anneals (>825K) as there are no sub-surface peaks in the MEIS spectra.

However, it has recently been shown that the stopping power varies dramatically from the values given by the SRIM code when low impact parameter collisions are involved (i.e. the very type of collisions being utilized in double alignment geometry experiments).⁶ Hence the estimate of the depth of the sub-surface features may be inaccurate.

In an attempt to gain some insight into the origin of this sub-surface peak, we took MEIS data in pseudo random incidence geometries. In this case, the sample was aligned along the 3-layer incident geometry (35.3° from the surface normal), then rotated by 7° away from this geometry (i.e. to 42.3° from the surface normal).

In this case, there should be little shadowing of near surface atoms (or blocking provided that the outgoing direction is selected carefully). The pseudo random

incidence geometry MEIS data are presented in Figure 3.3.2.9 as a function of pre-annealing temperature.

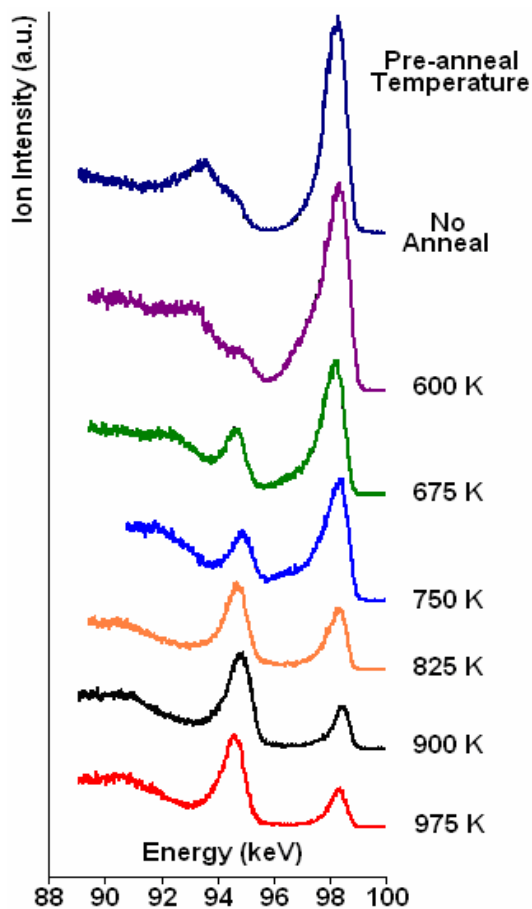


Fig 3.3.2.9 - MEIS Plot of Intensity vs. Energy as a function of annealing temperature. The cuts were taken along a pseudo random incidence geometry

The Au related peak now appears as a single broad feature rather than a double feature. This indicates that the Au composition gradually decays into the subsurface. On annealing to 600 K, the peak becomes broader and annealing to 675 and 750 K results in a loss of intensity in the surface peak. The surface peak continues to decrease in intensity at higher pre-annealing temperature, but now the peak becomes much less broad.

The next step is to estimate the composition of the sub-surface as a function of depth in the 0-10 layer range to determine whether there is a threshold sub-surface Au

composition above which the subsurface peak is visible in the 1-, 2- and 3-layer aligned geometries. To achieve this aim, we needed to make several assumptions as to the peak shape and peak width of the contribution to each layer to the overall signal.

The shape of a peak corresponding to 1 layer of a material is known to be asymmetric. This is caused by the existence of loss features related to electronic excitation within the target atoms induced by the impinging ions. These electronic losses are manifested by a tail on the low energy side of the surface peak. The peak shape has been accurately calculated recently by a combination of experiment and theory by Woodruff and co-workers.⁷

In our case, we will approximate the shape of the peak due to an individual layer of material by an asymmetric Gaussian function. The FWHM of the peak can be estimated to be ~0.64 kV by measuring the peak width of the clean Pd surface peak in a 1-layer geometry. The peak due to the second layer is offset by 0.189 kV from the surface peak.

This is calculated using the stopping power for Au derived from the SRIM code for an incident angle of 42.3° from the surface normal and a scattering angle of 90° . (The value of the stopping power should be more accurate as we are using a pseudo-random geometry).

In addition, we constrain the maximum area of any of the peaks to a value corresponding to 1 ML of Au. (This value is achieved via calibration against the peak area of a Pd peak in a 1-layer geometry with appropriate normalisation to the scattering cross-section). These data are shown in Figures 3.3.2.10-3.3.2.14.

In the unannealed 3-4 ML Au on Pd{111} case, we find that the top two layers are almost exclusively Au but that the remainder of the Au is distributed down to ~10 layers. Since we know from STM that the surface is not perfectly flat, one interpretation of the depth profile is that the Au overlayer is of a variable thickness from 0-10 ML with an average thickness of 3-4 layers. Alternatively, one could conclude that from the 3rd layer onwards Au is present in the form of a Pd/Au alloy of varying composition. In reality, it is probable that a combination of these effects is occurring.

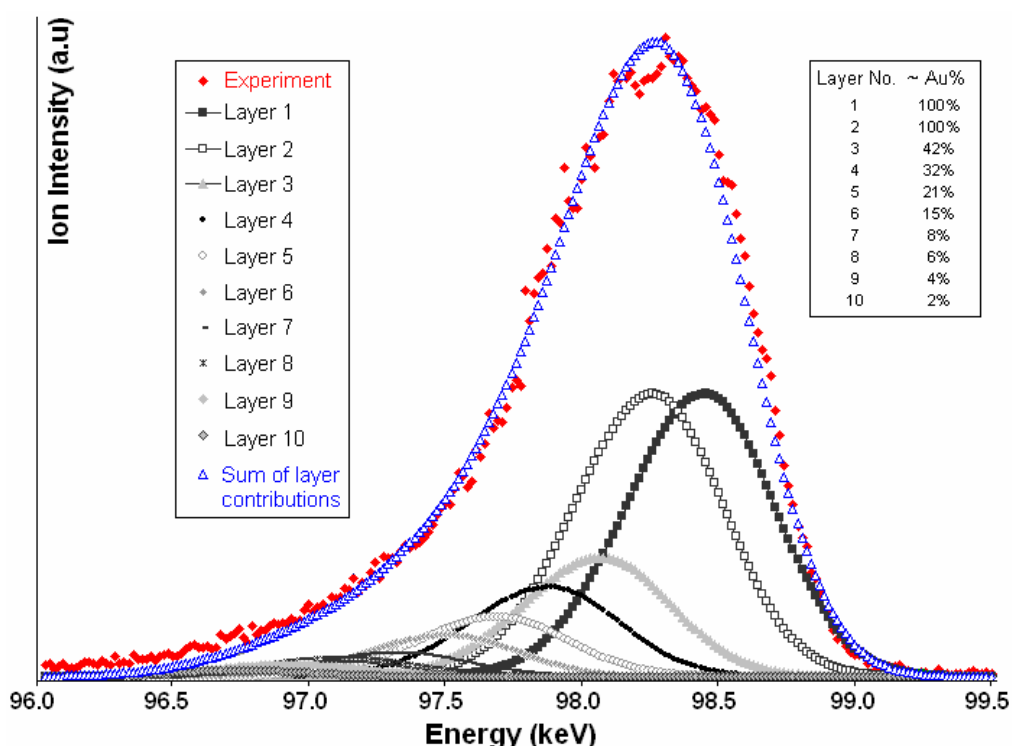


Fig 3.3.2.10 – Plot of ion intensity v ion energy for a ~3 ML Au film on Pd{111} (unannealed) . Only the region of the MEIS spectrum corresponding to ions scattered from Au atoms is displayed. The spectrum is fitted to 10 asymmetric Gaussian peaks corresponding to the contribution from Au in each of the top 10 layers of the surface.

Annealing the sample to 600 K leads to a significant increase in the amount of Au in the sub-surface layers. This is indicative of the Au diffusing down into the lower layers. There is a subtle bulge in profile which can be assigned to a 20% Au concentration in the tenth layer.

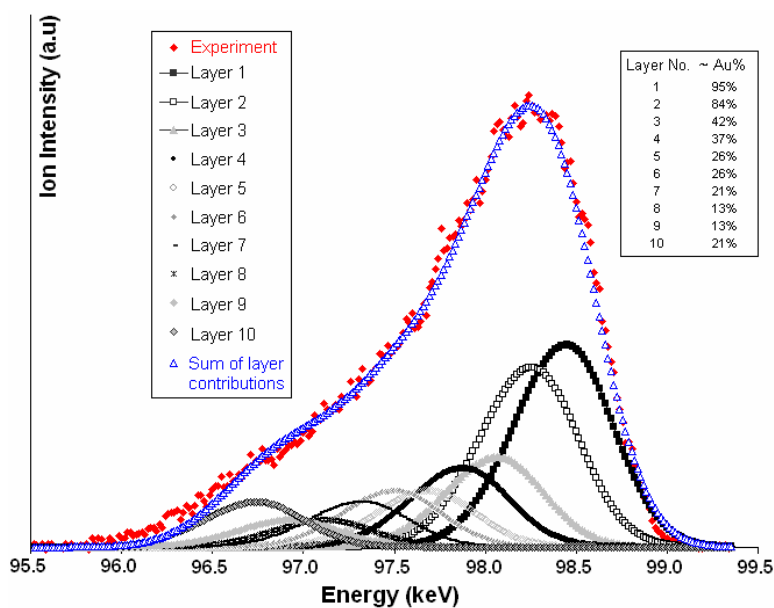


Fig 3.3.2.11 – Plot of ion intensity v ion energy for a ~3 ML Au film on Pd{111} annealed to 600 K . Only the region of the MEIS spectrum corresponding to ions scattered from Au atoms is displayed. The spectrum is fitted to 10 asymmetric Gaussian peaks corresponding to the contribution from Au in each of the top 10 layers of the surface.

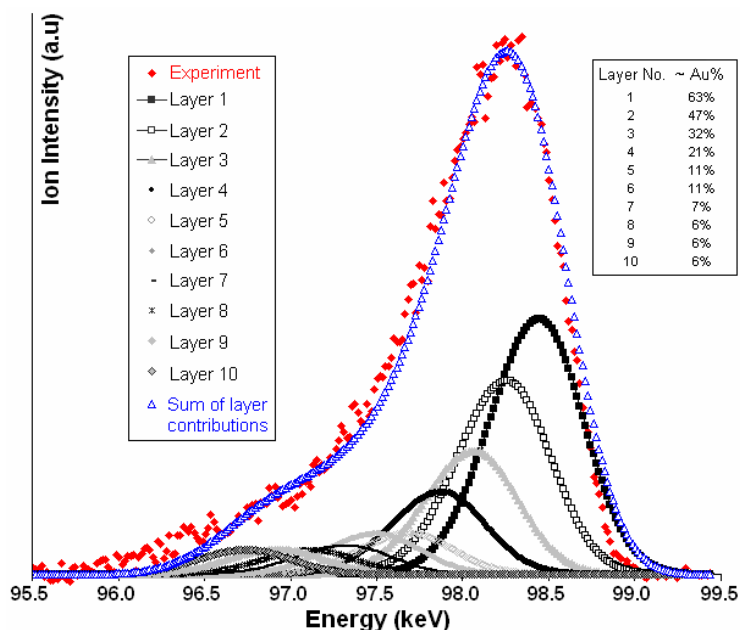


Fig 3.3.2.12 – Plot of ion intensity v ion energy for a ~3 ML Au film on Pd{111} annealed to 675 K . Only the region of the MEIS spectrum corresponding to ions scattered from Au atoms is displayed. The spectrum is fitted to 10 asymmetric Gaussian peaks corresponding to the contribution from Au in each of the top 10 layers of the surface.

In both the 675 K and 750 K experiments there is still a significant (>10%) Au concentration down to the 6th/7th layers. In addition to this, the top couple of layers still contain over 40% of Au.

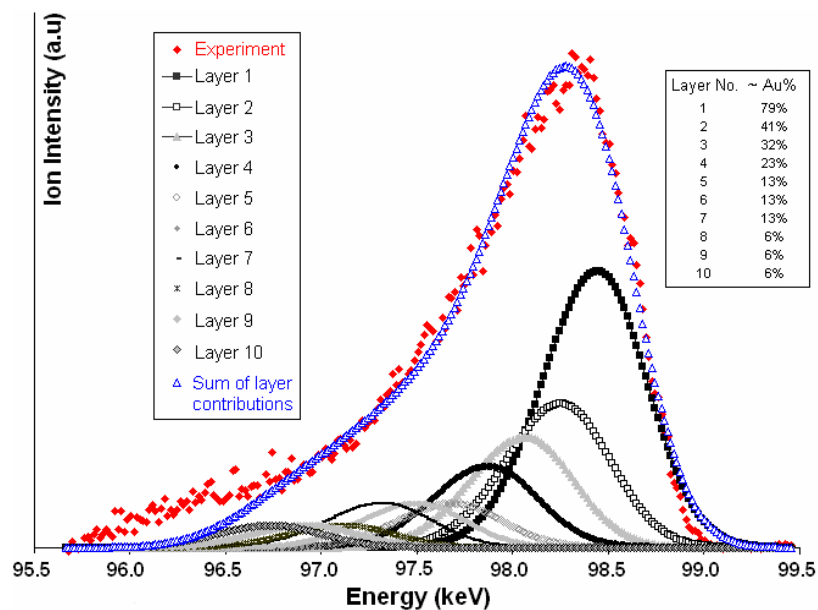


Fig 3.3.2.13 – Plot of ion intensity v ion energy for a ~3 ML Au film on Pd{111} annealed to 750 K . Only the region of the MEIS spectrum corresponding to ions scattered from Au atoms is displayed. The spectrum is fitted to 10 asymmetric Gaussian peaks corresponding to the contribution from Au in each of the top 10 layers of the surface.

In the 750 K experiment it should also be noted that the curve fit isn't very good at the low energy end. This is indicative of there being significant Au at >10 layers deep.

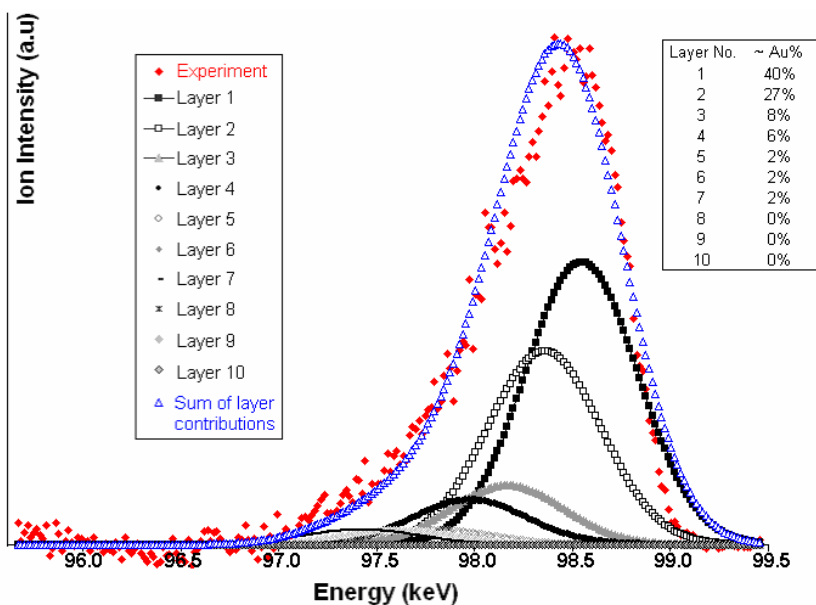


Fig 3.3.2.14 – Plot of ion intensity v ion energy for a ~3 ML Au film on Pd{111} annealed to 825 K . Only the region of the MEIS spectrum corresponding to ions scattered from Au atoms is displayed. The spectrum is fitted to 10 asymmetric Gaussian peaks corresponding to the contribution from Au in each of the top 10 layers of the surface.

By the time we reach the 825 K pre-annealing temperature, the curve-fit essentially shows that all the significant Au is in the top and second layers and there is no appreciable Au in any of the lower sub-surface layers.

In the 900 K and 975 K experiments, there is no sub-surface peak and it is estimated that these cases will mimic the 825 K results but with even less Au visible in the lower sub-surface layers.

It is worth noting that the analysis is semi-quantitative since we are using an approximate figure for the stopping power of He^+ through a bimetallic film of unknown composition.

3.3.3 Surface and Sub-Surface Structure

MEIS spectra can also be used to determine the structure of surface and sub-surface regions to detect any subtle changes in structure across a range of experiments. The theory relating to the use of MEIS for structure determination can be found in Chapter 2.5.4 and will not be discussed here.

It is possible to garner both structural and compositional data from the same MEIS spectra and hence the same experiments used in 3.3.2 were used for the structural work. By taking a “cut” across a specific area of the raw data tile (corresponding to the position of the Pd peak, the position of the Au peak or the top of the Pd bulk area) graphs of Intensity versus Scattering Angle can be produced for Au Surface, Pd Surface and Pd Bulk as a function of temperature. These are shown in Figures 3.3.3.1 – 3.3.3.3 overleaf.

(Note that the three labelled blocking dips **A**, **B** and **C** correspond to the scattering angles 84.2° , 90.0° and 109.4° respectively. These are the expected blocking dips corresponding to the 2-layer, 3-layer and 1-layer specific geometries as shown in Fig. 3.2.1 previously.)

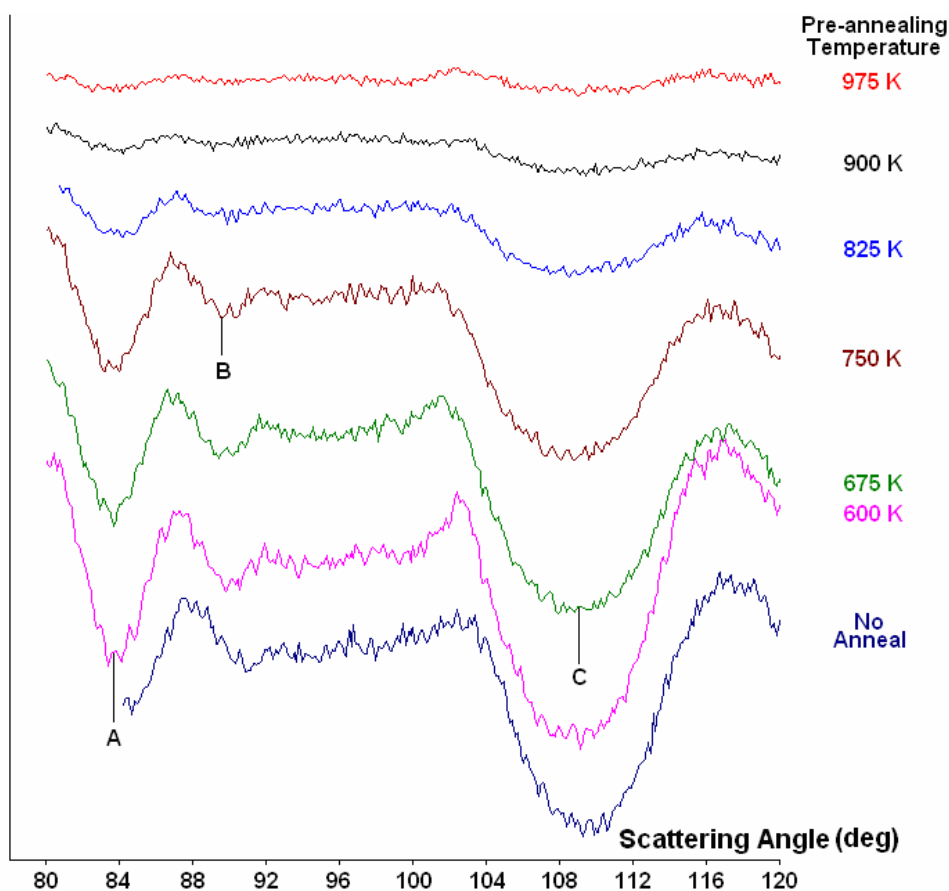


Fig 3.3.3.1 – Scattering Angle vs. Intensity plot taken from the Au Surface area of the MEIS spectra as a function of pre-annealing temperature.

In the Au surface cuts, the intensity of the blocking features drops as the pre-annealing temperature increases due to the fact that the amount of Au in the top layers diminishes and therefore the number of counts in the Au surface peak drops.

There is a slight shift in peak positions as we go from unannealed to the 600 K pre-anneal which may be due to the Au overlayer flattening slightly and shifting into a more Pd-like lattice constant compared to the post deposition value. By 800 K, there are essentially no blocking features in the Au which is further evidence that the vast majority of the detectable Au remaining in is at the surface.

Looking at the Pd surface data, there is no appreciable change in peak positions as the pre-annealing temperature increases and there is only a very slight deepening in the 2-layer channel at 84.2° when the anneal temperature is in the “high-T” region (>825 K). The 3-layer channel becomes much better defined as we increase the pre-annealing temperature.

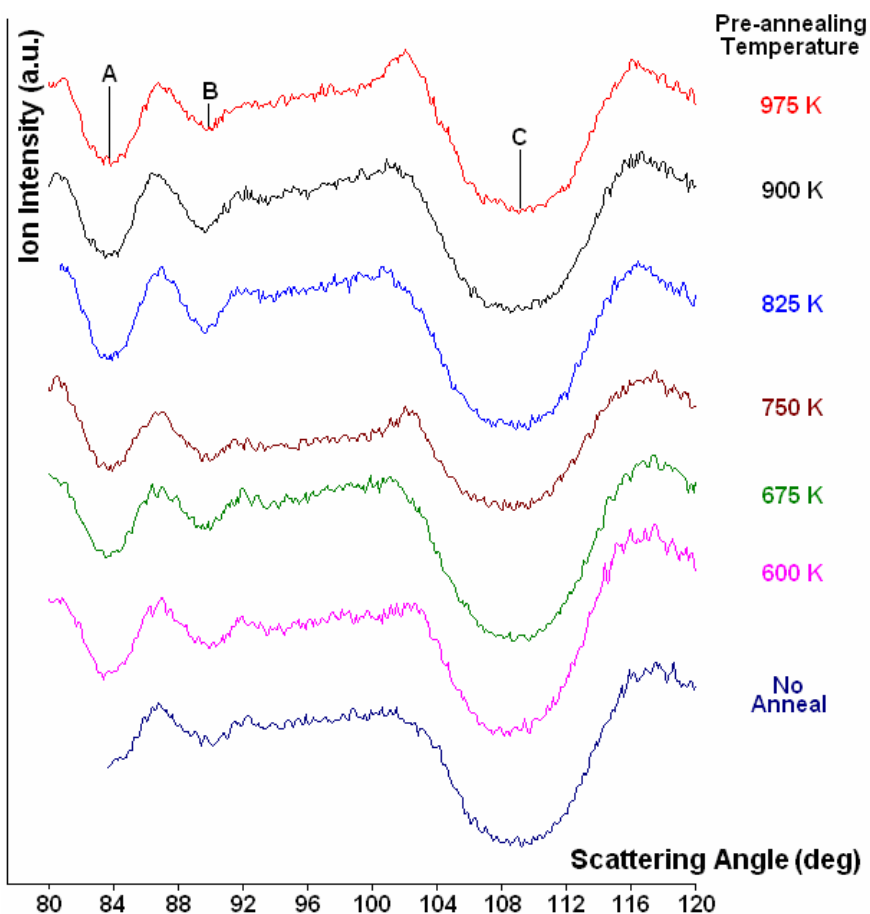


Fig 3.3.3.2 – Scattering Angle vs. Intensity plot taken from the Pd Surface area of the MEIS spectra as a function of pre-annealing temperature

It should be noted that, unlike the Au case, there is no significant change in the intensity of the blocking features for each trace indicating that the variation in Pd concentration in the near surface region is relatively small. There is a minor change in the 1-layer peak as it goes from being slightly asymmetric in the Au-rich “lower -T” region to being almost completely symmetric as the anneal temperature reaches 900 K.

There is no shift in the positions of the peaks as the anneal temperature increases in the Pd bulk case. In this case there is a slight shallowing of the blocking dips rather than a deepening as we saw in the Pd surface scenario.

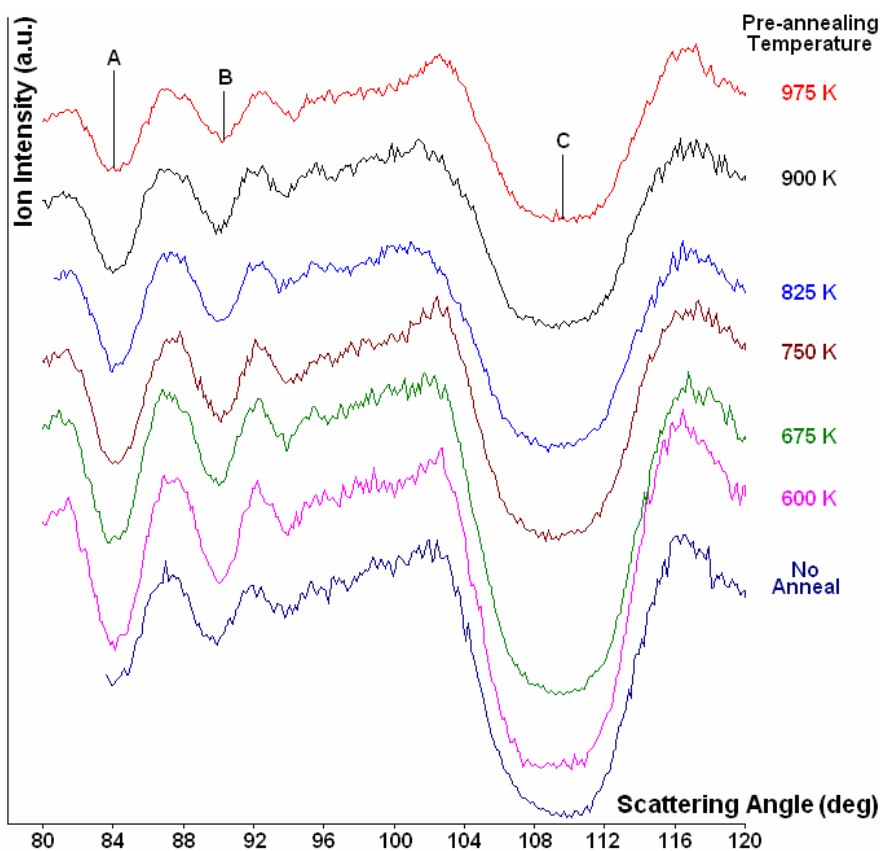


Fig 3.3.3.3 – Scattering Angle vs. Intensity plot taken from the Pd Bulk area of the MEIS spectra as a function of pre-annealing temperature

The 1-layer channel seems to get shallower by a much larger amount relative to the 2- and 3-layer channels. There is no real change in the shape of the peaks as a function of anneal temperature. It was expected that the Pd Bulk trace would be unchanged as the cut is taken at a depth where it is unlikely that there would be any Au present to influence the blocking curves. However, the diffusion of the Au into the bulk means reported earlier in the chapter means that there will be slight differences as the pre-anneal temperature varies.

By comparing the three different Intensity versus Angle plots for each pre-anneal temperature it may be possible to detect subtle differences in the blocking curves which would indicate that the Pd and Au atoms are not quite in the same lattice arrangement.

Figures 3.3.3.4 - 3.3.3.7 show the stacked Scattering Angle vs. Ion Intensity plots for all three regimes at each individual pre-anneal temperature.

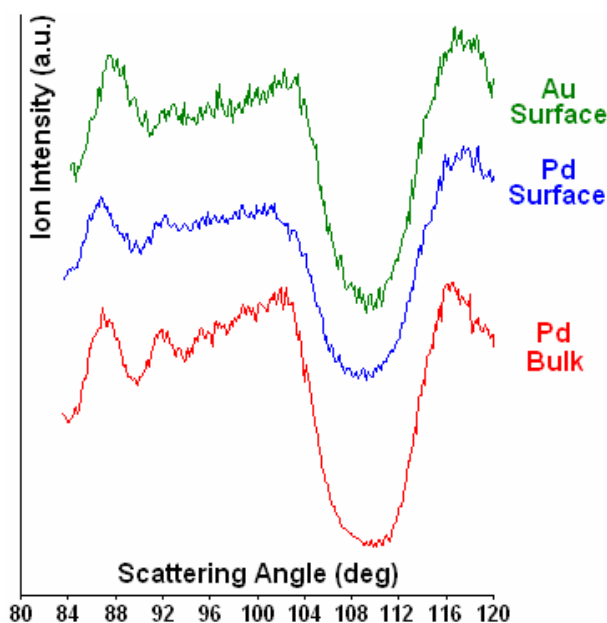


Fig 3.3.3.4 – MEIS plot of Scattering Energy vs. Ion Intensity for the unannealed Pd{111}/~2ML Au surface

In the unannealed case the 2-layer blocking dip which is expected at 84.2° isn't properly visible due to a slight problem with the analyser position at Daresbury. The 3-layer dip however shows a subtle difference in position between the Au surface and Pd surface which is indicative of the two metals being in slightly different lattices.

As we pre-anneal to 600 K, the Pd surface shows an asymmetric blocking dip at 109.4° corresponding to the 1-layer geometry. The Au surface also has a slightly asymmetric shape at the 1-layer case, although the asymmetry is mirrored to that of

the Pd case in the 675 K pre-anneal situation. The 3-layer blocking dip in the Pd surface is becoming slightly better defined as the annealing temperature is being increased.

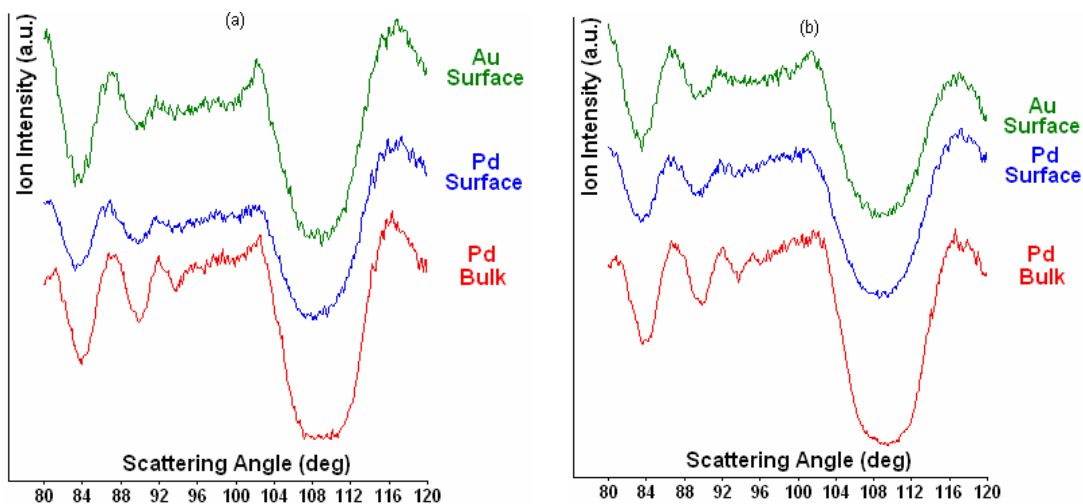


Fig 3.3.3.5 – MEIS plot of Scattering Energy vs. Ion Intensity for a Pd{111}/~2ML Au surface pre-annealed to (a) 600 K and (b) 675 K

The 750 K data is very similar to the 675 K but raising the pre-annealing temperature to 825 K shows a distinctive change in the blocking curves in both the Pd surface and Au surface case. The Pd surface blocking curve is beginning to very closely resemble the Pd bulk one, in shape, position and depth of peak whilst the Au surface peak has lost intensity, although the peaks are still evident in the expected places.

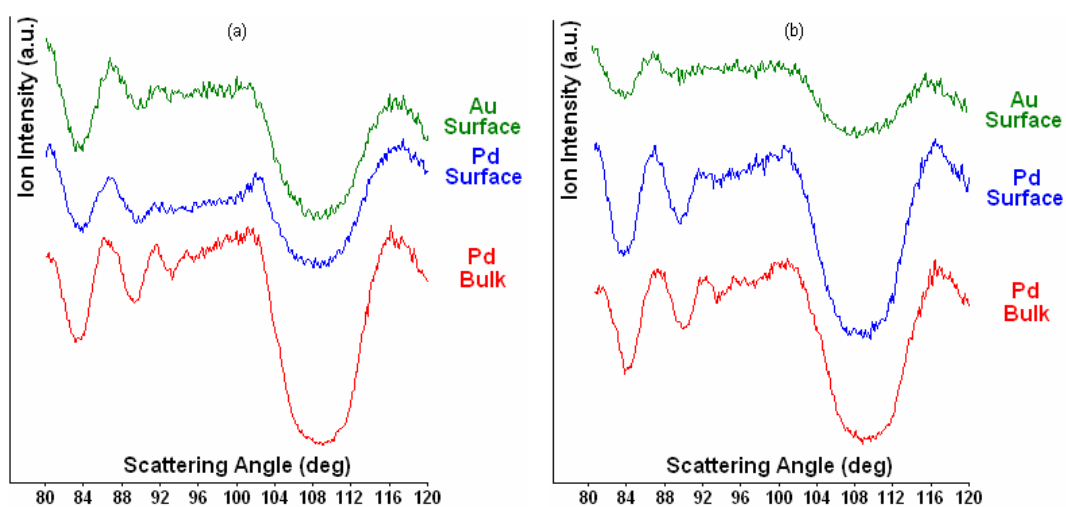


Fig 3.3.3.6 – MEIS plot of Scattering Energy vs. Ion Intensity for a Pd{111}/~2ML Au surface pre-annealed to (a) 750 K and (b) 825 K.

This effect is even more obvious as the pre-annealing temperature reaches 900 K and above. The ion intensity resulting from the Au surface has all but disappeared and the Pd surface and Pd bulk are very similar.

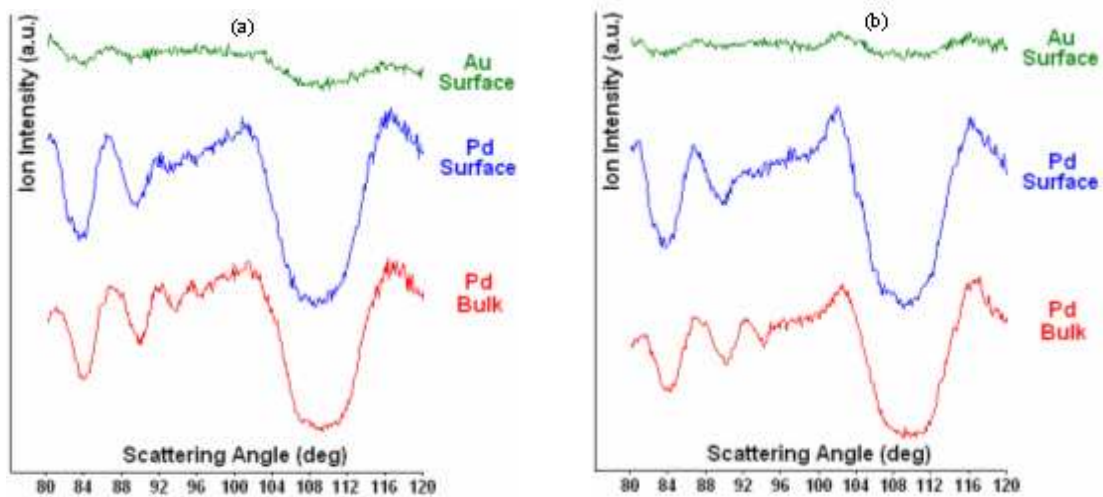


Fig 3.3.3.7 – MEIS plot of Scattering Energy vs. Ion Intensity for a Pd{111}/~2ML Au surface pre-annealed to (a) 900 K and (b) 975 K.

3.4 Discussion

Baddeley *et al.*⁸ carried out work on the coupling of acetylene to benzene on Au/Pd{111} in the early 1990s and they concluded that ordered surface alloys were not found, instead a range of disordered Pd/Au alloys with continuously varying compositions are generated. They found that the Au overlayers began to intermix with Pd substrate at 200 K higher than for the inverse Pd/Au{111} system (i.e. about 600 K). Another difference in the two systems came when comparing the idea of composition stability. For Pd/Au{111}, the system forms a stable, crystalline surface alloy of composition Pd₂Au in the range 450-700 K.^{9,10} In the Au/Pd{111} case however there was no temperature regime over which there is a surface of constant composition. The difference between these has been put down to the different mobilities of Au in Pd¹¹ and Pd in Au.¹²

Our STM studies of the surface morphology in the Au on Pd{111} system have identified numerous characteristics. Initial growth has been found to be dendritic and nucleated at the step-edges of the Pd{111} surface. Second layer growth is found to begin before the completion of the first layer in what could be described as the *Volmer-Weber* growth mode (second layer growth precedes completion of first layer growth), although the growth mode is open for debate. Using the old surface science tools such as Auger to characterise the growth mode would give either a *Franck-van der Merwe* (layer by layer) or *Stranski-Krastanov* (monolayer followed by island) mode. With STM you can see some second layer growth but largely speaking, the layers are complete. *Volmer-Weber* could be interpreted as a very 3-D type growth where there is lots of substrate still visible even after 10 ML deposition which is clearly not the case in this scenario.

When 1-2 ML of Au have been deposited, we observed a Moiré structure with a periodicity of ~8nm, indicating that the Au overlayer does not grow exactly on top of the Pd{111} at multi-layer coverages.

Moiré structures are essentially caused by a mismatch between two lattices with the overlayer lattice going in and out of registry with the substrate periodically (an example of this is shown in Figure 3.3.1.5 in Chapter 3.3).

Using LEED, Baddeley *et al.* reported that the surface lattice parameter for a 4 ML Au film deposited at 300 K is 4.8% larger than that of Pd{111} (bulk nearest neighbour distance of 2.75 Å) and corresponds exactly to the value for Au{111}, which has a bulk nearest neighbour distance of 2.88 Å. Annealing at 600 K resulted in a small contraction (corresponding to marginal intermixing), whilst there is a linear decrease from 600-900 K to a value just above the Pd{111} clean value. Between 900-1200 K there is a return to the Pd{111} surface value.

If Au grew with its own lattice structure (nearest neighbour spacing = 2.884 Å on Pd{111} as reported by Baddeley *et al.* then 20 Au atoms would take up 57.68 Å which is equivalent to 21 Pd atoms (57.75 Å). The fact that the periodicity in our experiment is larger than 57 Å implies either a slightly contracted Au-Au spacing (~2.85 Å) or that the Moiré structure arises due to the lattice mismatch between a Pd/Au near-surface alloy and Pd{111}. It may be that by the time 4ML of Au has been deposited, Au has reverted to growing in its own lattice parameter, hence the findings of Lambert and co-workers detailed above. The structural data also appears to indicate that Au is sitting in an arrangement which is close to the Pd{111} lattice structure but significantly different so as to cause a slight change in the blocking

curve. A 4.8% lattice mismatch would have only a subtle effect on the blocking curves of the Au and Pd whereas a bimetallic surface like Au/Ni{111} (which has a much larger ~16% mismatch) exhibits significant shifts in blocking features in the structural data as reported by Jones *et al* to the extent that the blocking features in the Au surface data are completely different from those seen in the Ni bulk data.

Despite the similarities between the surface Au, surface Pd and bulk Pd blocking spectra under all conditions, the intensity v energy plots in the low temperature annealing range display “sub-surface” peaks which can only be derived from a slight difference in structure between the surface and the bulk. In the unannealed case, one possible explanation for the appearance of subsurface peaks in the Intensity versus Energy plots is as follows. In the unannealed case, if the sample consisted of a flat pseudomorphic 3 ML Au film on Pd{111}, the intensity v energy plots in a 1-, 2- or 3- layer geometry should, to a first approximation reveal just a surface Au peak and no surface Pd peak. If the overlayer has a variable thickness (as evidenced by STM), but is still pseudomorphic, the appearance of the intensity v energy plots should still reveal narrow surface Au and surface Pd peaks with the Pd signal being derived from those areas of the surface where the Au coverage, θ , is in the range $0 < \theta < 3$ ML. Hence the appearance of subsurface Au and Pd features can only be explained by a mismatch between the surface and the sub-surface lattice parameters. In this case, if the surface structure is close to that of bulk Pd but expanded or contracted in the {111} plane and/or perpendicular to the {111} plane, then aligning the sample along a bulk crystallographic direction of Pd{111} (i.e. the 3-layer incidence geometry) will not quite correspond to a 3-layer incidence geometry of the overlayer. Hence not only will the overlayer atoms be visible in the $I v E$ plots, but a proportion of the underlying lattice will also be visible. Subsurface features will be observed both in the Au and Pd

signal (from incomplete shadowing/blocking of deeper lying Au and Pd atoms). If the overlayer has a variable thickness, then the energy at which subsurface features will be detected will also be variable since the pathlength of the beam in the lattice determines the inelastic energy loss. Figure 3.6.1 shows a schematic of this effect.

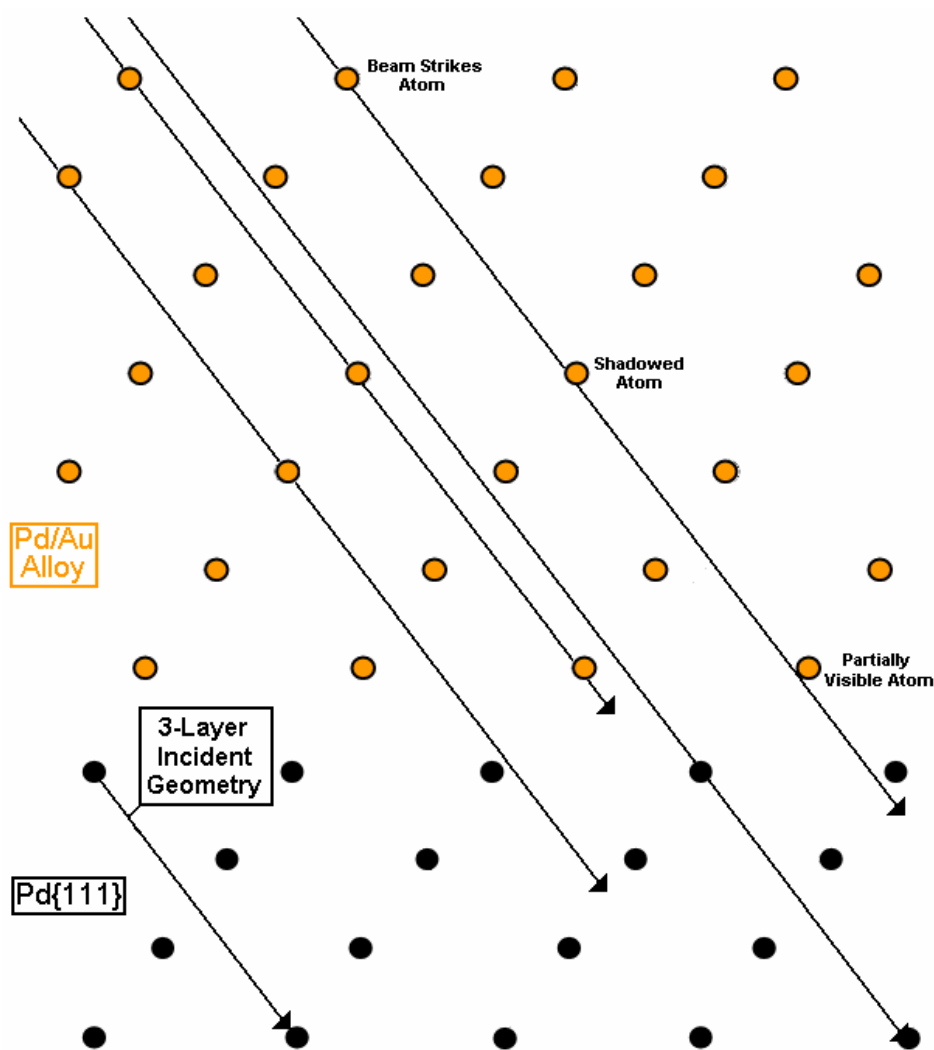


Figure 3.6.1 – Schematic showing an alloy overlayer with a 20% expansion relative to the Pd{111} crystal. The arrows indicate the path of the incoming beam and show that some lower lying atoms will be visible to the beam whilst some atoms nearer the surface will be shadowed.

We believe that the surface is covered by a Au film of a thickness between 0 and 10 ML. Our analysis of the random incidence geometry data (Figures 3.3.2.10 – 3.3.2.14) suggests that the Au concentration drops in a relatively smooth manner with increasing depth into the sample. By contrast, in the aligned experiments, there is a

clear dip in intensity between the surface feature and the “sub-surface” features in the intensity v energy plots. The top two layers in this case are close to pure Au and the composition tails off so there is about 20% Au by the time we reach the fifth layer.

Heating the sample to 600 K results in a loss of some of the Au in the top 2 layers which is replaced at the surface by Pd from the near-surface layers, while the composition of the layers beneath become more Au rich as a consequence. This is characterised by the drop in the intensity of the Au peak as we go to higher anneal temperatures in Figures 3.3.2.1 – 3.3.2.3. This can be interpreted in terms of alloying with Au beginning to diffuse into the sample and Pd beginning to diffuse to the surface. In this case, the composition of the 3rd to 6th layers beneath the surface ranges from Pd₆₅Au₃₅ to Pd₈₀Au₂₀. There is a clear bulge in the Au sub-surface region corresponding to 20% of an Au layer 10 layers down, indicating we are able to detect the diffusion of Au into the subsurface. There is a clear dip in the aligned intensity v energy plots in both the Au and Pd data. This is best explained by a relatively thick surface alloy with a slightly different lattice parameter to pure Pd. The alignment of the beam along the 3-layer incidence geometry of Pd{111} is also approximately a 3-layer incidence geometry of the bimetallic region. However, since the alignment on the alloy layers is not perfect, shadowing and blocking is progressively less effective the deeper the beam penetrates into the alloy. Hence there is a dip in intensity in the aligned data below the surface peaks which is not observed in the “pseudo-random” incidence data (compare Figures 3.3.2.7 and 3.3.2.9).

Annealing further to 675 K results in a further depletion of Au from the surface region, now the surface composition is ~Pd₄₀Au₆₀ while in layers 4 to 6, the composition is ~Pd₉₀Au₁₀. The composition of the near surface remains relatively

constant on further annealing to 750 K. At anneal temperatures <750 K the surface is rough and consists of islands of Au sat on top of the Pd and there is intermixing at the Au/Pd interface resulting in an alloy structure with a different lattice parameter to bulk Pd{111}. The fit of experimental to simulation at the low energy end isn't exact, possibly indicating that there is significant Au at depths of greater than 10 layers.

The fact that the subsurface feature shifts to lower energy with increasing annealing temperature can be explained by assuming that the lattice mismatch between Pd and a relatively Au rich alloy will be relatively large. Hence, the depth at which subsurface atoms become visible in the aligned experiments is relatively shallow. As the alloy becomes more Pd rich, the lattice becomes closer in structure to Pd{111} and the depth at which subsurface atoms become visible in the aligned experiments becomes significantly deeper.

Annealing to 825 K results in the top layer retaining a considerable $\sim 40\%$ Au composition. The fit essentially shows that all the significant Au is in the top two layers and the Au concentration in the sub-surface is essentially negligible. Under these conditions, the lattice parameter in the near surface region begins to match closely with the Pd lattice, hence no subsurface features are observed in MEIS and the morphology of the terraces in STM becomes essentially flat.

Hence the observation of the sub-surface features correlates with the situations where the top one or two layers are Au rich and when there is $>10\%$ Au in layers 5-10, i.e. where the lattice parameter of the sub-surface is significantly different to that of Pd. Pure Pd has a lattice parameter of 2.75 \AA whereas pure Au is 2.88 \AA . Assuming a linear variance in lattice parameter with composition, a 10% Au alloy would have a value of $\sim 2.76\text{-}2.77 \text{ \AA}$. It appears that this subtle change in lattice constant is enough

to make the sub-surface visible. Once the Au concentration in the sub-surface drops to ~2-3%, then the different in lattice parameter is insignificant which explains why the sub-surface alloy cannot be observed in the aligned experiments.

The curve fitting of the pseudo random data is in qualitative agreement with the measurements of alloy depth from the aligned data. In the 600 K data for example, there is a significant amount of Au (20%) in the 9th layer and the alloy depth is estimated to be between 1.4 and 2.0 nm, which corresponds to a very similar value. Also, looking at the 750 K data, the sub-surface peaks appears at about 2.6-3.0 nm below the surface (i.e. about 10-13ML) and the curve fitting suggests that there is significant Au at this depth.

In the lower temperature experiments the Au is located closer to the surface, and in larger quantities, hence the sub-surface feature in the aligned data appears at a shallower depth.

On further annealing, the Au begins to flatten and more closely resemble the large, flat terraces and straight step edges of the clean Pd{111} surface. As the annealing temperature increases, the lattice parameter of the alloy becomes progressively closer to that of Pd{111} as the concentration of Au becomes depleted and the alloyed region becomes deeper. Hence the subsurface features become deeper with respect to the surface features and are undetectable for the higher pre-annealing temperatures (>825 K). Since Au and Pd are known to produce a continuous series of solid solutions, one may assume that the lattice parameter of the mixed layer is at an intermediate value between bulk Au and bulk Pd. Using a similar argument to that presented above, an alloy overlayer will still be expanded in all three directions

relative to Pd{111}. Hence, using a 3-layer incident geometry with respect to bulk Pd{111} will cause not only the illumination of the top three layers of alloy but also a significant fraction of material in the layers beneath. Since the effect of the lattice mismatch becomes more exaggerated the further one travels into the bulk, the atoms close behind the target atom will be shadowed more effectively than atoms in deeper positions. This is manifested in the Intensity v Energy spectrum as an initial dip at energies below the surface peak followed by an increase in scattered ion intensity.

The difference in depth of the features below the Au and Pd surface is difficult to explain. It may be that it is due to rumpling (static disorder) within layers caused by accommodating the larger Au atoms. Au atoms sitting in sites away from Pd lattice sites will be less effectively shadowed and hence the depth at which Au atoms begin to contribute to the I v E spectrum is shallower than the distance measured for Pd.

3.5 Conclusions and Further Work

1. The growth of Au on Pd{111} is close to pseudomorphic. The 4.8% lattice mismatch means that the first couple of Au layers grow in a slightly strained manner, resulting in the Moiré structure with an 80\AA periodicity. The Au grows as islands on the Pd{111} surface. As the pre-annealing temperature increases the surface becomes flatter and more Pd-rich until, by 975 K pre-annealing temperature, the surface is flat with large terraces, mimicking pure Pd{111}.
2. Au/Pd{111} forms two distinct regimes depending on the pre-anneal temperature (and as a result on the %Au in the top couple of layers).
 - At low pre-annealing temperatures (<750 K) there is a distinct amount of Au in the near sub-surface layers and as a result there is a significant region of the sub-surface (7-13 layers) that exists as a Pd/Au alloy which has a slightly larger (2.77\AA rather than 2.75\AA at 10% Au) lattice constant to pure Pd.
 - At high pre-anneal temperatures (825 K) the amount of Au in the sub-surface has dropped to a level such that it no longer has a significant presence in the alloy. This is due to the Au diffusing further down into the bulk and so diluting the amount of Au per layer. Analysis has shown that as the %Au drops below 10% in the lower layers, the alloy no longer becomes visible to the MEIS beam, indicating a near-pseudomorphic alloy integrated into the Pd{111} crystal structure.

Additional work on this system could include further studies covering a wider range of initial Pd/Au surface compositions; either by using different pre-anneal temperatures or different multilayer coverages of Au. Additionally, extra variables such as C, AcOH (as we have done in Chapter 4), K or C_2H_4 could be incorporated.

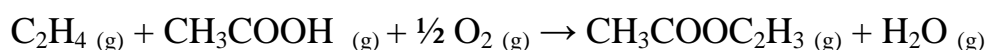
3.6 References

- ¹ *European Patent EP 1175939A1 (2002)*
- ² J.W.M.Frenken, R.M.Tromp and J.F.van der Veen, *Nuc. Ins. Meth. B*, **17**, 334 (1986)
- ³ C.J.Baddeley, L.H.Bloxham, S.C.Laroze, R.Raval, T.C.Q.Noakes and P.Bailey, *J. Phys. Chem. B*, **105**, 2766 (2001)
- ⁴ T.E.Jones, T.C.Q.Noakes, P Bailey and C.J. Baddeley, *Surf. Sci.*, **600**, 2129 (2005)
- ⁵ <http://www.srim.org/SRIM/SRIM2003.htm>
- ⁶ R.C.Fadanelli, P.L.Grande and G.Schiwietz, *Nuc. Ins. Meth. B*, **230**, 17 (2005)
- ⁷ P.Bailey, T.C.Q.Noakes, C.J.Baddeley, S.P.Tear and D.P.Woodruff, *Nuc. Ins. Meth. B*, **183**, 62 (2001)
- ⁸ C.J.Baddeley, R.M.Lambert, M.S.Tikhov, C.Hardacre and J.R.Lomas, *J. Phys. Chem.*, **100**, 2189 (1996)
- ⁹ C.J.Baddeley, R.M.Lambert, A.W.Stephenson and M.S.Tikhov, *Surf Sci.*, **398**, 172-183 (1998)
- ¹⁰ C.J.Baddeley, R.M.Lambert, A.W.Stephenson and R.M.Ormerod, *J. Phys Chem.*, **99(14)**, 5148 (1995)
- ¹¹ Y.Kuk, L.C.Feldman and P.J.Silverman, *Phys. Rev. Letts.*, **50**, 511 (1983)
- ¹² L.Hilaire, P.Legare, Y.Hull and G.Maire, *Surf. Sci.*, **103**, 125 (1981)

CHAPTER 4: AcOH/C/Au/Pd{111}

4.1 Introduction

The synthesis of vinyl acetate monomer (VAM) from ethylene, acetic acid (AcOH) and oxygen was first reported by Moiseev *et al.*¹ using homogeneous Pd based catalysts.



Subsequently, the production of VAM has become a very important industrial process^{2,3,4}. It is found that the selectivity of the catalytic process can be enhanced by the use of silica supported bimetallic Pd/Au catalysts promoted by potassium acetate. The promoting role of Au has been proposed to be related to the modification of active ensembles of Pd atoms^{5,6} giving greater control over the VAM forming reaction at the expense of competing partial and total combustion routes (yielding CO and CO₂). There are a number of examples where Au/Pd catalysts outperform the pure Pd analogues (e.g. acetylene trimerisation over Au/Pd colloidal catalysts)⁷. In general, the enhanced behaviour is ascribed to electronic and/or geometric effects caused by the formation of bimetallic surface AuPd alloys^{8,9,10}.

A number of studies have been reported of AcOH adsorption on metal surfaces and these have been discussed in depth in Chapter 1.4 and hence will not be revisited here. We use temperature-programmed desorption (TPD) and reflection absorption infrared spectroscopy (RAIRS) to investigate the adsorption and decomposition characteristics of AcOH on Au/Pd{111} surfaces as a function of surface composition. We examine how this behaviour is modified by the presence of co-adsorbed carbon. Scanning Tunnelling Microscopy (STM) is used to determine how

the morphology of the bimetallic surface varies with temperature. We use the technique of Medium Energy Ion Scattering (MEIS)¹¹ to quantify the surface composition at each stage of the annealing process and to measure the extent to which AcOH causes the segregation of Pd to the bimetallic surface.

4.2 Experimental section

Experimental and sample preparation procedures were carried out as detailed in Chapter 2.7. The STM/RAIRS, TPD and MEIS experiments were all carried out in separate chambers at different facilities and therefore on slightly different pre-annealed surfaces.

TPD experiments sample preparation and characterisation was carried out as follows:

- Pd{111} single-crystal cleaned by argon ion bombardment and high temperature (1000 K) annealing cycles and checked for impurities by AES and LEED.
- Once cleaned; Au deposited at room temperature by vapour deposition and verified upon completion by LEED and AES.
- Pd/Au surface annealed to the required pre-annealing temperature for 5 minutes and allowed to cool to room temperature.
- Surface composition verified by AES.
- AcOH dosed via a leak valve.
- TPD experiment carried out .
- Pd{111} crystal cleaned in preparation for next experiment.

MEIS experiments followed the sequence:

- Pd{111} single-crystal cleaned by argon ion bombardment and high temperature (1000 K) annealing cycles and checked for impurities by AES and LEED.
- Once cleaned; Au deposited at room temperature from a K-cell and the amount verified on completion by AES Pd/Au surface annealed to the required

pre-annealing temperature for 5 minutes and allowed to cool to room temperature.

- Pd/Au annealed surface transferred to scattering chamber and analysed by MEIS.
- Sample returned to preparation chamber.
- Required amount of AcOH dosed through a leak valve.
- Dosed sample transferred back to scattering chamber and analysed by MEIS.
- Sample returned to preparation chamber and surface composition analysed by AES.
- Pd {111} crystal cleaned in preparation for next experiment.

STM/RAIRS experiments followed a third sequence:

- Pd{111} single-crystal cleaned by argon ion bombardment and high temperature (1000 K) annealing cycles and checked for impurities by LEED and STM.
- Once cleaned; Au deposited at room temperature by vapour deposition and checked periodically by STM until the required amount was present.
- Pd/Au surface annealed to the required pre-annealing temperature for 5 minutes and allowed to cool to room temperature.
- Pd/Au annealed surface analysed by STM.
- Sample transferred to RAIRS chamber.
- RAIRS experiment carried out by sequential dosing of AcOH at a sample temperature of 300 K (through a leak valve) and IR analysis until desired amount had been deposited.
- Sample transferred back to preparation chamber and analysed by STM.
- Pd{111} crystal cleaned in preparation for next experiment.

In all cases, the cleaning step was taken out in order to carry out the C-contaminated experiments. It is important to note that due to the high confidence in the calculated Au:Pd ratio (discussed in Chapter 3.2) for a given geometry we can confidently say that a change in measured Au composition following AcOH adsorption of a few percent is a real effect since the error associated with calculating the composition is a systematic error which operates in precisely the same direction for both the clean and adsorbate covered surfaces.

4.3 Results

4.3.1 - Surface Morphology (STM)

The STM behaviour of the Pd/Au bimetallic surface during the pre-annealing process has been studied previously in Chapter 3.3.1.

Figures 4.3.1.1 – 4.3.1.5 display STM images of the Au/Pd{111} surfaces prepared in the following way. ~2 ML Au are deposited onto Pd{111} and the sample annealed to a chosen temperature prior to STM measurements. The sample is then exposed to AcOH at 300 K then annealed to a higher annealing temperature whence further STM measurements are taken. Hence, in these experiments, STM is being used as a post-TPD analytical probe.

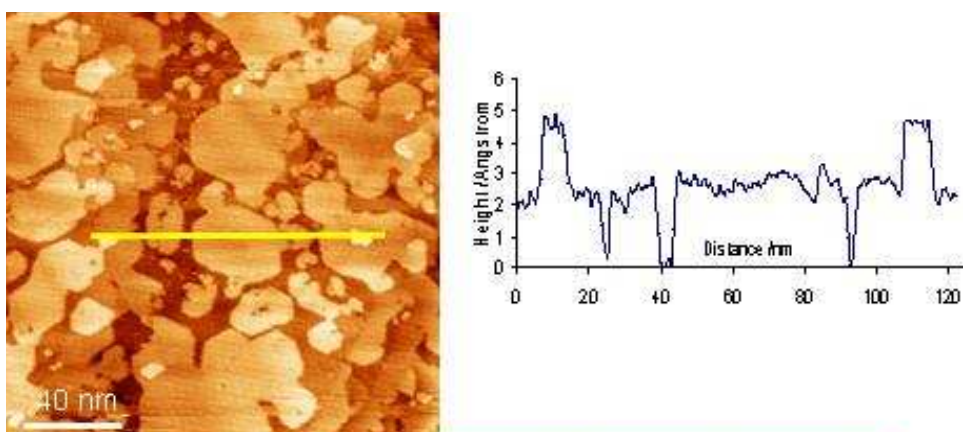


Figure 4.3.1.1 - STM image (180 nm x 180 nm) following the deposition of ~2 ML of Au on Pd{111} at 300 K (inset shows a line profile displaying the onset of 2nd layer Au growth prior to the completion of the first monolayer).

The morphology of the bimetallic surface during the course of the experiments is similar to that of the samples described in Chapter 3. There is an initial growth of Au on the Pd surface and it can be seen from Figure 4.3.1.1 that 2nd layer growth of Au begins before completion of the 1st monolayer.

During subsequent anneal treatments, the surface does become flatter and more uniform until a Pd-like surface is seen after the final anneal to 975 K.

However, following a pre-annealing treatment to 600 K, exposure to AcOH at 300 K and a subsequent anneal to 675 K, additional material is observed in the STM image at step edges (Figure 4.3.1.2).

Exposure of this surface to AcOH and a further anneal to 775 K results in a large number of small particles distributed over the whole surface (Figure 4.3.1.3).

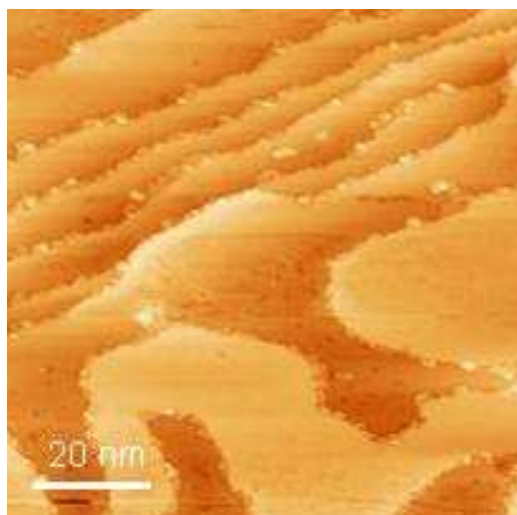


Figure 4.3.1.2 - STM image (90 nm x 90 nm) following the deposition of ~2 ML of Au on Pd{111} at 300 K and anneal to 600 K. The sample was exposed to 30 L AcOH at 300 K and subsequently annealed to 675 K.

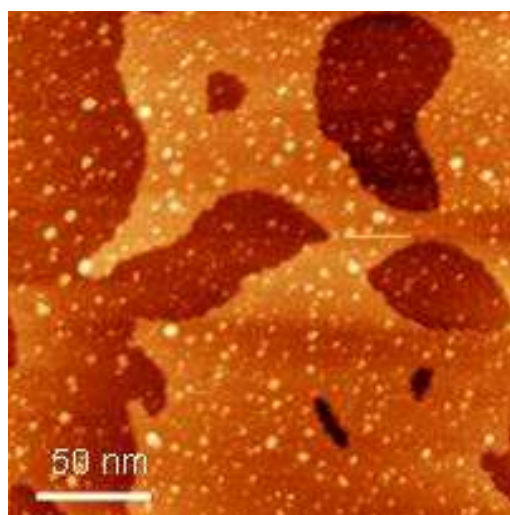


Figure 4.3.1.3 - STM image (220 nm x 220 nm) following the exposure of the sample shown in 4.3.1.2 to 30 L AcOH at 300 K and subsequent anneal to 775 K.

The particles are typically 1-2 nm in diameter and ~0.2 nm deep. The number density and size of particles increases with further exposure to AcOH and annealing cycles as can be seen in Figures 4.3.1.4 and 4.3.1.5.

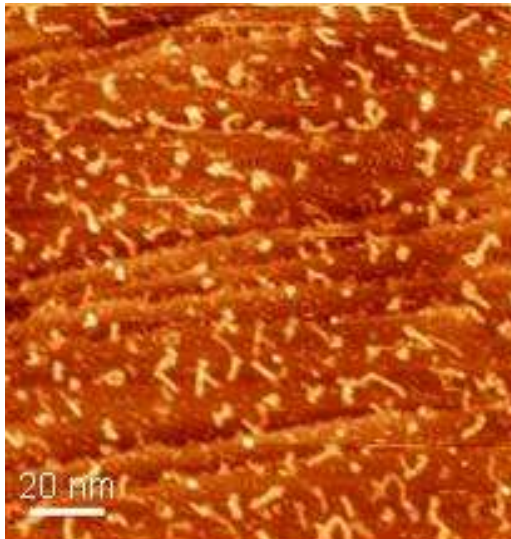


Figure 4.3.1.4 - STM image (130 nm x 130 nm) following the exposure of the sample in 4.3.1.3 to 30 L AcOH at 300 and subsequent anneal to 850 K.

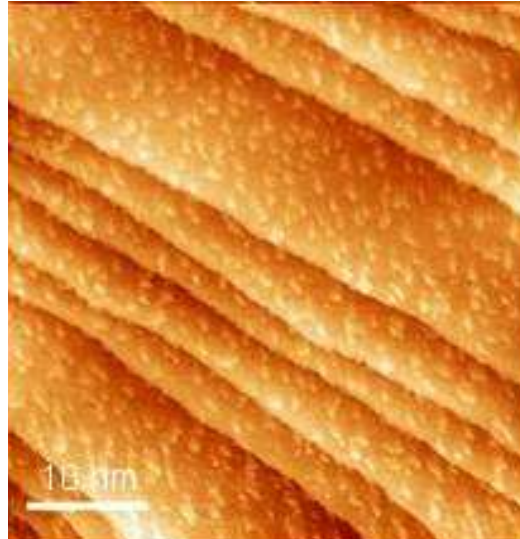


Figure 4.3.1.5 - STM image (42 nm x 42 nm) following the exposure of the sample in 4.3.1.4 to 30 L AcOH at 300 and subsequent anneal to 925 K.

Additionally, material was found to congregate at the step edges when post-RAIRS STM scans were carried out, prior to removal of the AcOH by annealing (examples can be found in Figures 4.3.1.6 and 4.3.1.7). This was true for both the high (“Pd-rich”):

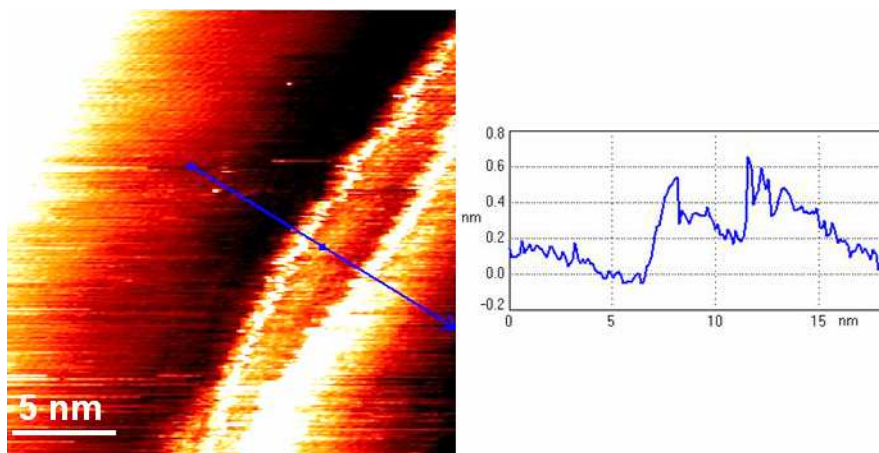


Figure 4.3.1.6 - STM image (25 nm x 25 nm) following the RAIRS experiment carried out on a Pd/Au surface (prepared as in Fig. 4.3.1.1) which was then annealed to 730 K and treated to a saturation dose of AcOH (128L total). Inset graph shows a line profile along the blue cross-section arrow.

and low (“Au-rich”) pre-annealing temperature surfaces and it is indicative of AcOH being present at the step-edges.

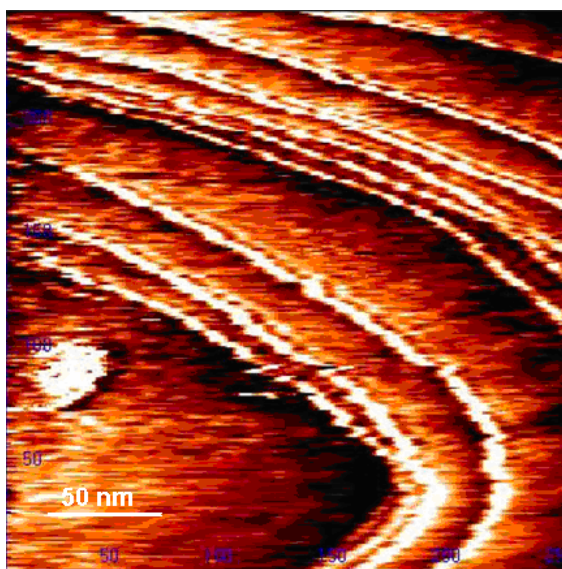


Figure 4.3.1.6 - STM image (250 nm x 250 nm) following the RAIRS experiment carried out on a Pd/Au surface (prepared as in Fig. 4.3.1.1) which was then annealed to 930 K and treated to a saturation dose of AcOH (128L total).

Analogous scans for the in situ contaminated surfaces were found not to contain this step-edge material (except for the initial experiment in the run where there was obviously no contamination yet), probably due to the pre-adsorbed material taking up the available sites on the step-edges which would normally be the ones populated by AcOH.

4.3.2 – Surface Structure and Composition (MEIS)

MEIS experiments were carried out on surfaces prepared by depositing 3-4 ML Au on Pd{111} as a function of pre-annealing temperature. The surface was re-prepared between each experiment.

Figure 4.3.2.1 shows the concentration of Au (in atom %) (derived from the MEIS data) of the uppermost two layers of the bimetallic surface as a function of pre-annealing temperature. After each pre-annealing treatment, the surface is exposed to

acetic acid and a new composition measured by MEIS. These data are also presented in Figure 4.3.2.1.

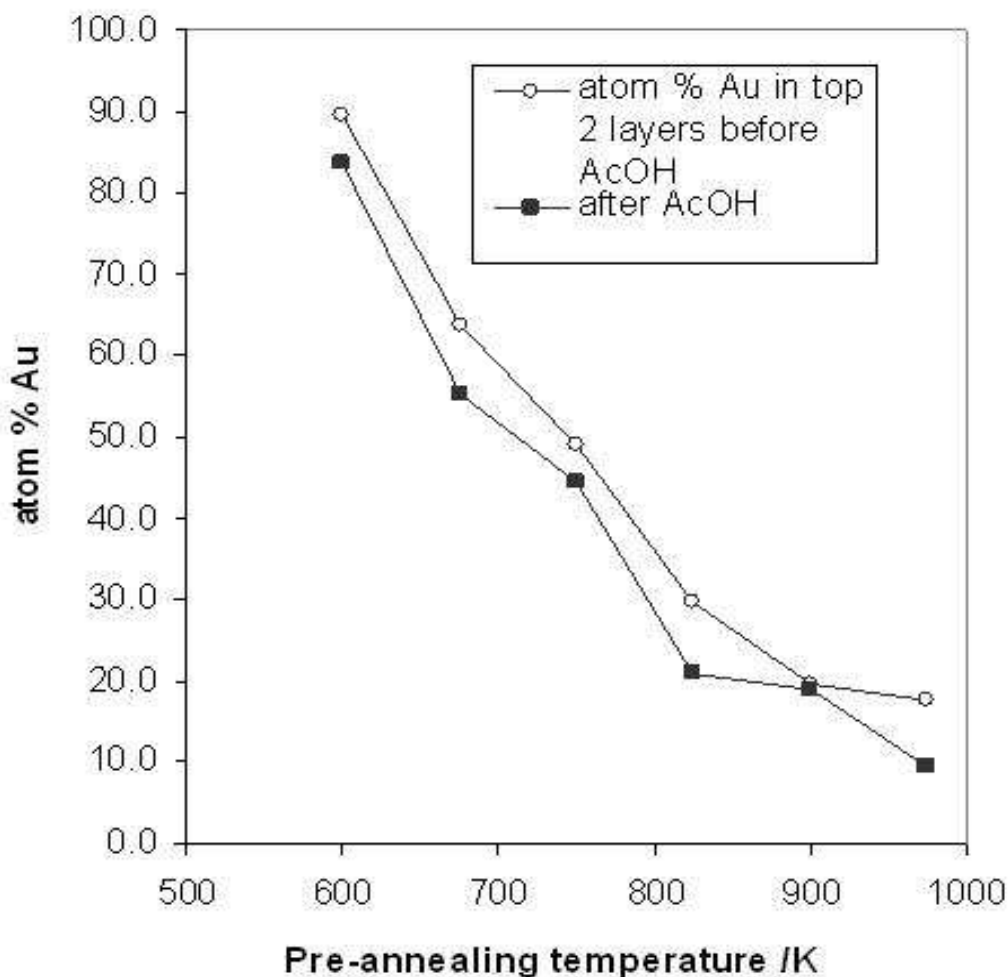


Figure 4.3.2.1 - Concentration of Au (in atom %) of the uppermost two layers of the bimetallic surface as a function of pre-annealing temperature. After each pre-annealing treatment, the surface is exposed to acetic acid (at 300 K) and a new composition measured by MEIS.

At low pre-annealing temperatures, the surface is Au rich. A clear decrease in Au composition is observed with increasing pre-annealing temperature. Following an annealing treatment to 950 K, the surface is strongly enriched in Pd in agreement with previous LEED/AES measurements on the Pd{111}/Au system¹⁰. There is a systematic trend observed in the composition of the top two layers after treatment with 30L AcOH. In each case there is a significant drop in the atom %Au following the adsorbate dose.

Figure 4.3.2.2 shows the MEIS intensity versus energy spectra (1-layer geometry) for the surface prepared by annealing a 3-4 ML Au film to 950 K before and after exposure to 30L AcOH at 300 K. A clear decrease in the Au signal is observed after the AcOH treatment.

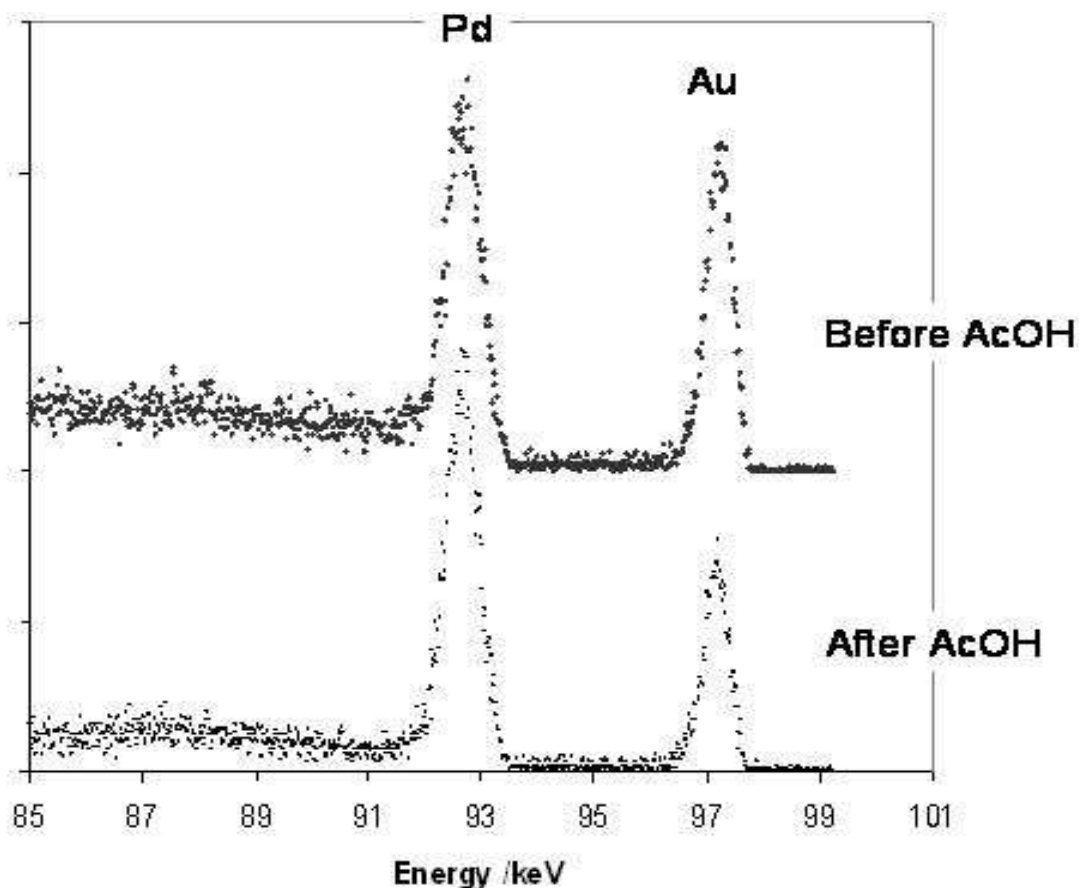


Figure 4.3.2.2 - MEIS intensity versus energy spectra (1-layer geometry) for the surface prepared by annealing a 3-4 ML Au film to 975 K before and after exposure to 30L AcOH at 300 K.

Figure 4.3.2.3 shows the composition (derived from the MEIS data) of the uppermost two layers of the bimetallic surface as a function of pre-annealing temperature for the analogous experiment to the STM experiments shown in Figures 4.3.1.1 – 4.3.1.5.

In these experiments, no attempt was made to stop the in situ contamination of the surface after each cycle of pre-anneal and acetic acid dose. After each pre-annealing treatment, the surface is exposed to acetic acid and a new composition measured by MEIS. These data are also presented in Figure 4.3.2.3.

As is the case with the non-contaminated individual re-prepared surface experiments (Figure 4.3.2.1) a clear decrease in Au composition is observed with increasing pre-annealing temperature. A systematic trend is also observed following treatment in AcOH, with a significant decrease in the amount of Au present in the top two layers.

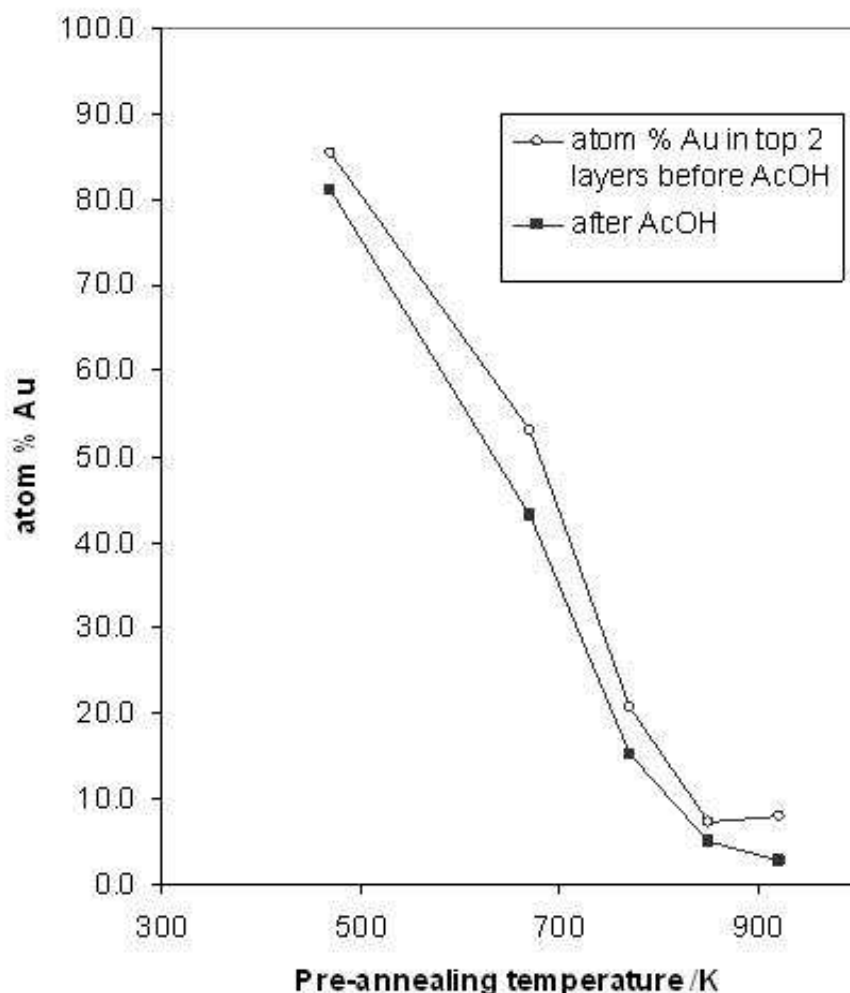


Figure 4.3.2.3 - Concentration of Au (in atom %) of the uppermost two layers of the bimetallic surface as a function of pre-annealing temperature. After each pre-annealing treatment, the surface is exposed to acetic acid (at 300 K) and a new composition measured by MEIS.

4.3.3 – Acetic Acid adsorption and decomposition (TPD/RAIRS)

Figure 4.3.3.1 shows the RAIRS spectra following saturation exposure of AcOH onto 1-2 ML Au on Pd{111} at a sample temperature of 300-310 K as a function of pre-annealing temperature. The sample was re-prepared in between each cycle of

deposition/anneal/RAIRS (in the same way as the MEIS experiments whose results are shown in Figure 4.3.1.1) to give a similar starting Au coverage for each surface.

Following the lowest pre-annealing treatment (630 K), AcOH adsorption results in a band in the RAIR spectrum at 1453 cm^{-1} and additional weak features at ~ 1880 and 2020 cm^{-1} . The bands in the $1800\text{-}2100\text{ cm}^{-1}$ range increase in intensity with increasing annealing temperature. In addition, following pre-annealing treatments above 830 K a weak band is observed at $\sim 1080\text{ cm}^{-1}$. After a 930 K pre-anneal, a new band is observed at 1719 cm^{-1} .

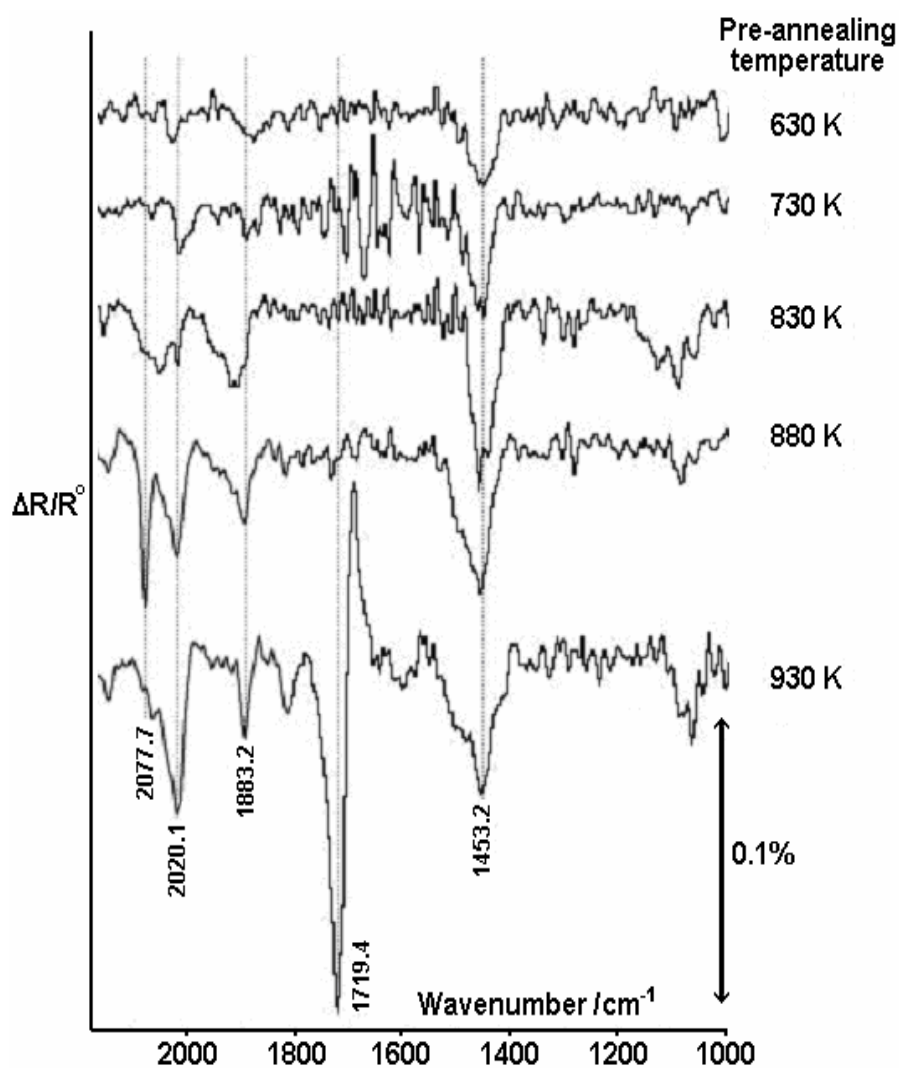


Figure 4.3.3.1 - RAIRS spectra following a saturation (30 L) exposure of AcOH on 1-2 ML Au on Pd{111} at a sample temperature of 300-310 K as a function of pre-annealing temperature. In between each experiment the sample was freshly prepared.

RAIRS spectra as a function of AcOH dose were also produced and an example is shown in figure 4.3.3.2.

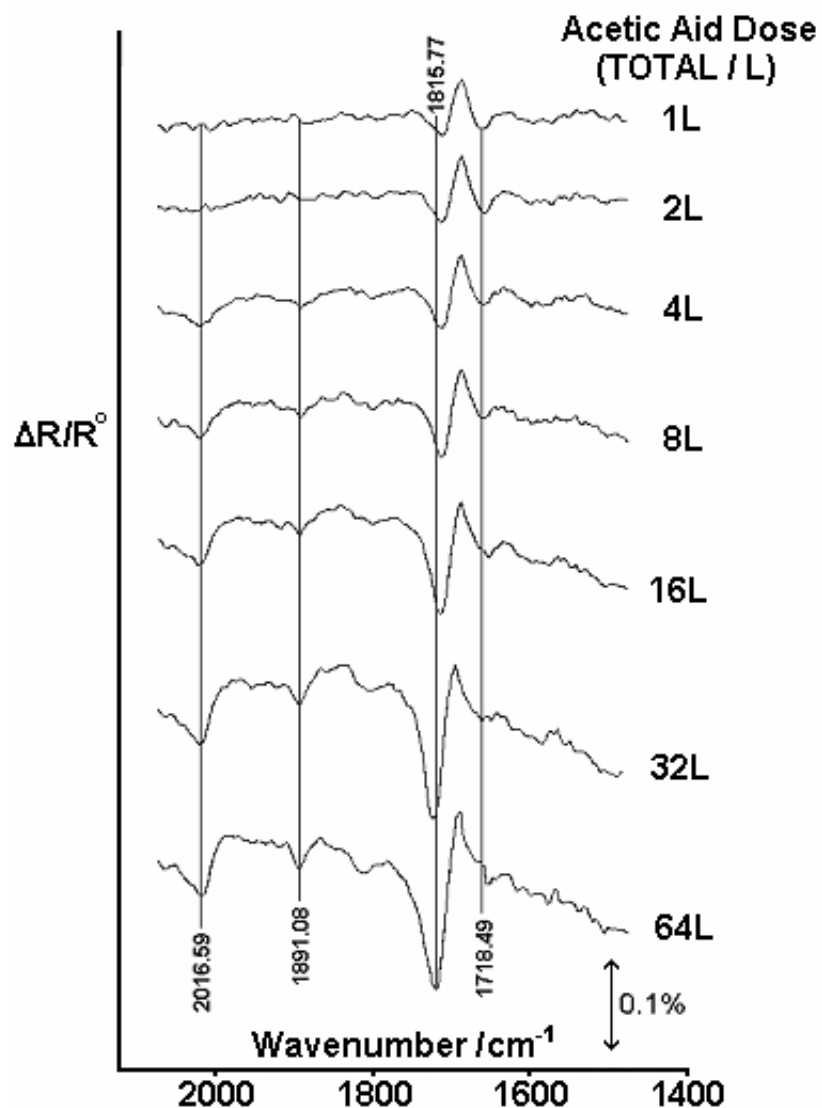


Fig 4.3.3.2 - RAIRS spectra on a sample of 1-2 ML Au on Pd{111}, which was pre-annealed to 950 K, as a function of AcOH dose. The AcOH was dosed at a sample temperature of 300 – 310 K.

It can be seen that a saturation dose of AcOH has been achieved by the time 30L have been dosed and there is no change in the peak positions as the dose of AcOH is increased.

Figure 4.3.3.3 shows a series of TPD spectra (mass 44, CO_2) following the adsorption of acetic acid on a Pd{111}-4ML Au as a function of pre-annealing temperature. In

between each experiment the sample was cleaned by Ar^+ bombardment and annealing to 1000 K until the Pd surface was clean, as confirmed by LEED and AES experiments. A fresh Au film of approximately the same thickness was deposited and annealed to the chosen temperature and in each case the sample was exposed to a 30 L AcOH dose at 300-310 K after annealing and cooling.

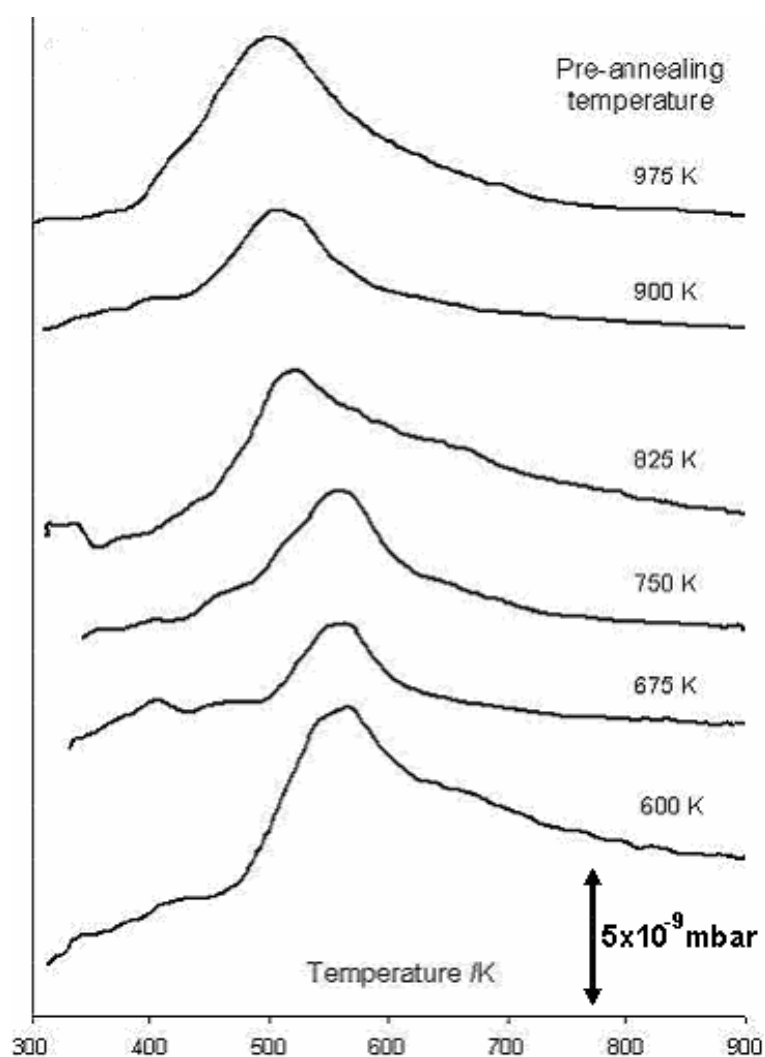


Figure 4.3.3.3 - A series of TPD spectra (mass 44, CO_2) following the adsorption of acetic acid on 3-4 ML Au on Pd{111} as a function of pre-annealing temperature. In between each experiment the sample was freshly prepared.

In the pre-annealing temperature range 600-750 K, the main CO_2 desorption peak has a maximum at ~ 560 K with a shoulder at higher temperature visible particularly in the 600 K pre-annealed sample. After annealing to 825 K, the maximum in the CO_2 desorption shifts to slightly lower temperature (510 K). This shift continues as the

sample is pre-annealed to even higher temperatures with T_{\max} eventually reaching 500 K following a pre-annealing treatment to 975 K.

Figure 4.3.3.4 shows a series of TPD spectra (mass 2, H_2) following the adsorption of acetic acid on a Pd{111}-4ML Au as a function of pre-annealing temperature.

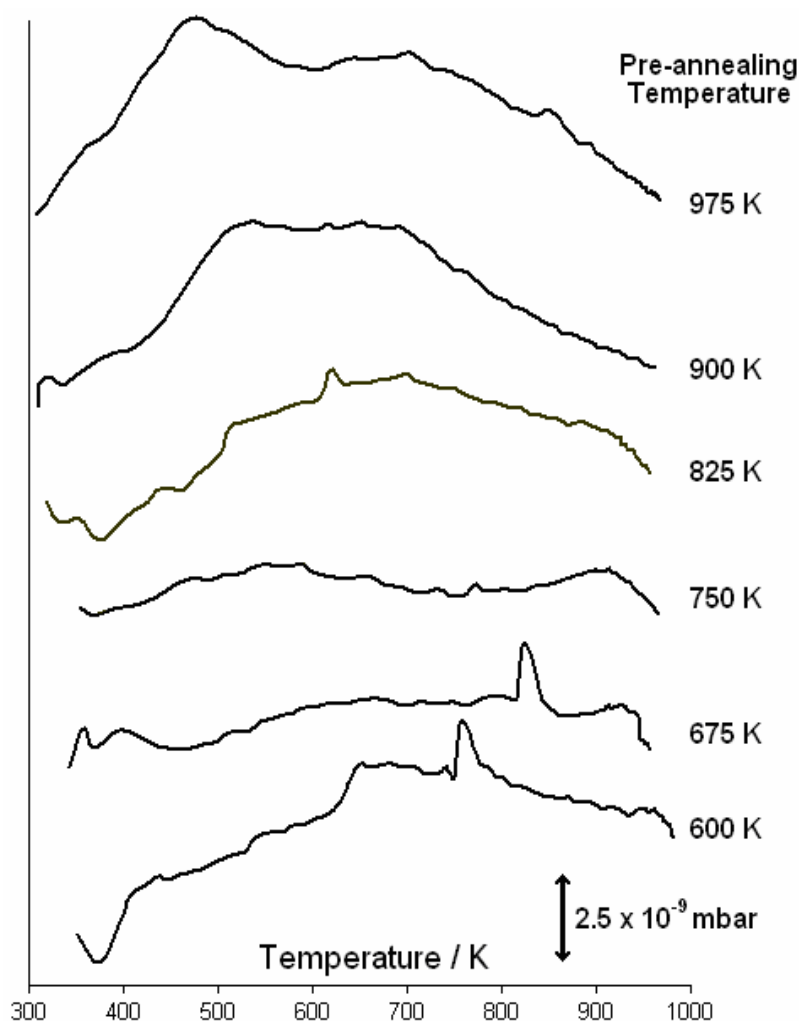


Figure 4.3.3.4 - A series of TPD spectra (mass 2, H_2) following the adsorption of acetic acid on 3-4 ML Au on Pd{111} as a function of pre-annealing temperature. In between each experiment the sample was freshly prepared.

In the 600–750 K pre-annealing temperature range there is little in the way of significant desorption peaks although there are two features visible at ~500 K and ~900 K. At the higher pre-annealing temperature of 900 K there is a feature with a T_{\max} of 520 K which drops to 480 K when the pre-annealing temperature is 975K.

There is also a second, slightly-smaller, feature with a T_{\max} of around 700 K in both the 900 and 975K cases.

Figure 4.3.3.5 shows the RAIRS data from the analogous experiment to the STM experiments described in Figures 4.3.1.1 – 4.3.1.5. These are the experiments in which no attempt has been made to avoid surface contamination after each experimental cycle.

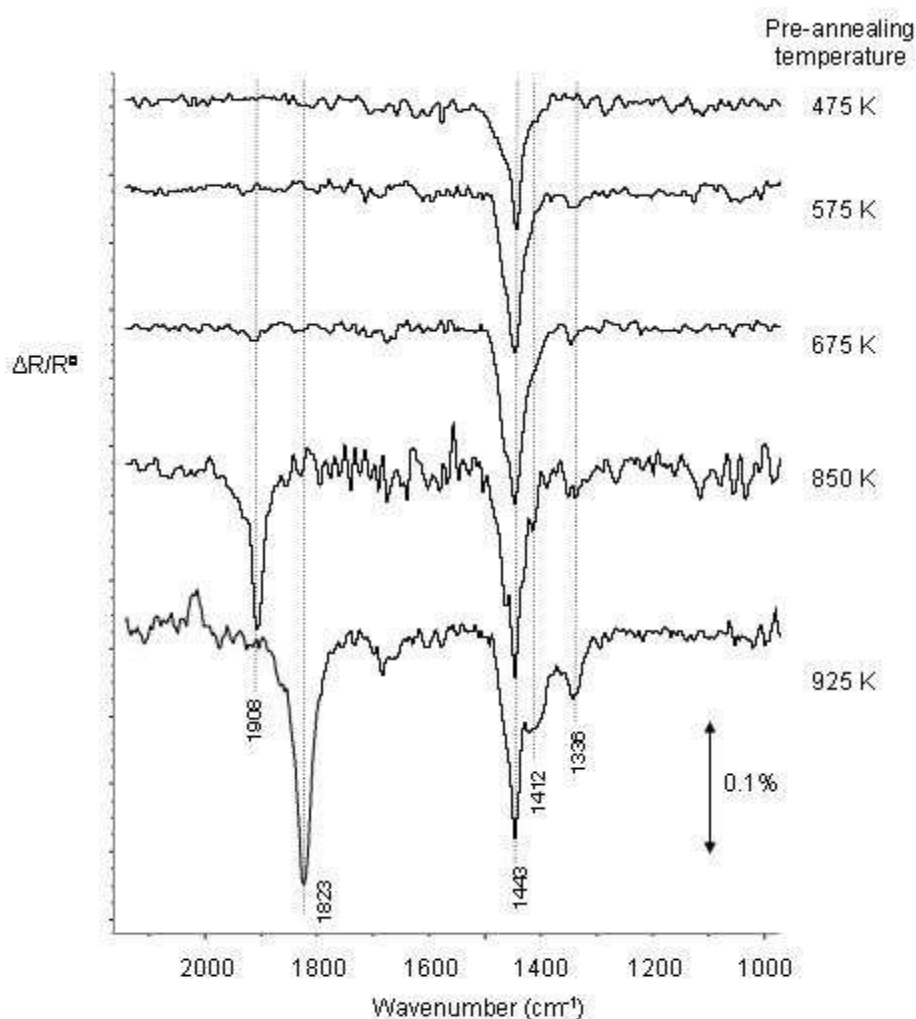


Figure 4.3.3.5 - RAIRS spectra following a saturation (30 L) exposure of AcOH on 1-2 ML Au on Pd{111} at a sample temperature of 300-310 K as a function of pre-annealing temperature. The sample was not cleaned between cycles of AcOH exposure and annealing.

Following the lowest pre-annealing treatment, the only band observed is at 1443 cm^{-1} . Annealing the AcOH exposed surface to 575 K and then dosing once again with 30 L

AcOH at 300 K results in a similar spectrum as does the analogous procedure involving a pre-annealing treatment to 675 K. Annealing to 850 K and exposing the surface to 30 L AcOH at 300 K results in the appearance of a weak band at 1336 cm^{-1} and a relatively intense feature at 1908 cm^{-1} . Annealing to 925 K and subsequent exposure to AcOH at 300 K results in the observation of a single band in the $\nu(\text{CO})$ region at 1823 cm^{-1} . Bands are observed at 1412 and 1336 cm^{-1} in addition to the more intense feature at 1443 cm^{-1} .

RAIRS spectra as a function of AcOH dose were also produced and two examples (high and pre-annealing temperatures) are shown as Figures 4.3.3.6 and 4.3.3.7

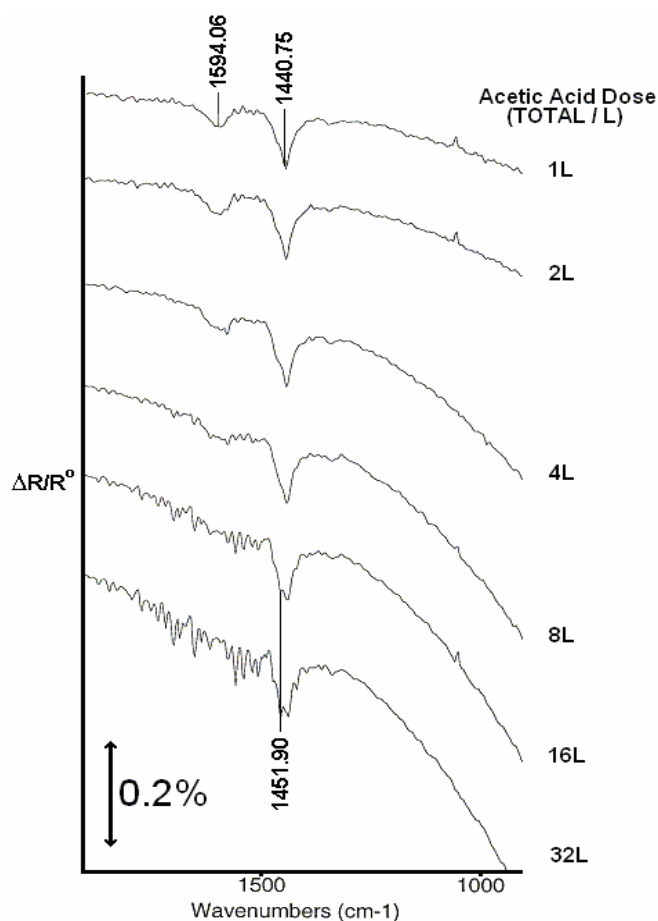


Fig 4.3.3.6 - RAIRS spectra on a sample of 1-2 ML Au on Pd{111}, which has been pre-annealed as far as 575 K, as a function of AcOH dose. The AcOH was dosed at a sample temperature of 300 – 310 K and the sample has not been re-prepared after the 475 K pre-anneal and RAIRS experiment.

It is interesting that in the 1 L dose experiment at the 575 K pre-anneal temperature there is a band at 1590 cm^{-1} which is the asymmetric stretch of the carboxylate. This suggests that the orientation of the carboxylate changes as a function of exposure (by application of the metal surface selection rule). Also, in the 925 K experiment, it appears that the carboxylate is formed first followed by the formation of CO, this may be an indication that the geometry of acetate changes from bidentate (CO_2 forming) to monodentate (CO forming) as the dose increases.

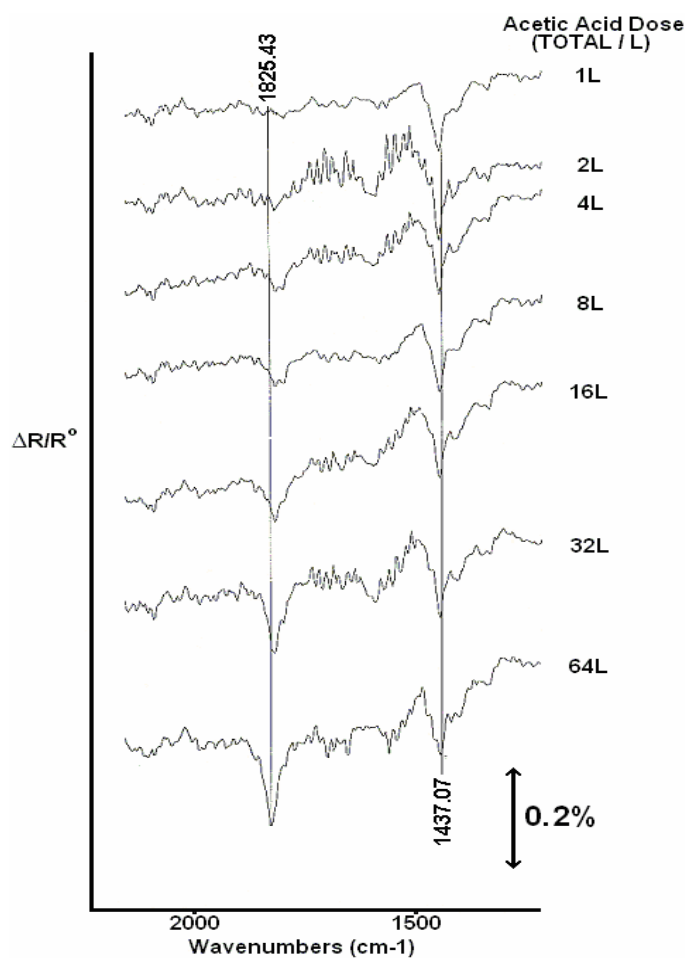


Fig 4.3.3.7 - RAIRS spectra on a sample of 1-2 ML Au on Pd{111}, which has been pre-annealed as far as 925 K, as a function of AcOH dose. The AcOH was dosed at a sample temperature of 300 – 310 K and the sample had not been re-prepared after the 475, 575, 675, and 850 K pre-anneals and RAIRS experiments.

In both cases it is clear that after dosing 30L of AcOH, there is no significant growth in the main peaks and so it can be concluded that a saturation dose has been achieved.

Figure 4.3.3.8 shows TPD data analogous to those presented in Figure 4.3.3.2. However, in these experiments a 4 ML Au film was deposited onto the Pd{111} surface at 300 K and the sample was exposed to 30 L AcOH at 300 K. At the end of the TPD experiment, the sample was annealed to a higher temperature, cooled to 300 K and then exposed to 30 L AcOH. This procedure was repeated for a series of increasing pre-annealing temperatures.

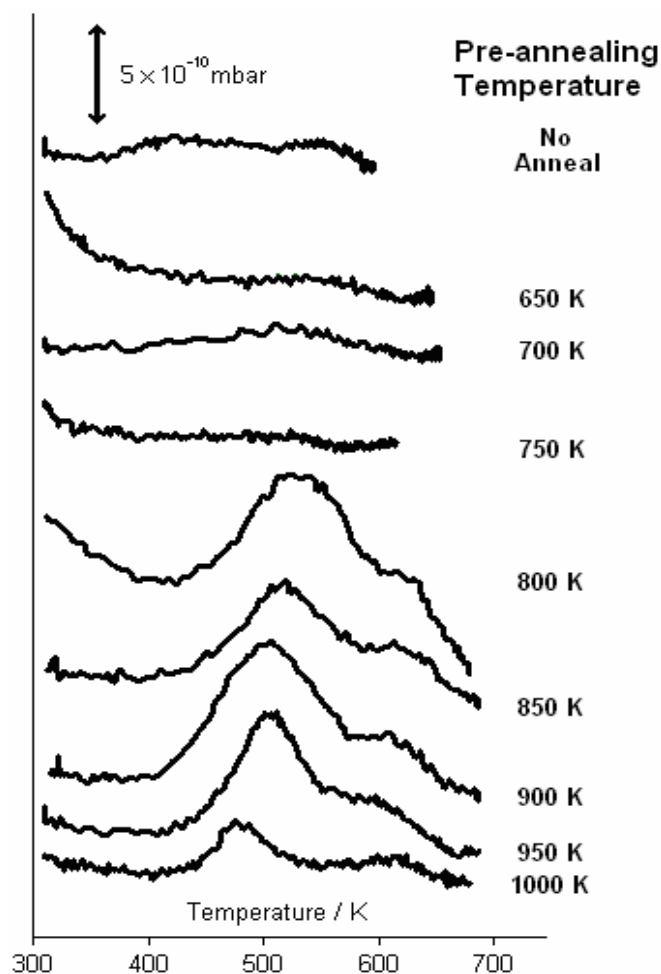


Figure 4.3.3.8 - A series of TPD spectra (mass 44, CO₂) following the adsorption of acetic acid on 3-4 ML Au on Pd{111} as a function of pre-annealing temperature. The sample was not cleaned between cycles of AcOH exposure and annealing.

Again, the major difference between the TPD data presented in Figures 4.3.3.3 - 4.3.3.4 and those in Figure 4.3.3.8 is that no effort is made to avoid the accumulation of C_(ads) on the surface.

Following AcOH adsorption on the as-prepared Au film, CO₂ is observed to desorb in two peaks, one with a T_{max} of 550 K and the other a broader feature whose onset occurs at ~375 K. Pre-annealing to 750 K results in a similar 550 K desorption feature. At pre-annealing temperatures of 850-1000 K, a new high temperature feature appears at 630 K and there is a large increase in the relative intensity of the lower temperature desorption which is now visible as a well-defined peak with a T_{max} at 530 K. As the pre-annealing temperature increases, the T_{max} of the lower temperature desorption state decreases gradually until by a pre-annealing temperature of 1000 K, the T_{max} value reaches 485 K. No useful H₂ TPD data could be produced for the C-contaminated experiments.

4.4 Discussion

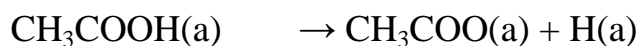
The growth of Au on Pd{111} during the annealing process has been covered in depth in Chapter 3 and the reader is referred to the relevant discussion in that chapter (Section 3.3.1).

The adsorption of AcOH on Pd{111} has been reported previously by Davis and Barteau²¹ and by Haley *et al.*¹⁸. In each case, AcOH was adsorbed at cryogenic temperatures and the nature of adsorbed species was monitored, as a function of temperature, by vibrational spectroscopy (high resolution electron energy loss spectroscopy, HREELS). TPD was used to monitor desorbing species.

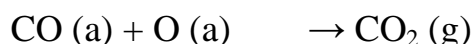
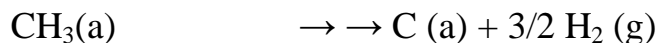
Essentially, two competing pathways are proposed to exist for acetic acid decomposition. In pathway (1), adsorbed acetate decomposes in a single step to yield gas phase CO₂ and in pathway (2), the decomposition of adsorbed acetate results in the formation of CO_(a).

Haley *et al.* further proposed that pathway (1) was associated with a bidentate acetate species, while pathway (2) occurred via a monodentate species.¹⁸

Pathway (1)



Pathway (2)



The adsorption of acetic acid at 300 K has been studied on Pd{110}¹⁷ and Rh{111}¹² and occurs via these two dissociative pathways – one which leads to adsorbed acetate and hydrogen, the other which leads to adsorbed CH_x, hydrogen, CO and oxygen. Subsequently annealing the surface results in desorption of CO, H₂O, CO₂ and H₂. A significant amount of adsorbed carbon remains on the surface. On Rh{111}, adsorption of acetic acid at 300 K was found to produce an acetate phase 50% more dense than that produced following adsorption at 200 K¹².

Following the highest pre-annealing treatment employed in the RAIRS and TPD experiments of Figures 4.3.3.1 – 4.3.3.4, the surface has a composition close to that of pure Pd. Under these conditions, the RAIR spectrum displays bands at 2020, 1893, 1719, 1455 and 1087 cm⁻¹. We assign the first two of these bands to adsorbed CO on contiguous Pd sites⁶. The 1719 cm⁻¹ band is most likely to correspond to a carbonyl stretching vibration. Haley *et al.*¹⁸ reported a peak at 1735 cm⁻¹ in their HREEL spectrum which they tentatively assigned to monodentate acetate. We similarly make the tentative assignment of the 1719 cm⁻¹ to monodentate acetate. [Note that the positive component to this band is likely to be due to the displacement of an adsorbed

species by AcOH exposure – one possibility is that this species corresponds to a contaminant such as acetyl which may adsorb as the result of an impurity in the RAIRS chamber while background RAIR spectra are being acquired. A band at a similar frequency was observed for acetyl on Pt{111} by Rodriguez et al.¹². We assign the 1087 cm⁻¹ band to a C-C stretching frequency.

In Figures 4.3.3.1 and 4.3.3.5, we observe bands in the 1440-1455 cm⁻¹ range which we assign to the $\nu_{\text{sym}}(\text{OCO})$ mode of a bidentate acetate species. In both previous studies of AcOH adsorption on Pd{111}, peaks were observed in the HREEL spectrum at 1415 cm⁻¹ which were assigned to this vibrational mode of a bidentate acetate species^{18,21}. The symmetric carboxylate stretching band has been reported at a similarly high frequency following the adsorption of acetate on other metallic surfaces, for example 1434 cm⁻¹ (Cu{110})¹³ and on Ru{0001}¹³ where two bands were observed which were assigned to the bidentate chelating (1445 cm⁻¹) and bidentate bridging (1425 cm⁻¹) species. The key difference between the experiments in our work and the previous Pd{111} investigations is the adsorption temperature – in our case all AcOH exposures were carried out at 300 K.

It is interesting to note that, in the previous Pd{111} studies^{18,21}, desorption of CO₂ as a result of the thermal decomposition of adsorbed acetate occurred at a much lower temperature than reported in the present study. For example, Haley et al. reported that CO₂ desorption was complete by ~400 K¹⁸. In our case, the *onset* of CO₂ desorption occurs above 400 K. Bowker et al. have recently shown that adsorption of acetic acid on Pd{110} at 300 K results in the deposition of surface C and a significant increase in the desorption temperature of CO₂¹⁷. It was proposed that the presence of C_(a) modifies the decomposition kinetics of adsorbed acetate. Similar behaviour was

reported for AcOH on Rh{111}¹². We conclude that adsorbed carbon substantially alters the stability of the acetate species on Pd{111} resulting in a higher decomposition temperature and an increase in the carboxylate symmetric stretching frequency.

The lower the pre-annealing temperature employed in a given experiment, the more Au-rich the surface becomes. The RAIR spectra of Figure 4.3.3.1 show that the formation of CO_(a) is quenched as the surface becomes more Au rich. The CO band at 2078 cm⁻¹ can be assigned to CO bound to Pd atoms at the centre of PdAu₆ ensembles^{6,14}. The lack of even this feature at the lowest pre-annealing temperatures suggests that the presence of Au quenches the pathway to CO formation from acetate decomposition.

In addition, the desorption temperature of CO₂ increases with increasing Au concentration at the bimetallic surface. The desorption temperature of CO₂ is indicative of the temperature of surface catalysed decomposition of the acetate species and hence gives considerable information as to the stability of the acetate species on the metal surface.

It has been shown that co-adsorbed C influences the decomposition of acetate on Pd{110}¹⁷, and co-adsorbed O and K have considerable effects on the decomposition temperature of acetate on Rh{111}¹². Indeed the presence of co-adsorbed oxygen causes a shift of up to 150 K in the acetate decomposition temperature on Rh{111}¹². The CO₂ desorptions are relatively broad in this study in contrast to the very narrow CO₂ desorption peaks following autocatalytic acetate decomposition on e.g. Ni{110}¹⁵; Rh{110}¹¹; Rh{111}¹² and Pd{110}^{16,17}.

The following mechanism has been proposed to explain the desorption process ¹².

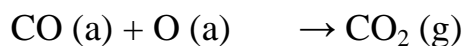
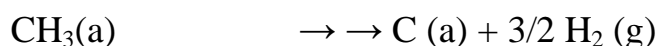


where subscripts (a) and (g) represent adsorbed state and gas phase respectively, and * is an empty site. The empty sites freed by the desorption of CO₂ are then responsible for the "surface explosion". The desorption rate of CO₂ depends crucially on the number of empty sites adjacent to the acetate species. In this context, we may assume that an empty site refers to an adjacent Pd site since a Au atom would be expected to be inert. When Pd is alloyed with Au on a {111} surface, the probability of a Pd atom having one nearest neighbour Pd atom will clearly increase as a function of increasing Pd composition. Hence one may explain the observation of the gradual shift of the CO₂ desorption state to lower temperature as a function of increasing pre-annealing temperature as being due to the fact that the presence of Au slows down the decomposition rate of acetate by reducing the number of adjacent "empty" Pd sites. This effect is observed in both the "clean" and the "carbon-contaminated" experiments.

The STM images of Figures 4.3.1.1 – 4.3.1.5 display the growth of adsorbed clusters as the sample is progressively annealed to higher temperatures after each AcOH exposure. Since it is known that AcOH adsorption at 300 K on Pd{110}¹⁷ and Rh{111}¹² results in the deposition of carbon and we were able to detect C in post-TPD Auger spectra (but not oxygen), we assign these features to adsorbed carbon in the form of nanoparticles. A comparison of the RAIRS data presented in Figures 4.3.3.1 and 4.3.3.5 shows that the build up of surface carbon reduces the tendency of CO to occupy linear adsorption sites.

When the surface is deliberately contaminated with C in our experiments the main consequence is the observation of a high temperature CO₂ desorption at >600 K which occurs in addition to the main CO₂ desorption occurring around 500 K (Figure 8). Since this peak is much more intense than in the “clean” experiments, it follows that this high temperature CO₂ desorption is related to the presence of surface C. It is unlikely that this peak derives from the decomposition of an acetate species since the desorption temperature is ~150 K higher than that observed for an analogous experiment by Bowker *et al.* for acetate on a Pd{110} surface deliberately contaminated with carbon¹⁷. A more likely explanation is that the peak is due to recombination reactions of carbon with oxygen (from pathway (2) acetate decomposition) to form CO followed by a further recombinative step of CO_(a) + O_(a) to form CO₂. Support for this explanation comes from the coincident desorption of CO which would clearly compete with the recombination step to form CO₂. Similar behaviour has been reported by Bowker *et al.*¹⁵ following the treatment of a carbon covered Pd{110} surface with oxygen.

The surface oxygen species presumably come from the decomposition of surface acetate via *Pathway 2*:



Evidence for this competing pathway is found in the RAIRS data at higher pre-annealing temperatures (i.e. on more Pd rich surfaces) where a considerable amount of CO(a) is observed to form following acetate exposure. Indeed, following the highest pre-annealing temperature the peak at 1720 cm^{-1} may reflect the presence of a monodentate acetate species which could be the precursor to this competing decomposition route. Further evidence of acetate decomposing to $\text{CO}_{2(\text{g})} + \text{CH}_3$ comes from the presence of the high T H_2 desorption trace on the “Pd-rich” surfaces which is indicative of the stepwise decomposition of $\text{CH}_3 \rightarrow \text{CH}_2 \rightarrow \text{CH} \rightarrow \text{C}$. This starts at roughly the same temperature as the CO_2 desorption. This supports the previous findings of Goodman and co-workers^{5,6} who suggest that a role of Au is to restrict the undesirable decomposition of acetate to C(a), CO and CO_2 . From our work, we can conclude that not only does Au restrict this competing decomposition route – the bimetallic surface also stabilises the bidentate form of acetate compared with pure Pd.

The assignment of the adsorbed nanoparticles observed in STM to clusters of carbon may provide an alternative interpretation to the data of Bowker *et al.*¹⁷ who accounted for the unexpectedly large Pd/C XPS ratio following the treatment of Pd{110} with acetic acid by proposing that C dissolves into the sub-surface where it remains accessible to be burnt off the surface as CO or CO_2 by treatment in oxygen. At higher AcOH exposures, one may anticipate that the nanoparticles would become more 3-dimensional accommodating relatively large amounts of carbon but due to the relatively small footprint, the attenuation of the Pd XPS signal would be much less dramatic than if the surface was covered in a C film of uniform thickness.

The evolution of surface C as a function of bimetallic surface composition is interesting. On relatively Au rich surfaces (*e.g.* Figures 4.3.1.2 and 4.3.1.3), the

nucleation of material post-TPD is evident at step edges. On more Pd rich surfaces (*e.g.* Figures 4.3.1.3 – 4.3.1.5), material is observed on the terraces of the bimetallic surface. This further implies that the reaction pathway to acetate decomposition is inhibited by the presence of Au in the surface.

Though often difficult to measure, the phenomenon of adsorbate induced segregation is well known. MEIS is one of the few techniques capable of quantifying the layer-by-layer composition of bimetallic surfaces under the influence of the adsorbate.

Adopting a similar approach to that used by Deckers *et al.* for the investigation of oxygen induced segregation in the PtNi{111} surface¹⁶, we have reported adsorbate induced segregation in a number of systems. Our initial work focused on the chloroethene/PdCu{110} system^{17,18,19} One of the key findings of the PdCu work was that the presence of hydrocarbon fragments and Cl_(a) had a negligible effect on the visibility of surface and subsurface metal atoms. The explanation for this observation can be found by considering a combination of two physical characteristics of the MEIS experiment. Firstly, this type of adsorbate atom is highly unlikely to adopt an adsorption site corresponding to a continuation of the underlying lattice – hence in the experimental geometries utilized adsorbate atoms will be ineffective at both shadowing and blocking. In addition, since the shadow cone radius is proportional to the square root of the atomic number of the target atom²², adsorbates such as C, H and O are relatively ineffective at shadowing underlying atoms.

More recently, we have reported that in the Au/Ni{111} system both tartaric acid²⁰ and methylacetoacetate²¹ induce segregation of Ni to the surface. Recently, Chen *et al.* proposed an extremely elegant model for the active site of vinyl acetate formation

over Au/Pd catalysts⁶. The variation in the turnover frequency of formation of VAM as a function of (clean) surface composition was quite different for the AuPd{100} surface compared with the {111} surface. Essentially, the turnover frequency of the {100} surface was much higher than the activity of the {111} surface at relatively low initial Pd concentrations. The authors proposed that the enhanced rates of VAM formation for low Pd coverages relative to high Pd coverages on Au single-crystal surfaces demonstrate that the critical reaction site for VA synthesis consists of two noncontiguous, suitably spaced, Pd monomers. It was proposed that the role of Au is to isolate single Pd sites that facilitate the (desired) coupling of critical surface species, while inhibiting the formation of undesirable reaction by-products. The authors' analysis did not take into account the possibility that the surface composition could be altered by the adsorption of species from the gas phase.

For the AuPd system, it is predicted from thermodynamic arguments that the surface composition should be enriched in Au with respect to the bulk if a bulk alloy particle is allowed to equilibrate in an inert gas environment (or a vacuum)²². By contrast, exposing the sample to a reactive gas should result in the segregation of the more reactive element (Pd) to the surface. The extent to which segregation is possible is strongly dependent on the rate of diffusion (and therefore the adsorption temperature)²³.

In this work, we have shown that exposure of the {111} surface of an AuPd alloy to AcOH at 300 K under UHV conditions results in measurable segregation of Pd to the surface. One may therefore conclude that, in the experiments described by Chen *et al.*⁶, the actual surface composition of the bimetallic surface under reaction conditions is more Pd-rich than the composition prior to exposure to reactive gases. The

diffusion of Pd to the surface may be relatively slow at a typical reaction temperature of ~450 K, hence the equilibration of the surface composition in response to the gas phase may be kinetically hindered.

For fcc NiFe alloys, it has been shown that oxygen induced Ni segregation is more rapid at the {100} surface than segregation at the {111} surface²⁴. Hence the effect of adsorbate induced segregation may be more dramatic at the PdAu{100} surface. We conclude therefore that the remarkable catalytic behaviour reported by Chen *et al.* may require a more complex explanation than the proposed ensemble effect. The extent of segregation expressed in terms of the number of Au lost from the top two layers does not depend strongly on the initial composition. This observation, coupled with the detection of adsorbed material (likely to be carbon) at step edges, may be an indication that segregation occurs primarily at defects or step sites on the surface.

4.5 Conclusions and Further Work

1. AcOH adsorption at 300 K occurs via two competing pathways on Au/Pd{111}. A first pathway, involving the formation of adsorbed acetate, is observed at all compositions. A second pathway also occurs on Pd-rich surfaces whereby $\text{CO}_{(a)}$ and $\text{O}_{(a)}$ is formed at 300 K.
2. The presence of Au quenches the rate of decomposition of acetate $_{(ads)}$ resulting in a shift of ~ 50 K in the T_{max} of the associated CO_2 desorption peak compared with Pd{111}.
3. The adsorption of AcOH on Au/Pd bimetallic surfaces causes a significant segregation of Pd to the top two layers of the surface.
4. AcOH decomposition results in the formation of clusters of surface carbon. The presence of surface carbon may quench the pathway to the formation of $\text{CO}_{(a)}$ from acetic acid.

Additional work on this system could include:

- TPD, RAIRS and STM analysis of the two systems as a function of initial Au dose which, in conjunction with specific anneal temperatures and further MEIS analysis, can be used to create a whole range of bimetallic surfaces with different Pd/Au ratios and surface alloy coverages.
- TPD and STM analysis of the two systems using non-saturation AcOH doses.
- Incorporating a third variable (as we have done with K in Chapter 5) such as O_2 , H_2O or ethene in a bid to more accurately mimic the industrial reaction conditions.

4.6 Chapter 4 References

- ¹ J.J.Mosieev, M.N.Vargaftik and Y.K.Syrkin, *Dokl. Akad. Nauk. SSSR*, **133**, 380 (1960)
- ² B.T.Charles, *US Patent 4048096* (1977)
- ³ M.Nakamura, Y.Fujiwara and T.Yasui, *US Patent 4087622* (1978)
- ⁴ K.Sennewald and H.Glaser, *US Patent 3761513* (1973)
- ⁵ Y.F.Han, J.H.Wang, D.Kumar, Z.Yan and D.W.Goodman, *J. Catal.*, **232**, 467 (2005)
- ⁶ M.S.Chen, D.Kumar, C.W.Yi and D.W.Goodman, *Science*, **310**, 291 (2005)
- ⁷ A.F.Lee, C.J.Baddeley, C.Hardacre, R.M.Ormerod, R.M.Lambert, G.Schmid and H.West, *J. Phys. Chem.*, **99**, 6096 (1995)
- ⁸ M.Ruff, S.Frey, B.Gleich, and R.J.Behm, *J. Appl. Phys. A*, **66**, S513 (1998)
- ⁹ D.L.Weissman-Wenocur and W.E.Spicer, *Surf. Sci.*, **133**, 499 (1983)
- ¹⁰ C.J.Baddeley, M.S.Tikhov, C.Hardacre, J.R.Lomas and R.M.Lambert, *J. Phys. Chem.*, **100**, 2189 (1996)
- ¹¹ R.M.Tromp, *Practical Surface Analysis, Vol. 2: Ion and Neutron Spectroscopy*, 2nd Ed., D. Briggs and M. Seah (Eds.), John Wiley and Sons, **1992**
- ¹² J.LRodriguez, E.Pastor, X.H.Xia and T.Iwasita, *Langmuir*, **16**, 5479 (2000)
- ¹³ S.M.York, S.Haq, K.V.Kilway, J.M.Phillips and F.M.Leibsl, *Surf. Sci.*, **522**, 34 (2003)
- ¹⁴ B.Gleich, M.Ruff and R.J.Behm, *Surf. Sci.*, **386**, 48 (1997)
- ¹⁵ M.Bowker, C.Morgan, N.Perkins, R.Holroyd, E.Fourre, F.Grillo and A.MacDowall, *J. Phys. Chem. B*, **109**, 2377 (2005)
- ¹⁶ S.Deckers, F.Habraken, W.F.van der Weg, A.W.D.van der Gon, J.F.van der Veen and J.W.Geus, *Appl. Surf. Sci.*, **45**, 121 (1990)
- ¹⁷ C.J.Baddeley, L.H.Bloxham, S.C.Laroze, R.Raval, T.C.Q.Noakes and P.Bailey, *J. Phys. Chem. B*, **105**, 2766 (2001)
- ¹⁸ C.J.Baddeley, L.H.Bloxham, S.C. Laroze, R.Raval, T.C.Q.Noakes and P.Bailey, *Surf. Sci.*, **435**, 827 (1999)
- ¹⁹ T.C.Q.Noakes, P.Bailey, S.Laroze, L.H.Bloxham, R.Raval and C.J.Baddeley, *Surf. and Interf. Anal.*,
- ²⁰ T.E.Jones, T.C.Q.Noakes, P.Bailey and C.J.Baddeley, *J. Phys. Chem. B*, **108**, 4759 (2004)
- ²¹ T.E.Jones, T.C.Q.Noakes, P.Bailey and C.J.Baddeley, *Surf. Sci.*, **569**, 63 (2004)
- ²² D.Tomanek, S.Mukherjee, V.Kumar and K.H.Bennemann, *Surf. Sci.*, **114**, 11 (1982)
- ²³ J.H.Hodak, M.Henglein, M.Giergsig and G.V.Hartland, *J. Phys. Chem. B*, **104**, 11708 (2000)
- ²⁴ S.P.Chenakin, *Appl. Surf. Sci.*, **84**, 1995 (91)

CHAPTER 5: AcOH/K/Au/Pd{111}

5.1 Introduction

Alkali metal promoters have been used extensively in many important industrial reactions. The current vinyl acetate monomer synthesis reaction uses a Pd/Au catalyst and a K modifier (usually in the form of acetate to convert ethene, oxygen and acetic acid to vinyl acetate and water. A review of the current literature surrounding K on Pd has been carried out in Chapter 1.6 and will not be repeated here.

In this chapter a variety of techniques have been used to investigate the effect of K on the AcOH/Au/Pd{111} system in an effort to understand the promoting role K may have. MEIS has been used to investigate the changing Pd/Au surface composition upon addition of K as a function of annealing temperature following Au deposition. Two distinct coverages of K were used in the study which also investigated the adsorption of AcOH on K/Au/Pd{111} surfaces.

RAIRS and TPD experiments have been utilised to probe the behaviour of acetic acid at the Pd/Au/K interface, both in regards to its interaction with the surface and also the surface decomposition pathway, whilst LEED and AES have been used to assist surface characterisation.

5.2 Experimental Section

Experimental and sample preparation procedures were carried out as detailed in Chapter 2.7. The MEIS, RAIRS and TPD experiments were carried out in separate chambers at different facilities and therefore on slightly different pre-annealed Au/Pd{111} surfaces.

For **RAIRS** experiments, sample preparation and characterisation was carried out as follows:

- Pd{111} single-crystal cleaned by argon ion bombardment and high temperature (1000 K) annealing cycles and checked for impurities by LEED and STM
- Once cleaned; Au deposited at room temperature by vapour deposition and checked periodically by STM until the required amount was present
- Pd/Au surface annealed to the required pre-annealing temperature for 5 minutes and allowed to cool to room temperature
- Pd/Au annealed surface analysed by STM
- K dosed at room temperature via a calibrated SAES getter source
- Pd/Au/K surface analysed by STM
- K annealed to 523 K for 7 mins
- Pd/Au/K surface analysed by STM
- Sample transferred to RAIRS chamber and RAIRS experiment carried out by sequential dosing of AcOH at a sample temperature of 300 K (through a leak valve) and IR analysis until desired amount had been deposited
- Sample transferred back to preparation chamber and analysed by STM
- Pd{111} crystal cleaned in preparation for next experiment

MEIS experiments followed the sequence:

- Pd{111} single-crystal cleaned by argon ion bombardment and high temperature (1000 K) annealing cycles and checked for impurities by AES and LEED
- Once cleaned; Au deposited at room temperature from a K-cell and the amount verified, on completion, by AES
- Pd/Au surface annealed to the required pre-annealing temperature for 5 minutes and allowed to cool to room temperature
- Pd/Au annealed surface transferred to scattering chamber and analysed by MEIS
- Sample returned to preparation chamber and K dosed via a calibrated SAES getter source
- Amount of K present checked by AES
- *If required (depending on nature of experiment)* - K annealed to 523 K for 7 minutes
- *If required* - Surface composition recorded by AES
- Pd/Au/K surface transferred to scattering chamber and analysed by MEIS
- Sample returned to preparation chamber required amount of AcOH dosed through a leak valve
- Dosed sample transferred back to scattering chamber and analysed by MEIS
- Sample returned to preparation chamber and surface composition analysed by AES
- Pd{111} crystal cleaned in preparation for next experiment

TPD experiments followed a third sequence:

- Pd{111} single-crystal cleaned by argon ion bombardment and high temperature (1000 K) annealing cycles and checked for impurities by AES and LEED
- Once cleaned; Au deposited at room temperature by vapour deposition and verified upon completion by LEED and AES
- Pd/Au surface annealed to the required pre-annealing temperature for 5 minutes and allowed to cool to room temperature
- K dosed via a calibrated SAES getter source
- Surface composition verified by AES
- *If required (depending on nature of experiment)* - annealed to 523 K for 7 mins
- *If required* - Surface composition recorded by AES
- AcOH dosed via a leak valve
- TPD experiment carried out
- Pd{111} crystal cleaned in preparation for next experiment

5.3 Results

5.3.1 AcOH /K/Pd{111} system

A variety of K coverages were deposited on a clean Pd{111} sample and were analysed by AES to determine the respective coverages. By using the ratio of the Pd peak, which appears at 330eV, to the K peak at 240eV an approximate K coverage can be determined. Six experiments were carried out in total;

- Clean Pd{111} *i.e.* No K dose
- 15 mins K dose from a SAES getter source
- 30 mins K dose from a SAES getter source
- 45 mins K dose from a SAES getter source
- 60 mins K dose from a SAES getter source
- 60 mins K dose from a SAES getter source, followed by a 7 minute anneal to 523 K – *The “Annealed-K” case*

Table shows the K:Pd ratio for the various depositions of K on Pd{111}. Using this as a rough guide to coverages we can deduce that the annealed-K scenario is equivalent to a deposition time of approximately 18 minutes and the results would be expected to be similar to the 15 minute and 30 minute cases.

K Dose Time / min	K/Pd Value
15	0.50
30	1.53
45	4.00
60	∞
Annealed	0.71

Table 5.3.1.1 – K to Pd ratios as a function of K dosing time for the deposition of K on Pd{111}.
Nb: The K/Pd Value is calculated by dividing the height of the K Auger peak found at 240 eV by the height of the Pd Auger peak at 330 eV. Also note that the value of ∞ for the 60 minute dose comes about as the Pd 330 eV is completely undetectable. This scenario is classed in this instance as “saturation”

It can be seen that the relationship is not linear, which is to be generally expected for the deposition of one metal on another, we can assume that K does saturate on Pd{111} at between 45 – 60 minutes dosing under the experimental conditions employed during this study. In fact, there is no way of proving the surface has saturated or not using AES and, all we can say is that there is no Pd visible and so the surface is expected to behave like K. A (2x2) LEED pattern was seen after the K was annealed but during the deposition there was no discernable LEED pattern detected.

Temperature Programmed Desorption (TPD) experiments were carried on the various K/Pd{111} surfaces that were created as above. In each case 30L AcOH was dosed onto the surface after the AES experiment used to calculate relative coverages was completed. These are shown for a variety of m/z values in Figures 5.3.1.1 – 5.3.1.4.

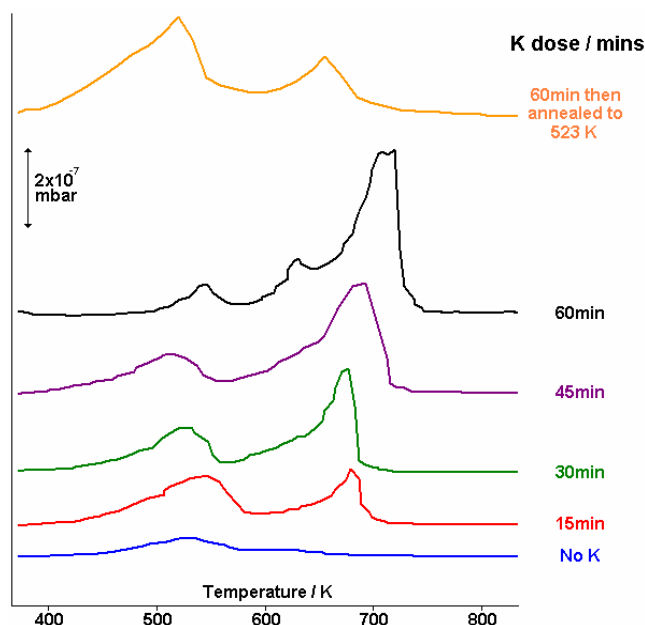


Fig 5.3.1.1 - A series of TPD spectra (mass 44, CO₂) following the adsorption of acetic acid on a K/Pd{111} surface as a function of K dosing time

The low temperature CO₂ desorption (as in Figure 5.3.1.1) that is seen on clean Pd{111} at *ca.* 520 K remains relatively consistent as the K pre-coverage increases, although the desorption trace is slightly broader and larger in the annealed-K case.

There is a second CO₂ desorption, which only exists when K is present, that sees an increase in T_{\max} from 680 K to *ca.* 720 K as the pre-coverage of K increases. In this instance, the annealed case does seem to closely mimic the behaviour of the 15 minute dose experiment, as predicted from the Auger data previously presented.

As a result of adding K to the clean Pd{111} surface, the CO desorption trace seen on the clean surface at *ca.* 430 K disappears and is replaced by a pair of peaks between 620 K and 680 K (see Figure 5.3.1.2).

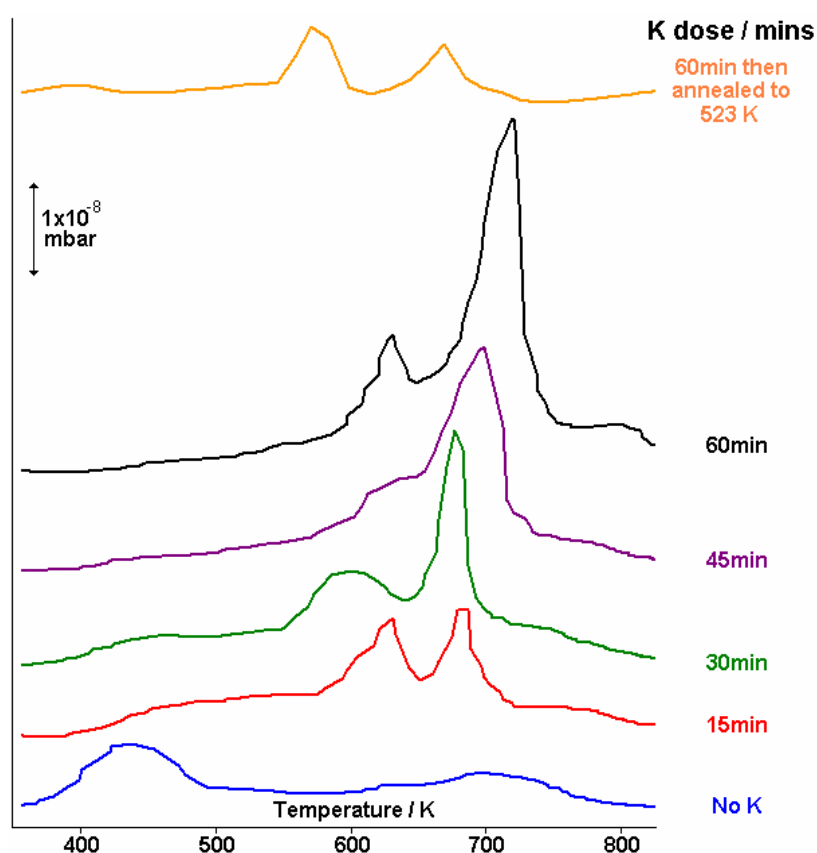


Fig 5.3.1.2 - A series of TPD spectra (mass 28, CO) following the adsorption of acetic acid on a K/Pd{111} surface as a function of K dosing time

Initially the two peaks are of similar size but the higher temperature peak becomes the more dominant of the two as the coverage of K increases. The T_{\max} of the higher temperature CO desorption increases slightly with increasing K pre-coverage from 680 K to *ca.* 720 K in a similar fashion to CO₂. Once again, the CO desorption of the

sample which was annealed after K deposition closely resembles the 15 minute K dose experiment.

H₂O desorption (Figure 5.3.1.3) is not detected in the experiment on clean Pd{111} but there are two small peaks at *ca.* 430 K and *ca.* 670 K in the 15 minute anneal experiment. As the K pre-coverage increases, the peak at 670 K becomes more prominent as well as shifting to a slightly higher T_{max} of *ca.* 720 K by the time of the “saturation-dose” experiment. There are also two lower temperature H₂O desorptions at *ca.* 450 K and 530K in the highest K coverage experiment which are not present in any of the other cases.

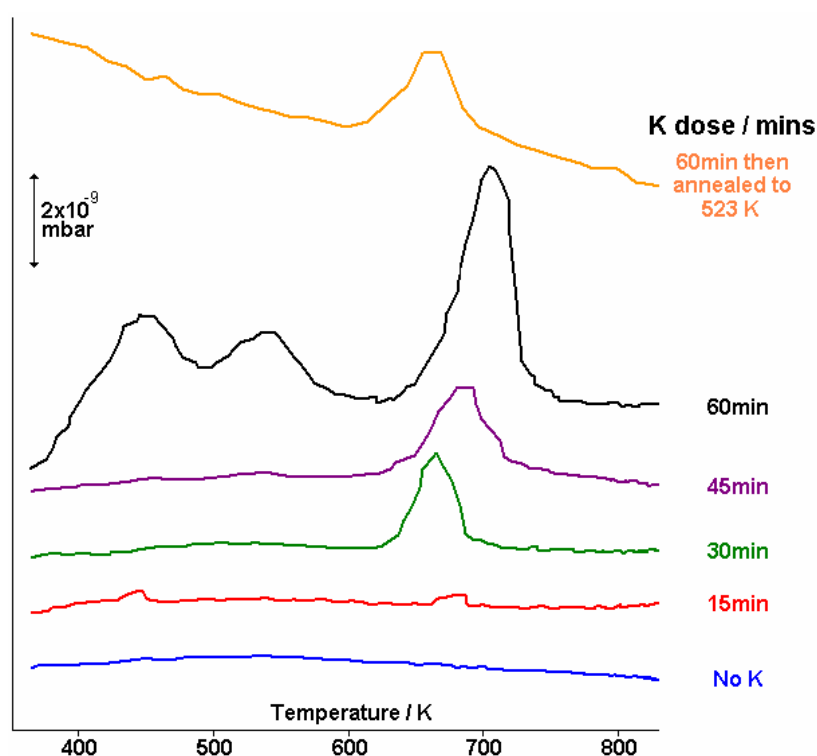


Fig 5.3.1.3 - A series of TPD spectra (mass 18, H₂O) following the adsorption of acetic acid on a K/Pd{111} surface as a function of K dosing time

Unlike CO and CO₂, the desorption of H₂O in the annealed K case more closely resembles the desorption trace of the 30 minute experiment and not the 15 as for the other two.

The initial broad H₂ desorption, with a T_{max} of *ca.* 650 K, which is seen on clean Pd{111} becomes sharper as the coverage of K on the surface increases. There is also a gradual shift in the T_{max} from *ca.* 700 K to *ca.* 730 K by the time of the highest K coverage experiment (Figure 5.3.1.4). H₂ desorption on the annealed-K on Pd{111} surface resembles the 15 minute non-annealed experiment in a similar manner to CO₂ and CO.

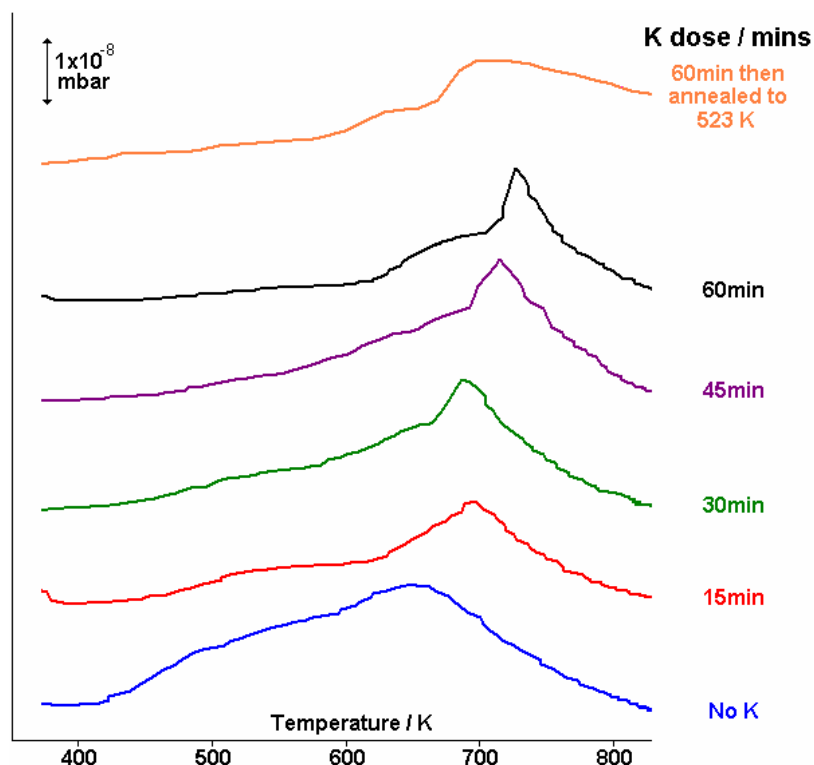


Fig 5.3.1.4 - A series of TPD spectra (mass 2, H₂) following the adsorption of acetic acid on a K/Pd{111} surface as a function of K dosing time

5.3.2 AcOH/K/Au/Pd{111}

Auger experiments investigating the deposition of K on various Au/Pd{111} bimetallic surfaces were carried out as a function of the pre-annealing temperature. Using similar analysis to that employed in 5.3.1 it has been calculated that the amount of K on the surface (relative to the amount of Pd *i.e.* the K/Pd value) increases as the amount of Pd{111} in the top layer increases.

In fact, when the AES spectrum was run after K was dosed on a Au/Pd{111} surface which had been previously annealed to 900 K, there was no evidence of the Pd 330 eV peak and a very small Au peak at *ca.* 70 eV. The only major peak visible was the K peak at 240 eV which was seen in the previous experiments.

MEIS experiments were also carried out on the K/Au/Pd{111} system with the intention of investigating the effect of K on the composition of the Au/Pd{111} bimetallic system.

We chose to concentrate on the more well-defined high pre-annealing temperature regime primarily due to time-constraints using the MEIS facility Daresbury. Since the STM and MEIS experiments reported in Chapters 3 and 4 reveal a complex morphology of the Pd/Au surfaces in the low pre-annealing temperature regime, it was decided to concentrate only on the systems where the pre-annealing temperature was >800 K, in other words, those systems with negligible sub-surface peaks in the Intensity versus Energy plots shown in Chapter 3.3.2.

K was deposited onto a Au/Pd{111} bimetallic surface, which had been initially characterised using MEIS. The K coverage was checked by AES and the sample was not annealed, leaving a large amount of K still on the surface. LEED was not carried out on the sample so as to avoid damaging the surface. A second MEIS experiment was then undertaken before the K/Au/Pd{111} surface was exposed to 30 L AcOH and a third MEIS run was carried out.

Table 5.3.2.1 overleaf shows the composition of the top two layers of the surface; before and after K deposition and following the AcOH dose.

Pre-Anneal Temperature	Atom % Au in top two layers		
	After Au deposition and anneal	After K deposition	After AcOH dose
800 K	36%	32%	36%
850 K	21%	14%	19%
900 K	21%	15%	16%
950 K	10%	10%	8%

Table 5.3.2.1 – Atom %Au in the top two layers of various Au/Pd{111} bimetallic surfaces prior to K deposition, after K deposition and after AcOH dose. The sample was not annealed after K was deposited.

A similar experiment was carried out, except in this case the K was annealed to 523 K after deposition and AES characterisation but prior to MEIS analysis. After annealing and cooling, the surface was investigated by LEED and a (2x2) pattern was invariably seen, albeit not as sharp as the (1x1) pattern seen for pure Pd{111}. Again, due to time constraints it was only possible to carry out two complete experiments on this system and the well-defined high pre-anneal temperature systems were investigated

Table 5.3.2.2 shows the composition of the top two layers of the surface; before and after K deposition and following the AcOH dose for the annealed K systems.

Pre-Anneal Temperature	Atom % Au in top two layers		
	After Au deposition and anneal	After K deposition	After AcOH dose
900 K	10%	5%	8%
950 K	14%	8%	14%

Table 5.3.2.2 – Atom %Au in the top two layers of various Au/Pd{111} bimetallic surfaces prior to K deposition, after K deposition and after AcOH dose. The sample was annealed to 523 K after K was deposited.

In addition to the MEIS experiments, TPD experiments were carried out on the AcOH/K/Au/Pd{111} system, involving both annealed and non-annealed K doses as a function of anneal temperature. In both cases, investigation of a wider range of starting Au/Pd{111} surfaces was possible. As in the K/Pd{111} case, 30L AcOH

was dosed onto the K/Au/Pd{111} surfaces and Figures 5.3.2.1 – 5.3.2.5 show various m/z traces in the **non-annealed** K scenario.

CO₂ desorbs from K/Au/Pd{111} surfaces in three states at 550 K, 625 K and 750 K following an anneal to 600 K (Figure 5.3.2.1 overleaf). Increasing the pre-anneal temperature to 700 K results in a change to two desorption states with T_{max} values of 540 K and 710 K. The 800 K and 900 K experiments both show the same desorption states although the dominant species changes slightly. In the 600 K case, the higher temperature state (750 K) dominates and in the 675 K experiment, the 710 K peak is the main feature. However, the lower temperature state at 540 K is the larger of the two in both the 800 K and 900 K pre-annealing temperature experiments.

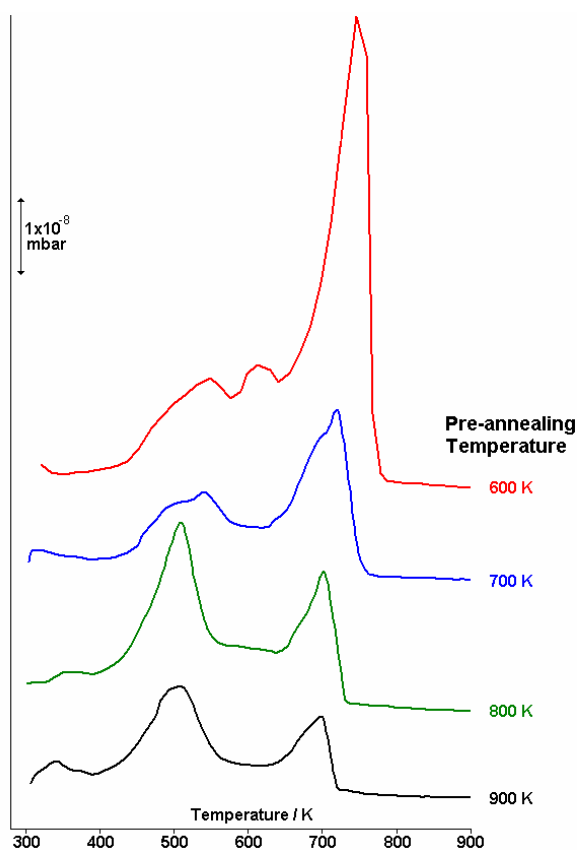


Fig 5.3.2.1 - A series of TPD spectra (mass 44, CO₂) following the adsorption of acetic acid on a K/Au/Pd{111} surface as a function of pre-annealing temperature. The sample was not annealed after K was deposited.

In these later experiments, data for $m/z = 39$ (*i.e.* K) were also acquired and are shown in Figure 5.3.2.2. K desorbs from the surface in three states at 470K, 550K and 750K on a bimetallic surface that was pre-annealed to 600 K. The dominant state in this case is the lowest temperature peak. Increasing the pre-anneal temperature to 700 K results in the loss of the two lower temperature desorption states but the retention of the high temperature feature at 750 K. The only significant change as we go from 700 K to 800 K and on to 900 K is that the area of the peak gets smaller with increasing anneal temperature.

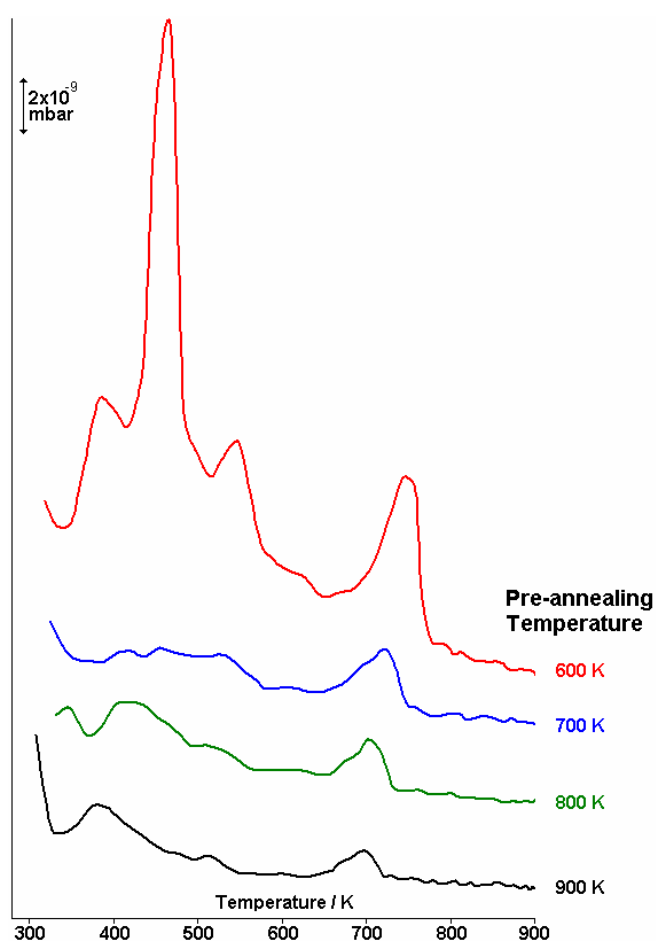


Fig 5.3.2.2 - A series of TPD spectra (mass 39, K) following the adsorption of acetic acid on a K/Au/Pd{111} surface as a function of pre-annealing temperature. The sample was not annealed after K was deposited.

CO desorbs from the K/Au/Pd{111} surfaces in two distinct states under all conditions investigated (Figure 5.3.2.3). One state is manifested by a large, sharp peak with a T_{\max} which drops gradually from *ca.* 750 K to *ca.* 700 K as the pre-annealing

temperature increases. There is a slight drop in peak area along with this downshift of the peak. In the 600 K case there is significantly more CO being desorbed than for the other systems but this is probably an artefact rather than a real effect. The other desorption state corresponds with the much smaller, broader which has a T_{\max} of *ca.* 450 – 500 K in all cases. As with the higher temperature state, there is a slight drop in the T_{\max} as the pre-annealing temperature rises.

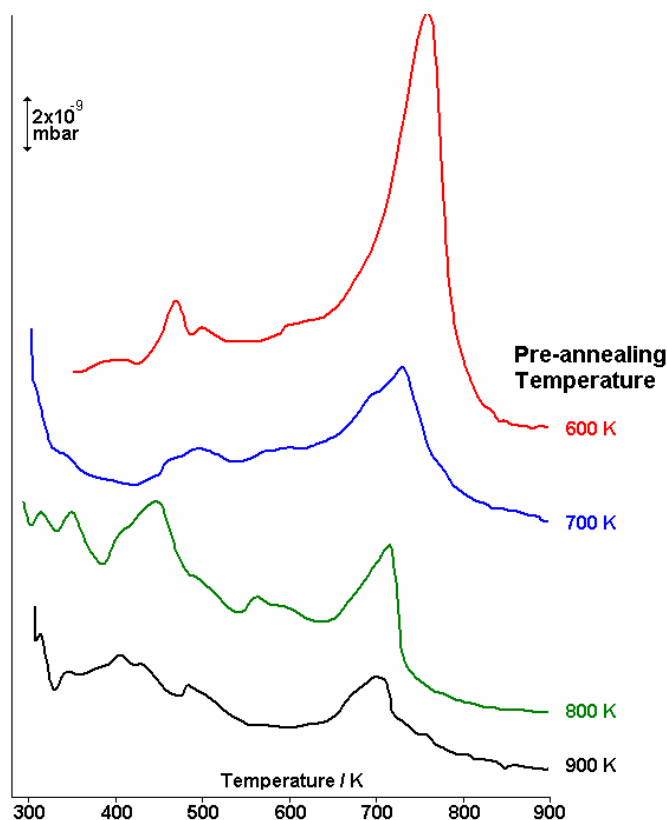


Fig 5.3.2.3 - A series of TPD spectra (mass 28, CO) following the adsorption of acetic acid on a K/Au/Pd{111} surface as a function of pre-annealing temperature. The sample was not annealed after K was deposited.

In a manner almost identical to CO, H₂O has a high temperature desorption state which sees both a drop in intensity and a drop in T_{\max} from *ca.* 750 K to 700K as the pre-annealing temperature increases. The peak profile and T_{\max} positions coincide with desorption of CO₂ as well as K and CO implying a link between the species being desorbed at the particular temperature.

In addition to the high temperature desorption state, H₂O desorbs from the K-covered surface in two lower temperature states at *ca.* 325 K and 410 K when the surface has been pre-annealed to 600 K prior to K deposition. Both these peaks are substantial in area and also have a very well-defined, narrow shape to them. There is some evidence that desorption state at 325 K is also present in the other systems but it is certainly not the dominant feature (Figure 5.3.2.4).

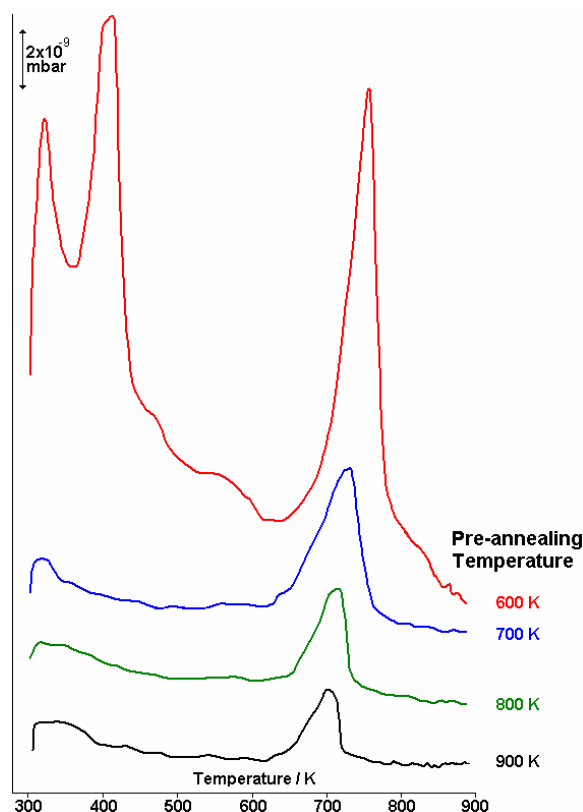


Fig 5.3.2.4 - A series of TPD spectra (mass 18, H₂O) following the adsorption of acetic acid on a K/Au/Pd{111} surface as a function of pre-annealing temperature. The sample was not annealed after K was deposited.

H₂ desorption (Figure 5.3.2.5 overleaf) only occurs with any great significance in the 600 K pre-annealed surface whereas there is a desorption state at *ca.* 800 K. There is evidence of smaller desorption states at similar T_{max} values for the 700 K and 800 K surfaces but there is very little evidence of H₂ desorption on the K/Au-900K/Pd{111} system .

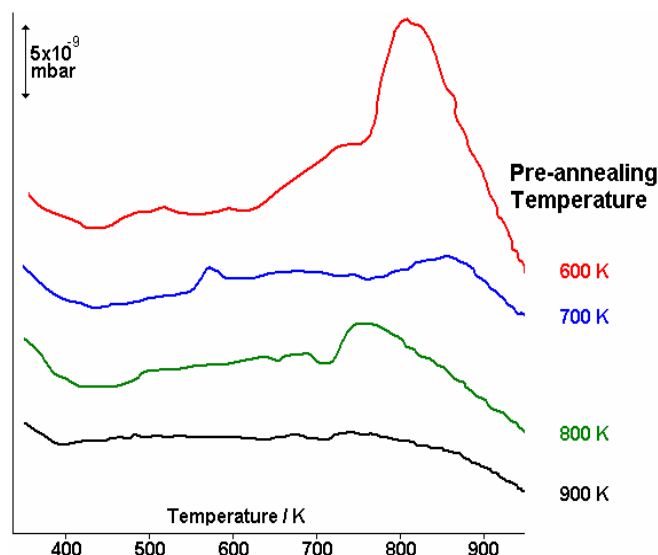


Fig 5.3.2.5 - A series of TPD spectra (mass 2, H₂) following the adsorption of acetic acid on a K/Au/Pd{111} surface as a function of pre-annealing temperature. The sample was not annealed after K was deposited.

The coincident desorption of CO₂, CO, H₂O and K at ~750 K is an interesting result which will be discussed later in Chapter 5.4. It also should be noted that the desorption traces for CO, CO₂, H₂O and H₂ for the K/Au-600K/Pd{111} system very closely resemble those for a “full” dosage of K on Pd{111}. It is possible that in both cases, the K overlayer formed is (for whatever reason) sufficiently thick for there to be no interaction between AcOH and the substrate. That is, both systems could be simply behaving as AcOH on K. In both cases the AES data contains a substantial K peak at 240 eV and very little else, which supports this theory.

Analogous TPD experiments to those in Figures 5.3.2.1 – 5.3.2.5 were carried out on Au/Pd{111} surfaces to which K had been deposited and then **annealed** up to 523 K, as a function of pre-annealing temperature after the Au deposition. Faint, poorly-defined (2x2) LEED patterns were seen for all of the surfaces after the post-K deposition anneal. The data for the same m/z values as before is provided in Figures 5.3.2.6 – 5.3.2.10. Note that in each case the 900 K experiment appears to be anomalous and it is contained within the Figures merely for completion. Analysis of

the AES as to the possible reasons for the strange data set have proven to be inconclusive

At lower pre-annealing temperatures (<750 K) CO₂ only has one desorption state with a T_{max} of *ca.* 550 K (Figure 5.3.2.6). This state remains as the pre-annealing temperature is increased but a second desorption state is now seen at a T_{max} of *ca.* 750 K. As the Au/Pd{111} pre-annealing temperature increases, the higher state becomes the more dominant one and we see a slight drop in the T_{max} of this peak to *ca.* 720 K.

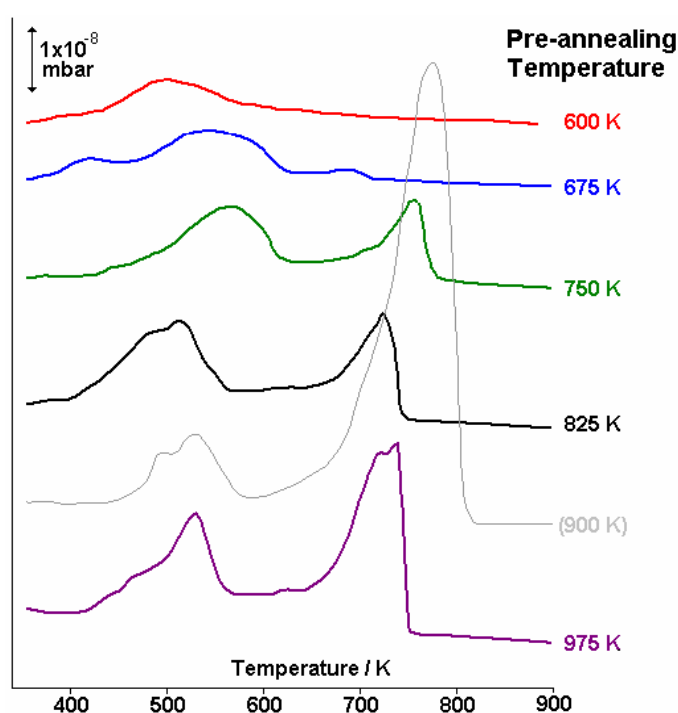


Fig 5.3.2.6 - A series of TPD spectra (mass 44, CO₂) following the adsorption of acetic acid on a K/Au/Pd{111} surface as a function of pre-annealing temperature. The sample was annealed to 523 K after K was deposited.

One K desorption state is observed on annealed K/Au/Pd{111} surfaces for low pre-annealing temperatures such as 600 K (Figure 5.3.2.7 overleaf). The T_{max} of the peak is *ca.* 515 K and this rises slightly when the sample has been pre-annealed to 675 K.

Once the pre-annealing temperature rises above 700 K there appears a second, higher temperature desorption state at *ca.* 760 K. This desorption state grows in intensity as

we raise the pre-annealing temperature and its T_{\max} value drops to *ca.* 710 K. The lower temperature desorption state is still there at 500 K but is much less prominent as pre-annealing temperature increases.

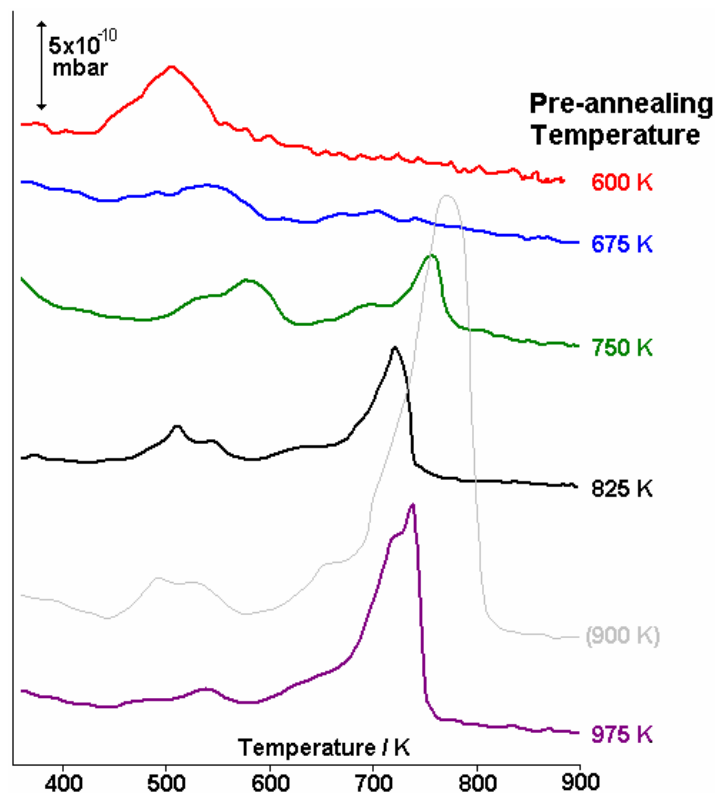


Fig 5.3.2.7 - A series of TPD spectra (mass 39, K) following the adsorption of acetic acid on a K/Au/Pd{111} surface as a function of pre-annealing temperature. The sample was annealed to 523 K after K was deposited.

We find that CO exhibits a very similar desorption trace pattern to K in that there is once again a high temperature peak (T_{\max} 750 K) which grows larger and drops to a slightly lower temperature as the pre-annealing temperature rises (Figure 5.3.2.8. overleaf).

There is also a lower temperature desorption state which has a T_{\max} of between 500 K and 580 K and is more prominent in the lower pre-anneal temperature cases which don't feature the high temperature desorption state favoured in the higher pre-annealing temperature samples.

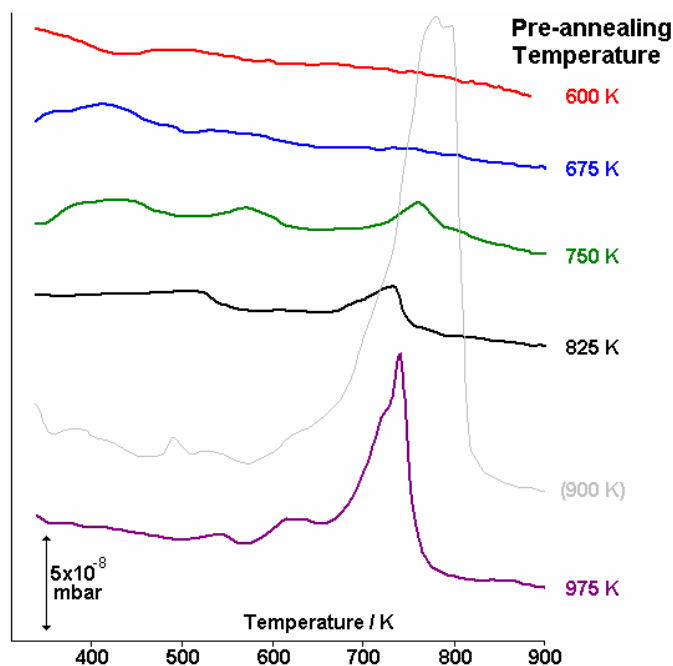


Fig 5.3.2.8 - A series of TPD spectra (mass 28, CO) following the adsorption of acetic acid on a K/Au/Pd{111} surface as a function of pre-annealing temperature. The sample was annealed to 523 K after K was deposited.

H₂ desorption is relatively insignificant except in the very high pre-anneal temperature experiments (Figure 5.3.2.9 overleaf).

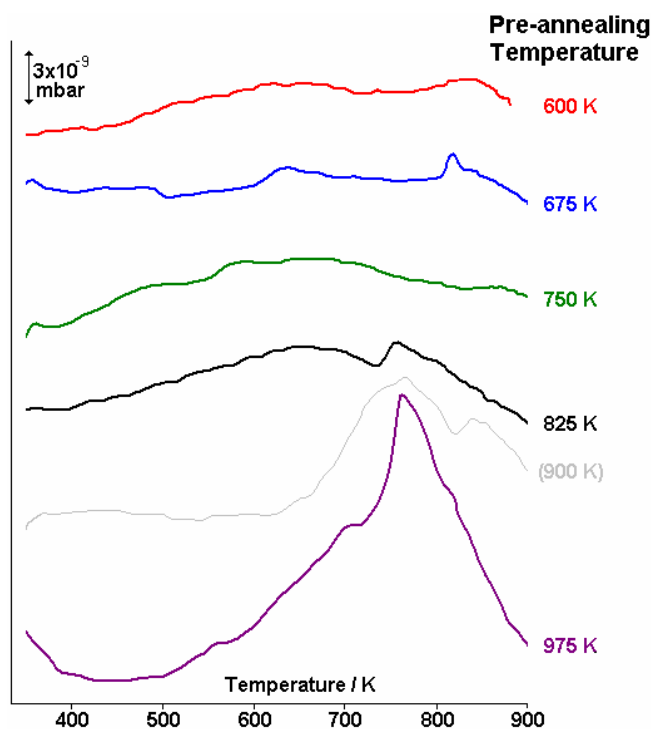


Fig 5.3.2.9 - A series of TPD spectra (mass 2, H₂) following the adsorption of acetic acid on a K/Au/Pd{111} surface as a pre-annealing temperature. The K was annealed to 523 K after being deposited.

There is a single desorption state with a T_{\max} of *ca.* 760 K observed on the 975 K surface and although the peak itself is sharp at its tip, desorption appears to take place over a large range as evidenced by the broad nature of the peak. It could be argued that there are two shallow peaks in the 600 K system with T_{\max} values of 600 K and 870 K but the intensity of these peaks is very small.

H₂O desorbs from the annealed K/Au/Pd{111} surfaces with a single strong desorption feature at a T_{\max} of *ca.* 750 K for pre-anneal temperatures above 700 K. The intensity of the peak increases as the pre-annealing temperature increases and there is also a slight downshift to a lower T_{\max} by 20-30 K (Figure 5.3.2.10)

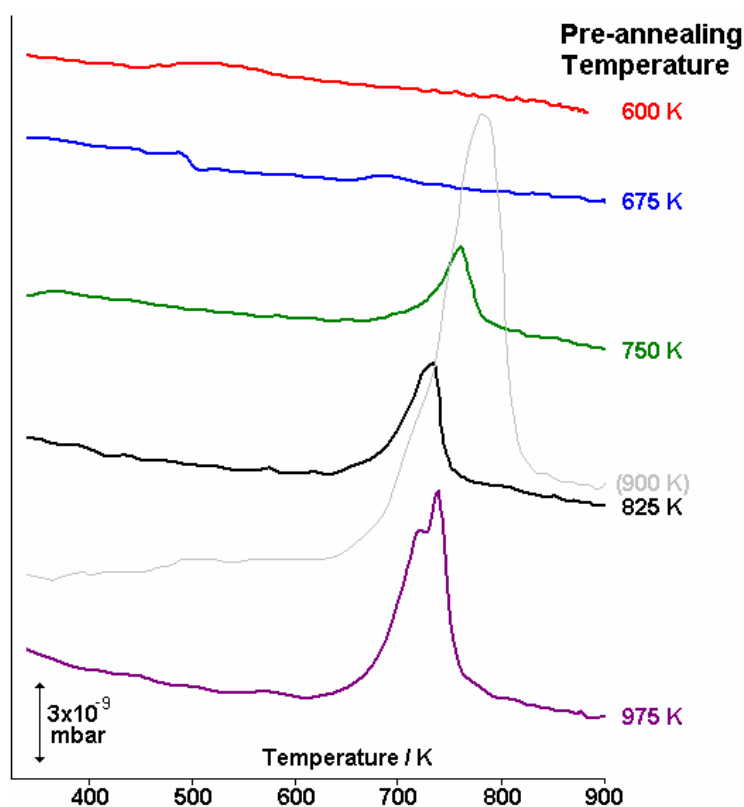


Fig 5.3.2.10 - A series of TPD spectra (mass 18, H₂O) following the adsorption of acetic acid on a K/Au/Pd{111} surface as a pre-annealing temperature. The K was annealed to 523 K after being deposited.

In addition to the TPD work carried out, RAIRS experiments were undertaken on the annealed K/Au/Pd{111} systems as a function of AcOH dose. Figures 5.3.2.11 – 5.3.2.13 show RAIRS data following the dosing of AcOH onto a variety of K/Au/Pd{111} surfaces.

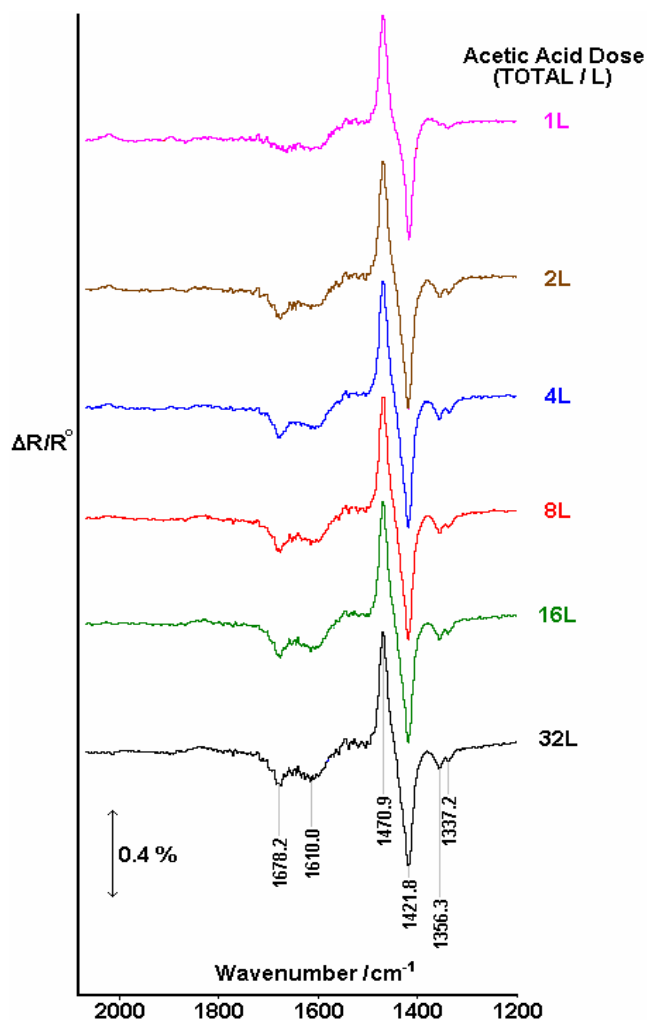


Fig 5.3.2.11 - RAIRS spectra on a sample of K/Au/Pd{111}, which was pre-annealed to 900 K, as a function of AcOH dose. The AcOH was dosed at a sample temperature of 300 – 310 K and the sample was re-annealed to 523 K between K deposition and AcOH dose

On the surface prepared with a pre-annealing temperature of 900 K, an AcOH dose of 1L appears to correspond to a saturation dose. There are two critical peaks, a positive band and a negative band respectively at 1471 and 1422 cm^{-1} , seen as soon as AcOH is dosed. These correspond to the $\nu_{\text{asym}}(\text{CO})$ stretch of carbonate being lost and simultaneously the presence of the $\nu_{\text{asym}}(\text{OCO})$ stretch of acetate. There are other

smaller negative bands present at 1678 cm^{-1} (probably a carbonyl stretch) and 1610 (the $\nu_{\text{sym}}(\text{OCO})$ of acetate, as well as CH_3 bend features at 1356 cm^{-1} and 1337 cm^{-1} .

Pre-annealing to 800 K instead of 900 K has a slight effect of the RAIRS data recorded in the annealed K on Au/Pd{111} case (Figure 5.3.2.12).

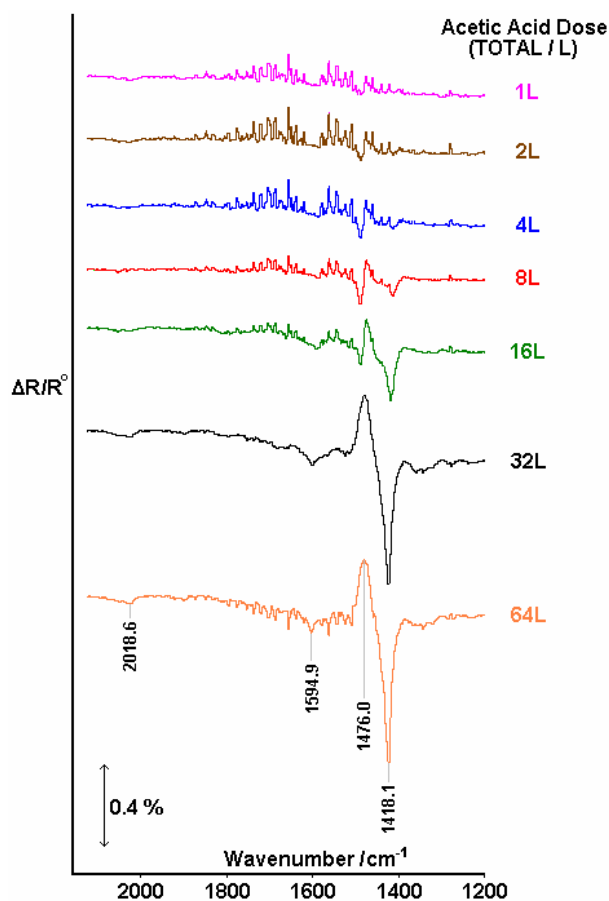


Fig 5.3.2.11 - RAIRS spectra on a sample of K/Au/Pd{111}, which was pre-annealed to 800 K , as a function of AcOH dose. The AcOH was dosed at a sample temperature of $300 - 310\text{ K}$ and the sample was re-annealed to 523 K between K deposition and AcOH dose

The positive band corresponding to the loss of carbonate (1476cm^{-1}) and the negative band representing the presence of acetate (1418cm^{-1}) are still present although it is not until a total AcOH dose of 64 L that we see saturation. There are also two small peaks at 2019 cm^{-1} ($\text{CO}_{(\text{ads})}$) and 1595 cm^{-1} ($\nu_{\text{asym}}(\text{OCO})$).

In the annealed K/Au/Pd{111} system where the bimetallic surface is annealed to 600 K prior to K treatment, there is no clear evidence of any band present in the RAIRS spectrum (Figure 5.3.2.12).

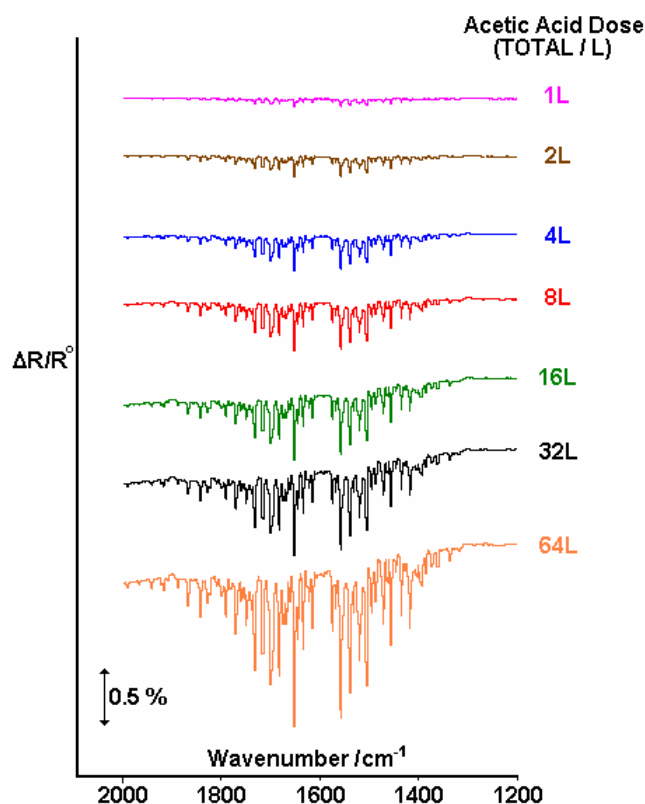


Fig 5.3.2.13 - RAIRS spectra on a sample of K/Au/Pd{111}, which was pre-annealed to 600 K, as a function of AcOH dose. The AcOH was dosed at a sample temperature of 300 – 310 K and the sample was re-annealed to 523 K between K deposition and AcOH dose

Despite the poor signal-to-noise ratio of the spectra at higher total AcOH dose (due to problems with water miscancellation) it can be seen that there neither positive nor negative peak bands are observed in the spectra. The most significant peaks would be those previously seen at *ca.* 1480 and 1420cm⁻¹ in the other systems. It is obvious that, even despite the noise, these peaks are not present in the data as presented.

5.4 Discussion

There have been a large number of studies of alkali metals (particularly K) on transition metal single crystal surfaces which have mainly focused on the addition of small molecules such as CO^{1,2,3}, CO₂^{3,4,5} as well as formate^{6,7} and carbonate⁸ containing species. In industrial synthesis of VAM, K is used as an alkali metal promoter in conjunction with silica supported bimetallic Pd/Au nanoparticles. AcOH is one of the feed stocks of the process but very little work has been reported on the industrially used Pd/Au/K/AcOH system.

Starting with the K/Pd{111} system, AES and LEED experiments concluded that when K is deposited on the surface it can form a multi-layer coverage if dosed for long enough, as evidenced by the presence of no other peaks in the AES except the one resulting from K at 240 eV. No STM images were found for this system and LEED experiments only showed the (1x1) pattern, associated with clean Pd{111}, and a high background.

Following on from the work by Over *et al.*⁹ we tried to recreate the $(\sqrt{3}\times\sqrt{3})R30^\circ$ overlayer that they previously saw with K/Pd{111}. However, initial experiments found that annealing to 523 K produced the LEED pattern associated with the (2x2) overlayer structure and not the $(\sqrt{3}\times\sqrt{3})R30^\circ$ as might be expected. Over *et al.* reported the presence of a $(\sqrt{3}\times\sqrt{3})R30^\circ$ overlayer after annealing the K/Pd{111} surface to 470 K whilst an anneal of 604 K was required in order to produce the (2x2) structure. However, we have been unable to recreate the $(\sqrt{3}\times\sqrt{3})R30^\circ$ overlayer and subsequently found that, in our UHV system, an anneal to 523 K is enough to recreate the (2x2) with a reasonably satisfactory LEED pattern.

It may be possible however, that the adsorption of background gases prevented the formation of the LEED patterns. The annealed K experiment was in very close agreement the data from the non-annealed K experiment after 15 minutes dosing. It is possible therefore to make the assumption that 15 minutes dose approximates to a $\frac{1}{4}$ ML of K which is the amount that would be present if K was forming a (2x2) overlayer structure on Pd{111}.

Further work on the K/Au/Pd{111} has found that an anneal to 523 K forms a very diffuse (2x2) LEED pattern. AES experiments seem to indicate that when the surface has an appreciable amount of Au on the surface (as in the 600 K pre-anneal case) the amount of K on the surface increases drastically when compared with a Pd rich surface for the same expected dose.

This phenomenon results in the TPD data for the experiment in which AcOH was dosed on the surface which has been pre-annealed to 600 K but not annealed after K deposition (Figures 5.3.2.1 – 5.3.2.5), being very similar to the AcOH on K/Pd{111} TPD when the K coverage is at “saturation” *i.e.* No Pd is visible on the surface in either case and we are essentially looking at the desorption trace of AcOH on K. It is known that Au and Na form an alloy on Au{111}¹⁰ and it is possible that K maybe do something similar on Au{111}. In fact Barth *et al.*¹¹ concluded that the Au{111} surface is reactive towards K atoms and forms mixed KAu surface layers at K coverages greater than 0.33 ML.

TPD results from the AcOH/K/Pd{111} systems show coverage dependent behaviour which is similar to the coverage dependent behaviour in the AcOH/Au/Pd{111} system discussed in Chapter 4. The concurrent desorption of CO₂, CO and H₂O

(arguably H₂ could be included as well) at a temperature of *ca.* 690 – 730 K (depending on the surface coverage) suggests that all the desorption products are derived from the same surface species.

The decomposition of a carbonate (CO₃²⁻) or bicarbonate (HCO₃⁻) would account for the CO₂ product, and probably the CO as well, whilst H₂O would most likely be formed by the reaction of O (from carbonate) with H_(ads) which is formed from the decomposition of acetate via CH_x species. This decomposition likely takes place at *ca.* 520 K and is responsible for the CO₂ peak at this temperature. The CO desorption at 600 K would then come from the recombination of C_(ads) and O_(ads) – each derived from the decomposition of acetate - and it is possible that the small peak in the CO₂ trace at the same temperature maybe from a similar recombination.

Liu *et al.* have seen a similar effect when they adsorbed K and CO₂ onto Pt{111}.⁵ They dosed K onto Pt{111} at 112 K and found CO₂ easy to adsorb. IR showed no peaks in the 1400cm⁻¹ region but annealing to 200 K produced peaks at 1440 and 1600cm⁻¹ which were assigned to carbonate via disproportionation of CO₂ into CO and CO₃²⁻. TPD experiments on this system found that CO desorbed at 640 K whilst CO₂ desorbed at slightly higher the temperatures of 674 K and 790 K. It is plausible to assign the high T peak to decomposition of carbonate and the other two to recombination reactions involving species created by the decomposition of acetate.

Incorporation of Au into the system seems to have a relatively insignificant effect when the sample is covered in the non-annealed “full” K dose experiments. This is to be expected as we are really investigating the interaction of acetic acid with a saturated K surface and so the effect of the Au is expected to be fairly negligible and

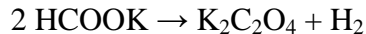
the concentration of Au at the surface of the alloy prior to K deposition is largely irrelevant. The decomposition of carbonate is still present as evidenced by the coincident desorption of K, CO₂, CO, H₂O and H₂ at *ca.* 700 K. There is also a fairly typical acetate related CO₂ desorption state at 500 K. The only slight anomaly in the data in the behaviour of these systems is the stark contrast between the 600 K pre-anneal surface and the rest, although this has been rationalised previously as being very similar in behaviour to the saturated K on Pd{111} case.

By contrast, the presence of Au makes a significant difference when the K is annealed prior to AcOH dose. As in the previous experiments, there is generally a coincident desorption of H₂O, H₂, CO, CO₂ and K at *ca.* 750 K which is once again assigned to the decomposition of carbonate. However, there is a considerable variation in intensity as a function of pre-annealing temperature which correlates with the Au coverage, to the extent that in the presence of Au rich surfaces (*i.e.* when the pre-anneal T is <700K) we see no evidence of carbonate decomposition at high temperature. The sensible conclusion is that we are forming either K₂CO₃ or KHCO₃.

There are two probably routes to this species; either by reaction of acetate on the K-covered surface to form carbonate or the reaction of background CO and/or CO₂ with the K-covered surface. The latter is more likely on the basis that a similar effect has been seen previously by, amongst others, Pratt and King,¹ in the absence of acetate species. Pratt and King adsorbed CO and CO₂ onto K-dosed Pd{110} and found evidence of carbonate formation. In the CO₂ case, which sticks very easily to Pd{110}, they found evidence for the $\nu_{\text{sym}}(\text{CO})$ of carbonate by RAIRS and also discovered the presence of a surface compound, K₂CO₃ which was stable up to 600 K. CO sticks less readily to K-dosed Pd{110} but high exposure at 320 K results in an IR

peak at 1440cm^{-1} which was assigned to the $\nu_{\text{asym}}(\text{CO})$ of carbonate. They also found that formate could be created on $\text{Pd}\{110\}$ by reaction with a contaminant – $\text{H}_{(\text{ads})}$.

Carbonate species have also been found on $\text{Co}\{10\bar{1}0\}$ by Toomes and King, by reaction of both CO and CO_2 with the K-dosed metal.^{2,3} In both cases, evidence was found by way of a carbonate related IR band at *ca.* 1460cm^{-1} . Further work by Toomes and King centred around dosing formic acid onto $\text{Co}\{10\bar{1}0\}$ modified by K. Following the anneal of the formic acid covered surface to 400 K an IR band was observed at 1479cm^{-1} which was immediately assigned to carbonate. Other bands at 759, 1317 and 1609 were assigned to the oxalate species which was also present on the surface. Annealing above 520 K led to an extra band at 880cm^{-1} which was eventually assigned to an out of plane bending of carbonate. Toomes and King rationalised the formation of carbonate and oxalate as follows;⁶



Herreraferro *et al.* have also found evidence of carbonate formation, this time on $\text{Ag}\{111\}$ ⁴. They adsorbed CO_2 onto the K-dosed metal surface and observed a sharp peak at 1480cm^{-1} which was assigned to carbonate. TPD experiments yielded a high temperature CO_2 at 800 K which was also related to the presence of carbonate on the surface.

Returning to the lack of carbonate decomposition in the low pre-anneal T systems in which the surface is rich, it is realistic to say that the presence of a significant amount of Au quenches the formation of carbonate. This suggests that Pd plays a significant role in stabilising the CO or CO_2 prior to the formation of carbonate. In these low pre-

annealing temperature experiments however, there is a coincident desorption of K and CO₂ at *ca.* 500K which is very indicative that the acetate species decomposing in this case is potassium acetate.

Further evidence for the formation of carbonate is provided by the RAIRS spectra for AcOH on the annealed K/Au/Pd{111} surfaces. In the 900K pre-anneal system the main bands are a positive one at 1471cm⁻¹ (which corresponds to the loss of the $\nu_{\text{asym}}(\text{CO})$ stretch of carbonate as a result of AcOH dosing) and a band due to the simultaneous presence of acetate (the $\nu_{\text{asym}}(\text{OCO})$ stretch at 1422cm⁻¹). There are other smaller bands present at 1678 (probably a carbonyl stretch), 1610 (the $\nu_{\text{sym}}(\text{OCO})$ of acetate) and two CH₃ bend features at 1356 and 1337 cm⁻¹. This leads us to conclude that the carbonate is probably formed by reaction of background CO and CO₂ with K on the surface to form K₂CO₃ or a different CO₃²⁻ species. Some of this is then displaced by acetate when the AcOH is dosed, hence the positive band in the RAIRS. Adsorbed acetate then decomposes upon heating at *ca.* 550 K and the remaining carbonate itself decomposes at *ca.* 740 K leading to the coincidental desorption of CO, CO₂, H₂O, H₂ and K. When a pre-annealing temperature of 800 K the only difference is that it takes a much larger total AcOH dose to achieve a similar amount of carbonate displacement (64 L as opposed to 1L).

A pre-annealing temperature of 600 K does not result in the presence of the positive carbonate band, which is unsurprising as we have determined from the TPD experiments that the carbonate does not form but rather acetate is the active species. The fact that we do not see any acetate on the surface in the RAIRS may be down to the fact that the acetate forms an AcOK type species which is either IR inactive or not detectable by IR.

However, there is definitely CO₂ present in the TPD and it is also possible that the acetate bands are swamped in the RAIRS by water as it is more likely for negative bands (such as acetate) to be hidden by water than positive ones. These data may suggest that the sticking probability of AcOH on K-covered bimetallic surfaces is strongly dependent on the bimetallic composition. On more Au-rich surfaces, it is possible that the formation of bimetallic Au-K compounds may limit the reactivity of K to AcOH adsorption.

The MEIS data suggest that K induces Pd segregation to the bimetallic surface. K has been found to desorb at *ca.* 980 K from Pd{110}¹² and the enthalpy of adsorption for this process was calculated to be *ca.* 260 kJmol⁻¹ using the Redhead equation,¹³

$$E_{des} = R.T_{max} \left[\ln \left(\frac{\nu.T_{max}}{\alpha} \right) \times 3.64 \right]$$

The segregation of one metal over another on a bimetallic surface can be related to the enthalpies of adsorption of the adsorbate and the two metals.¹⁴ The enthalpy of adsorption of K on Au is not known at this time and so it is difficult to predict which metal will segregate to the surface in this system. Further work would be required but our initial prediction is that it is the thermodynamics that are in favour of Pd segregation due to a larger enthalpy of adsorption for K on Pd rather than Au. It is also possible that a KAu surface alloy is being formed at the surface, as has been found previously by Barth *et al.*¹¹ If this is the case then the visibility of Au to the MEIS beam may be altered as a result of Au changing its structure in order to alloy with the K. This might result in there being a noticeable change in the apparent surface concentration after K deposition despite there being no significant alteration in the surface and sub-surface structure. Structural analysis is possible with MEIS and

further investigation into this system would be necessary to examine the validity of these arguments.

In Chapter 4, we showed that AcOH adsorption also induces Pd segregation. However, in the MEIS experiments shown in this chapter, it was shown that AcOH adsorption reversed the K induced Pd segregation returning the surface composition to a value close to the initial value. It seems therefore that AcOH adsorption results in the formation of a “potassium acetate” species (indeed we were able to identify a coincident desorption of K and CO₂ at ~550 K in some TPD spectra). This could be catalytically significant as the presence of KOAc may, at least to an extent, limit the leaching of Pd from the bimetallic particles which would be predicted to extend the lifetime of the catalyst by maintaining the integrity of the bimetallic particles. This hypothesis requires future studies.

5.5 Conclusions and Future Work

1. K_2CO_3 (or a related carbonate species) forms rapidly when K is deposited on Pd{111} at room temperature, by the reaction of background CO and CO_2 with K on the surface. The carbonate is also formed on Au/Pd{111} surfaces when there is a significantly low (<10%) amount of Au in the surface layer.
2. Upon annealing to 523 K following the K dose, a p(2x2) overlayer structure is formed on the surface with a nominal K coverage of 0.25 ML in both the Pd{111} and Au/Pd{111} cases. The Pd{111} must play an important role in the stabilisation of CO and CO_2 on the surface prior to reaction with K, as in cases of high Au coverages the carbonate is not formed upon addition of K.
3. Deposition of K to the Au/Pd{111} bimetallic surface at room temperature also results in the segregation of Pd{111} to the surface, which manifests as a drop in the Au composition of the top two layers.
4. Dosing AcOH at 300 K to the K/Au/Pd{111} surface results in the formation of surface AcOK species and the loss of some carbonate. At high initial Pd surface concentrations this process reaches equilibrium quickly (1L AcOH on a 900 K pre-annealed surface) whereas at intermediate coverages the AcOH dose needs to be higher before saturation acetate coverage is achieved. (>32L AcOH on a 800 K pre-annealed surface). At lower initial Pd surface concentrations there is no carbonate to be removed. Additionally, dosing AcOH onto the K-covered Au/Pd{111} results in the composition of the top two layers reverting back to its initial pre-K value. The net effect of adsorbing AcOH on K/Au/Pd{111} is that there is no real segregation of Pd – in contrast to AcOH/Au/Pd{111} in Chapter 4.
5. Heating of the AcOH/K/Au/Pd{111} surface from room temperature results in the loss of decomposition of an acetate species (with associated desorptions) at

low T (*ca.* 500 K) followed by the decomposition of carbonate (with associated desorptions) at higher T. In the lower pre-anneal T cases (higher Au concentration at the surface) there is only desorption of acetate recorded. In the case of low Au coverages, there is a subtle drop in the T_{\max} of carbonate desorption as the Pd concentration grows larger.

Clearly, there is a concern with carrying out experiments using K on Pd{111} as the surface is extremely reactive to background gases. To surmount this problem it may be possible to carry out experiments whereby KOAc is dosed in vacuum to limit the formation of surface carbonate species. Other future work resulting from this chapter will be covered in Chapter 6.2 as this work will form a large part of the future work resulting from this thesis.

5.6 References

- ¹ S.J.Pratt and D.A.King, *Surf. Sci.*, **540**, 185 (2003)
- ² R.L.Toomes and D.A.King, *Surf. Sci.*, **349**, 19 (1996)
- ³ R.L.Toomes and D.A.King, *Surf. Sci.*, **349**, 65 (1996)
- ⁴ P.Herrerafierro, K.L.Wang, F.T.Wagner, T.E.Moylan, G.S.Chottiner and D.A.Scherson, *J. Phys. Chem.*, **96**, 3788 (1992)
- ⁵ Z.M.Liu, Y.Zhou, F.Solymosi and J.M.White, *Surf. Sci.*, **245**, 289 (1991)
- ⁶ R.L.Toomes and D.A.King, *Surf. Sci.*, **349**, 43 (1996)
- ⁷ M.D.Weisel, J.G.Chen, F.M.Hoffman, Y.K.Sun and W.H.Weinberg, *J. Chem. Phys.*, **97**, 9396 (1992)
- ⁸ A.Berna, A.Rodes, J.M.Feliu, F.Illas, A.Gil, A.Clotet and J.M.Ricart, *J. Phys. Chem. B*, **108**, 17928 (2004)
- ⁹ H.Over, Y.D.Kim and S.Schwegmann, *Phys. Chem. Chem. Phys.* **1**, 2001 (1995)
- ¹⁰ S.L.M.Schröder, A.Neumann, T.Solomon, P.Lenz-Solomon and K.Christmann, *Surf. Sci.*, **337**, 285 (1995)
- ¹¹ J.V.Barth, R.Schuster, R.J.Behm and G.Ertl, *Surf. Sci.*, **348**, 280 (1996)
- ¹² S.J.Pratt, D.K.Escott and D.A.King, *Phys. Rev. B*, **68**, 235406 (2003)
- ¹³ S.J. Garrett, CEM924 course notes, Michigan State University, Spring, **6.1**, 13.5 (2001)
- ¹⁴ D.Tomanek, S.Mukherjee, V.Kumar and K.H.Bennemann, *Surf. Sci.*, **114**, 11 (1982)

CHAPTER 6: Summary, Future Work and Publications

6.1 Summary

The role of Au in the Pd-catalysed synthesis of VAM has been examined using a variety of surface science techniques. The behaviour of the bimetallic Pd{111}/Au surface has been investigated, both on its own and in relation to the adsorption and decomposition of AcOH. Studies with co-adsorbed C have also been incorporated into the system and an initial study of the AcOH/K/Au/Pd{111} system has been reported.

The growth of Au on Pd{111} is close to pseudomorphic. The 4.8% lattice mismatch means that the first couple of Au layers grow in a slightly strained manner, resulting in the Moiré structure with an 80Å periodicity. The Au grows as islands on the Pd{111} surface. Au/Pd{111} forms two distinct regimes depending on the pre-anneal temperature (and as a result on the %Au in the top couple of layers):

- **At low pre-annealing temperatures** (<750 K) there is a distinct amount of Au in the near sub-surface layers and as a result there is a significant region of the sub-surface (7-13 layers) that exists as a Pd/Au alloy which has a slightly larger (2.77Å rather than 2.75Å at 10% Au) lattice constant to pure Pd.
- **At high pre-anneal temperatures** (>825 K) the amount of Au in the sub-surface has dropped to a level such that it no longer has a significant presence in the alloy. This is due to the Au diffusing further down into the bulk and so diluting the amount of Au pre layer. Analysis has shown that as the %Au drops below 10% in the lower layers, the alloy no longer becomes visible to the MEIS beam, indicating a near-pseudomorphic alloy integrated into the Pd{111} crystal structure. With increasing pre-annealing temperature the surface becomes flatter and more Pd-rich until, by 975 K pre-annealing

temperature, the surface is flat with large terraces, mimicking the pure Pd{111} surface.

The adsorption of AcOH on Au/Pd bimetallic surfaces causes a significant segregation of Pd to the top two layers of the surface. AcOH adsorption at 300 K occurs via two competing pathways on Au/Pd{111}. One adsorption pathway, involving the formation of adsorbed acetate, is observed at all compositions. A second pathway also occurs on Pd-rich surfaces whereby $\text{CO}_{(a)}$ and $\text{O}_{(a)}$ is formed at 300 K. The presence of Au quenches the rate of decomposition of adsorbed acetate resulting in a shift of ~ 50 K in the T_{max} of the associated CO_2 desorption peak compared with Pd{111}. AcOH decomposition results in the formation of clusters which we assign to surface carbon. The presence of surface carbon may quench the pathway to the formation of $\text{CO}_{(a)}$ from acetic acid.

Deposition of K to the Au/Pd{111} bimetallic surface at room temperature also results in the segregation of Pd to the surface, which manifests itself as a drop in the Au composition of the top two layers. However dosing AcOH onto the K-covered Au/Pd{111} results in the composition of the top two layers reverting back to its initial pre-K value. The net effect of adsorbing AcOH on K/Au/Pd{111} is that there is no real segregation of Pd – in contrast to the Au/Pd{111} system in the absence of K.

K_2CO_3 (or a related carbonate species) forms rapidly when K is deposited on Pd{111} at room temperature, by the reaction of background CO and CO_2 with K on the surface. The carbonate is also formed on Au/Pd{111} surfaces when there is a significantly low (<10%) amount of Au in the surface layer. Following annealing of

the potassium covered surface to 523 K, a p(2x2) overlayer structure is formed on the surface with a nominal K coverage of 0.25 ML in both the Pd{111} and Au/Pd{111} cases. The Pd{111} must play an important role in the stabilisation of CO and CO₂ on the surface prior to reaction with K, as in cases of high Au coverages the carbonate is not formed upon addition of K.

Dosing AcOH at 300 K to the K/Au/Pd{111} surface results in the formation of surface AcOK species and the loss of some carbonate. At high initial Pd surface concentrations this process reaches equilibrium quickly (1L AcOH on a 900 K pre-annealed surface) whereas at intermediate coverages the AcOH dose needs to be higher before saturation acetate coverage is achieved. (>32L AcOH on a 800 K pre-annealed surface). At lower initial Pd surface concentrations no carbonate removal is detected which is in line with the observation from TPD that no carbonate is formed on Au rich surfaces.

Heating of the AcOH/K/Au/Pd{111} surface from room temperature results in the loss or decomposition of an acetate species (evidenced by the desorption of CO₂) at low temperature (*ca.* 500 K) followed by the decomposition of carbonate (evidenced by a coincident desorption of CO₂, CO, H₂O and K) at higher temperature. In experiments carried out at the lower pre-annealing temperatures (i.e. higher Au concentration at the surface) acetate decomposition only is detected. In the case of low Au coverages, there is a subtle drop in the T_{max} of carbonate desorption as the Pd concentration grows larger.

6.2 Future Work and Publications

6.2.1 Suggested Further Work

Possible future work resulting from this project may include:

- Further study of the Au/Pd{111} bimetallic system encompassing a greater range of starting surface compositions with particular emphasis on trying to solve some of the structural questions posed by this work.
- Further study of the AcOH/K/Au/Pd{111} system encompassing a greater range of values for starting Pd/Au composition and K coverage.
- Study of the K/Au/Pd{111} systems using AcOK instead of separate K and AcOH.
- Incorporation of other VAM synthesis feed stocks into the system (such as ethene, O₂ and vinyl acetate) either in a 5/6 component system or individually as we have done for AcOH.
- A move towards studying supported clusters and colloid particles rather than single-crystals. This will help to shift the research towards a more industrially relevant direction.

6.2.2 Publications

“The Effects of Gold and Co-adsorbed Carbon on the Adsorption and Thermal Decomposition of Acetic Acid on Pd{111}” **Journal of Physical Chemistry B (in press)**

- T.G. Owens, T.E. Jones, T.C.Q. Noakes, P. Bailey and C.J. Baddeley

6.2.3 Publications in Preparation

“The structure and composition of near-surface Pd/Au alloys formed by thermal treatment of ultra-thin Au films on Pd{111}” **to be submitted to Surface Science**

- T.G. Owens, T.E. Jones, T.C.Q. Noakes, P. Bailey, D.J. O’Connor and
C.J. Baddeley

“The influence of co-adsorbed potassium on adsorption of acetic acid on {111}-oriented Pd/Au surfaces” **to be submitted to Journal of Physical Chemistry B**

- T.G. Owens, T.E. Jones, T.C.Q. Noakes, P. Bailey and C.J. Baddeley